GRAVITATIONAL EFFECTS ON FLOW INSTABILITY AND TRANSITION IN LOW DENSITY JETS

FINAL REPORT

Ajay K. Agrawal
Ramkumar Parthasarathy

School of Aerospace and Mechanical Engineering
865 Asp Avenue, Room 212
University of Oklahoma
Norman, Oklahoma 73019

NASA Grant NAG 3-2388

November 2004

ABSTRACT

Experiments were conducted in Earth gravity and microgravity to acquire quantitative data on near field flow structure of helium jets injected into air. Microgravity conditions were simulated in the 2.2-second drop tower at NASA Glenn Research Center. The jet flow was observed by quantitative rainbow schlieren deflectometry, a non-intrusive line of sight measurement technique suited for the microgravity environment. The flow structure was characterized by distributions of helium mole fraction obtained from color schlieren images taken at 60 Hz. Results show that the jet in microgravity was up to 70 percent wider than that in Earth gravity. Experiments reveal that the global flow oscillations observed in Earth gravity are absent in microgravity. The report provides quantitative details of flow evolution as the experiment undergoes change in gravity in the drop tower.

Next, rainbow schlieren deflectometry combined with high-speed digital imaging was used to study buoyancy effects on flow structure of a helium jet discharged vertically into air at jet Reynolds number of 490 and jet Richardson number of 0.11, for which buoyancy is often considered unimportant. Experimental results show global oscillations at a frequency of 27 Hz in Earth gravity. In microgravity, the jet oscillations vanished and the jet width increased. Results provide a direct physical evidence of the importance of buoyancy on the flow structure of low-density gas jets at a Richardson number considered too small to account for gravity.

A computational analysis of buoyancy-induced instability in the near-field of an isothermal helium jet injected into quiescent ambient air environment was also conducted. Laminar, axisymmetric, unsteady flow conditions were considered for the analysis. The transport equations of helium mass fraction coupled with the conservation equations of mixture mass and momentum were solved using a staggered grid finite volume method. The jet Richardson numbers of 1.5 and 0.018 were considered to encompass both buoyant and inertial jet flow regimes. Buoyancy effects were isolated by initiating computations in Earth gravity and subsequently, reducing gravity to simulate the microgravity conditions. Computed results concur with experimental observations that the periodic flow oscillations observed in Earth gravity subside in microgravity.

The effects of the mean velocity profiles on the instability characteristics in the near-injector region of axisymmetric low-density gas jets injected vertically upwards into a high-density gas medium were investigated using linear inviscid stability analysis. The flow was assumed to be

isothermal and locally parallel. Three velocity profiles, signifying different changes in the mean velocity in the shear layer, were used in the analysis. The effects of the inhomogeneous shear layer and the Froude number (signifying the effects of gravity) on the instability for each set of mean profiles were delineated. The temporal stability results indicated that a reduction in the growth rate with a decrease in the Froude number. At large Froude numbers (negligible gravity), a critical density ratio was identified for each of the three profiles at which the jet just became absolutely unstable. The jet became absolutely unstable for all the density ratios smaller than the critical density ratio and was convectively unstable for the density ratios greater than the respective critical density ratio, thus, demarcating the boundary between absolute and convective instability regimes. The critical density ratio was around 0.5 for the uniform profiles and was around 0.8 for the parabolic profile. The critical density ratio for each velocity profile increased as the Froude number is reduced. A critical Froude number was also determined for the three profiles, below which the jet became absolutely unstable for all the density ratios less than unity. The value of the critical Froude number was around 1. The effects of buoyancy on the absolute instability characteristics of the jet were substantial for the Froude numbers below the critical Froude numbers, thus differentiating the momentum-driven regime and the buoyancy-driven regime.

1. INTRODUCTION

Low-density gas jets are found in many engineering applications and natural phenomena, for example, exhaust from engines and stacks in industry, fuel leaks and accidental fires, diffusion flames, and geophysical events such as volcanic eruptions. Several recent studies [1-3] have focused on the far-field behavior of low-density jets using helium as the jet fluid. However, the near field jet behavior has direct influence on the acoustic noise and flow development in the far field. Thus, an understanding of the flow structure in the near field of low-density gas jets is of significant fundamental importance. Subbarao and Cantwell [4] studied the near field flow behavior of helium jets issued from a vertical tube into a co-flow of air. The jets were characterized as buoyant for jet Richardson number, $Ri = [gd(\rho_a-\rho_j)/ \rho_j U_j^2$ where g is the gravitational acceleration, d is the tube inside diameter, ρ_a and ρ_j are, respectively, the free-stream and jet densities, and U_j is the mass-averaged jet exit velocity] in experiments varying between 0.5 and 6.0. They observed an extremely regular flow field consisting of periodic formation and breakdown of helium-containing vortical cells. Measurements revealed large centerline velocity fluctuations, and early and abrupt breakdown of the potential core. Even the large-scale structure after the breakdown repeated itself with regularity. The Strouhal number, $St =[f\ d/U_j$ where f is the oscillation frequency] of the oscillating mode was independent of the Reynolds number. For $Ri > 1.0$, St scaled with Ri, indicating buoyancy-dependent instability mode. However, for $Ri < 0.5$, the Strouhal number was independent of the Richardson number. They speculated that perturbations in the air stream, for example, on the surface boundary layer outside the jet tube, were likely to dominate the flow instability and transition processes.

Pulsations in the near field of helium jets flowing into quiescent air were also observed by Hamins et al [5], who found that a minimum jet velocity was required to trigger the oscillations. The measured St correlated with Froude number, $Fr =[gd/U_j^2$ or inverse Richardson number), suggesting that the oscillations were buoyancy induced. They found that the St-Fr correlation for helium jets differed from that for flickering flames, implying differences in the buoyancy effects in non-reacting and reacting jets. Mell et al [7] performed numerical simulations to helium jets in air and found excellent agreement between computed oscillation frequencies with those obtained experimentally by Hamins et al [6] over a range of Froude numbers.

Experiments in naturally unstable helium jets by Cetegen and Kasper [7] extended the operating regime of Richardson numbers to those in pool fires and buoyant plumes. The oscillation frequency was represented by a correlation between St and Ri for Ri varying from 1.5 to $5.0x10^4$. Phase resolved laser-Doppler velocity measurements revealed buoyant acceleration of the jet fluid accompanied with strong radial inflow of the surrounding air. A toroidal vortex ring was formed near the jet exit in the region of the highest centerline velocity. As the vortex convected downstream, it interacted with and affected the primary jet flow structure. Cetegen [8] reported similar mechanistic details of vortex formation and convection using particle image velocimetry. Flow oscillations in the near field of low-density jets have also been observed at smaller Richardson numbers [9-12].

Although oscillations in the near field of low-density gas jets at Richardson numbers above unity are attributed to buoyancy, no direct physical evidence has been acquired in previous experiments. Thus, the present study was conducted to investigate the effects of buoyancy on the stability and flow structure of low-density gas jets. It involves experiments in Earth gravity and microgravity, computational fluid dynamics (CFD) analysis, and stability analysis. Each of these components is discussed separately in the following sections.

2. EXPERIMENTAL STUDY

The jet flow was quantified by helium concentration measurements obtained using the quantitative Rainbow Schlieren Deflectometry (or RSD) technique [13]. The RSD is a non-intrusive optical diagnostics technique, especially suited for whole field measurements in the microgravity environment. In RSD technique, the optical setup is tolerant to minor mechanical vibrations or misalignments, power-consuming lasers often unsuitable for use in microgravity are not required, and seeding of the flow presenting unique challenges in microgravity is avoided. The technique has been used for measurements of concentration in helium jets [15-16], and temperature in diffusion flames in Earth gravity [16-17] and microgravity [18]. The microgravity environment was simulated in the 2.2-second drop tower facility at the NASA Glenn Research Center. The experimental approach, results and conclusions of the study are presented in the following sections.

2.1 Experimental Setup.

The experimental setup is housed in a drop rig, 840-mm high, 960-mm long and 400-mm wide, with a standard aluminum A-frame. Al-Ammar [18], who conducted experiments with hydrogen gas-jet diffusion flames in Earth gravity and microgravity, completed the initial setup. The experimental setup was modified for helium jet experiments of the present study. It consists of three major components: flow system, rainbow schlieren apparatus, and image recording system. Helium gas was supplied from two 1000 cm^3 pressurized cylinders. A pressure relief valve set at 1.38 MPa (200 psig) was placed between the cylinders. The pressure regulator maintained the gas supply pressure at 690 kPa (100 psig). A calibrated mass flow meter was used to measure the helium gas flow rate. A metering valve controlled the gas flow rate. A solenoid valve was used to instantaneously activate or block the gas flow. A positioning jack was used to locate the jet tube with respect to the schlieren field of view. Jet tubes of 19.1mm and 31.8mm inside diameter were used in this study. The upstream and bend regions of the jet tube were filled with steel wool to minimize the flow non-uniformities. Steel screens were placed at the inlet and exit sections of the bend region. The straight length of the jet tube was 0.30m because of the spatial constraints of the drop rig. Tube outside was tapered to reduce the wall thickness at the jet exit to 1.3mm and 0.3mm, respectively, for the larger and smaller diameter tubes. Unlike Cetegen [6-7], no screen to affect flow uniformity at the jet exit was used. Thus, the present experiment represents naturally occurring conditions at the jet exit, providing true representation of such jets in practical applications.

The jet flow structure was visualized and quantified by the rainbow schlieren apparatus. The light input to a 5-μm wide and 3-mm high source aperture is provided by a 150-W halogen light source connected through a 600-μm diameter fiber-optic cable. The source aperture is placed at the focal point of an 80-mm diameter, 310-mm focal length collimating lens. The collimated light rays passing through the test section are deflected by density gradients in the flow field. The light rays are decollimated by an 80-mm diameter, 1000-mm focal length decollimating lens. Because of space constraints of the setup, a pair of 100-mm diameter, aluminum coated flat surface mirrors was used to fold the rays by 180 degrees. The folded light rays form the displaced image of the source aperture on a 3.5-mm wide, computer generated, symmetric rainbow filter, placed at the focal point of the decollimating lens. A camera lens of 75-mm focal length is used to image the test section onto the CCD array.

2.2 Schlieren Analysis

The angular deflection of a light ray by an axisymmetric refractive index field is given for small deflections by the following relationship:

$$\varepsilon(y) = 2y\int_{y}^{\infty} \frac{d\delta}{dr}\frac{dr}{\sqrt{\left(r^2 - y^2\right)}}, \quad (1)$$

where $\delta = (\eta\text{-}1)$ is the refractive index difference, and η is the refractive index of the test medium normalized by that of the surrounding air. In the RSD technique, the deflection angle is determined from measurements of color (or hue) in the schlieren image and the color filter calibration curve [13]. The refractive index difference is computed from Abel inversion of Eq. (1) expressed in discrete form as

$$\delta(r_i) = \delta(i.\Delta r) = \sum_{j=i}^{NN} D_{ij}.\varepsilon_j, \quad (2)$$

where Δr is the sampling interval and D_{ij} are geometric coefficients given by [19]. In an ideal gas at constant temperature (T) and pressure (P), the refractive index difference is:

$$\delta = \frac{P}{\bar{R}T}\sum_{l}\kappa_l X_l M_l, \quad (3)$$

where $\bar{R}$ is the universal gas constant, κ is the Dale-Gladstone constant, X is the species mole fraction, and M is the species molecular weight. The summation in Eq. 3 is taken over three species, i.e., oxygen, nitrogen, and helium. Equation 3 was used to construct a table between δ and helium mole fraction, assuming nitrogen to oxygen mole ratio of 3.76 in standard air.

2.3 Results and Discussion (Buoyant Jets)

Experiments were performed to capture the flow structure in the near-, mid-, and far- field of steady and unsteady jets in Earth gravity. Thus, at least three experiments were conducted for each test condition. In this paper, only the near-field data are presented for a steady and an unsteady jet in Earth gravity as listed below. The jet exit Reynolds number is defined as $Re = U_j.d/\nu$, where ν is the kinematic viscosity of helium.

Summary of Test Conditions

Case	d, mm	U_j, m/s	Re	Ri Earth gravity	f, Hz
Case 1	19.1	1.54	240	0.49	Steady
Case 2	31.8	1.15	300	1.44	12.2

Oscillating Jet (Case 2)

For test conditions of Case 2, the flow exhibited self-excited periodic oscillations in Earth gravity. Figure 1 shows a sequence of contour plots (1/60s apart) of helium mole fraction to depict an oscillation cycle in Earth gravity. Results show that the helium mole fraction varied throughout the flow field during the oscillation cycle. In Fig. 1(a), the buoyancy-induced acceleration of light jet fluid in heavier surroundings results in contraction of the jet boundary until about z/d=0.35. This process continues in the next Fig. 1(b), where the jet compression is observed until about z/d=0.75. In the next plot (Fig. 1c), a vortex is present near z/d=1.4 in between the two radial locations of the 0.50 mole fraction contour. Subsequently, the jet expands near the exit as the vortex moves downstream of the field-of-view. The cycle repeats itself with

radial inflow of air compressing the jet core region as shown in Fig. 1(f). The contour plot in Fig. 1(f) is similar, though not identical, to that in Fig. 1(a) suggesting that the oscillation frequency is approximately 12Hz. This is confirmed by frequency power spectra of angular deflection at several locations shown in Fig. 2. The power-spectra reveal a dominant frequency of 12.2 Hz at all locations suggesting global oscillations of the flow field.

The evolution of the jet flow structure with change in gravity is depicted in Fig. 3 by a sequence of contour plots of helium mole fraction. In Earth gravity (t=0.0s in Fig. 3a), the jet compression near the exit is accompanied with radial inflow of the surrounding air. Immediately after the drop is initiated (t=1/60s in Fig. 3b), a vortex is observed at z/d=1.3. The jet has also expanded radially near the exit region. At t=1/30s in Fig. 3(c), the vortex has moved downstream of the field-of-view while the jet continues to widen near the exit region. Subsequently, the jet expands gradually in the downstream regions as the steady microgravity conditions are reached. The helium mole fraction contours in microgravity are straight lines reminiscent of the non-buoyant jet. In microgravity, the jet width exceeded the field of view of the schlieren apparatus. In the absence of a reference point in the surrounding medium (air), systematic errors were introduced during Abel inversion process in the downstream region. Thus, the contours lines in Fig. 3(f) did not diverge fully as expected in non-buoyant jets. Smaller tubes were considered to avoid this problem. However, the resulting oscillation frequency exceeded the temporal resolution of the imaging system used in this study.

Power spectra of angular deflection were obtained to assess characteristics of jet oscillations in microgravity. The analysis was performed using 1.1s of data taken at the beginning and towards the end of the drop to distinguish initial transients from steady microgravity conditions. The power spectra in Fig. 4 show oscillations without a distinct frequency, when data at the beginning of the drop are used. Data taken at the end of the drop however did not produce any detectable oscillation frequency. These results provide direct physical evidence that flow oscillations in low-density jets are buoyancy induced.

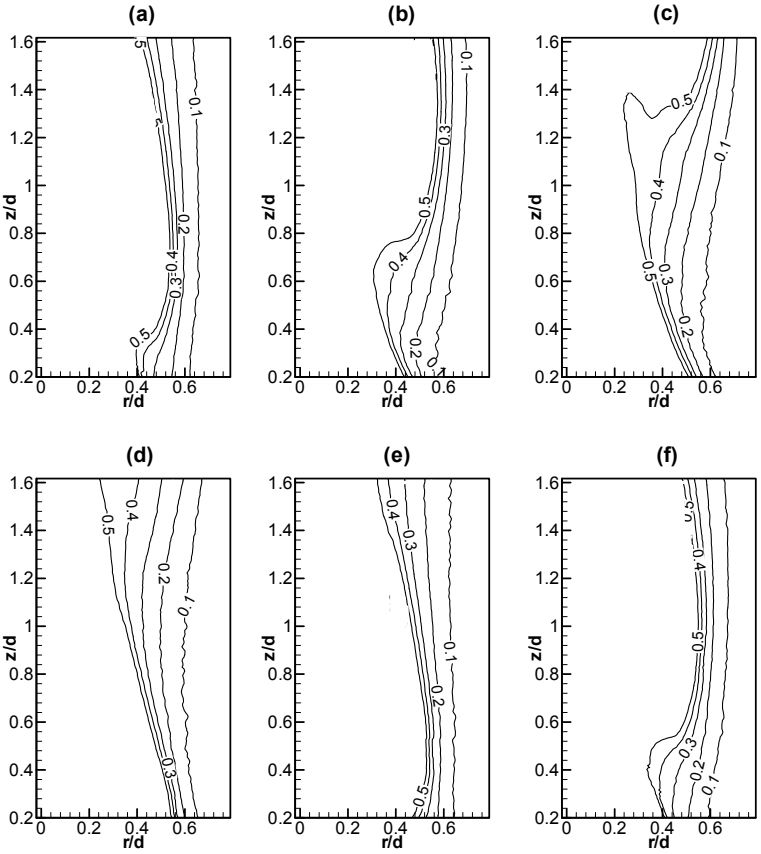

Figure 1. Contours of helium mole fraction during a flicker cycle in Earth gravity for Case 2 (d=31.8mm, Re=300); (a) t = 0.0s, (b) t = 1/60s, (c) t = 2/60s, (d) t= 3/60s, (e) t = 4/60s, and (f) t = 5/60s.

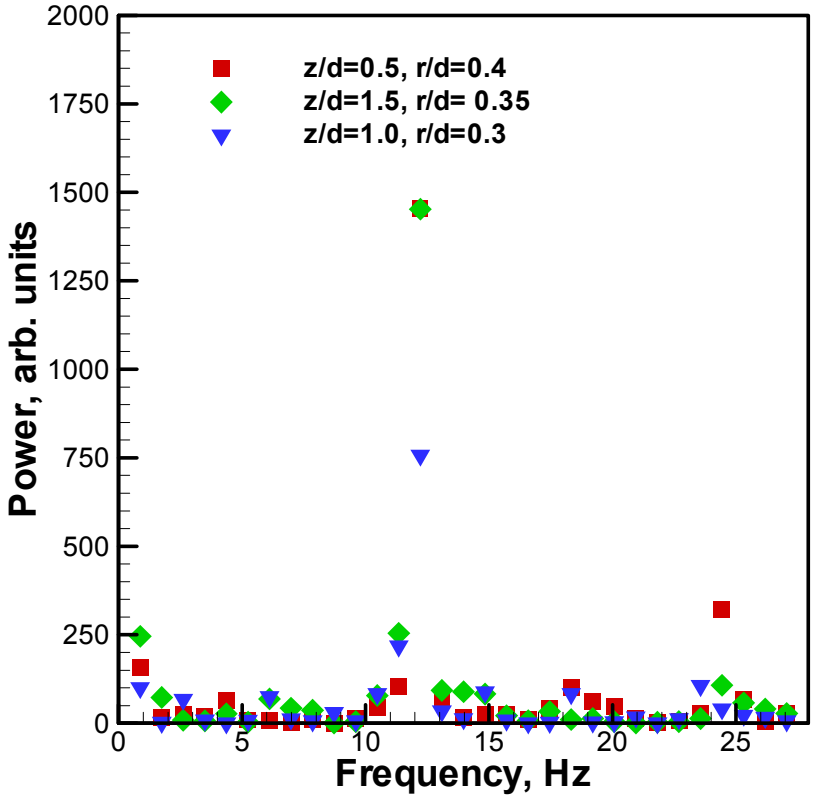

Figure 2. Frequency power spectra in Earth gravity for various locations for Case 2 (d=31.8mm, Re=300).

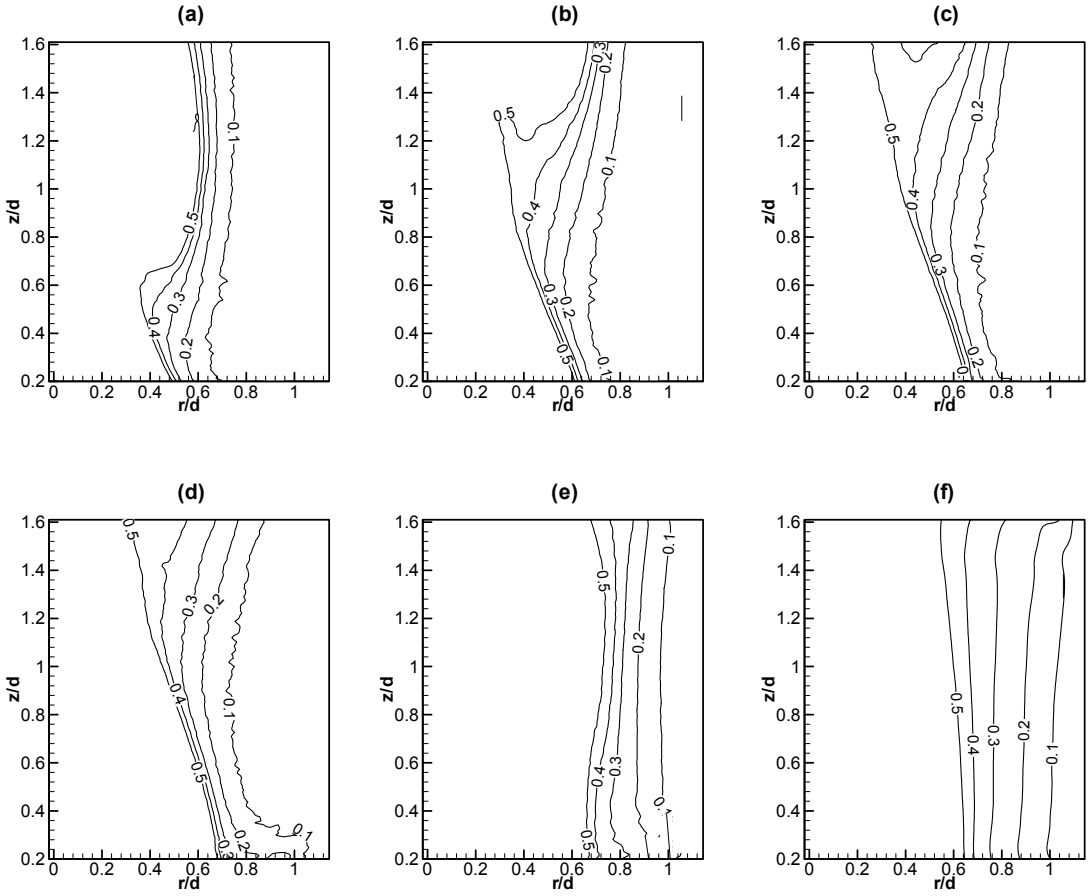

Figure 3. Contours of helium mole fraction during transition from Earth gravity to microgravity for Case 2 (d=31.8mm, Re=300); (a) t = 0.0s (denotes release of the package), (b) t = 1/60s, (c) t = 2/60s, (d) t= 3/60s, (e) t = 13/60s, and (f) t = 2.0s.

2.4 Results and Discussion (Momentum-Dominated Jet)

Figure 4 shows a portion of space-time images constructed from 700 schlieren images to span about 700ms; 260ms in Earth gravity and 440ms in free fall. These images are shown for z/d=0.01, 0.5, 1.0, 1.5, and 2.5, where z represents the distance downstream of the tube exit. The horizontal black line in each image denotes the approximate release time (t=1.06s) of the experiment in the drop tower. Thus, the jet flow experiences Earth gravity for $t \leq 1.06$s and free fall for t>1.06s. Figure 4 provides detailed visualization of how the jet flow evolves temporally and spatially. In Earth gravity, the flow oscillations are observed at all axial locations shown in Fig. 4. The oscillation amplitude at z/d=0.01 is small (discernable upon magnification) and it increases with downstream locations. Oscillations penetrated farther into the jet center region at downstream locations. The wavy structure at z/d=0.5 represents the cyclic bulging and contracting of the primary jet. However, at z/d=1.0 and further downstream, the primary jet appears to separate from the outer flow to signify the presence of an outer toroidal structure. Figure 4 reveals a highly repeatable flow structure between consecutive cycles in Earth gravity. At all axial locations, about 7 cycles are completed in 260ms duration of Earth gravity suggesting that the flow oscillates globally at a frequency of approximately 27Hz.

The image portion above the black line in Fig. 4 represents temporal evolution of the flow structure during change from Earth gravity to microgravity in the drop tower. Results show oscillations persisting during a brief initial period of free fall. The increased time between successive structures at the onset of free fall signifies a decrease in the oscillation frequency. The decay in jet oscillations appears to start from the jet exit and works it way downstream. For example, at t=1.2s, oscillating structure is observed at z/d=2.5 although the flow at z/d=0.5 appears steady. The flow oscillations at all locations have seized after about 200ms of free fall or t=1.25s. Two factors account for the persistence of oscillations after the drop is initiated; the time required for attaining microgravity conditions in the drop tower and the flow adjustment time. The microgravity conditions are reached after 100ms of free fall and the flow convection time based on the average jet exit velocity is about 15ms. Thus, oscillations continue mainly because of the finite gravitational level existing during the initial period of free fall. Results show that the jet in microgravity is wider than that in Earth gravity. Lack of buoyancy in microgravity causes the jet to spread mainly by the molecular diffusion. Accordingly, the density varies gradually to produce smaller angular deflections in the radial direction, reflected by fewer color gradations in schlieren images in microgravity. Results in Fig 4 provide direct physical evidence that the flow oscillations in Earth gravity are buoyancy induced.

An analysis of the power spectra of the flow field is presented. The analysis is based on Fast Fourier Transform (FFT) of hue values at a specified point in the flow field, obtained from 512 successive (in time) images, at a resolution of 1Hz. Three partially overlapping 512-image subsections of data were used in the FFT analyses to represent the early, mid, and late duration of microgravity. Figure 5 shows the power spectra at z/d=0.5 and 1.5 for r/d=0.5. In Fig. 5a, a characteristic peak in the power spectra is observed at a frequency of 27Hz for the "early" period $0.85\text{s} \leq t \leq 1.51\text{s}$, where the free fall begins at t=1.06s and microgravity conditions are reached at t=1.16s. Evidently, the FFT analysis captures the dominant frequency of Earth gravity oscillations persisting during the early microgravity period. Note that Earth gravity oscillation frequency of approximately 27Hz was also determined from visual observations in the previous section. The curve for the "mid" period $1.00\text{s} \leq t \leq 1.51\text{s}$ in Fig 5a also shows a peak near 27Hz, signifying Earth gravity as the source of oscillations. A peak is also observed near 0 Hz. The

27Hz peak has disappeared and the 0 Hz peak has intensified for the "late" period 1.20s ≤ t ≤ 1.71s spanning only the microgravity data. Similar results are obtained at a downstream location (z/d=1.5) as shown in Fig. 5b. Clearly, the self-excited oscillations in Earth gravity diminish in microgravity.

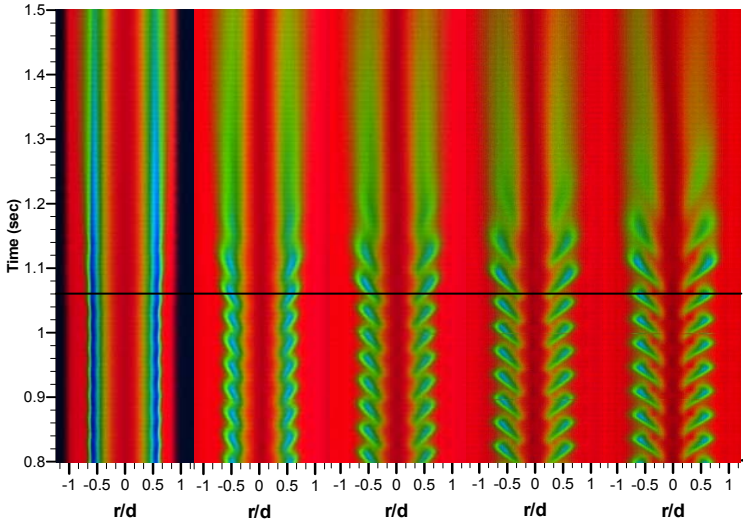

Figure 4. Space-time images at z/d=(a) 0.01, (b) 0.5, (c) 1.0, (d) 1.5, and (e) 2.5, from left to right, respectively. The black line at t=1.06-s indicates start of microgravity.

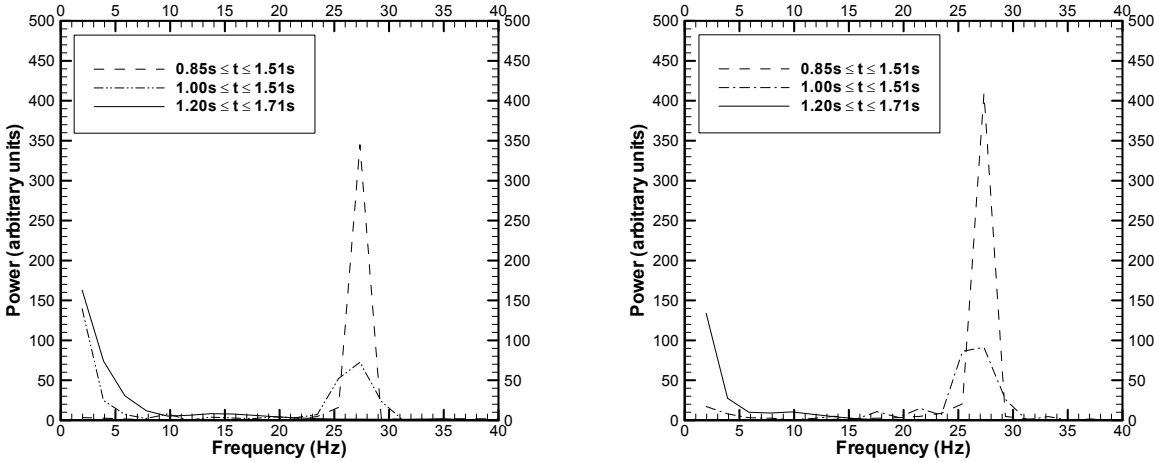

Figure 5. Power spectra (a) at r/d = 0.5, z/d = 0.5 and (b) at r/d = 0.5, z/d = 1.5.

3. COMPUTATIONAL STUDY

3.1 Governing Equations

Numerical formulation is based on unsteady, laminar, and axisymmetric flow behavior. The following additional approximations were made to simplify the analysis: (i) the flow is incompressible, (ii) temperature and pressure variations are negligible and (iii) the flow is a binary fluid system with air treated as a single species. Accordingly, the governing equations are expressed as follows:

$$\frac{\partial \rho}{\partial t} + \frac{1}{r}\frac{\partial}{\partial r}(\rho v r) + \frac{\partial}{\partial z}(\rho w) = 0 \qquad (1)$$

$$\frac{\partial (\rho r \phi)}{\partial t} + \frac{\partial}{\partial r}(\rho v r \phi) + \frac{\partial}{\partial z}(\rho r w \phi) = \frac{\partial}{\partial r}\left(\Gamma^{\phi} r \frac{\partial \phi}{\partial r}\right) + \frac{\partial}{\partial z}\left(\Gamma^{\phi} r \frac{\partial \phi}{\partial z}\right) + S^{\phi} \qquad (2)$$

Equation (1) represents the continuity equation and Equation (2) is the generalized transport equation, which represents the momentum, or species conservation equation depending on the variable ϕ. Γ^{ϕ} and S^{ϕ} are, respectively, the transport coefficient and source term of the variable ϕ, as listed in Table 1.

Table 1. Transport coefficients and source terms in Equation 2

Variable	ϕ	Γ^{ϕ}	S^{ϕ}
Axial Velocity	w	μ	$-r\frac{\partial p}{\partial z} + r(\rho_{\infty} - \rho)g + \frac{\partial}{\partial z}\left(r\mu\frac{\partial w}{\partial z}\right) + \frac{\partial}{\partial r}\left(r\mu\frac{\partial v}{\partial z}\right) - \frac{2}{3}\left[\frac{\partial}{\partial z}\left(r\mu\frac{\partial v}{\partial r}\right) + \frac{\partial}{\partial z}\left(r\mu\frac{\partial w}{\partial z}\right)\right]$
Radial Velocity	v	μ	$-r\frac{\partial p}{\partial r} - \frac{2}{3}\mu\frac{v}{r} + \frac{\partial}{\partial z}\left(r\mu\frac{\partial w}{\partial r}\right) + \frac{\partial}{\partial r}\left(r\mu\frac{\partial v}{\partial r}\right) - \frac{2}{3}\left[\frac{\partial}{\partial r}\left(r\mu\frac{\partial v}{\partial r}\right) + \frac{\partial}{\partial r}\left(r\mu\frac{\partial w}{\partial z}\right)\right]$
Helium mass fraction	f	ρD_b	0

Density was computed from the equation of state for incompressible ideal gas. The dynamic viscosity was calculated using Wilke's mixture averaged formula. The binary diffusion coefficient of helium into air, D_b was specified as a constant. In microgravity, the gravitational acceleration was specified as 100□g, where g is the gravitational acceleration on Earth.

3.2 Boundary Conditions

The computational domain extended 15d in the axial direction and 6d in the radial direction where "d" is the tube inside diameter. These dimensions were established after trials indicating that the near-field flow behavior was independent of the domain size. The upstream boundary was placed at a distance of 1d from the jet exit plane to account for the diffusion upstream of the jet exit observed in experimental studies. Symmetric boundary condition was imposed along the jet centerline. At the tube inlet, the velocity profile was fully developed and the helium mole fraction was unity. No slip and zero mass diffusion conditions were imposed at the tube walls. At the exit boundary, pressure outlet condition was implemented where flow properties are

extrapolated from the interior. Pressure inlet and outlet conditions were specified, respectively, at the upstream and far-field radial boundaries. All flow properties were set to zero at the start of the computations. The operating pressure and temperature were specified, respectively, as 1 atm and 300K.

3.3 Computational Procedure

An orthogonal non-uniform grid system was used to split the computational domain into five sub regions. The grid elements in the radial direction were concentrated in the flow oscillation region. The grid size was increased gradually in the axial direction. The governing equations were solved sequentially using a segregated approach. The pressure-velocity coupling was achieved using the SIMPLEC algorithm. Grid sensitivity analysis was performed to obtain grid-independent solution. Striking a balance between computational time and accuracy, a grid with 31093 and 80021 nodes was used, respectively, for buoyant and inertial jet analysis. The time step for buoyant and inertial jet computations was 1.6ms and 0.3ms, respectively. The small time step was needed to resolve the high-frequency oscillations in the inertial jet. The numerical code was validated with experimental data.

3.4 Results and Discussion

Time-dependent simulations of the isothermal helium jet injected into the ambient air environment were performed with the objective of quantifying buoyancy effects in the near-field. Although computations were performed for several cases, detailed results are presented for only one buoyant jet and one inertial jet at operating conditions listed in Table 1.

Table 1. Summary of Test Conditions

Case	*Re*	*Ri*	*d, mm*	U_j, *m/s*	*f , Hz (Computed)*	*f,Hz (Measured)*
Case 1(Buoyant)	*300*	*1.52*	*31.8*	*1.15*	*14.5*	*12.5*
Case 2(Inertial)	*800*	*0.018*	*14.05*	*6.75*	*150*	*120*

3.4.1 Buoyant Jet

3.4.1.1 Flow and Concentration Fields in Earth Gravity

Figure 6 shows a sequence of helium mole percentage contours superimposed with velocity vectors for the buoyant jet (case 1). At t=0.0ms, buoyancy accelerates the jet core, which contracts to conserve the mass. This results in entrainment of ambient fluid producing a toroidal vortex represented by the flow recirculation. Note that the vortex core represented by a black dot is located at z/d=0.12 in Fig.6. In the next plot at t=13.6ms, the vortex is characterized by a larger recirculation region accompanied with greater contraction of the jet core, evident from the inward indentations in the concentration field near z/d=0.2. Subsequently, between t=27.3ms and 54.7ms, the vortex grows in size and convects downstream to contaminate a greater portion of the jet core. The vortex gains its strength by momentum transfer from the jet core. This feature is evident in Fig. 6 wherein the velocity vectors downstream of the vortex core are larger than those upstream before interacting with the jet core. As the vortex propagates downstream, the jet expands near the tube exit inducting buoyant fluid to initiate another vortex at t=68.4ms to repeat the oscillation cycle. These results illustrate self-excited periodicity in the jet at a frequency of 14.6Hz, in excellent agreement with the measured oscillation frequency of 12.5Hz.

3.4.1.2 Flow and Concentration Fields during Change from Earth gravity to Microgravity

Computations were performed to visualize the jet flow during change from Earth gravity to microgravity and to depict how the jet flow adjusts itself in the absence of buoyancy. As a first step, the simulation results were compared with experiments[13] to validate the computational model. Figure 7 shows a series of computational-experimental helium mole fraction contour plots during change from Earth gravity to microgravity. At the onset of microgravity denoted as T=0.0s, the indentations in the helium concentration level higher than 50% signify a vortex located at z/d=0.7. After change to microgravity at T=16.66ms, the vortex convects downstream as the jet expands in the near exit region. At T=50.0ms, the jet has expanded at the exit to r/d= 0.7. The indentations in the concentration contours have weakened, signifying the diminishing nature of the vortex. Subsequently, the jet widens gradually throughout the near-field with diminishing oscillations as steady conditions are reached in microgravity. The helium mole fraction contours in microgravity are straight lines reminiscent of a non-buoyant jet. The above-mentioned features replicate similar phenomena observed in experiments showing self-excited oscillations gradually subsiding after microgravity was initiated. Judging from the plots in Figure 7, it is inferred that computations reproduced experimental observations, proving model's capability in predicting the flow structure during change from Earth gravity to microgravity.

Figure 8 shows contours of helium mole percentage overlapped by velocity vectors during change from Earth gravity to microgravity to highlight the interaction of the flow field with the concentration field. At T=0.0ms, a vortex with core located at z/d=0.7 characterizes the entrainment of ambient fluid into the jet. At this instant the jet flow is similar to that at T=27.3ms in Fig. 6(c). The jet width characterized by the 10% helium concentration contour extends to r/d=0.6 near the exit. In microgravity at T=33.33ms, the jet at the exit has expanded to r/d=0.7. The vortex has convected downstream with its core located at z/d=1.8. Velocity vectors show a weakening of the vortical structure at this instant. At T=66.6ms, the weakened vortex has moved downstream of the field-of-view while another vortex is formed near the jet exit at z/d=0.3. At T=133.3ms, flow recirculation has diminished as the jet expands to r/d=0.78 near the exit. Similar features are exhibited at t=166.6ms with the flow approaching steady conditions in microgravity. Finally, at T=2000ms the jet has assumed a steady columnar shape. The flow velocity decreases in the radial direction as the jet fluid mixes with ambient air. Further details about the flow structure are provided by spatio-temporal plots during the change from Earth gravity to microgravity.

3.4.1.3 Temporal Evolution of Axial Velocity and Concentration Fields

Figure 9 depicts temporal evolution of the concentration field during the change from Earth gravity to microgravity. Computed and measured time traces of helium mole fraction at z/d=1.0 illustrate that the oscillating jet flow expands radially after the change in gravity. Results show that the oscillations sustain during a brief initial period of microgravity, with steady conditions reached within T=0.75s. Again, the experimental trends are predicted well by the computations. Figure 10 shows time trace plots of helium mole percentage and axial velocity at selected locations during the change from Earth gravity to microgravity. Near the jet exit at z/d=0.15, the helium concentration at the jet center (r/d=0) is constant at 100% throughout. In contrast, the axial velocity at the jet center fluctuates between 2.3m/s and 2.6m/s in Earth gravity. In microgravity, the axial velocity initially decreases and then reaches a steady value of 2.2m/s at T=0.1s. In the entrainment region at r/d=0.45, the helium mole percentage in Earth gravity varied between 45% and 94%. During change to microgravity, the helium concentration peaked

to 100% within 0.08s. Afterwards, minor oscillations occurred before a steady value of 95% was reached within T=0.3s. Correspondingly, the axial velocity reached a steady value of 0.4m/s in microgravity. Near the jet boundary at r/d=0.6, low amplitude oscillations in the concentration field are observed in Earth gravity. In microgravity, the helium mole percentage rose to 70% prior to reaching a steady value of 52% within T=1.0s. In Earth gravity, the axial velocity profile at this radial location shows troughs with negative velocity indicating flow recirculation.

At a downstream location, z/d=2.0, pure helium is present throughout at the jet center. The axial velocity and its oscillation amplitude have increased at this location, signifying buoyant acceleration in Earth gravity. The flow oscillations diminish within 0.5s of microgravity as steady value of 2.1m/s is reached. At r/d=0.45, high amplitude concentration oscillations are observed in Earth gravity. At r/d=0.6, helium reaches peak concentration level of 60% during change from Earth gravity to microgravity and reaches a steady value of 56% at T=0.6s. The axial velocity profiles at the above radial locations depict flow behavior similar to that observed upstream. These features agree with time traces of concentration field measured experimentally.

3.4.2 Inertial Jet

3.4.2.1 Flow and Concentration Fields in Earth Gravity

Figure 11 shows a sequence of helium mole percentage contours superimposed with velocity vectors to depict an oscillation cycle. In this case, the computed results are presented only between r/d=0.3 and 0.65 to visualize the flow oscillation region in greater detail. At t=0.0s, buoyant acceleration contracts the jet core leading to entrainment and formation of a toroidal vortex. The flow structure during the oscillation cycle is similar to that of the buoyant jet. The nature and propagation of the toroidal vortex are the same as already explained.

Although self-excited flow oscillations were observed in both buoyant and inertial jets, some aspects of the flow field were found to be different. First, based on the concentration field, the inertial jet is wider compared to the buoyant jet. This implies that helium diffuses farther in an inertial jet. This effect is opposite to constant density jets where the jet width decreases with increasing initial jet momentum. Contraction and mixing by entrainment are confined to a narrow region in the inertial case compared to the buoyant case. The oscillation frequency for the inertial jet (150 Hz) is much higher than that for the buoyant case (14.5Hz). The above results illustrate self-excited periodicity in the flow field irrespective of the initial jet momentum, which agrees qualitatively and quantitatively with experiments.

3.4.2.2 Flow and Concentration Fields during change from Earth gravity to Microgravity

Figure 12 shows the contours of helium mole percentage overlapped by velocity vectors during change from Earth gravity to microgravity and then to zero gravity to highlight the interaction of flow field with concentration field. At the onset of microgravity (T=0.0ms), a toroidal vortex is located at $z/d \cong 0.75$. The vortex convects downstream and a new one is formed near the exit as shown in Fig. 12(b) for T=24ms. Subsequently, the jet flow maintains a periodic structure in microgravity as by Figs. 12(c)-(e) representing an oscillation cycle. The curvature of concentration contours is less severe and the vortex is narrower in microgravity compared to those in Earth gravity. The last plot in Fig. 12 pertains to the results obtained in zero gravity, simulated by completely turning off the gravity. In this case, the jet assumes a steady non-oscillatory state to support buoyancy as the cause of the instability. Results show that minor buoyant acceleration destabilizes the inertial jet.

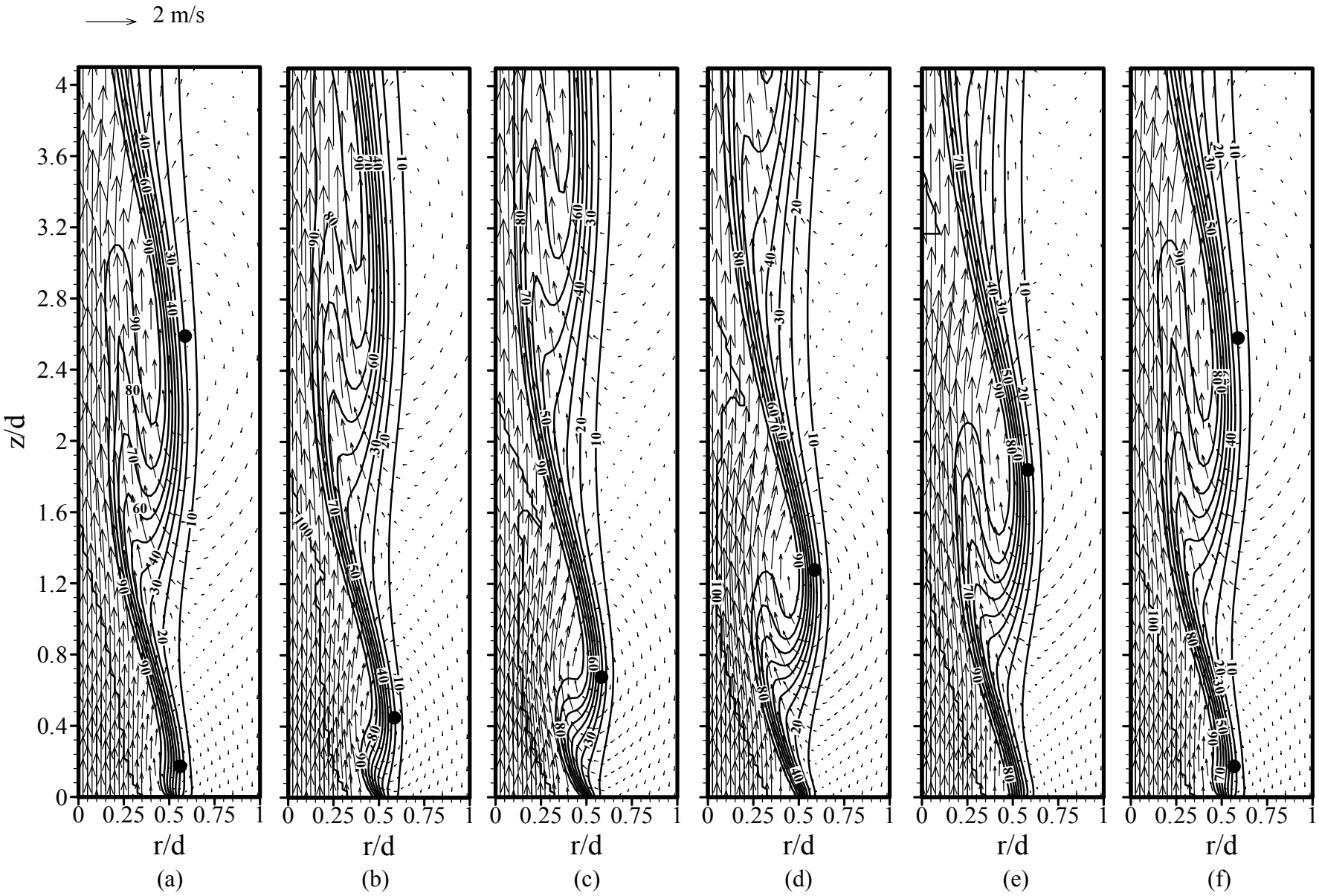

Figure 6. Contours of helium mole percentage superimposed by velocity vectors during an oscillation cycle in Earth gravity for Re=300, Ri=1.52, and d=31.8mm. (a) t=0.0ms; (b) t=13.6ms; (c) t=27.3ms; (d) t=41.0ms; (e) t=54.7ms; (f) t=68.4ms.

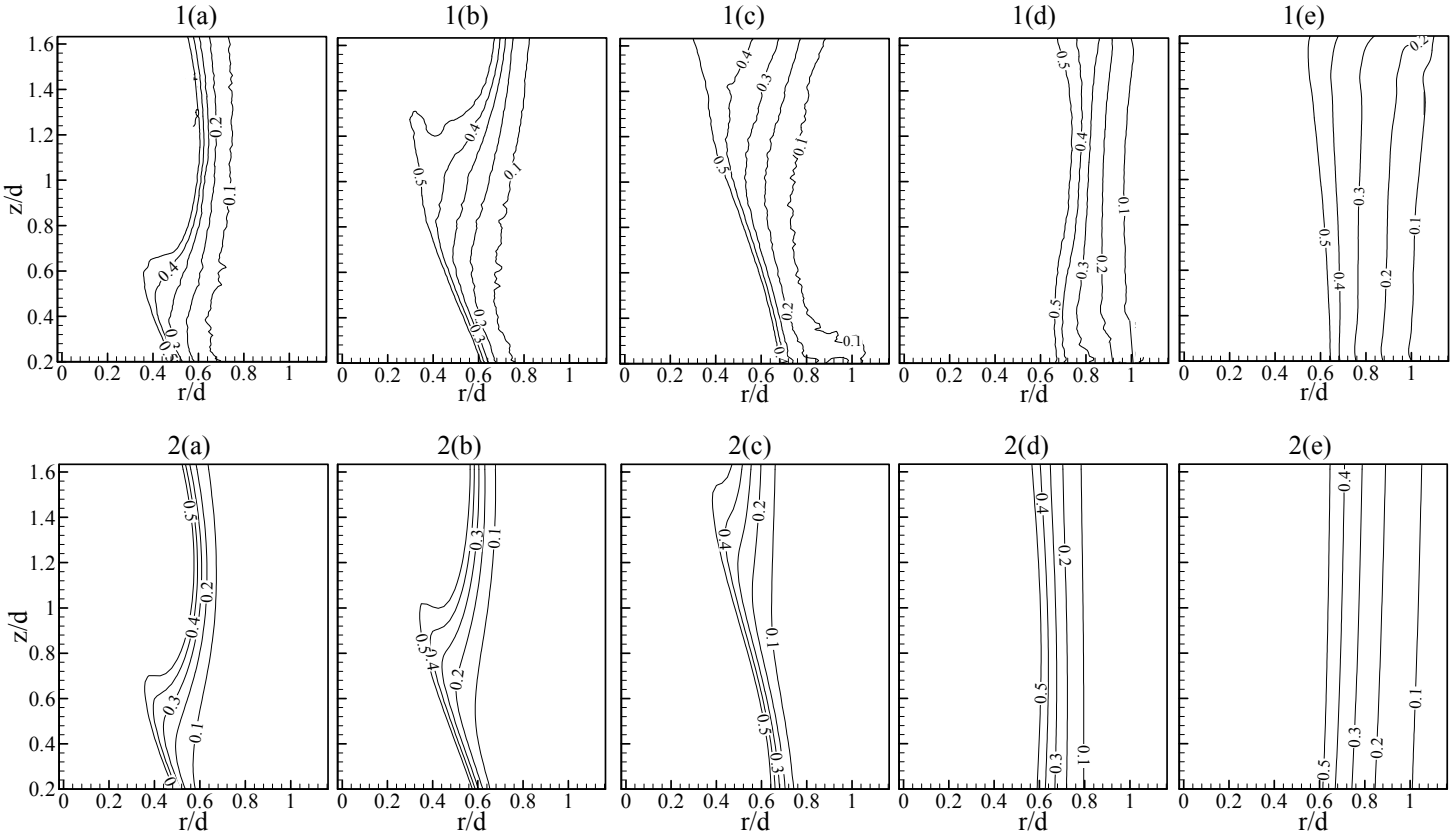

Figure 7. Measured (1) and Computed (2) helium mole fraction contours during change from Earth gravity to microgravity. Re = 300, Ri = 1.52, and d=31.8mm. (a) T=0.0ms; (b) T=16.66ms; (c) T=50.00ms; (d) T=216.66ms; (e) T=2000ms.

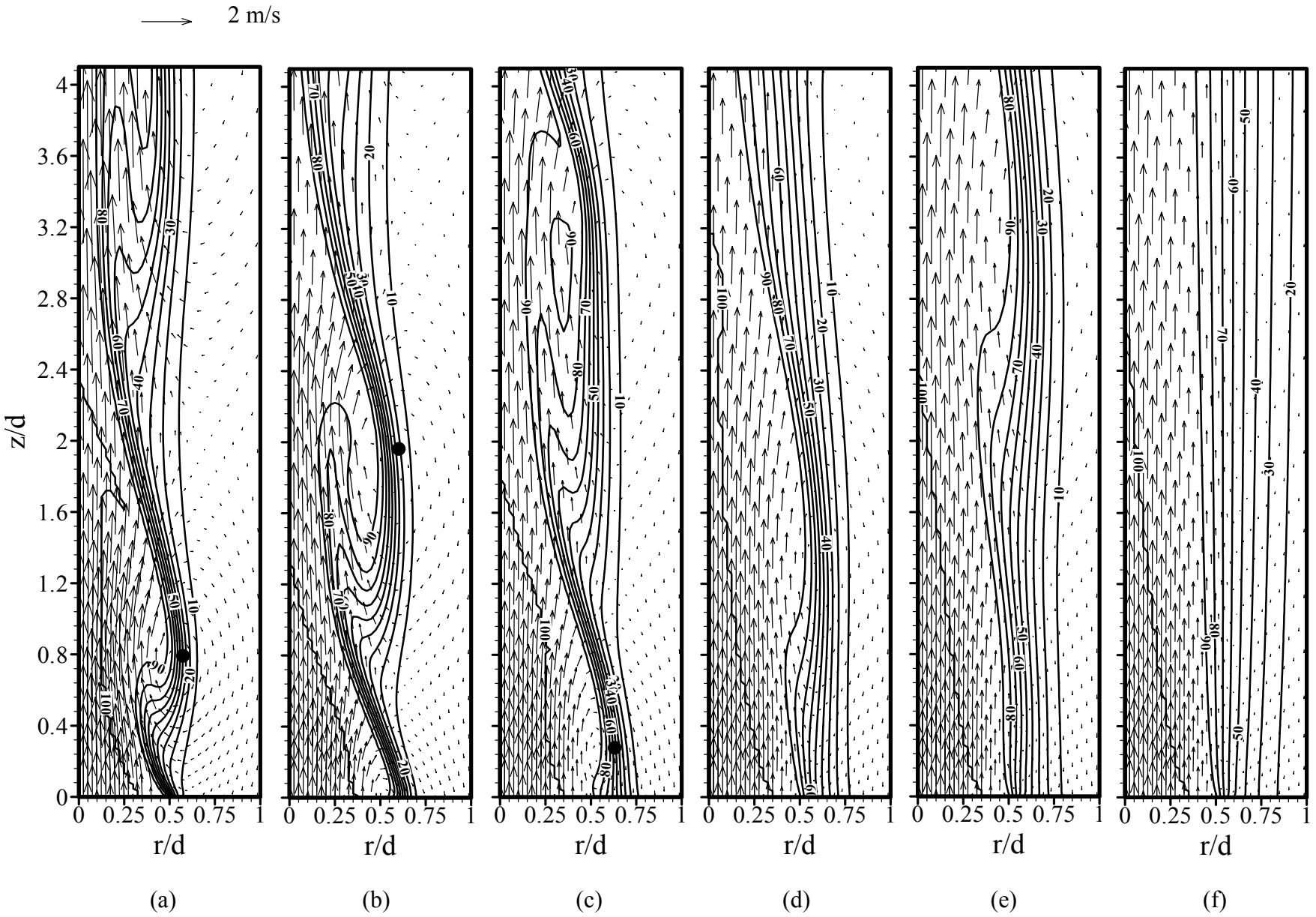

Figure 8. Contours of helium mole percentage superimposed by velocity vectors during change from Earth gravity to microgravity for Re=300, Ri=1.52, and d=31.8mm (a) T=0.0ms; (b) T=33.33ms; (c) T=66.66ms; (d) T=133.33ms; (e) T=166.66ms; (f) T=2000ms.

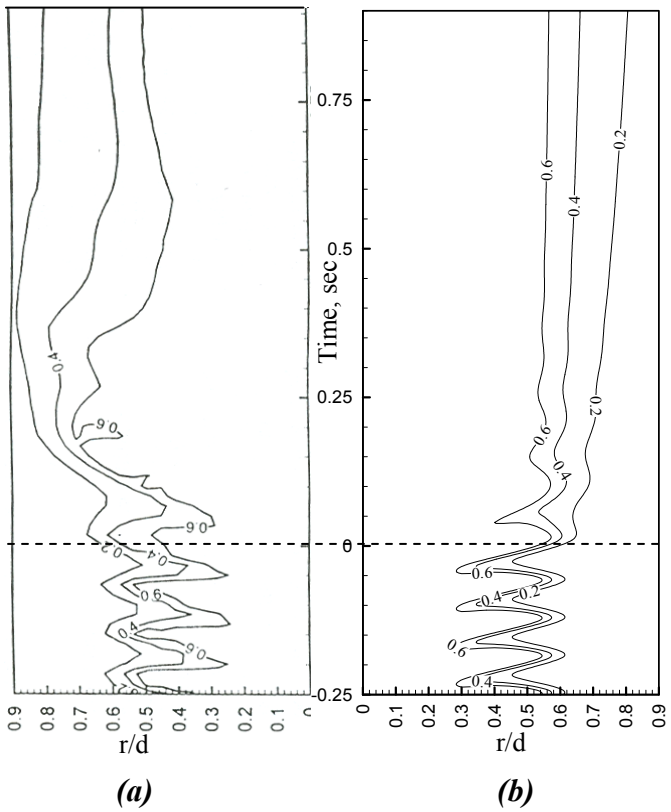

Figure 9. Measured (a) and Computed (b) time traces of helium mole fraction during change from Earth gravity to microgravity. Re=300, Ri=1.52 and d=31.8mm at z/d=1.0.

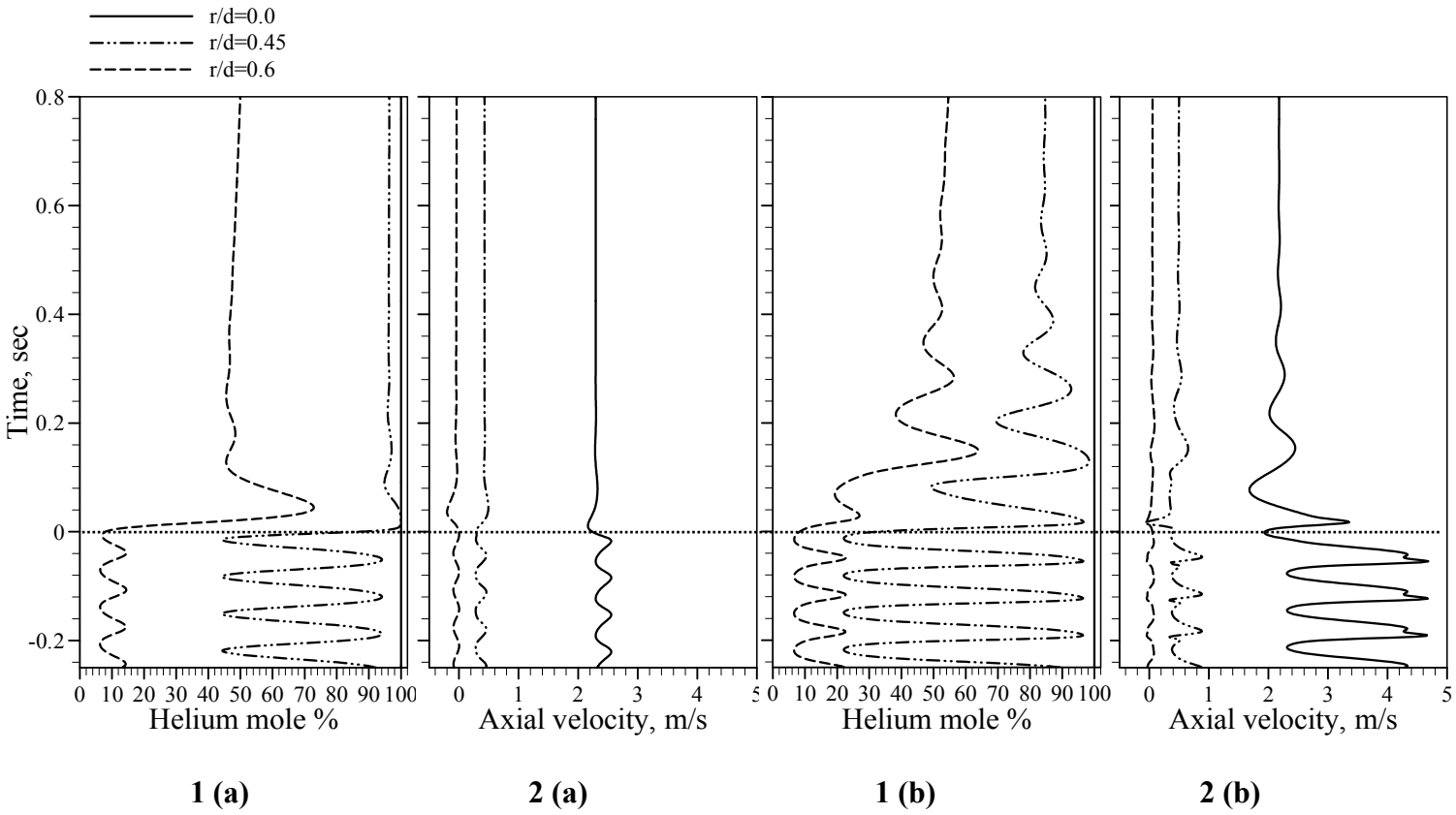

Figure 10. Time traces of 1) helium mole percentage and 2) axial velocity during change from Earth gravity to microgravity for Re=300, Ri=1.52 and d=31.8mm. a) z/d=0.15 b) z/d=2.0.

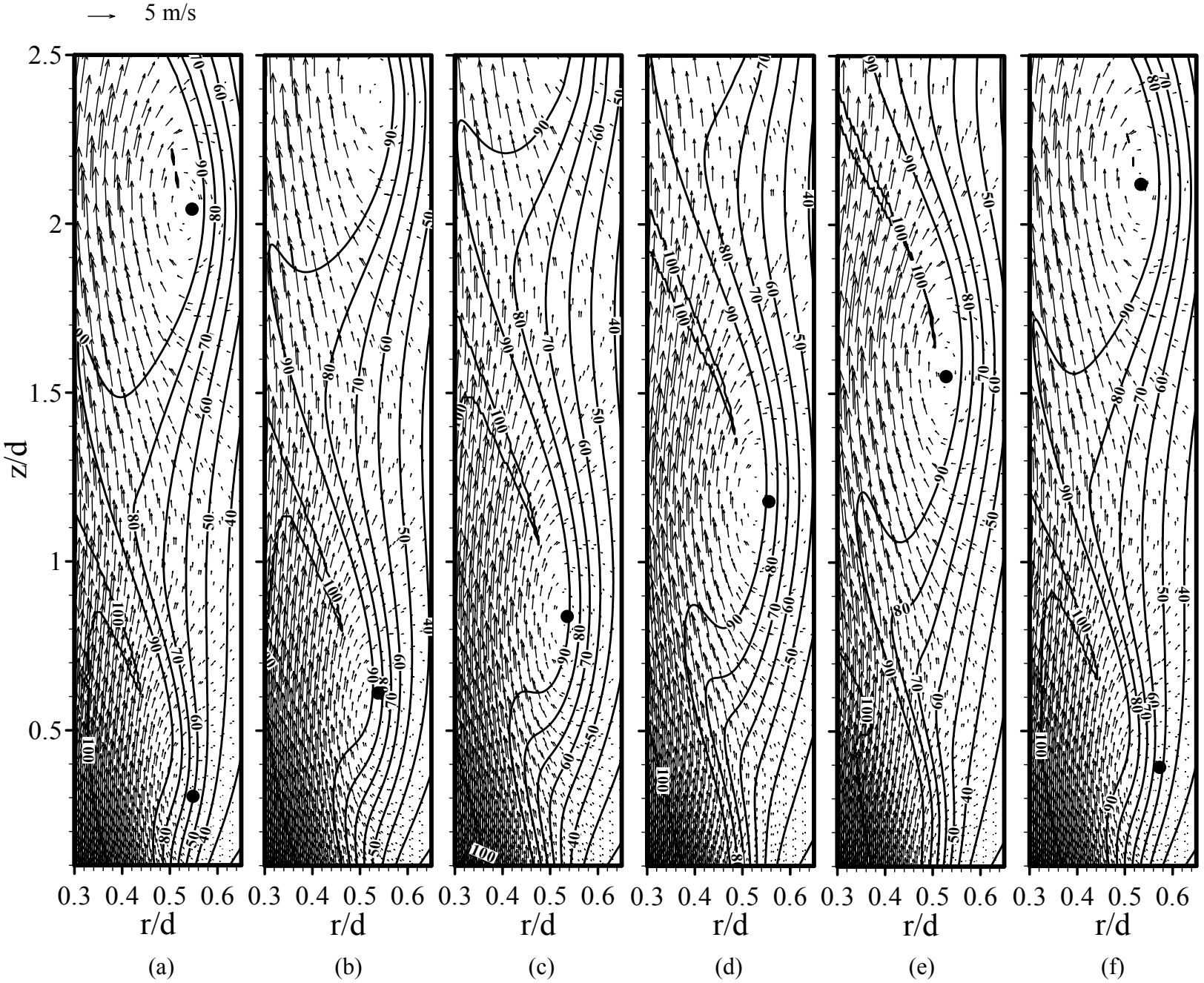

Figure 11. Contours of helium mole percentage superimposed by velocity vectors during an oscillation cycle in Earth gravity for Re=800, Ri=0.018 and d=14.05mm. (a) t=0.0ms; (b) t=1.2ms; (c) t=2.4ms; (d) t=3.6ms; (e) t=4.8ms; (f) t=6.6ms.

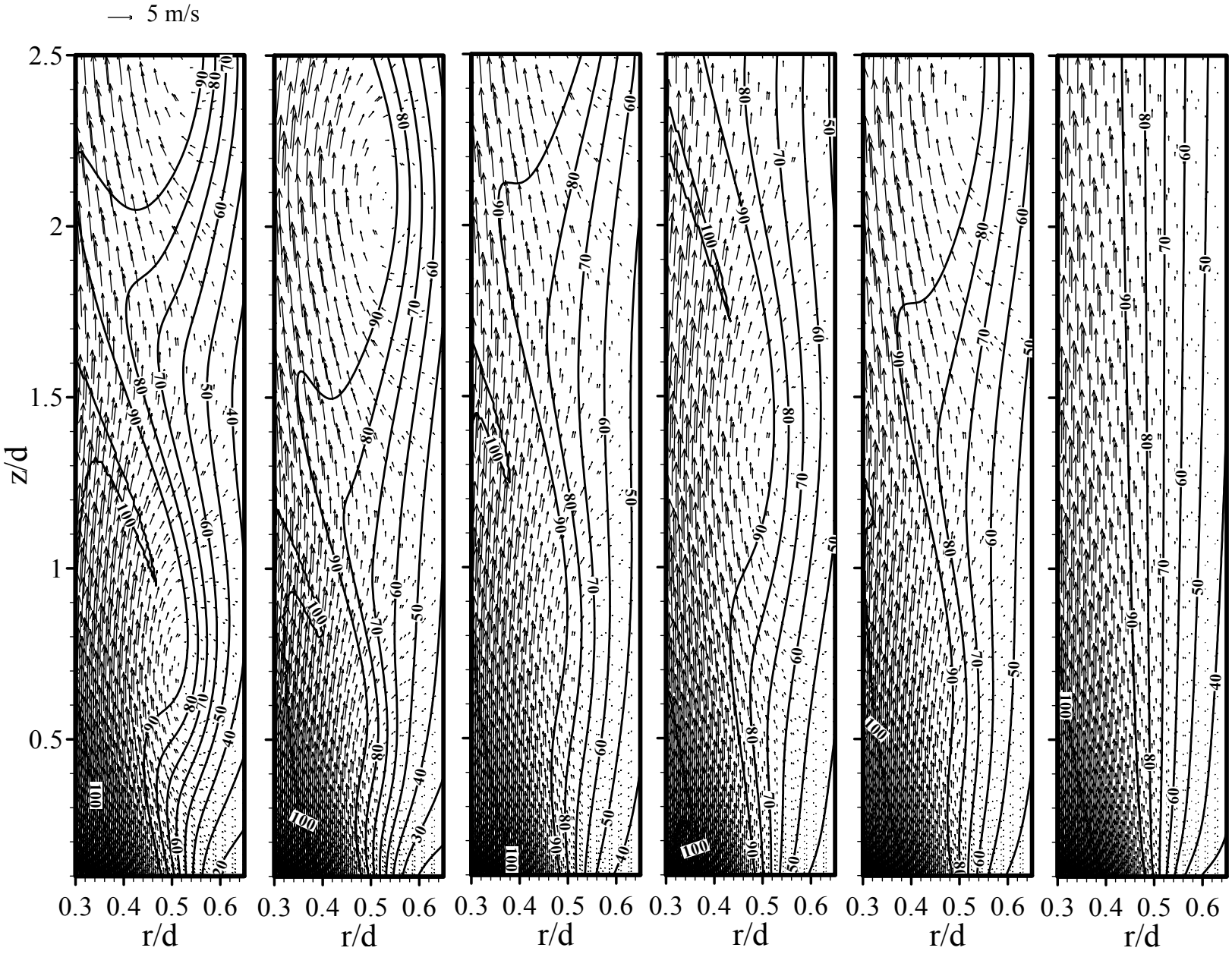

Figure 12. Contours of helium mole percentage superimposed by velocity vectors during change from Earth gravity to microgravity for Re=800, Ri=0.018 and d=14.05mm. (a) T=0.0ms; (b) T=24ms; (c) T=400ms; (d) T=402.5ms; (e) T=405.8ms; (f) zero gravity.

4. LINEAR STABILITY ANALYSIS

4.1 Mean Flow and the Disturbance equation

The formulation and the equations underlying the present analysis are as follows. A round jet of a low-density gas injected vertically upwards into a high-density quiescent ($U_\infty = 0$) gas is considered, with ρ_j and ρ_∞ being the densities of low-density and high-density gas respectively. The centerline velocity of the jet is U_j and R is the half jet width. Since the jet is round and axisymmetric, cylindrical coordinates centered at the origin of the jet are chosen for convenience. r is the radial distance from the jet centerline. The flow is assumed to be laminar, isothermal, and locally parallel. Viscous and diffusion effects are ignored.

Using Reynolds decomposition, the jet flow can be divided into two parts; a mean flow, and a disturbed flow superimposed on the mean flow. The mean flow is specified as,

$$\bar{u} = \bar{u}(r), \quad \bar{v} = 0, \quad \bar{w} = 0, \quad \bar{p} = \bar{p}(r), \quad \bar{\rho} = \bar{\rho}(r) \tag{1}$$

and the disturbed components of the fluid quantities admit the following normal mode exponential form:

$$\left(u', v', w', p', \rho'\right) = \left[\hat{u}(r), \hat{v}(r), \hat{w}(r), \hat{p}(r), \hat{\rho}(r)\right] . e^{i(kx - \Omega t)} \tag{2}$$

where, $\hat{u}(r)$, $\hat{v}(r)$, $\hat{w}(r)$, $\hat{p}(r)$, and $\hat{\rho}(r)$ are the velocity, pressure and density amplitudes of the disturbance wave. Here, $k = k_r + ik_i$ and $\Omega = \Omega_r + i\Omega_i$ are the complex wavenumber and the complex frequency, respectively. The real wavenumber k_r is related to the wavelength λ by $k_r = 2\pi/\lambda$, and the real circular frequency Ω_r is proportional to the Strouhal number based on the jet exit velocity and half jet-width. The imaginary quantities k_i and Ω_i are the spatial and temporal amplification rates of disturbances, respectively.

Introducing (1) and (2), in the basic conservation equations, and if all other quantities are eliminated in favor of the pressure disturbance amplitude, a second-order linear differential equation in $\hat{p}$ is obtained as given in (3):

$$\frac{d^2\hat{p}}{dr^2} + \left[\frac{1}{r} - \frac{2\frac{d\bar{u}}{dr}}{\bar{u} - \frac{\Omega}{k}} - \frac{1}{\rho}\frac{d\bar{\rho}}{dr}\left(1 + \frac{ig}{k\left(\bar{u} - \frac{\Omega}{k}\right)^2} \right) \right] \frac{d\hat{p}}{dr} - k^2\hat{p} = 0 \tag{3}$$

If the density gradient is zero, Eq. (3), reduces to the disturbance equation used by Michalke and Hermann (1982) for constant-density jets. Further, if $r \to \infty$ and the effects of gravity are neglected, Eq. (3) turns into the disturbance equation used by Yu and Monkewitz [23] for the instability analysis of inertial jets. The present analysis includes the effects of buoyancy in the form of an additional term in the disturbance equation. In the present analysis, all lengths are normalized by the half jet-width R, the density is normalized by the ambient fluid density ρ_∞, the velocity is normalized by the exit velocity U_j and the pressure is normalized by $\rho_j U_j^2$. The acceleration due to gravity g in (3), when normalized, yields the Froude number, Fr, defined as the ratio of inertial forces to buoyancy forces.

$$Fr^2 = \frac{U_j^2}{gR}\frac{\rho_j}{\rho_\infty - \rho_j} \tag{4}$$

If $Fr \to 0$, it represents that buoyancy force is more dominating i.e. gravity has large effect. If $Fr \to \infty$, represents a weak buoyancy force i.e. gravity has negligible effect.

4.2 Mean Velocity and Density Profiles

In order to solve the disturbance equation (3), mean velocity and density profiles need to be assumed. For the present analysis, three sets of mean velocity and density profiles are assumed to perform the linear stability analysis. Figures 13 and 14 illustrate the three velocity and density profiles assumed.

The first set of mean velocity and density profiles used for this study are the hypertan profiles used by Michalke and Hermann [22]:

$$\frac{\bar{u}(r)}{U_j} = 0.5\left\{1 - \tanh\left[0.25\,\frac{R}{\theta}\left(\frac{r}{R} - \frac{R}{r}\right)\right]\right\} \tag{5}$$

where, R/θ is the jet parameter that characterizes the jet velocity profile at various axial locations:

$$\frac{R}{\theta} = \frac{100}{3\frac{x}{R} + 4} \tag{6}$$

The density profile in the shear layer is assumed to be similar to the velocity profile and is given by Eq. (7).

$$\bar{\rho}(r) = 0.5\rho_\infty\left\{2 + \left(\frac{\rho_j}{\rho_\infty} - 1\right)\left(1 - \tanh\left[0.25\frac{R}{\theta}\left(\frac{r}{R} - \frac{R}{r}\right)\right]\right)\right\} \tag{7}$$

The second set of mean velocity and density profiles used are those assumed by Monkewitz and Sohn [23].

$$\frac{\bar{u}(r)}{U_j} = \left[1 + \left[\exp\left(r^2\ln 2\right) - 1\right]^N\right]^{-1}$$

$$\text{where, } N^{-1} = \begin{cases} 0.02 + 0.869\left(x/L\right) - 0.031(x/L)^{6.072}, & x < 1.35L \\ 1, & x \geq 1.35L \end{cases} \tag{8}$$

$$L = \left[8.0 + 2.5\ln\left(S_e\right)\right]$$

In the present analysis, the value of jet parameter x/L is varied such that it is well within the near-injector region allowing for the effects of buoyancy to manifest as the jet proceeds downstream from $x/L = 0$. Depending upon the value of N, the velocity profiles lie between a cylindrical vortex sheet ($N\rightarrow\infty$) and a Gaussian profile (N=1) suitable for the asymptotic region. Based on the experimental results of Reichardt discussed by Schlichting, a relation is specified between the velocity and density profiles as,

$$\frac{1/\rho - 1}{1/S - 1} = \left(\frac{\bar{u}(r)}{U_j}\right)^P$$

$$P = \begin{cases} 1, & x \leq 0.64L \\ 0.8 + 0.2\,\mathrm{Cos}\left[2.49(x/L) - 1.60\right], & 0.64L < x < 1.90L \\ 0.6, & 1.90L \leq x \end{cases} \tag{9}$$

where, the exponent P is the turbulent Prandtl number. The third set of mean profiles includes a parabolic velocity profile (assuming a fully-developed pipe flow) and a hyperbolic tangent density profile.

$$\frac{\bar{u}(r)}{2U_j} = \left[1 - \left(\frac{r}{R}\right)^2\right] \tag{10}$$

The jet velocity at various axial locations is characterized by the jet parameter, R/θ. The density profile assumed is the hyperbolic tangent profile same as that of the hypertan profiles given in Eq. (7).

4.3 Method of Solution

By specifying the mean velocity and density profiles, (3) is solved for the eigenvalues that satisfy the boundary conditions given in (11).

$$\begin{aligned} &\hat{p}(\infty) \to 0 \quad \text{for all } m \\ &\hat{p}(0) \text{ is finite} \quad \text{when } m = 0 \end{aligned} \tag{11}$$

Since $d\bar{u}/dr$ and $d\bar{\rho}/dr$ vanish as $r \to 0$ and $r \to \infty$, the asymptotic solutions that satisfy the boundary conditions are

$$\begin{aligned} \hat{p}^{(i)} &= C_1 I_0(kr) \\ \hat{p}^{(o)} &= C_2 K_0(kr) \end{aligned} \tag{12}$$

where, the superscripts i and o represent the inner and outer solutions respectively. The inner solution is valid close to the jet centerline and the outer solution is valid in the far-field. Here I_0 and K_0 are the modified Bessel functions of order zero, and C_1 and C_2 are the arbitrary constants. For the parabolic profiles, $d\bar{u}/dr$ vanishes as $r \to \infty$ but it does not vanish as $r \to 0$ (equal to zero only at $r = 0$). Hence, the asymptotic solutions given in (12) do not hold well. Alternately, a Frobenius series solution for (3), satisfying the boundary conditions given in (11), is obtained for $r \to 0$.

A classical fourth-order Runge-Kutta scheme with adaptive step-size control is used to integrate the pressure disturbance equation given in (3). The infinite integration domain extending from the jet centerline to a far field away from the centerline, $0 < r < \infty$ is divided into two finite domains: an inner domain $0 \le r \le R$ and an outer domain $R \le r \le r_\infty$, where R is the half jet width and r_∞ is a specified large radius. The far field integration limit, r_∞ for this analysis is appropriately chosen as $4R$ at which the velocity and density gradients are small and almost negligible. A shooting method is used to determine $\Omega(k)$ such that both $\hat{p}$ and $d\hat{p}/dr$ are continuous at $r = R$. Two kinds of analysis, namely, temporal and spatio-temporal analysis are conducted. In temporal stability analysis, the complex frequency, Ω is determined as a function of real wavenumber, k. In spatio-temporal stability analysis, both Ω and k are considered complex.

4.4 Criteria for Absolute and Convective Instability

According to Briggs [21] and Bers [20], to determine whether the existing spatio-temporal instability is absolute or convective it is important to locate the saddle point in the complex (Ω^0, k^0) domain and to check whether it meets the pinching requirements. When the jet is absolutely unstable, the initially localized disturbances grow with time and space, and eventually infect the entire flow. Whereas, if the jet is convectively unstable, the disturbances grow as they are convected downstream and at a particular spatial location these disturbances appear to die with time. The nature of instability is determined depending upon the imaginary part, Ω_i^0 of the complex frequency Ω^0 of the pinch point. The Ω_i^0 represents the temporal amplification rate of

the disturbances. If, $\Omega_i^0>0$, then the flow is absolutely unstable and if, $\Omega_i^0<0$ then the flow system is convectively unstable. The temporal and absolute instability characteristics are obtained by locating the pinch points for the three sets of mean velocity and density profiles by varying the parameters such as x/L, R/θ, Fr and ratio of density of the jet to the density of the ambient gas S.

4.5 Results and Discussion

The computational scheme was validated by comparing the present results with those obtained by Monkewitz and Sohn [23] and Michalke and Hermann [22].

4.5.1 Temporal Analysis Results

In order to determine the limits in the complex k-plane, for the mesh searching process used to locate the saddle points and pinch points for the absolute analysis, and also to explore the effects of the inhomogeneous shear-layer and buoyancy on the temporal evolution of the disturbances, a temporal stability analysis is first performed. The temporal analysis was carried out at a normalized axial distance of x/R = 2 from the jet exit, where the jet parameter value for the hypertan and parabolic profiles is R/θ=10 and for the Sohn's profiles, the combination of x/L and density ratio S (ρ_j/ρ_∞) is equivalent to x/R = 2.

The effects of the buoyancy on the jet temporal instability are determined by considering finite values of the Froude number. The density ratio is fixed at 0.14 and the Froude number is varied from infinity (very large value) to 1. The lower the value of the Froude number, the more dominant are the effects of buoyancy on the jet instability characteristics.

The variation of the temporal growth rate with the wavenumber for the three profiles, at x/R = 2, as the Froude number is reduced from infinity to 1 is illustrated in Fig. 15. The temporal growth rates are increased with the decrease in the Froude number for all the three profiles. The variation of temporal growth rate with the wavenumber for the three profiles exhibits a similar trend with the decrease in the Froude number. As the Froude number is reduced from a very large value (infinity) to 5, the maximum temporal growth rate shows no significant change. A small increase in the maximum temporal growth rate is observed as the Froude number is reduced from 5 to 2. But, as the Froude number is further reduced from 2 to 1, a large increase in the maximum temporal growth rate for all the three profiles is observed. As the Froude number is reduced from infinity to 1, the wavenumber corresponding to the maximum temporal growth rate and the range of unstable wavenumbers for the hypertan profiles remain unchanged. For the Sohn's profiles, the wavenumber corresponding to the maximum temporal growth rate and the range of unstable wavenumbers exhibit no significant change except for Fr = 1. For the parabolic profiles, the wavenumber corresponding to the maximum temporal amplification rate remains unchanged for $Fr \geq 5$ and decreases for $Fr \leq 2$, and the range of unstable wavenumbers decreases as the Froude number is reduced.

4.5.2 Spatio-Temporal Analysis Results

4.5.2.1 Effects of Variable Density Ratio

A constant-density jet flow is convectively unstable. But, as the density ratio is reduced gradually, keeping the Froude number constant at a very large value, the nature of instability of the jet is changed from convective instability to absolute instability. The density ratio at which

the absolute temporal growth rate changes its sign, i.e. the density ratio at which $\Omega_i^0 = 0$, where the jet first becomes absolutely unstable, is referred to as the critical density ratio, S_c.

The variation of absolute temporal growth rate of disturbances, Ω_i^0, with the density ratio for the three profiles is depicted in Fig. 16. For the hypertan and the parabolic profiles, the absolute temporal growth rate is negative (convectively unstable) at the density ratio of 0.99 and as the density ratio decreases from 0.99 to 0.14, the absolute growth rate gradually increases to a positive value and further. The critical density ratio, S_c, is found to be 0.525 for the hypertan profiles and 0.843 for the parabolic profiles. For the Sohn's profiles, the absolute temporal growth rate increases as the density ratio decreases from 0.99 to 0.3, and as the density ratio is further decreased from 0.3 to 0.14, the absolute temporal growth rate decreases. The critical density ratio for the Sohn's profiles is found to be 0.515. For the Sohn's profiles, the jet is absolutely unstable for the density ratios between 0.181 and 0.515, and is convectively unstable for all other density ratios. The critical density ratio for the Sohn's profiles is almost equal (only 1.8% difference) to the critical density ratio for the hypertan profiles. The critical density ratio for the parabolic profiles is about 61% greater than the critical density ratio for the hypertan profiles.

Effects of Buoyancy

The critical density ratio for each profile increases as the Froude number is reduced. Fig. 17 illustrates the variation of the critical density ratio with the Froude number for the three profiles at $x/R = 2$. For the hypertan profiles, at large Froude numbers, the critical density ratio is 0.525. A critical Froude number of 1.58 is determined for the hypertan profiles below which the jet is absolutely unstable for all the density ratios less than 1.0, i.e. for any low-density gas jet injected into high-density gas medium. That means, for the hypertan profiles the jet is absolutely unstable for all the density ratios less than 0.525 for any Froude number, and for $Fr < 1.58$, the jet is absolutely unstable for all the density ratios less than 1.0.

For the Sohn's profiles, at large Froude numbers, the jet is absolutely unstable for the density ratios between 0.181 and 0.515. The critical Froude number for the Sohn's profiles is found to be 1.83. Hence, at $x/R = 2$, the jet becomes absolutely unstable for all the density ratios between 0.181 and 0.515 for any Froude number, and for $Fr < 1.83$, the jet is absolutely unstable for any low-density gas injected into high-density ambient gas. For the parabolic profiles, at large Froude numbers the critical density ratio is 0.843 and the critical Froude number for the parabolic profiles is determined to be 3.74. Thus, for the parabolic profiles, the jet is absolutely unstable for all the density ratios below 0.843 for any Froude number, and for $Fr < 3.74$, any low-density gas injected into high-density ambient gas becomes absolutely unstable. A large increase in the absolute temporal growth rate is observed for the three profiles as the Froude number is reduced below the respective critical Froude numbers. Hence, a substantial effect of buoyancy on the temporal growth rates is evident at the Froude numbers below the respective critical Froude numbers. A similar substantial effect of buoyancy on the absolute frequency Ω_r^0, the absolute wavenumber k_r^0, and the absolute spatial growth rate $-k_i^0$ is also observed.

To conclude, as the density ratio was reduced, the temporal amplification rate of the disturbances for the hypertan and the parabolic profiles was increased, while the temporal growth rate for the Sohn's profiles was decreased. The temporal growth rate of the disturbances for the three profiles was increased as the Froude number was reduced. A decrease in the Froude number increases the effects of buoyancy (gravity), which serves to destabilize the shear layer. The destabilizing role played by buoyancy was observed to be the same for all the profiles. For a

large Froude number (negligible gravity), a critical density ratio was found for the three profiles at which the jet first became absolutely unstable. The critical density ratio for the hypertan and the Sohn's profiles was almost equal (S_c = 0.525 and S_c = 0.515 respectively). The critical density ratio for the parabolic profiles was higher (S_c = 0.843). The reason could be that the parabolic profiles include a parabolic velocity profile, with a steep velocity gradient in the central region of the jet. For all the profiles, the jet became more absolutely unstable as the density ratio was reduced further below the critical density ratio and the jet was convectively unstable for the density ratios above the critical density ratio. As the Froude number reduced, the critical density ratio for the three profiles was increased. Thus, reducing the Froude number had the effect of causing the jet to become absolutely unstable at higher density ratios. A critical Froude number was found for the three profiles, below which the jet was absolutely unstable for all the density ratios less than unity. The critical Froude number for the hypertan and the Sohn's profiles was almost equal (Fr = 1.58 and Fr = 1.83 respectively). The critical Froude number for the parabolic profiles (Fr = 3.74) was higher than that of the other two profiles. The reason could be again the assumption of an idealistic profile for the velocity distribution (parabolic velocity profile). For all the three sets of mean flow profiles, the effects of buoyancy (gravity) on the absolute instability characteristics of the jet were substantial for the Froude numbers below the respective critical Froude numbers. Thus, the critical Froude number demarcated the jet flow into the momentum-dominated regime and the buoyancy-dominated regime.

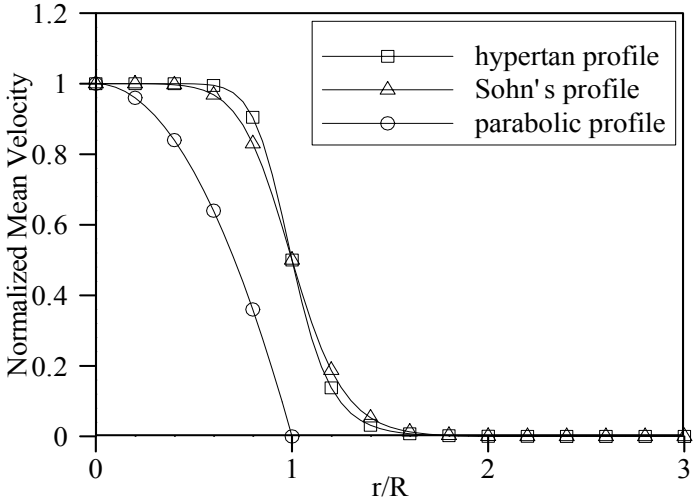

Fig. 13. Normalized mean velocity profiles at a location equivalent to x/R = 2.

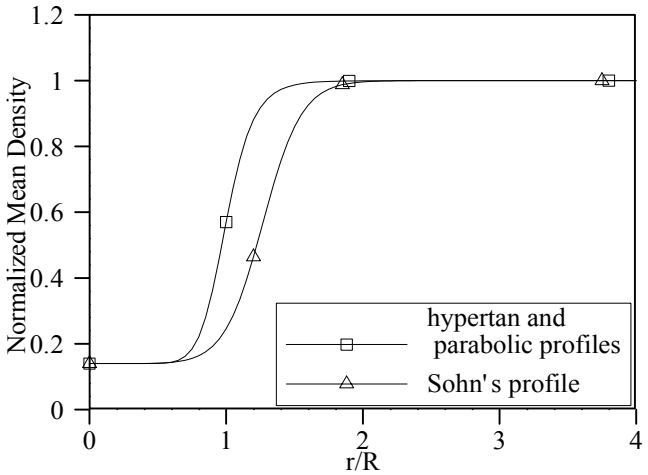

Fig. 14. Normalized mean density profiles at a location equivalent to x/R = 2.

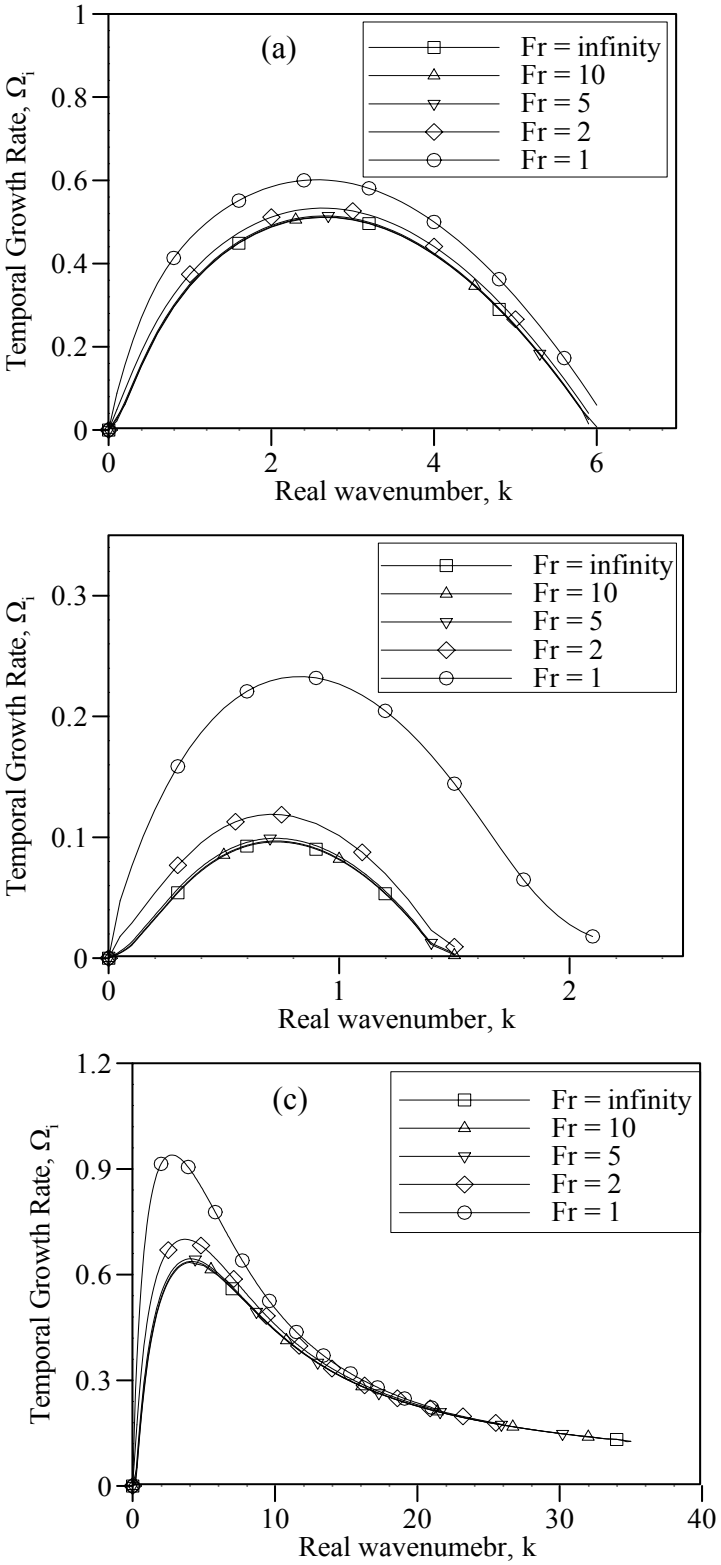

Fig. 15. The variation of temporal growth rate Ω_i with the wavenumber k for (a) the hypertan profiles, (b) the Sohn's profiles, and (c) the parabolic profiles at x/R = 2, S = 0.14

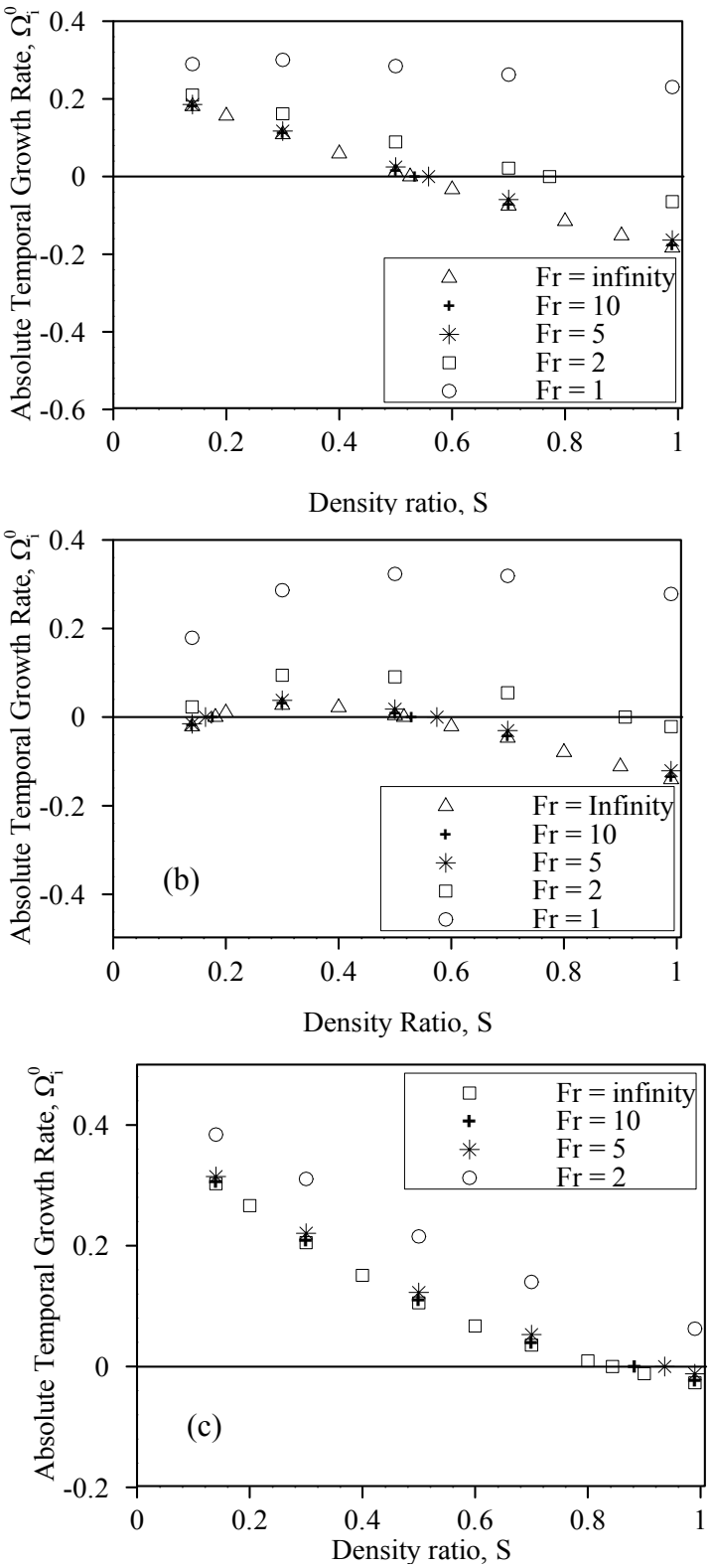

Fig. 16. The variation of the absolute temporal growth rate Ω_i^0 with the density ratio S for (a) the hypertan profiles, (b) the Sohn's profiles, and (c) the parabolic profiles at x/R = 2, and Fr = ∞, 10, 5, 2, and 1.

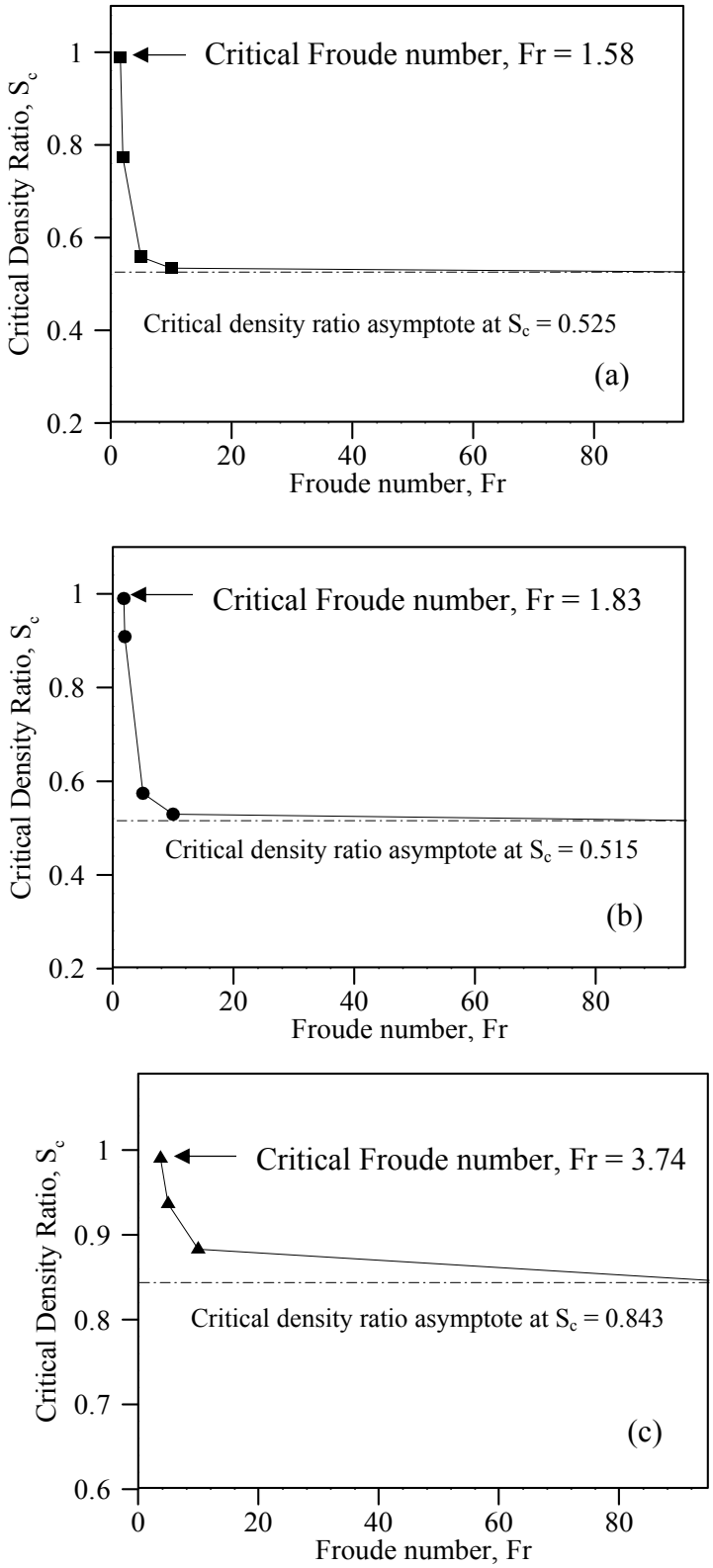

Fig. 17. Critical density ratio, S_c vs. Froude number, Fr at x/R = 2 for (a) the hypertan Profiles, (b) the Sohn's profiles, and (c) the parabolic profiles.

5. REFERENCES

1. So, R.M.C., Zhu, J.Y., Otugen, M.V., and Hwang, B.C., "Some Measurements in a Binary Gas Jet," *Experiments in Fluids*, Vol. 9, 1990, pp. 273-284.

2. Richards, C.D., and Pitts, W.M., "Global Density Effects on the Self Preservation Behaviour of Turbulent Free Jets," *Journal of Fluid Mechanics*, Vol. 254, 1993, pp. 417-435.

3. Panchapakesan, N.R., and Lumley, J.L., "Turbulence Measurements in Axisymmetric Jets of Air and Helium. Part 2. Helium Jet," *Journal of Fluid Mechanics*, Vol. 246, 1993, pp. 225-248.

4. Subbarao, E.R., and Cantwell, B.J., "Investigation of a Co-Flowing Buoyant Jet: Experiments on the Effect of Reynolds Number and Richardson Number," *Journal of Fluid Mechanics*, Vol. 245, 1992, pp. 69-90.

5. Hamins, A., Yang, J.C., and Kashiwagi, T., "An Experimental Investigation of the Pulsating Frequency of Flames," *Proceedings of the Combustion Institute*, Vol. 24, 1992, pp. 1695-1705.

6. Mell, W.E., McGrattan, K.B., and Baum, H.R., "Numerical Simulation of Combustion in Fire Flumes," *Proceedings of the Combustion Institute*, Vol. 26, 1996, pp. 1523-1530.

7. Cetegen, B.M., and Kasper, K.D., "Experiments on the Oscillatory Behavior of Buoyant Plumes of Helium and Helium-Air Mixtures," *Physics of Fluids*, Vol. 8, 1996, pp 2974-2984

8. Cetegen, B.M., "Measurements of Instantaneous Velocity Field of a Non-Reacting Pulsating Buoyant Plume by Particle Image Velocimetry*" Combustion Science and Technology*, Vol. 123, 1997, pp. 377-387.

9. Monkewitz, P.A., Bechert, D.W., Barsikow, B., and Lehmann, B., "Self-Excited Oscillations and Mixing in a Heated Round Jet," *Journal of Fluid Mechanics*, Vol. 213, 1990, pp. 611-639.

10. Screenivasan, K.R., Raghu, S., and Kyle, D., "Absolute Instability in Variable Density Round Jets," *Experiments in Fluids*, Vol. 7, 1989, pp. 309-317.

11. Kyle, D.M., and Sreenivasan, K.R., "The Instability and Breakdown of a Round Variable-Density Jet," *Journal of Fluid Mechanics*, Vol. 249, 1993, pp. 619-664.

12. Richards, C.D., Breuel, B.D., Clark, R.P., and Troutt, T.R., "Concentration Measurements in a Self-Excited Jet," *Experiments in Fluids*, Vol. 21, 1995, pp. 103-109.

13. Greenberg, P.S., Klimek, R.B., and Buchele, D.R., "Quantitative Rainbow Schlieren Deflectometry," *Applied Optics*, Vol. 34, 1995, pp. 3819-3822.

14. Al-Ammar, K., Agrawal, A.K., Gollahalli, S.R., and Griffin, D.W., "Application of Rainbow Schlieren Deflectometry for Concentration Measurements in an Axisymmetric Helium Jet," *Experiments in Fluids*, Vol. 25, 1998, pp. 89-95.

15. Pasumarthi, K.S., "Full Field Scalar Measurements in a Pulsating Helium Jet Using Rainbow Schlieren Deflectometry," *M.S. Thesis*, University of Oklahoma, 2000.

16. Albers, B.W., and Agrawal, A.K., "Schlieren Analysis of an Oscillating Gas-Jet Diffusion Flame," *Combustion and Flame*, Vol. 119, 1999, pp. 89-94.

17. Shenoy, A.K., Agrawal, A.K., and Gollahalli, S.R., "Quantitative Evaluation of Flow Computations by Rainbow Schlieren Deflectometry," *AIAA Journal*, Vol. 36, 1998, pp. 1953-1960

18. Al-Ammar, K., Agrawal A.K., and Gollahalli, S.R., "Quantitative Measurements of Laminar Hydrogen Gas-Jet Diffusion Flames in a 2.2 s Drop Tower," *Proceedings of the Combustion Institute*, Vol. 28, 2000, pp. 1997-2004.

19. Agrawal, A.K., and Albers, A.K., "Abel Inversion of Deflectometric Measurements in Dynamic Flows," *Applied Optics*, Vol. 38, 1999, pp. 3394-3398.

20. Bers, A. "Linear Waves and Instabilities," *Plasma Physics*, edited by C. DeWitt and J. Peyraud, Gordon and Breach, New York, 1975, p. 117.

21. Briggs, R. J., *Electron Stream Interaction with Plasmas*, MIT Press, Cambridge, Massachusetts, 1964.

22. Michalke, A. and Hermann, G., "On the Inviscid Instability of a Circular Jet with External Flow," Journal of Fluid Mech. Vol. 114, 1982, pp. 343.

23. Monkewitz, P. A. and Sohn, K. D., "Absolute Instability in Hot Jets," AIAA Journal, 1988, Vol. 26, pp. 911.

24. Yu, M. H. and P.A. Monkewitz, P. A., "The Effect of Nonuniform Density on the Absolute Instability of Two-Dimensional Inertial Jets and Wakes," Physics of Fluids A, 1990, Vol. 2, pp. 1175.

DEGREES GRANTED[1]

PhD

1. Pasumarthi, K.S., 2004, "Buoyancy Effects on Flow Structure and Instability of Low-Density Gas Jets," PhD Dissertation, School of Aerospace and Mechanical Engineering, University of Oklahoma.

2. Lawson, A. L. 2001, "Instability Analysis of a Low-Density Gas Jet Injected into a High-Density Gas," PhD Dissertation, School of Aerospace and Mechanical Engineering, University of Oklahoma.

Masters

1. Bekir S. Yildirim, 2004, "Concentration Measurements in Self-Excited, Momentum-Dominated Helium Jets," MS Thesis, School of Aerospace and Mechanical Engineering, The University of Oklahoma, Norman.

2. Nanda K. Vedantam, 2003, "The Effect of Mean Flow Profiles on the Instability Characteristics of a Low-Density Gas Jet Injected into a High-Density Gas," MS Thesis, School of Aerospace and Mechanical Engineering, The University of Oklahoma, Norman.

3. P. Leptuch, 2002, "Analysis of Buoyancy Effects in Helium Jets using High-Speed Rainbow Schlieren Deflectometry," M.S. Thesis, School of Aerospace and Mechanical Engineering, University of Oklahoma.

4. T-W, Yep, 2001, "Scalar Measurements and Analysis of Helium Jets in Earth Gravity and Microgravity using Rainbow Schlieren Deflectometry," M.S. Thesis, School of Aerospace and Mechanical Engineering, University of Oklahoma, December 2001,.

5. Kasyap S. Pasumarthi, 2000, "Full Field Scalar Measurements in a Pulsating Helium Jet using Rainbow Schlieren Deflectometry," M.S. Thesis, School of Aerospace and Mechanical Engineering, University of Oklahoma.

[1] Copies of theses abstract at provided in this report.

PUBLICATIONS

Journal Papers[2]

Published/In Press

1. Yep, T-W., Agrawal, A.K., and Griffin, D.W., 2003, "Gravitational Effects on Near Field Flow Structure of Low-Density Gas Jets," *AIAA Journal*, vol. 41, pp. 1973-1979.

2. Pasumarthi, K., and Agrawal, A.K., 2003, "Schlieren Measurements and Analysis of Concentration Field in Self-Excited Helium Jets," *Physics of Fluids*, vol. 15, pp. 3683-3692.

3. Yildirim, B.S., and Agrawal, A.K., "Full-Field Concentration Measurements of Self-Excited Oscillations in Momentum-Dominated Helium Jets," *Experiments in Fluids*, in press, 2004.

4. Pasumarthi, K., and Agrawal, A.K., "Buoyancy Effects on Flow Transition in Low-Density, Inertial Gas Jets," *Experiments in Fluids*, in press, 2005.

In Review

5. Leptuch, P.A., and Agrawal, A.K., "High-Speed Rainbow Schlieren Visualization of an Oscillating Helium Jet Undergoing Gravitational Change," *Journal of Visualization*, submitted, July 2003.

6. Satti, R., and Agrawal, A.K., "Numerical Analysis of Gravitational Effects in Buoyant and Inertial Helium Gas Jets," *AIAA Journal*, submitted, August 2004.

7. Lawson, A. L. and Parthasarathy, R. N. "Linear Stability Analysis of Gravitational Effects on a Low-Density Gas Jet Injected into a High-Density Medium," in review, *Physics of Fluids*.

In preparation[3]

8. Pasumarthi, K., Agrawal, A.K., and Griffin, D.W. "Oscillatory Behavior of Momentum-Dominated Low Density Gas Jets Undergoing Gravitational Change," *Journal of Fluid Mechanics*.

9. Satti, R., and Agrawal, A.K., "Computational Analysis of Flow Structure in the Near-Field of Low-Density Gas Jets," *International Journal of Heat and Fluid Flow*

10. Satti, R., and Agrawal, A.K., "Transient Analysis of Flow Evolution in Low-Density Gas Jets," *ASME Journal of Fluids Engineering*

11. Vedantam, N. K. and Parthasarathy, R. N. "Effects of Mean Velocity Profiles on the Instability of Variable Density Jets."

---

[2] Copies of journal papers published, in press, and in review are included in this report.
[3] Copies of journal papers in preparation are not included, as they will be available at the time of submission.

PUBLICATIONS

Conference Papers (Published)

1. Pasumarthi, K., and Agrawal, A.K., 2004, "Schlieren Measurements of Buoyancy Effects on Flow Transition in Low-Density Gas Jets," ASME Heat Transfer-Fluid Engineering Conference, *ASME HT-FED2004-56810*, July 2004.

2. Satti, R.P., and Agrawal, A.K., 2004, "Numerical Analysis of Flow Evolution in a Helium Jet Injected into Air," ASME Heat Transfer-Fluid Engineering Conference, *ASME HT-FED2004-56811*, July 2004.

3. Vedantam, N. K. and Parthasarathy, R. N. 2004, "Effects of Mean Flow Profiles on the Instability of a Low-Density Gas Jet Injected into a High-Density Gas," ASME Heat Transfer-Fluid Engineering Conference, *ASME HT-FED2004-56794*.

4. Yildrim, B.S., Pasumarthi, K.S., and Agrawal, A.K., 2004, "Concentration Measurements in Self-Excited Momentum-Dominated Low-Density Gas Jets," AIAA Paper-2004-1279.

5. Satti, R., Pasumarthi, K.S., and Agrawal, A.K., 2004, "Numerical Simulations of Buoyancy Effects in Low-Density Gas Jets," AIAA Paper-2004-1317.

6. Yep, Tze-Wing, Agrawal, A.K., and Griffin, D.W., 2002, "Gravitational Effects on Near Field Flow Structure of Low-Density Gas Jets," *AIAA Paper 2002-0761*.

7. Lawson, A. L. and Parthasarathy, R. N. 2002, "Linear Temporal Instability Analysis of a Low-Density Round Gas Jet Injected into a High-Density Gas," *ASME 2002 Energy Technology Conference and Exposition*, ASME Paper ETCE2002/CAE-29010.

PUBLICATIONS

Presentations[4]

1. Vedantam, N. K. and Parthasarathy, R. N., 2004, "Absolute Instability of Low-Density Jets," 24th AIAA/ASME Symposium, Oklahoma Christian University, Oklahoma City, OK.

2. Satti, R., and Agrawal, A.K., 2004, "Computational Analysis of Gravitational Effects in Buoyant and Momentum-Dominated Helium Gas Jets," 24th Oklahoma *AIAA/ASME Symposium*, Oklahoma City, OK.

3. Yildrim, B.S., and Agrawal, A.K., 2003, "Analysis of Flow Structure in Momentum Dominated Helium Jets," 23rd Oklahoma *AIAA/ASME Symposium*, Norman, OK.

4. K.S. Pasumarthi, Agrawal, A.K, and Parthasarathy, R., 2003, "Computational Analysis of Buoyancy Induced Instability in a Helium Jet," 23rd Oklahoma *AIAA/ASME Symposium*, Norman, OK.

5. Agrawal, A. K. and Parthasarathy, R. N. and D. Griffin, 2002, "Effect of Gravity on the Near Field Flow Structure of Helium Jet in Air," presented at the *Sixth Microgravity Fluid Physics and Transport Phenomena Conference*, Cleveland, OH.

6. Leptuch, P.A., and Agrawal, A.K., 2002, "Characteristics of Helium Jets Flowing Into Air Upon Removal of Gravitational Forcing," 22nd Oklahoma *AIAA/ASME Symposium*, Tulsa, OK

7. Lawson, A. L. and Parthasarathy, R. N. 2001, "Instability Analysis of a Low-Density Gas Injected into a High-Density Gas," presented at the *21st Oklahoma AIAA/ASME Symposium* Tulsa, OK.

8. Agrawal, A.K, Parthasarathy, R., Pasumarthi, K., and Griffin, D., "Gravitational Effects on Flow Instability and Transition in Low-Density Jets," *Fifth Microgravity Fluids Physics and Transport Phenomena Conference*, August 9-11, 2000, Cleveland, Ohio.

[4] Copies of presentation are not included in this report.

DEGREES GRANTED

PhD

1. Pasumarthi, K.S., 2004, "Buoyancy Effects on Flow Structure and Instability of Low-Density Gas Jets," PhD Dissertation, School of Aerospace and Mechanical Engineering, University of Oklahoma.

2. Lawson, A. L. 2001, "Instability Analysis of a Low-Density Gas Jet Injected into a High-Density Gas," PhD Dissertation, School of Aerospace and Mechanical Engineering, University of Oklahoma.

Masters

1. Bekir S. Yildirim, 2004, "Concentration Measurements in Self-Excited, Momentum-Dominated Helium Jets," MS Thesis, School of Aerospace and Mechanical Engineering, The University of Oklahoma, Norman.

2. Nanda K. Vedantam, 2003, "The Effect of Mean Flow Profiles on the Instability Characteristics of a Low-Density Gas Jet Injected into a High-Density Gas," MS Thesis, School of Aerospace and Mechanical Engineering, The University of Oklahoma, Norman.

3. P. Leptuch, 2002, "Analysis of Buoyancy Effects in Helium Jets using High-Speed Rainbow Schlieren Deflectometry," M.S. Thesis, School of Aerospace and Mechanical Engineering, University of Oklahoma.

4. T-W, Yep, 2001, "Scalar Measurements and Analysis of Helium Jets in Earth Gravity and Microgravity using Rainbow Schlieren Deflectometry," M.S. Thesis, School of Aerospace and Mechanical Engineering, University of Oklahoma, December 2001,.

5. Kasyap S. Pasumarthi, 2000, "Full Field Scalar Measurements in a Pulsating Helium Jet using Rainbow Schlieren Deflectometry," M.S. Thesis, School of Aerospace and Mechanical Engineering, University of Oklahoma.

UNIVERSITY OF OKLAHOMA

GRADUATE COLLEGE

BUOYANCY EFFECTS ON FLOW STRUCTURE AND INSTABILITY OF LOW-DENSITY GAS JETS

A Dissertation

SUBMITTED TO THE GRADUATE FACULTY

in partial fulfillment of the requirements for the

degree of

Doctor of Philosophy

By

Kasyap Sriramachandra Pasumarthi
Norman, Oklahoma
2004

ABSTRACT

A low-density gas jet injected into a high-density ambient gas is known to exhibit self-excited global oscillations accompanied by large vortical structures interacting with the flow field. The primary objective of the proposed research is to study buoyancy effects on the origin and nature of the flow instability and structure in the near-field of low-density gas jets. Quantitative rainbow schlieren deflectometry, Computational fluid dynamics (CFD) and Linear stability analysis were the techniques employed to scale the buoyancy effects.

The formation and evolution of vortices and scalar structure of the flow field are investigated in buoyant helium jets discharged from a vertical tube into quiescent air. Oscillations at identical frequency were observed throughout the flow field. The evolving flow structure is described by helium mole percentage contours during an oscillation cycle. Instantaneous, mean, and RMS concentration profiles are presented to describe interactions of the vortex with the jet flow. Oscillations in a narrow wake region near the jet exit are shown to spread through the jet core near the downstream location of the vortex formation. The effects of jet Richardson number on characteristics of vortex and flow field are investigated and discussed.

The laminar, axisymmetric, unsteady jet flow of helium injected into air was simulated using CFD. Global oscillations were observed in the flow field. The computed oscillation frequency agreed qualitatively with the experimentally measured frequency. Contours of helium concentration, vorticity and velocity provided information about the evolution and propagation of vortices in the oscillating flow field.

Buoyancy effects on the instability mode were evaluated by rainbow schlieren flow visualization and concentration measurements in the near-field of self-excited helium jets undergoing gravitational change in the microgravity environment of 2.2s drop tower at NASA John H. Glenn Research Center. The jet Reynolds number was varied from 200 to 1500 and jet Richardson number was varied from 0.72 to 0.002. Power spectra plots generated from Fast Fourier Transform (FFT) analysis of angular deflection data acquired at a temporal resolution of 1000Hz reveal substantial damping of the oscillation amplitude in microgravity at low Richardson numbers (~0.002). Quantitative concentration data in the form of spatial and temporal evolutions of the instability data in Earth gravity and microgravity reveal significant variations in the jet flow structure upon removal of buoyancy forces. Radial variation of the frequency spectra and time traces of helium concentration revealed the importance of gravitational effects in the jet shear layer region.

Linear temporal and spatio-temporal stability analyses of a low-density round gas jet injected into a high-density ambient gas were performed by assuming hyper-tan mean velocity and density profiles. The flow was assumed to be non parallel. Viscous and diffusive effects were ignored. The mean flow parameters were represented as the sum of the mean value and a small normal-mode fluctuation. A second order differential equation governing the pressure disturbance amplitude was derived from the basic conservation equations. The effects of the inhomogeneous shear layer and the Froude number (signifying the effects of gravity) on the temporal and spatio-temporal results were delineated.

A decrease in the density ratio (ratio of the density of the jet to the density of the ambient gas) resulted in an increase in the temporal amplification rate of the disturbances. The temporal growth rate of the disturbances increased as the Froude number was reduced. The spatio-temporal analysis performed to determine the absolute instability characteristics of the jet yield positive absolute temporal growth rates at all Fr and different axial locations. As buoyancy was removed ($Fr \rightarrow \infty$), the previously existing absolute instability disappeared at all locations establishing buoyancy as the primary instability mechanism in self-excited low-density jets.

UNIVERSITY OF OKLAHOMA

GRADUATE COLLEGE

INSTABILITY ANALYSIS OF A LOW-DENSITY GAS JET INJECTED INTO A HIGH-DENSITY GAS

A DISSERTATION

SUBMITTED TO THE GRADUATE FACULTY

in partial fulfillment of the requirements for the

degree of

DOCTOR OF PHILOSOPHY

By

Anthony Layiwola Lawson
Norman, Oklahoma
2001

ABSTRACT

The objective of this study was to determine the effects of buoyancy on the absolute instability of low-density gas jets injected into high-density gas mediums. Most of the existing analyses of low-density gas jets injected into a high-density ambient have been carried out neglecting effects of gravity. In order to investigate the influence of gravity on the near-injector development of the flow, a linear temporal stability analysis and a spatio-temporal stability analysis of a low-density round jet injected into a high-density ambient gas were performed. The flow was assumed to be isothermal and locally parallel; viscous and diffusive effects were ignored. The variables were represented as the sum of the mean value and a normal-mode small disturbance. An ordinary differential equation governing the amplitude of the pressure disturbance was derived. The velocity and density profiles in the shear layer, and the Froude number (signifying the effects of gravity) were the three important parameters in this equation. Together with the boundary conditions, an eigenvalue problem was formulated. Assuming that the velocity and density profiles in the shear layer to be represented by hyperbolic tangent functions, the eigenvalue problem was solved for various values of Froude number. The temporal growth rates and the phase velocity of the disturbances were obtained. It was found that the presence of variable density within the shear layer resulted in an increase in the temporal amplification rate of the disturbances and an increase in the range of unstable frequencies, accompanied by a reduction in the phase velocities of the disturbances. Also, the temporal growth rates of the disturbances were increased as

the Froude number was reduced (i.e. gravitational effects increased), indicating the destabilizing role played by gravity. The spatio-temporal stability analysis was performed to determine the nature of the absolute instability of the jet. The roles of the density ratio, Froude number, Schmidt number, and the lateral shift between the density and velocity profiles on the jet's absolute instability were determined. Comparisons of the results with previous experimental studies show good agreement when the effects of these variables are combined together. Thus, the combination of these variables determines how absolutely unstable the jet will be. Experiments were carried out to observe the qualitative differences between a round low-density gas jet injected into a high-density gas (helium jet injected into air) and a round constant density jet (air jet injected into air). Flow visualizations and velocity measurements in the near-injector region of the helium jet show more mixing and spreading of the helium jet than the air jet. The vortex structures develop and contribute to the jet spreading causing the helium jet to oscillate.

UNIVERSITY OF OKLAHOMA

GRADUATE COLLEGE

CONCENTRATION MEASUREMENTS IN SELF-EXCITED, MOMENTUM-DOMINATED HELIUM JETS

A THESIS

SUBMITTED TO THE GRADUATE FACULTY

in partial fulfillment of the requirements for the degree of

MASTERS OF SCIENCE

By

Bekir Sedat Yildirim

Norman, Oklahoma

2004

ABSTRACT

Flow structure of momentum-dominated pure helium jets discharged vertically into ambient air was investigated using high-speed rainbow schlieren deflectometry (RSD) technique. Effects of the operating parameters, i.e., Reynolds number (Re) and Richardson number (Ri), on the oscillatory behavior of the flow were examined over a range of experimental conditions. To seek the individual effect of these parameters, one of them was fixed and the other was varied with certain constraints. The operating range was 350 to 2000 for Reynolds number and $1.17.10^{-3}$ to 0.1 for Richardson number.

Measurements revealed highly periodic oscillations in the laminar region as well as high regularity in transition and turbulent regions. Power spectra of angular deflection generated at different spatial locations revealed the same oscillation frequency, suggesting a global instability mode. Maximum spectral power profiles at different axial locations indicated the oscillation amplitude increasing until the breakdown of the jet in the turbulent regime.

The transition from the laminar to turbulent flow was also investigated. The transition plan was identified using root-mean-square deflection angle contours obtained from 2730 consecutive schlieren images. Fast Fourier transform analysis performed in the transition regime showed that the flow oscillates at a unique frequency, which was the same in the upstream laminar flow region. Normalized transition length was scaled with Richardson number for $Ri<2.10^{-2}$.

Measured deflection angle data were used in Abel inversion algorithm to construct the helium concentration fields. Instantaneous helium concentration contours

revealed changes in the flow structure and evolution of vortical structures during an oscillation cycle. The vortex formed near the jet exit and propagated downstream. The instability in the flow was shown by the changes in the concentrations contours during the oscillation cycle.

Temporal evolution plots of helium concentration at different axial locations were generate to provide detailed information about the oscillatory behavior of the flow. Plots showed repeatable oscillations at all axial and radial locations up to the turbulent regime.

A cross-correlation technique was applied to find the spatial displacements of the vortical structures. Correlation coefficient peaks in the generated field divulged the spatial displacements between consecutive schlieren images. Results show that the vortical structure convected and accelerated only in the axial direction.

UNIVERSITY OF OKLAHOMA

GRADUATE COLLEGE

EFFECTS OF MEAN FLOW PROFILES ON INSTABILITY OF A LOW-DENSITY GAS JET INJECTED INTO A HIGH-DENSITY GAS

A THESIS

SUBMITTED TO THE GRADUATE FACULTY

in partial fulfillment of the requirements for the

degree of

MASTER OF SCIENCE

By

Nanda Kishore Vedantam
Norman, Oklahoma
2003

Abstract

The objective of this study was to investigate the effects of the mean flow profiles on the instability characteristics in the near-injector region of low-density gas jets injected into high-density ambient gas mediums. To achieve this, a linear temporal stability analysis and a spatio-temporal stability analysis of a low-density round gas jet injected vertically upwards into a high-density ambient gas were performed by assuming three different sets of mean velocity and density profiles. The flow was assumed to be isothermal and locally parallel. Viscous and diffusive effects were ignored. The mean flow parameters were represented as the sum of the mean value and a small normal-mode fluctuation. A second order differential equation governing the pressure disturbance amplitude was derived from the basic conservation equations. The first set of mean velocity and density profiles assumed were those used by Monkewitz and Sohn (1988) for investigating absolute instability in hot jets. The second set of velocity and density profiles assumed for this study were the ones used by Lawson (2001). And the third set of mean profiles included a parabolic velocity profile and a hyperbolic tangent density profile. The effects of the inhomogeneous shear layer and the Froude number (signifying the effects of gravity) on the temporal and spatio-temporal results for each set of mean profiles were delineated.

A decrease in the density ratio (ratio of the density of the jet to the density of the ambient gas) resulted in an increase in the temporal amplification rate of the

disturbances for the second and the third set of profiles, while the amplification rate for the first set of profiles was decreased. The reason for this inverse behavior with the first set of profiles is not clear. The phase velocities of the disturbances for all the three sets of profiles were decreased as the density ratio was reduced. The temporal growth rate of the disturbances for all the three sets of mean flow profiles was increased as the Froude number was reduced indicating the sabotaging effect of gravity. The spatio-temporal analysis was performed to determine the absolute instability characteristics of the jet for the three sets of profiles. At a large Froude number (negligible gravity), a critical density ratio was found for the three profiles at which the jet became absolutely unstable. The critical density ratio for the first and the second set of profiles was almost equal (S_c = 0.515 and S_c = 0.525 respectively). The critical density ratio for the third set of profiles was higher (S_c = 0.843). The reason could be that the third set of profiles includes a parabolic velocity profile, with a steep velocity gradient in the central region of the jet. A critical Froude number was found for the three sets of profiles, below which the jet was absolutely unstable for all the density ratios less than unity. The critical Froude number for the first and the second set of profiles was almost equal (Fr = 1.83 and Fr = 1.58 respectively). The critical Froude number for the third set of profiles (Fr = 3.74) was higher. For all the profiles, the critical Froude number demarcated the jet flow into the momentum-driven regime and the buoyancy-driven regime similar to the Strouhal number regimes observed by Subbarao and Cantwell (1992).

University of Oklahoma

Graduate College

HIGH-SPEED RAINBOW SCHLIEREN DEFLECTOMETRY ANALYSIS OF HELIUM JETS FLOWING INTO AIR FOR MICROGRAVITY APPLICATIONS

A THESIS

SUBMITTED TO THE GRADUATE FACULTY

in partial fulfillment of the requirements

for the degree of

MASTERS OF SCIENCE

By

Peter A. Leptuch

Norman, Oklahoma

2002

Abstract

The flow phenomena of buoyant jets have been analyzed by many researchers in recent years. Few, however have studied jets in micro-gravity conditions, and the exact nature of the flow under these conditions has until recently been unknown. This study seeks to extend the work done by researchers at the University of Oklahoma in examining and documenting the behavior of helium jets in micro-gravity conditions. Quantitative rainbow schlieren deflectometry data have been obtained for helium jets discharging vertically into quiescent ambient air from tubes of several diameters at various flow rates using a high-speed digital camera. These data have obtained before, during and after the onset of microgravity conditions.

High-speed rainbow schlieren deflectometry has been developed for this study with the installation and use of a high-speed digital camera and modifications to the optical setup. Higher temporal resolution of the transitional phase between terrestrial- and micro-gravity conditions has been obtained, which has reduced the "averaging effect" of longer exposure times used in all previous schlieren studies.

Results include color schlieren images, color time-space images (temporal evolution images), frequency analyses, contour plots of hue and contour plots of helium mole fraction. The results, which focus primarily on the periods before and during the onset of microgravity conditions, show that the pulsation of the jets normally found in terrestrial-gravity ("earth"-gravity) conditions cease, and the gradients in helium diminish to produce a widening of the jet in micro-gravity conditions. In addition, the results show that the disturbances propagate upstream from a downstream source.

UNIVERSITY OF OKLAHOMA

GRADUATE COLLEGE

SCALAR MEASUREMENTS AND ANALYSIS OF HELIUM JETS IN EARTH GRAVITY AND MICROGRAVITY USING RAINBOW SCHLIEREN DEFLECTOMETRY

A THESIS

SUBMITTED TO THE GRADUATE FACULTY

in partial fulfillment of the requirements for the

degree of

MASTER OF SCIENCE

By

Tze Wing Yep

Norman, Oklahoma

2001

Abstract

Recent experiments have shown that low-density gas jets injected into a high-density gas undergo an instability mode leading to highly periodic oscillations in the flow field. The transition from laminar to turbulent flow in these jets is abrupt, without a gradual change in scales. Although this type of instability at high Richardson numbers has been attributed to buoyancy, direct physical evidence was not acquired through experiments. In this study, several experiments were conducted in Earth gravity and microgravity to acquire qualitative data on near field flow structure of helium jets injected into air. Microgravity conditions were simulated in the 2.2-second drop tower at NASA Glenn Research Center.

The operating parameters of this study included the tube inside diameter, the jet Reynolds number, and the jet Richardson number. Tubes with inside diameters of 19.05 mm and 31.75 mm were used in the experiments conducted in the drop tower. The jet flow was analyzed using quantitative rainbow schlieren deflectometry, a non-intrusive line of sight measurement technique for the whole field. The flow structure was characterized by distributions of angular deflection and the resulting helium mole fraction obtained from color schlieren images taken at 60 Hz. Three sets of experimental data with respect to three schlieren fields of view were acquired for each tube.

Results show that the jet in microgravity was up to 70 percent wider than that in Earth gravity. The global jet flow oscillations observed in Earth gravity were absent in microgravity, providing direct experimental evidence that the flow instability in the low-density jet was buoyancy-induced. This study provides quantitative details of temporal flow evolution as the experiments undergo change in gravity in the drop tower.

UNIVERSITY OF OKLAHOMA

GRADUATE COLLEGE

FULL FIELD SCALAR MEASUREMENTS IN A PULSATING HELIUM JET USING RAINBOW SCHLIEREN DEFLECTOMETRY

A THESIS

SUBMITTED TO THE GRADUATE FACULTY

in partial fulfillment of the requirements for

the degree of

MASTERS OF SCIENCE

By

Kasyap.S.Pasumarthi
Norman, Oklahoma
July 2000

Abstract

The flow structure of a pulsating helium jet was investigated using quantitative rainbow schlieren deflectometry. The operating parameters included the tube inside diameter, the jet Reynolds number and the jet Richardson number. The jet structure was characterized by the frequency spectrum, temporal evolution of the oscillations and mean and root-mean-square profiles of the species mole fraction, which in this case, was helium. Experiments were conducted using a variable nozzle facility. Angular deflection data were obtained using rainbow schlieren deflectometry across full field of color images taken at a temporal resolution of 60Hz.

The flicker cycle was analyzed by instantaneous rainbow schlieren images, contour plots of deflection angle and helium mole fraction placed sequentially in time. To observe the flow downstream, the tube was lowered with respect to the optical setup and images were taken at different axial planes. In this way, the laminar, transition and turbulent regions of the jet flow were observed. Abel inversion algorithm (Albers 1998) was utilized to reconstruct the refractive index field from the measurements of the beam deflection angle. The concentration field was then generated from the refractive index field. The phenomenon of vortex initiation and propagation in thee flicker cycle was described by correlating the ray deflection angle and concentration contour plots.

Experiments in the flickering jet reveal global oscillation in the flow field. The effect of jet exit Reynolds Number and jet Richardson Number on the flickering frequency was analyzed. The effect of jet Richardson Number was more pronounced than that of the jet exit Reynolds Number. The flow field was studied quantitatively in terms of temporal evolution and statistical description of helium mole fraction.

Journal Papers

Published/In Press

1. Yep, T-W., Agrawal, A.K., and Griffin, D.W., 2003, "Gravitational Effects on Near Field Flow Structure of Low-Density Gas Jets," *AIAA Journal*, vol. 41, pp. 1973-1979.

2. Pasumarthi, K., and Agrawal, A.K., 2003, "Schlieren Measurements and Analysis of Concentration Field in Self-Excited Helium Jets," *Physics of Fluids*, vol. 15, pp. 3683-3692.

3. Yildirim, B.S., and Agrawal, A.K., "Full-Field Concentration Measurements of Self-Excited Oscillations in Momentum-Dominated Helium Jets," *Experiments in Fluids*, in press, 2004.

4. Pasumarthi, K., and Agrawal, A.K., "Buoyancy Effects on Flow Transition in Low-Density, Inertial Gas Jets," *Experiments in Fluids*, in press, 2005.

In Review

5. Leptuch, P.A., and Agrawal, A.K., "High-Speed Rainbow Schlieren Visualization of an Oscillating Helium Jet Undergoing Gravitational Change," *Journal of Visualization*, submitted, July 2003.

6. Satti, R., and Agrawal, A.K., "Numerical Analysis of Gravitational Effects in Buoyant and Inertial Helium Gas Jets," *AIAA Journal*, submitted, August 2004.

7. Lawson, A. L. and Parthasarathy, R. N. "Linear Stability Analysis of Gravitational Effects on a Low-Density Gas Jet Injected into a High-Density Medium," in review, *Physics of Fluids*.

In preparation[1]

8. Pasumarthi, K., Agrawal, A.K., and Griffin, D.W. "Oscillatory Behavior of Momentum-Dominated Low Density Gas Jets Undergoing Gravitational Change," *Journal of Fluid Mechanics*.

9. Satti, R., and Agrawal, A.K., "Computational Analysis of Flow Structure in the Near-Field of Low-Density Gas Jets," *International Journal of Heat and Fluid Flow*

10. Satti, R., and Agrawal, A.K., "Transient Analysis of Flow Evolution in Low-Density Gas Jets," *ASME Journal of Fluids Engineering*

11. Vedantam, N. K. and Parthasarathy, R. N. "Effects of Mean Velocity Profiles on the Instability of Variable Density Jets."

[1] These papers are not included in the report.

AIAA JOURNAL
Vol. 41, No. 10, October 2003

Gravitational Effects on Near-Field Flow Structure of Low-Density Gas Jets

Tze-Wing Yep* and Ajay K. Agrawal†
University of Oklahoma, Norman, Oklahoma 73019
and
DeVon Griffin‡
NASA John H. Glenn Research Center at Lewis Field, Cleveland, Ohio 44135

Experiments were conducted in Earth gravity and microgravity to acquire quantitative data on near-field flow structure of helium jets injected into air. Microgravity conditions were simulated in the 2.2-s drop tower at NASA John H. Glenn Research Center. The jet flow was observed by quantitative rainbow schlieren deflectometry, a nonintrusive line-of-sight measurement technique suited for the microgravity environment. The flow structure was characterized by distributions of helium mole fraction obtained from color schlieren images taken at 60 Hz. Results show that the jet in microgravity was up to 70% wider than that in Earth gravity. Experiments reveal that the global flow oscillations observed in Earth gravity are absent in microgravity. Quantitative details are provided of flow evolution as the experiment undergoes change in gravity in the drop tower.

Introduction

LOW-DENSITY jets are found in many engineering applications and natural phenomena, for example, exhaust from engines and stacks in industry, fuel leaks and accidental fires, diffusion flames, and geophysical events such as volcanic eruptions. Several recent studies[1–3] have focused on the far-field behavior of low-density jets using helium as the jet fluid. However, the near-field jet behavior has direct influence on the acoustic noise and flow development in the far field. Thus, an understanding of the flow structure in the near field of low-density gas jets is of significant fundamental importance. Subbarao and Cantwell[4] studied the near-field flow behavior of helium jets issued from a vertical tube into a coflow of air. The jets were characterized as buoyant for jet Richardson number varying between 0.5 and 6.0 in experiments [where $Ri = gd(\rho_a - \rho_j)/\rho_j U_j^2$, where g is the gravitational acceleration, d is the tube inside diameter, ρ_a and ρ_j are the freestream and jet densities, respectively, and U_j is the mass-averaged jet exit velocity]. They observed an extremely regular flowfield consisting of periodic formation and breakdown of helium-containing vortical cells. Measurements revealed large centerline velocity fluctuations and early and abrupt breakdown of the potential core. Even the large-scale structure after the breakdown repeated itself with regularity. The Strouhal number ($Sr = fd/U_j$, where f is the oscillation frequency) of the oscillating mode was independent of the Reynolds number. For $Ri > 1.0$, Sr scaled with Richardson number, indicating buoyancy-dependent instability mode. However, for $Ri < 0.5$, the Strouhal number was independent of the Richardson number. They speculated that perturbations in the airstream, for example, on the surface boundary layer outside the jet tube, were likely to dominate the flow instability and transition processes.

Pulsations in the near field of helium jets flowing into quiescent air were also observed by Hamins et al.,[5] who found that a minimum jet velocity was required to trigger the oscillations. The measured Strouhal number correlated with Froude number ($Fr = gd/U_j^2$, or inverse Richardson number), suggesting that the oscillations were buoyancy induced. They found that the Strouhal number–Froude number correlation for helium jets differed from that for flickering flames, implying differences in the buoyancy effects in nonreacting and reacting jets. Mell et al.[6] performed numerical simulations of helium jets in air and found excellent agreement between computed oscillation frequencies with those obtained experimentally by Hamins et al.[5] over a range of Froude numbers.

Experiments in naturally unstable helium jets by Cetegen and Kasper[7] extended the operating regime of Richardson numbers to those in pool fires and buoyant plumes. The oscillation frequency was represented by a correlation between Strouhal number and Richardson number for Ri varying from 1.5 to 5.0×10^4. Phase-resolved laser-Doppler velocity measurements revealed buoyant acceleration of the jet fluid accompanied with strong radial inflow of the surrounding air. A toroidal vortex ring was formed near the jet exit in the region of the highest centerline velocity. As the vortex convected downstream, it interacted with and affected the primary jet flow structure. Cetegen[8] reported similar mechanistic details of vortex formation and convection using particle image velocimetry. Flow oscillations in the near field of low-density jets have also been observed at smaller Richardson numbers (see Refs. 9–12).

Although oscillations in the near field of low-density gas jets at Richardson numbers above unity are attributed to buoyancy, no direct physical evidence has been acquired in previous experiments. Thus, the present study was conducted to investigate the effects of buoyancy on the stability and flow structure of low-density gas jets. The jet flow was quantified by helium concentration measurements obtained using the quantitative rainbow schlieren deflectometry (RSD) technique.[13] RSD is a nonintrusive optical diagnostics technique, especially suited for whole-field measurements in the microgravity environment. In the RSD technique, the optical setup is tolerant to minor mechanical vibrations or misalignments, power-consuming lasers often unsuitable for use in microgravity are not required, and seeding of the flow presenting unique challenges in microgravity is avoided. The technique has been used for measurements of concentration in helium jets[14,15] and temperature in diffusion flames in Earth gravity[16,17] and microgravity.[18] The microgravity environment was simulated in the 2.2-s drop tower facility at the NASA John H. Glenn Research Center. The experimental approach, results, and conclusions of the study are presented in the following sections.

Received 7 November 2001; revision received 18 April 2003; accepted for publication 20 May 2003.

*Graduate Research Assistant, School of Aerospace and Mechanical Engineering.
†Associate Professor, School of Aerospace and Mechanical Engineering, Room 212, 865 Asp Avenue; aagrawal@ou.edu. Member AIAA.
‡Electro-Optical Engineer, Microgravity Science Division.

Experimental Approach

The experimental setup was housed in a drop rig, 840 mm high, 960 mm long, and 400 mm wide, with a standard aluminum A frame. Al-Ammar et al.,[18] who conducted experiments with hydrogen gas jet diffusion flames in Earth gravity and microgravity, completed the initial setup. The experimental setup was modified for helium jet experiments of the present study. It consists of three major components: flow system, rainbow schlieren apparatus, and image recording system.

Figure 1 shows a schematic of the flow system. Helium gas was supplied from two 1000-cm^3 pressurized cylinders. A pressure relief valve set at 1.38 MPa (200 psig) was placed between the cylinders. The pressure regulator maintained the gas supply pressure at 690 kPa (100 psig). A calibrated mass flow meter was used to measure the helium gas flow rate. A metering valve controlled the gas flow rate. A solenoid valve was used to instantaneously activate or block the gas flow. A positioning jack was used to locate the jet tube with respect to the schlieren field of view. Jet tubes of 19.1- and 31.8-mm inside diameter were used in this study. The upstream and bend regions of the jet tube were filled with steel wool to minimize the flow nonuniformities. Steel screens were placed at the inlet and exit sections of the bend region. The straight length of the jet tube was 0.30 m because of the spatial constraints of the drop rig. Tube outside was tapered to reduce the wall thickness at the jet exit to 1.3 and 0.3 mm, for the larger and smaller diameter tubes, respectively. Unlike the studies in Refs. 6 and 7, no screen to affect flow uniformity at the jet exit was used. Thus, the present experiment represents naturally occurring conditions at the jet exit, providing true representation of such jets in practical applications.

The jet flow structure was visualized and quantified by the rainbow schlieren apparatus shown in Fig. 2. The light input to a 5-μm-wide and 3-mm-high source aperture is provided by a

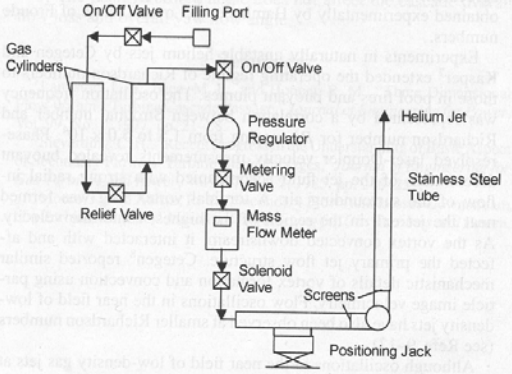

Fig. 1 Schematic diagram of the flow system.

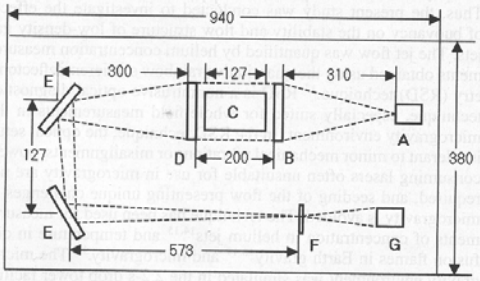

Fig. 2 Optical layout of the rainbow schlieren apparatus (all dimensions in millimeters): A, source aperture; B, collimating lens; C, test medium; D, decollimating lens; E, flat surface mirrors; F, color filter; G, and CCD array with lens.

150-W halogen light source connected through a 600-μm-diam fiber-optic cable. The source aperture is placed at the focal point of an 80-mm-diam, 310-mm focal length collimating lens. The collimated light rays passing through the test section are deflected by density gradients in the flowfield. The light rays are decollimated by an 80-mm-diam, 1000-mm-focal-length decollimating lens. Because of space constraints of the setup, a pair of 100-mm-diam, aluminum-coated flat surface mirrors was used to fold the rays by 180 deg. The folded light rays form the displaced image of the source aperture on a 3.5-mm-wide, computer-generated, symmetric rainbow filter, placed at the focal point of the decollimating lens. A camera lens of 75-mm focal length is used to image the test section onto the charge-coupled device (CCD) array. Schlieren images were acquired by the color camera at 60 field images per second, and digitized by a 24-bit color frame grabber installed in an onboard computer. Images were stored in tagged image file format (TIFF) at pixel resolution of 640 × 480.

The test sequence was automated by data acquisition and control systems resident on the computer. First, the computer fans were turned off to minimize the flow disturbances. Then, the solenoid valve was activated to turn on the jet flow. After the residual air in the jet tube was flushed out and the jet flow reached steady state, the frame grabber was activated to acquire the schlieren images. Next, the experiment was released to simulate microgravity conditions in the drop tower. After impact, the computer fans were turned on and the gas supply was turned off. After retrieving the drop rig, the image data were transferred from computer memory to an external data-storage device. For each experiment, the schlieren images were acquired for about 1.0 s in Earth gravity and 2.0 s in microgravity.

Schlieren Analysis

The angular deflection of a light ray by an axisymmetric refractive index field is given for small deflections by the following relationship:

$$\varepsilon(y) = 2y \int_y^\infty \frac{\mathrm{d}\delta}{\mathrm{d}r} \frac{\mathrm{d}r}{\sqrt{(r^2 - y^2)}} \tag{1}$$

where $\delta = (\eta - 1)$ is the refractive index difference and η is the refractive index of the test medium normalized by that of the surrounding air. In the RSD technique, the deflection angle is determined from measurements of color (or hue) in the schlieren image and the color filter calibration curve.[13,14] The refractive index difference is computed from Abel inversion of Eq. (1) expressed in discrete form as

$$\delta(r_i) = \delta(i \cdot \Delta r) = \sum_{j=i}^{NN} D_{ij} \cdot \varepsilon_j \tag{2}$$

where Δr is the sampling interval, NN is the number of intervals, and D_{ij} are geometric coefficients given in Ref. 19. In an ideal gas at constant temperature T and pressure P, the refractive index difference is

$$\delta = \frac{P}{\bar{R}T} \sum_l \kappa_l X_l M_l \tag{3}$$

where $\bar{R}$ is the universal gas constant, κ is the Dale–Gladstone constant, X is the species mole fraction, and M is the species molecular weight. The summation in Eq. (3) is taken over three species, that is, oxygen, nitrogen, and helium. Equation (3) was used to construct a table between δ and helium mole fraction, assuming nitrogen to oxygen mole ratio of 3.76 in standard air.

Measurement uncertainties arise from uncertainties in the image hue (or color) and propagate to uncertainties of angular deflection, refractive index difference, and helium mole fraction. For a given uncertainty in the image hue, the uncertainty in helium mole fraction increases exponentially toward the jet center.[14] Based on the image hue uncertainty derived from the filter calibration curve, the uncertainty of helium mole fraction is between 0.08 and 0.15 (absolute) for $r/d < 0.4$ and/or mole fractions above 0.8. Outside these

constraints, the helium mole fraction is accurate to within 8% of the measured value.

Results and Discussion

Experiments were performed to capture the flow structure in the near, mid, and far field of steady and unsteady jets in Earth gravity. Thus, at least three experiments were conducted for each test condition. In this paper, only the near-field data are presented for a steady and an unsteady jet in Earth gravity at operating conditions listed in Table 1. The jet exit Reynolds number is defined as $Re = U_j \cdot d/\nu$, where ν is the kinematic viscosity of helium.

Steady Jet (Case 1)

Figure 3 shows a sequence of contour plots of helium mole fraction during transition from Earth gravity to microgravity in the drop tower. Contour plots are shown only for one side of the jet because of the flow symmetry. Results shown are constrained to regions/values where data were considered reliable. Figure 3a shows that the jet in Earth gravity ($t = 0.0$ s) extends radially to about $r/d = 0.8$ near the tube exit. The jet width is nearly constant in the flow direction. Apparently, the radial growth of the jet shear layer between helium and air is constrained by the buoyant acceleration of the core region. Similar results were obtained by Pasumarthi,[15] who obtained detailed measurements of helium jets in Earth gravity. On entering microgravity, the jet widens at the exit where steady conditions are reached within $\frac{1}{5}$ s after the drop (Fig. 3e). The flow continues to evolve as downstream regions of the jet widen gradually. The contour plot toward the end of the drop ($t = 2.0$ s in Fig. 3f) represents steady microgravity conditions. Evidently, the jet width in microgravity is higher than that in Earth gravity by 35% at $z/d = 0.3$ and 70% at $z/d = 3.0$. In microgravity (Fig. 3f), helium mole fraction contour lines diverge away from the center, signifying a typical shear layer of a nonbuoyant jet. In contrast, the contour lines in Earth gravity (Fig. 3a) converge toward the center because of the buoyant flow acceleration. Figure 4 shows a comparison of radial profiles of helium mole fraction in Earth gravity and microgravity at $z/d = 1.5$. In microgravity, helium diffuses farther into air because of the absence of buoyancy. At this location, the jet in microgravity is about 65% wider than that in Earth gravity.

Previous studies in drop towers have raised concerns about the flow reaching steady state within the limited microgravity duration. Figure 5 shows time traces of helium mole fraction at $z/d = 1.5$ during the drop. Results show that, with the change in gravity, the jet widens initially and, thereafter, it contracts slightly before reaching steady conditions. The time delay of 0.08 s between peaks of 0.50

Table 1 Summary of test conditions

Case	d, mm	U_j, m/s	Re	Ri (in Earth gravity)	f, Hz
1	19.1	1.54	240	0.49	Nonoscillating
2	31.8	1.15	300	1.44	12.2

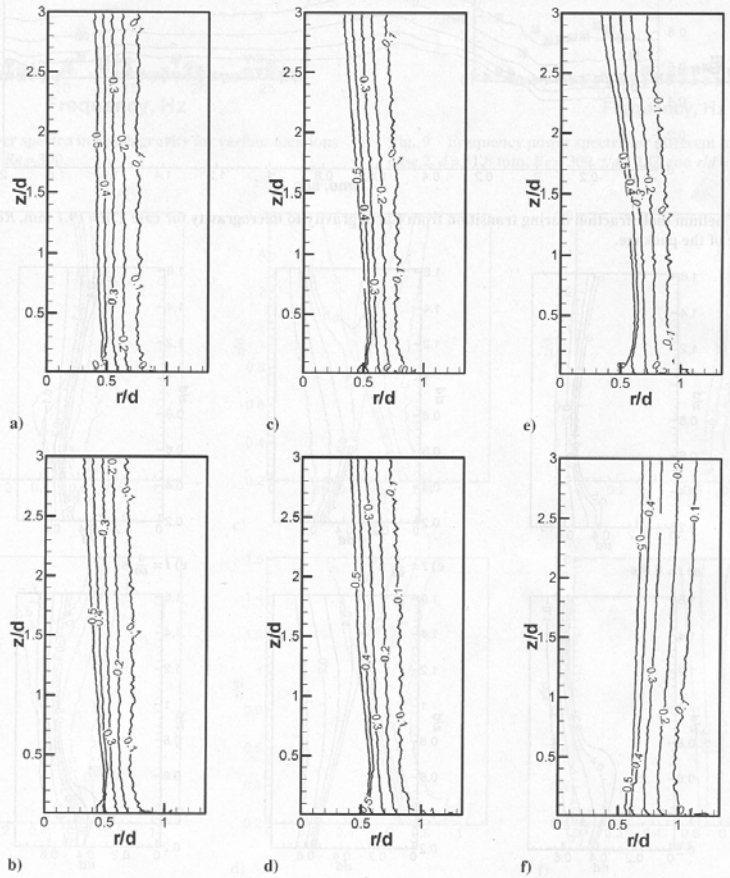

Fig. 3 Contours of helium mole fraction during transition from Earth gravity to microgravity for case 1, $d = 19.1$ mm, $Re = 240$: a) $t = 0.0$ s (denotes release of the package), b) $t = \frac{1}{30}$ s, c) $t = \frac{1}{15}$ s, d) $t = \frac{1}{10}$ s, e) $t = \frac{1}{5}$ s, and f) $t = 2.0$ s.

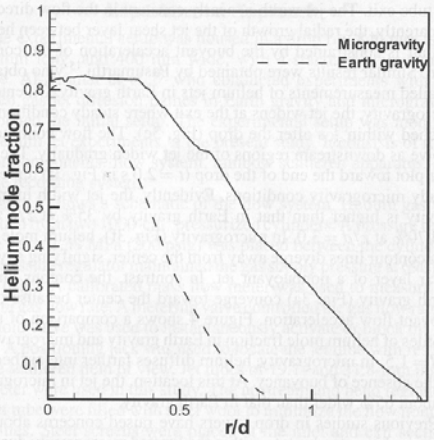

Fig. 4 Helium mole fraction in Earth gravity and microgravity for case 1, $d = 19.1$ mm, $Re = 240$, at $z/d = 1.5$.

and 0.10 helium mole fraction profiles indicates that the interior flow of the jet responds more quickly to the change in gravity. The jet expands until about $t = 0.65$ s, and steady conditions are reached throughout the jet flow after about $t = 1.0$ s. These results show that the 2.2-s duration of the drop was adequate for the experiment.

Oscillating Jet (Case 2)

For test conditions of case 2, the flow exhibited self-excited periodic oscillations in Earth gravity. Figure 6 shows a sequence of contour plots ($\frac{1}{60}$ s apart) of helium mole fraction to depict an oscillation cycle in Earth gravity. Results show that the helium mole fraction varied throughout the flowfield during the oscillation cycle. In Fig. 6a, the buoyancy-induced acceleration of light jet fluid in heavier surroundings results in contraction of the jet boundary until about $z/d = 0.35$. This process continues in the next plot (Fig. 6b), where the jet compression is observed until about $z/d = 0.75$. In the next plot (Fig. 6c), a vortex is present near $z/d = 1.4$ in between the two radial locations of the 0.50 mole fraction contour. Subsequently, the jet expands near the exit as the vortex moves downstream of the field of view. The cycle repeats itself with radial inflow of air compressing the jet core region as shown in Fig. 6f. The contour plot in Fig. 6f is similar, though not identical, to that in Fig. 6a, suggesting that the oscillation frequency is approximately 12 Hz. This

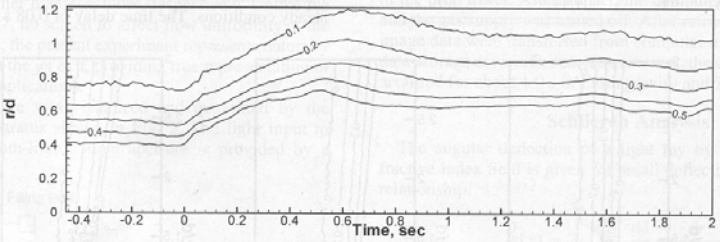

Fig. 5 Time traces of helium mole fraction during transition from Earth gravity to microgravity for case 1, $d = 19.1$ mm, $Re = 240$, at $z/d = 1.5$; time $t = 0.0$ s denotes release of the package.

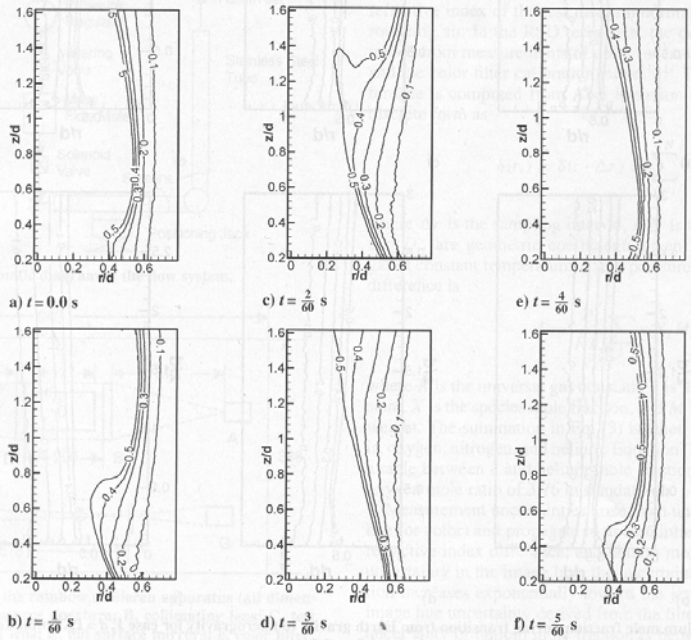

a) $t = 0.0$ s
c) $t = \frac{2}{60}$ s
e) $t = \frac{4}{60}$ s
b) $t = \frac{1}{60}$ s
d) $t = \frac{3}{60}$ s
f) $t = \frac{5}{60}$ s

Fig. 6 Contours of helium mole fraction during a flicker cycle in Earth gravity for case 2, $d = 31.8$ mm, $Re = 300$.

is confirmed by frequency power spectra of angular deflection at several locations shown in Fig. 7. The power spectra reveal a dominant frequency of 12.2 Hz at several locations, suggesting global oscillations in the flowfield.

The evolution of the jet flow structure with change in gravity is shown in Fig. 8 by a sequence of contour plots of helium mole fraction. In Earth gravity ($t = 0.0$ s in Fig. 8a), the jet compression near the exit is accompanied with radial inflow of the surrounding air. Immediately after the drop is initiated ($t = \frac{1}{60}$ s in Fig. 8b), a vortex is observed at $z/d = 1.3$. The jet has also expanded radially near the exit region. At $t = \frac{1}{30}$ s in Fig. 8c, the vortex has moved downstream of the field of view, while the jet continues to widen near the exit region. Subsequently, the jet expands gradually in the downstream regions as steady microgravity conditions are reached. The helium mole fraction contours in microgravity are straight lines reminiscent of the nonbuoyant jet in Fig. 3f. In microgravity, the jet width exceeded the field of view of the schlieren apparatus. In the absence of a reference point in the surrounding medium (air), systematic errors were introduced during Abel inversion process in the downstream region. Thus, the contours lines in Fig. 8f did not

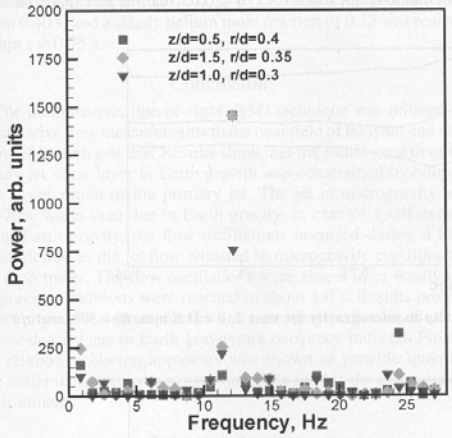

Fig. 7 Frequency power spectra in Earth gravity for various locations for case 2, $d = 31.8$ mm, $Re = 300$.

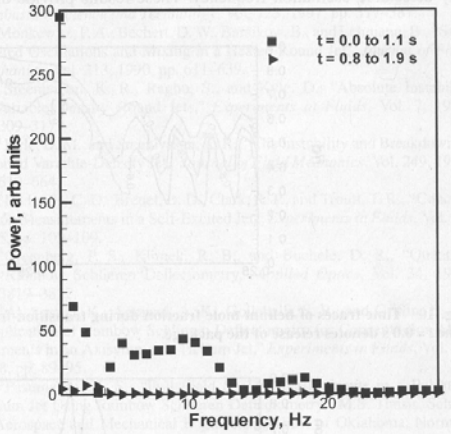

Fig. 9 Frequency power spectra for different microgravity periods for case 2, $d = 31.8$ mm, $Re = 300$, $z/d = 1.0$, and $r/d = 0.6$.

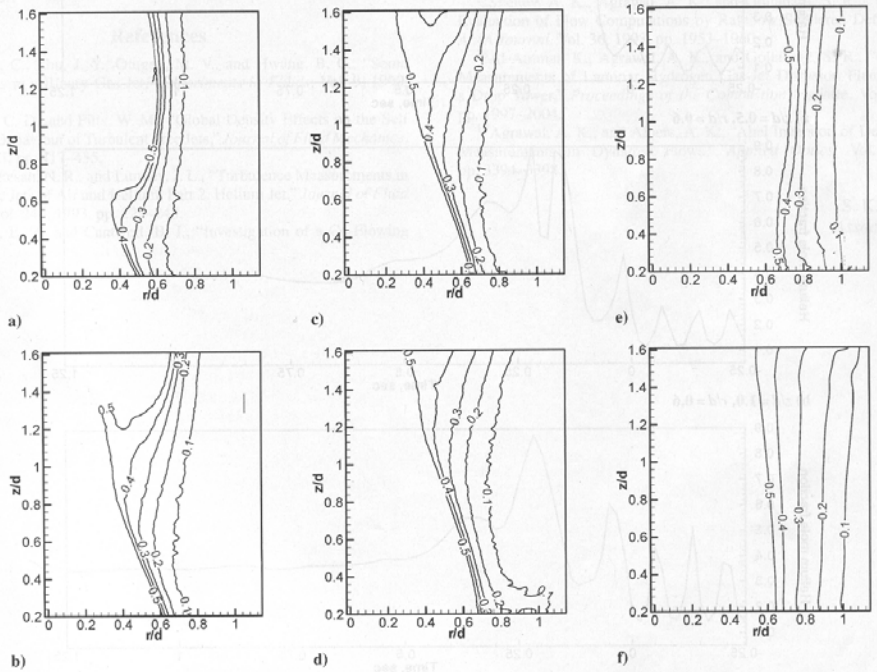

Fig. 8 Contours of helium mole fraction during transition from Earth gravity to microgravity for case 2, $d = 31.8$ mm, $Re = 300$: a) $t = 0.0$ s (denotes release of the package), b) $t = \frac{1}{60}$ s, c) $t = \frac{2}{60}$ s, d) $t = \frac{3}{60}$ s, e) $t = \frac{13}{60}$ s, and f) $t = 2.0$ s.

diverge fully as expected in nonbuoyant jets. Smaller tubes were considered to avoid this problem. However, the resulting oscillation frequency exceeded the temporal resolution of the imaging system used in this study.

Power spectra of angular deflection were obtained to assess characteristics of jet oscillations in microgravity. The analysis was performed using 1.1 s of data taken at the beginning and toward the end of the drop to distinguish initial transients from steady microgravity conditions. The power spectra in Fig. 9 show oscillations without a distinct frequency, when data at the beginning of the drop are used. Data taken at the end of the drop, however, did not produce any detectable oscillation frequency. These results provide direct physical evidence that flow oscillations in low-density jets are buoyancy induced.

The change in the jet flow during transition from Earth gravity to microgravity is shown in Fig. 10 by time traces of helium mole fraction at $z/d = 1.0$. The oscillating jet flow expands radially as it responds to the change in gravity. Figure 10 shows that the inner region of the jet expands before the outer region. Oscillations sustain during a brief initial period of microgravity, with steady conditions reached within $t = 1.0$ s. Further understanding of the jet flow during transition from Earth gravity to microgravity is obtained from Fig. 11, showing helium mole fraction profiles at different axial locations for $r/d = 0.6$. Near the jet exit at $z/d = 0.5$

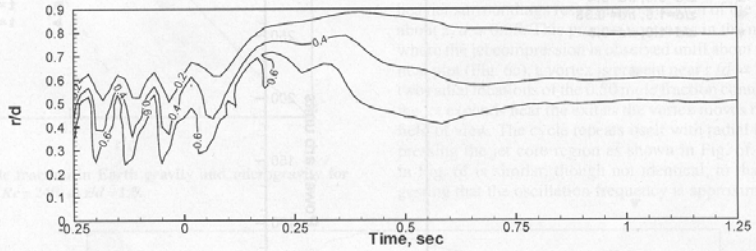

Fig. 10 Time traces of helium mole fraction during transition from Earth gravity to microgravity for case 2, $d = 31.8$ mm, $Re = 300$, and $z/d = 1.0$; time $t = 0.0$ s denotes release of the package.

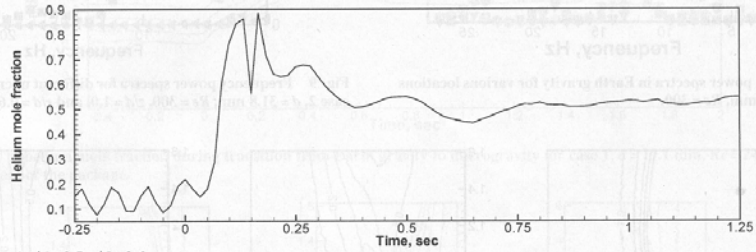

a) $z/d = 0.5$, $r/d = 0.6$

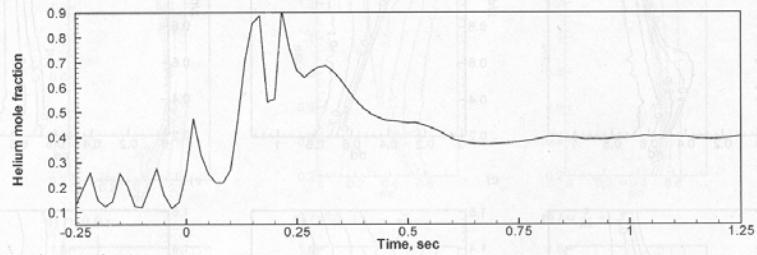

b) $z/d = 1.0$, $r/d = 0.6$

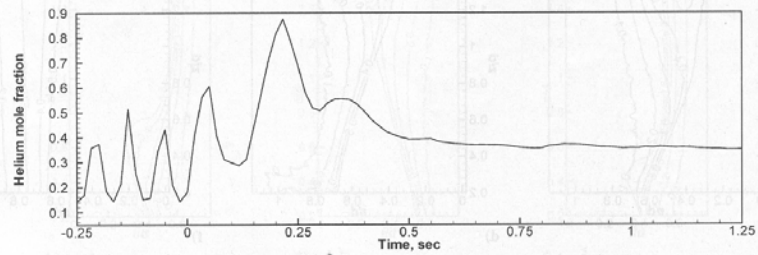

c) $z/d = 1.5$, $r/d = 0.6$

Fig. 11 Helium mole fraction during transition from Earth gravity to microgravity, time $t = 0.0$ s denotes release of the package.

(Fig. 11a), the helium mole fraction in Earth gravity varied between 0.10 and 0.20. As the jet expanded in microgravity, the helium fraction increased to about 0.90 within $t = 0.12$ s. Thereafter, the flow oscillations continued, although mean and amplitude of helium concentration decreased with time. Steady conditions corresponding to helium mole fraction of 0.55 were reached within $t = 1.0$ s. At $z/d = 1.0$ (Fig. 11b), the helium concentration peaked at $t = 0.17$ s. Subsequently, the jet oscillated briefly before reaching steady helium mole fraction of 0.40 within $t = 1.0$ s. Farther downstream at $z/d = 1.5$ (Fig. 11c), the helium concentration in Earth gravity varied between 15 and 40%. In this case, the peak helium concentration was reached at $t = 0.22$ s. The jet did not oscillate after about 0.40 s, and a steady helium mole fraction of 0.35 was reached within $t = 0.75$ s.

Conclusions

The nonintrusive, line-of-sight, RSD technique was utilized for quantitative flow measurements in the near field of buoyant and nonbuoyant helium gas jets. Results show that the radial growth of the steady jet shear layer in Earth gravity was constrained by buoyant flow acceleration of the primary jet. The jet in microgravity was 30–70% wider than that in Earth gravity. In case of a self-excited jet in Earth gravity, the flow oscillations occurred during a brief initial period as the jet flow adjusted to microgravity conditions in the drop tower. The flow oscillations were absent after steady microgravity conditions were reached in about 1.0 s. Results provide direct physical evidence, for the first time, that the flow oscillations in low-density jets in Earth gravity are buoyancy induced. Finally, the rainbow schlieren apparatus was shown to provide quantitative scalar measurements across the whole field in the microgravity environment.

Acknowledgment

This work was supported by the Physical Sciences Division of the NASA Office of Biological and Physical Research under Grant NAG 3-2388.

References

[1]So, R. M. C., Zhu, J. Y., Otugen, M. V., and Hwang, B. C., "Some Measurements in a Binary Gas Jet," *Experiments in Fluids*, Vol. 9, 1990, pp. 273–284.

[2]Richards, C. D., and Pitts, W. M., "Global Density Effects on the Self Preservation Behaviour of Turbulent Free Jets," *Journal of Fluid Mechanics*, Vol. 254, 1993, pp. 417–435.

[3]Panchapakesan, N. R., and Lumley, J. L., "Turbulence Measurements in Axisymmetric Jets of Air and Helium. Part 2. Helium Jet," *Journal of Fluid Mechanics*, Vol. 246, 1993, pp. 225–248.

[4]Subbarao, E. R., and Cantwell, B. J., "Investigation of a Co-Flowing Buoyant Jet: Experiments on the Effect of Reynolds Number and Richardson Number," *Journal of Fluid Mechanics*, Vol. 245, 1992, pp. 69–90.

[5]Hamins, A., Yang, J. C., and Kashiwagi, T., "An Experimental Investigation of the Pulsating Frequency of Flames," *Proceedings of the Combustion Institute*, Vol. 24, 1992, pp. 1695–1705.

[6]Mell, W. E., McGrattan, K. B., and Baum, H. R., "Numerical Simulation of Combustion in Fire Flumes," *Proceedings of the Combustion Institute*, Vol. 26, 1996, pp. 1523–1530.

[7]Cetegen, B. M., and Kasper, K. D., "Experiments on the Oscillatory Behavior of Buoyant Plumes of Helium and Helium–Air Mixtures," *Physics of Fluids*, Vol. 8, 1996, pp. 2974–2984.

[8]Cetegen, B. M., "Measurements of Instantaneous Velocity Field of a Non-Reacting Pulsating Buoyant Plume by Particle Image Velocimetry," *Combustion Science and Technology*, Vol. 123, 1997, pp. 377–387.

[9]Monkewitz, P. A., Bechert, D. W., Barsikow, B., and Lehmann, B., "Self-Excited Oscillations and Mixing in a Heated Round Jet," *Journal of Fluid Mechanics*, Vol. 213, 1990, pp. 611–639.

[10]Sreenivasan, K. R., Raghu, S., and Kyle, D., "Absolute Instability in Variable Density Round Jets," *Experiments in Fluids*, Vol. 7, 1989, pp. 309–317.

[11]Kyle, D. M., and Sreenivasan, K. R., "The Instability and Breakdown of a Round Variable-Density Jet," *Journal of Fluid Mechanics*, Vol. 249, 1993, pp. 619–664.

[12]Richards, C. D., Breuel, B. D., Clark, R. P., and Troutt, T. R., "Concentration Measurements in a Self-Excited Jet," *Experiments in Fluids*, Vol. 21, 1995, pp. 103–109.

[13]Greenberg, P. S., Klimek, R. B., and Buchele, D. R., "Quantitative Rainbow Schlieren Deflectometry," *Applied Optics*, Vol. 34, 1995, pp. 3819–3822.

[14]Al-Ammar, K., Agrawal, A. K., Gollahalli, S. R., and Griffin, D. W., "Application of Rainbow Schlieren Deflectometry for Concentration Measurements in an Axisymmetric Helium Jet," *Experiments in Fluids*, Vol. 25, 1998, pp. 89–95.

[15]Pasumarthi, K. S., "Full Field Scalar Measurements in a Pulsating Helium Jet Using Rainbow Schlieren Deflectometry," M.S. Thesis, School of Aerospace and Mechanical Engineering, Univ. of Oklahoma, Norman, OK, July 2000.

[16]Albers, B. W., and Agrawal, A. K., "Schlieren Analysis of an Oscillating Gas-Jet Diffusion Flame," *Combustion and Flame*, Vol. 119, 1999, pp. 89–94.

[17]Shenoy, A. K., Agrawal, A. K., and Gollahalli, S. R., "Quantitative Evaluation of Flow Computations by Rainbow Schlieren Deflectometry," *AIAA Journal*, Vol. 36, 1998, pp. 1953–1960.

[18]Al-Ammar, K., Agrawal, A. K., and Gollahalli, S. R., "Quantitative Measurements of Laminar Hydrogen Gas-Jet Diffusion Flames in a 2.2 s Drop Tower," *Proceedings of the Combustion Institute*, Vol. 28, 2000, pp. 1997–2004.

[19]Agrawal, A. K., and Albers, A. K., "Abel Inversion of Deflectometric Measurements in Dynamic Flows," *Applied Optics*, Vol. 38, 1999, pp. 3394–3398.

S. K. Aggarwal
Associate Editor

FULL-FIELD MEASUREMENTS OF SELF-EXCITED OSCILLATIONS IN MOMENTUM-DOMINATED HELIUM JETS

B.S. Yildirim and A.K. Agrawal*
School of Aerospace and Mechanical Engineering,
University of Oklahoma
Norman, Oklahoma 73019

ABSTRACT

Flow structure of momentum-dominated helium jets discharged vertically into ambient air was investigated using a high-speed rainbow schlieren deflectometry (RSD) apparatus operated at up to 2000 Hz. The operating parameters, i.e., Reynolds number and Richardson number were varied independently to examine the self-excited, flow oscillatory behavior over a range of experimental conditions. Measurements revealed highly periodic oscillations in the laminar region at a unique frequency as well as high regularity in the flow transition and initial turbulent regions. The buoyancy was shown to affect the oscillation frequency and the distance from the jet exit to the flow transition plane. Instantaneous helium concentration contours across the field of view revealed changes in the jet flow structure and the evolution of the vortical structures during an oscillation cycle. A cross-correlation technique was applied to track the vortices and to find their convection velocity. Time-traces of helium concentration at different axial locations provided detailed information about the oscillating flow.

* Corresponding Author
Associate Professor
865 Asp Avenue, Room 208
School of Aerospace and Mechanical Engineering
University of Oklahoma, Norman, OK 73019
Phone: (405) 325-1754, Fax: (405) 325-1088, email: aagrawal@ou.edu

1. Introduction

Flow structure and instability of gas jets has been the subject of several investigations in the past. When a low-density gas jet is injected into a high density environment, self-excited, highly periodic oscillations occur in the flow field under some conditions. Even in transition and turbulent flow regimes, large scale structures behave in a repetitive coherence. Several studies have been conducted to characterize the instability and its effects on the flow structure. The important parameters in these studies are the jet Reynolds number ($\mathrm{Re} = U_j d / \nu$ where U_j is the mean jet exit velocity, d is the jet exit diameter, and ν is the kinematic viscosity), the jet Richardson number ($Ri = g.d.(\rho_\infty - \rho_j)/(\rho_j.U_j^2)$ where g is the gravitational acceleration, ρ_∞ and ρ_j are the free-stream and jet densities, respectively) and the Strouhal number ($St = f.d/U_j$ where f is the flow oscillation frequency). Low-density jets are classified as either buoyancy-dominated (Ri>1.0) or momentum-dominated (Ri<<1.0).

Several researchers have studied self-excited oscillations in buoyancy-dominated jets using helium or helium/air mixture as the low-density fluid. Subbarao and Cantwell (1992) identified the oscillating and non-oscillating regimes for vertical helium jets in a co-flow of air. They reported the oscillating behavior of the helium jet at moderate values of Richardson numbers (0.5<Ri<6.0) and stated that this type of flow was subjected to an unusual type of transition to turbulence, consisting of a rapid but highly structured and repeatable breakdown and intermingling of the jet and free stream fluids. The strong dependence of Strouhal number on Richardson number indicated the dominance of the buoyancy effects. Hamins et al. (1992) used the shadowgraph technique to measure the oscillation frequency of helium jets in quiescent air over a range of Froude number (≈ 0.001 to ≈ 1) and Reynolds number (≈ 1 to ≈ 100). Flow

oscillations were not observed until a minimum jet exit velocity was attained. The Strouhal number correlated with inverse Froude number (or Ri), indicating strong buoyancy dependence. Similar observations in round and planar helium jets were made by Cetegen and Kasper (1996), Cetegen (1997), and Cetegen et al. (1998), who extended the operating regime of Richardson numbers to that in pool fires and buoyant plumes. Although self-excited oscillations in these studies were attributed to buoyancy, the direct physical evidence was provided by experiments of Yep et al. (2003) who found that the flow oscillations observed in Earth gravity vanished in the microgravity environment of the 2.2-sec drop tower.

Self-excited oscillations have also been observed in the momentum-dominated flow regime of low-density gas jets. Using helium and helium/air mixtures, Sreenivasan et al. (1989) found pure oscillations in the near field below a critical density of the jet fluid. Flow visualization revealed intermittent breakdown and spectacular spreading of the low-density jet, beyond a certain axial distance. Monkewitz et al. (1990) reported the spectacular spreading of unstable heated air jets below the critical value of density ratio (jet fluid density/ambient fluid density) of approximately 0.73. The spreading of the jet was characterized by the formation of vortex-ring structures and side-jets. Kyle and Sreenivasan (1993) studied the instability and the subsequent breakdown of axisymmetric jets of helium/air mixtures emerging into the ambient air. The oscillating behavior characterized by Strouhal number was shown to depend upon the density ratio, the jet diameter, and the jet momentum thickness, and it was nearly independent of the jet Reynolds number within the covered range $1500 < Re < 12{,}500$. The high degree of repeatability of the oscillating mode and strong interaction between jet flow and vortices led to large centerline velocity fluctuations. Richards et al. (1996) also found pure helium jets to display the self-excited behavior characterized by intense vortex interaction. Concentration measurements at

several radial locations obtained by an aspirating probe indicated increased mixing caused by the side jets. Global oscillations were reported for Reynolds numbers between 350 and 1850. Raynal et al (1996) observed similar self-excited oscillations in planar low-density helium jets.

While the self-excited oscillations in low-density jets at Ri>1.0 are caused by the buoyancy (Yep et al. 2003), the origin of the instability or oscillations in the momentum-dominated jets (Ri<<1.0) remains unknown. In past studies, the buoyancy was considered negligible in momentum-dominated jets and hence, it was ignored (Sreenivasan et al., 1989; Monkewitz et al., 1990; Kyle and Sreenivasan 1993; Richards et al., 1996). However, buoyancy may be important locally, especially in the jet shear layer where the axial momentum is small. In this study, we seek to study global features of flow oscillations in momentum-dominated helium jets at Ri<0.1 to examine the buoyancy effects by independently varying the two operating parameters, i.e., Reynolds number and Richardson number. The transition from laminar to turbulent flow will be investigated with the emphasis to identify the buoyancy effects. Later, we will present full-field helium concentration measurements to study the dynamics of the oscillating flow field. The diagnostics involves quantitative rainbow schlieren deflectomtery, a non-intrusive, optical technique for scalar measurements in non-reacting (Alammar et al., 1998; Pasumarthi and Agrawal, 2003) and reacting flows (Albers and Agrawal, 1999; Agrawal et al., 2002). Unlike previous applications of the rainbow schlieren technique, the present study utilizes a high-speed digital imaging system, needed to resolve the dynamics of the momentum-dominated low-density jets.

2. Experimental Approach

A compact test rig primarily designed and constructed for experiments in the 2.2-sec drop tower was used in this study. An external flow system was coupled with the test rig to increase the maximum flow rate. The flow system comprised of a high purity grade compressed helium cylinder, a pressure regulator, a needle valve to specify the helium flow rate, a calibrated mass flow meter, flexible plastic hoses and a vertically oriented straight tube to approximate fully-developed laminar flow at the jet exit. The tube outer surface was chambered at 30^0 to reduce its wall thickness to 1.0 mm at the exit.

The optical layout of the rainbow schlieren apparatus is similar to that of Yep et al. (2003), with changes made to achieve acceptable schlieren image quality using the high-speed digital camera. The 150-W halogen light source was integrated with a focusing optics assembly to maximize light collection at the inlet plane of the 600 μm diameter fiber optic cable. The source aperture was 3 mm high and 100 μm wide, the collimating lens was 80 mm diameter and 310 mm focal length achromat, the decollimating lens was 80 mm diameter and 1000 mm focal length achromat, and the symmetric rainbow filter was 3mm wide with hue ranging from 40^0 to 330^0. The rainbow schlieren images were acquired by Redlake Motion Xtra HG-TX high speed camera with a 75 mm focal length lens. For each experiment, 2700 images were taken at 1000 Hz or 2000 Hz depending upon the tube diameter, with the camera exposure time of 298 μs. The acquired images were stored digitally in TIFF format at pixel resolution of 384x512 or 144x512.

The color at a specific pixel location in the schlieren image is quantified by hue, uniquely related to the linear displacement of the light ray at the filter plane (Alammar et al, 1998). This relationship, established by calibrating the rainbow filter, provides angular deflection of light ray from measurement of hue in the color schlieren image. Subsequently, an Abel inversion

algorithm for axisymmetric media is utilized to reconstruct the refractive index field. Finally, the helium concentration field is determined by assuming isothermal flow in an ideal, binary gas system. Further details of the analysis procedure are given by Alammar et al. (1998) and Yep et al. (2003).

The uncertainties in the hue values leads to the uncertainties in the deflection angles, which propagate into the uncertainties in the refractive index and helium concentration. The uncertainty of deflection angle determined from the filter calibration curve was 5.0×10^{-4} degree compared to the maximum deflection angle of 4.0×10^{-2} degree. For a given uncertainty in hue (or deflection angle), the uncertainty in helium concentration increases exponentially as one approaches the jet center. (Alammar et al., 1998). This feature of Abel inversion combined with the small angular deflections in the center region (because of low density gradients) produced only qualitative helium concentration data for $r/d<0.2$ and/or concentration values above 90%. Outside these constraints, the uncertainty in helium concentration was 8% of the value. The uncertainty in the jet exit velocity was ± 0.013 m/s and the corresponding uncertainties in the Reynolds number and Richardson number were less than 1% of the value. The spatial resolution in the schlieren image was 0.18mm. The image blur caused by flow convection during finite exposure is another factor that affects the measurements. Based on the camera exposure time of 298 μm, the image blur for the test cases discussed in detail in this study was between 1 mm and 2 mm.

3. Results and Discussion

In this study, a total of nineteen different experiments were conducted spanning a range of Reynolds number from 350 to 2000 and Richardson number from 0.1 to 1.17×10^{-3}. The operating parameters, i.e., Re and Ri were varied independently using tubes with inside diameter of 10.5 mm, 14.5 mm, and 19.05 mm. Table 1 provides details of the experimental test conditions. In §

3.1, global features of flow oscillations will be discussed. The transition behavior from laminar to turbulent flow will be presented in § 3.2. Next, in § 3.3 we will show the instantaneous contour and time traces of helium concentrations to examine the oscillating flow structure. A cross-correlation technique will be utilized to track the large scale vortical structures.

3.1 Global Features and Flow Oscillations.

Figure 1 shows a typical rainbow schlieren image for Re=1200, Ri=8.58×10^{-3} and d=14.5mm. The image depicts the near field laminar region as well as the downstream turbulent region. Zero displacement of light rays at the jet axis and far away from it produces background hue in the schlieren image corresponding to that at the reference location (center) of the symmetric rainbow filter. Hue other than the background hue is produced by light rays deflected because of the finite density gradients in the media. A distinct advantage of the present schlieren technique is that the measurements of angular deflection of light rays are obtained simultaneously across the whole field without perturbing the flow. The Able inversion of angular deflection data however requires an axisymmetric medium. Thus, the field distributions of helium concentration were obtained only in the axisymmetic laminar flow regime and no concentration data are reported in the transition and turbulent flow regimes.

The jet oscillations were characterized by power spectra at a specific location in the flow field obtained by fast Fourier transform (FFT) of hue values acquired from 2048 consecutive schlieren images. Figure 2 shows the power spectra at a fixed axial location, z/d=1.0, for different radial locations, r/d=0.35, 0.41, and 0.5. Figure 2 reveals a dominant frequency of 234 Hz at all radial locations, suggesting global oscillations in the flow field. The spectral power is maximum at r/d=0.41, which is related to the jet core interacting with the outer vortical structure

as will be discussed later. Figure 3 shows power spectra at a fixed radial location, r/d=0.41, for different axial locations, z/d=0.05, 0.5, and 1.0 in the laminar flow regime. Again, a dominant frequency of 234 Hz is observed at all axial locations. Evidently, the flow oscillates immediately past the jet exit, i.e., z/d=0.05. The increase in the peak power signifies the flow oscillations growing in the streamwise direction.

Results in Figs. 2 and 3 demonstrated global oscillations in the laminar flow field. Moreover, the variations in the maximum spectral power suggested flow oscillation amplitude varying in the flow field. Next, we determined the maximum spectral power at various locations to construct the radial profiles at z/d=0.05, 0.5, and 1.0, shown in Fig. 4. Near the jet exit at z/d=0.05, a single peak in maximum power is observed at r/d=0.5 indicating that the flow oscillations are confined to a narrow region downstream of the tube wall. At z/d=0.5, the maximum power has increased by nearly an order of magnitude because oscillations have become more dominant. The radial profile of maximum power shows two peaks, respectively, at r/d=0.40 and 0.53. The double peak structure is attributed to the toroidal vortex around the jet core at this axial location. The separation distance between the peaks is an indication of the width of the vortex. At z/d=1, the maximum power has increased indicating more intense flow oscillations. The maximum power peaks occur at r/d=0.18 and 0.40 suggesting a greater portion of the jet core is affected by the vortex. The penetration of the vortex into the jet core is indicative of contraction of the jet caused by the buoyant acceleration. This situation is different from constant density jets, wherein the vortical structures contribute towards the radial spreading and growth of the jet.

Similar FFT analysis was performed for each experiment to find the global oscillation frequency listed in Table 1. The measured oscillation frequency ranged between 70 Hz and 813

Hz, which explains the need for the high-speed imaging system used in this study. The oscillation frequency increased with decreasing Richardson number, which limited the smallest Ri that could be probed using the 2000 Hz imaging system. It is instructive to compare our measurements using jet tube with d=19.05 mm to those of Richards et al. (1996) using contoured nozzle of 20 mm inside diameter. According to Fig. 5 the present results compare well with those of Richards et al. (1996), whereby the Strouhal number is nearly independent of the Reynolds number. Figure 5 also plots data obtained by Kyle and Sreenivasan (1993) using a contoured nozzle with d=9.3mm. These results indicate that the Strouhal numbers decrease for the small injector diameter.

A potential drawback of Fig. 5 is that the trend shown may be the combined effect of variations in both Re and Ri because Reynolds number and Richardson number are interdependent. Thus Re and Ri were varied independently during experiments. In Figure 6(a), the Strouhal number is plotted versus Reynolds number for fixed Richardson numbers. Results show that the Strouhal number increases slightly as the Reynolds number is increased. The Strouhal number is also affected by the Richardson number; higher Ri resulted in higher St. Figure 6(b) shows Strouhal number versus Richardson number for fixed Reynolds numbers. Again, St is shown to increase with increase in the Reynolds number and/or Richardson number. The dependence of Strouhal number on Richardson number suggests that buoyancy is important even though the jet flow is momentum-dominated. Results in Fig. 6 do not yield a direct correlation between Strouhal number and Re or Ri. In an effort to correlate experimental data, the oscillation frequency (f) was normalized using the buoyancy time scale or the time for a fluid element to move one jet diameter under the action of buoyancy or $\tau = [\rho_j d / g(\rho_\infty - \rho_j)]^{1/2}$. The normalized oscillation frequency $[f_n = f.\tau]$ correlated with Ri for all Reynolds numbers. Based

on a power law fit, the correlation is expressed as: $f_n = 0.434.Ri^{-0.465}$ with correlation coefficient of 0.963 in the range $1.17x10^{-3} < Ri < 4.4x10^{-2}$. Experimental data from Kyle and Sreenivasan (1993) and Richards et al. (1996) also agreed with this correlation as shown in Fig. 7.

3.2 Transition from Laminar to Turbulent Flow

In the previous section, measurements taken only in the laminar flow regime were presented. In this section, we extended the analysis to the transition from the laminar to turbulent flow. Figure 8 shows power spectra at a fixed radial location, r/=0.41, for different axial locations, z/d=1.5, 2.0, and 2.5. At z/d=1.5, the flow is undergoing the transition from the laminar to turbulent flow as shown by the image in Fig. 1. However, the flow oscillates at a unique frequency of 234 Hz, which is the same in the upstream laminar flow region. At z/d=2.0, the oscillation frequency is still the same, i.e. 234 Hz, even though the flow appears visibly turbulent in Fig. 1. The FFT analysis at other radial locations for z/d=1.5 and 2.0 yielded the same unique oscillation frequency (234 Hz), proving that the periodicity is maintained during the transition from the laminar to turbulent flow. Figure 8 shows that the flow is no longer periodic in the downstream turbulent regime at z/d=2.5, where the large scale vortical structures breakdown to produce a broadband power spectra.

Next, we examined the effect of operating parameters on the flow transition process. Figure 9 shows the color schlieren images obtained at different Reynolds numbers and Richardson numbers. Note that the scale of each image is different because several tube sizes were used for the experiments. In the upper set of schlieren images, the Richardson number is kept constant at $18x10^{-3}$ as the Reynolds number is varied from 510 to 1250. At the smallest Re, the jet is laminar in the field of view. At Re=830, the flow transition occurs near z/d=2.5. Further increase in the

Reynolds number causes the transition plane to move closer to the jet exit. The trend of decreasing normalized flow transition length (i.e., the distance from the jet exit to the transition plane divided by the tube inside diameter) with increasing Reynolds number is consistent with similar observations in low-density gas jet by Subbarao and Cantwell (1992), Takano and Kotani (1978), and Takahashi et al. (1982). In the lower set of schlieren images in Fig. 9, the Reynolds number is fixed at 1200 as the Richardson number is varied from 3.53×10^{-3} to 19×10^{-3}. Figure 9 shows that the normalized flow transition length decreases as the Richardson number increases, which is consistent with similar observations in buoyant low-density jets by Subbarao and Cantwell (1992). The size of the turbulent structures is also affected by the Richardson number; small scale structures are observed at lower Ri while structures are larger at higher Ri. These unexpected results clearly demonstrate that buoyancy affects the flow transition even for small Richardson numbers; a phenomenon ignored in past studies.

Next, a quantitative assessment of the flow transition length was conducted for various test cases in Table 1. In instantaneous schlieren images, the flow transition was marked by the appearance of small-scale structures across the width of the jet. For given test conditions, the location of the transition plane identified from instantaneous schlieren images however fluctuated with time. Thus, transition length was determined using mean and root-mean-square (rms) deflection angle contours obtained from 2730 consecutive schlieren images. Figure 10 shows contours of mean and rms angular deflection for Re=1600 and $Ri=4.83 \times 10^{-3}$. The contours are shown for only one side of the jet axis because of the symmetry. Mean angular deflection contours in Fig. 10(a) show the jet width increasing gradually, making it difficult to accurately identify the transition plane. However, the rms deflection angle contours provide a more direct measure of the transition plane. In the laminar region of the jet, the rms angular deflection was

small and the fluctuations were confined to a narrow shear layer region. Higher rms deflection angle values (on the order of mean deflection angle values) are observed for $z/d \geq 0.9$. Moreover, the rms contours also spread across the width of the jet for $z/d \geq 0.9$, signifying fluctuations caused by the small scale structures. The transition lengths obtained using this approach and measured directly from instantaneous schlieren images were within +/- 0.1d of each other. Figure 11 shows the summarized results of the normalized flow transition length (L/d) versus Richardson number for fixed Reynolds numbers. For a given Reynolds number, the normalized flow transition length decreases as Richardson number increases and the greatest effect of Ri is observed for $Ri<2.0x10^{-2}$. Furthermore, the normalized transition length at a given Richardson number increases as the Reynolds number is decreased. These results clearly demonstrate significant effects of buoyancy on the flow transition in the momentum-dominated low-density gas jets of the present study.

3.3 Full Field Concentration Measurements

Instantaneous Helium Concentration Contours. One of the major advantages of the rainbow schlieren technique is that the concentration measurements are obtained instantaneously across the whole field of view. Figure 12 shows contours of helium molar percentage during an oscillation cycle for Re=800, $Ri=4.4x10^{-2}$, and d=19.05 mm Results show that the helium concentration is changing throughout the cycle because of the instability of the flow field. The flow oscillation period is 9 ms because the contours at t=0 ms and t=9 ms are nearly identical. The FFT analysis for this case indicated flow oscillation frequency of 109 Hz, which matches with the oscillation period of 9 ms. Contours in Fig. 12 reveal features similar to those observed by Pasumarthi and Agrawal (2003) in buoyant helium jets. The curvature of the 80%

concentration contour at t=0 ms in Fig. 12 indicates that the jet contracts near the exit (z/d<0.5), expands in the mid region (<0.5 z/d < 1.0) and contracts again in the downstream region (z/d > 1.0). The contraction of the jet near the exit is attributed to the buoyant acceleration of the low-density fluid in the jet shear layer. Buoyant acceleration entrains the surrounding fluid to eventually produce a toroidal vortex around the jet core. For example, the contraction of the jet producing sharp concave curvature in the 80% concentration contour at t=2 ms signifies the presence of the vortex around z/d=0.65. This explanation is consistent with experimental observations of Cetegen and Kasper (1996) and computational fluid dynamic analysis of Satti et al (2004) in buoyant helium jets. During subsequent phases of the oscillation cycle, the region of concave curvature signifying the vortex propagates in the streamwise direction. In the meantime, the jet expands near the exit during t=4 ms to 7 ms. Subsequently at t=8 ms, the vortex has moved outside the field of view as the jet begins to contract near the exit to produce another vortex and hence, to sustain the oscillations.

Tracking Vortical Structures. The movement of the vortex was tracked using cross-correlation of consecutive pairs of schlieren images (Ben-Yaker and Hanson, 2002). A large scale structure was defined within a specified window of the first image using hue as the parameter. In the second image, a window was specified, where the structure predefined in the first image will be located. The cross-correlation between the two images was calculated at each pixel location of the second image window. The highest cross-correlation magnitude corresponds to the location of the predefined structure in the second image. Details of the procedure to efficiently calculate the cross-correlation magnitudes are discussed by Ben-Yaker and Hanson (2002).. Figure 13 plots the vortex convection velocity obtained by dividing the displacement of vortical structures between consecutive images by the time interval between images. Results

were obtained by tracking vortices for three oscillation cycles to ascertain the cycle to cycle variations. Figure 13 shows that the vortex convection velocity normalized by the average jet exit velocity (V-n) is about 0.4 for axial locations up to z/d=0.75. Subsequently, the vortex gains momentum from the jet core undergoing buoyant acceleration. As a result, the normalized vortex convection velocity increases to 0.7 at z/d=1.5. The vortex convection velocity is nearly the same for each oscillation cycle. These results suggest that the buoyancy is important in the formation and convection of vortical structures affecting the flow oscillations.

Time-Traces of Helium Concentration. One of the effective ways to visualize flow oscillations is by time-traces of helium concentration at a specified axial plane. In addition to monitoring the variations in the radial direction, it is also possible to examine the concentration fluctuations at a fixed radial location. Figure 14 shows time traces of helium mole fraction on one side of the jet centerline for 0.05 sec interval at z/d=0.05, 0.5, 1.0, and 2.0. Plots in Fig. 14 reveal that the flow repeats itself in time indicating an oscillatory mode. Based on the time interval between consecutive peaks (or valleys), an oscillation frequency of 109 Hz was found at all locations, which agrees with the frequency obtained from the FFT analysis. Near the jet exit at z/d=0.05, the concentration fluctuations are small. The helium concentration changes from 80% at r/d=0.45 to 10% at r/d=0.6, indicating a steep gradients in the radial direction. At z/d=0.5, diffusion of helium in the radial direction is observed by noting the helium concentration level of 10% at r/d=0.7. The concentration fluctuations have grown to a noticeable level and the oscillations are highly repeatable from cycle to cycle. The oscillations are most significant in the region between r/d=0.45 and r/d=0.60 with spatial amplitude on the order of 0.05d. For example, the 80% concentration curve fluctuates between r/d=0.45 and r/d=0.50. At z/d=1.0, the jet has expanded radially with 10% concentration level located at r/d=0.78. The

oscillation amplitude has increased at all radial locations. For example, the 80% concentration level resides between r/d=0.42 and r/d=0.53 which signifies near doubling of the spatial amplitude. The large oscillation amplitude signifies greater penetration of the surrounding fluid into the jet core at this axial plane. Further downstream at z/d=2.0, the jet has expanded radially with 10% concentration level located at r/d=0.87. The 80% concentration level fluctuates between r/d=0.30 and r/d=0.52, indicating that the spatial amplitude of oscillations has doubled again. Intense flow oscillations are accompanied with greater penetration of the surrounding fluid into the jet core. Figure 14 reveals time lag between concentration peaks (or valleys) at different axial locations associated with the passage of the vortex.

Effect of Operating Parameters. Figure 15 shows concentration contours during an oscillation cycle for Re=1200 and Ri=1.9×10^{-2}, d=19.05 mm. Again, the flow structure changes throughout the cycle because of the global instability mode. The oscillation period of about 6 ms corroborates with the oscillation frequency of 172 Hz determined from the FFT analysis. Figure 15 shows smaller curvature in concentration contours compared to the previous case (see Fig. 12). Figure 16 shows the corresponding time traces of helium concentration at axial planes, z/d=0.05, 0.5, 1.0, and 1.5. The trends observed in Fig. 16 are similar to those in the previous case (see Fig. 14), i.e., the jet width and oscillation amplitude increase in the axial direction. Moreover, the surrounding fluid penetrates deeper into the jet core at downstream locations.

For the above test case, the flow transition was visible in the field of view of the schlieren image. Thus, we applied the cross-correlation technique to track a large-scale structure passing through the transition/turbulent region. Figure 17 traces the path of a large-scale structure for four consecutive cycles. Unlike the laminar flow regime, the movement of the structure was observed in both axial and radial directions indicating radial spreading of the jet in the turbulent

flow regime. Nearly identical path during consecutive cycles suggests highly repeatable structures passing into the turbulent region. This coherence of flow structures confirms the results of the FFT analysis, showing a unique oscillation frequency in transition and initial turbulent flow regimes.

4. Conclusions

Rainbow schlieren deflectometry technique combined with high-speed digital imaging was applied to study self-excited oscillations in the momentum-dominated helium jets at Richardson numbers between 1.17×10^{-3} and 0.1. Results show global oscillations at a pure frequency in the laminar, transitional, and initial turbulent regions of the jet. The oscillation frequency normalized using the buoyancy time scale correlated with the Richardson number, suggesting that the flow oscillations were buoyancy-induced. The transition from the laminar to turbulent flow was also affected by the buoyancy. For a given Reynolds number, the length scales of turbulent structures were determined by the buoyancy-induced vortices in the upstream laminar regime. Instantaneous helium concentration contours revealed buoyancy-induced jet contraction producing highly periodic vortical structures during an oscillation cycle. The vortical structures were shown to accelerate as they convected downstream while maintaining their periodicity in the transitional and initial turbulent flow regimes. Time traces of helium concentration revealed that the flow oscillation amplitude and penetration of surrounding fluid into the jet core increased in the flow direction.

Acknowledgments

This work was supported by the Physical Sciences Division of NASA's Office of Biological and Physical research under grant NAG 3-2388.

References

Agrawal AK, Alammar KN, Gollahalli SR (2002) Application of rainbow schlieren deflectometry to measure temperature and oxygen concentration in a laminar gas-jet diffusion flame, Exp Fluids 32:689-691

Alammar K, Agrawal AK, Gollahalli SR, Griffin D (1998) Application of rainbow schlieren deflectometry for concentration measurements in an axisymmetric helium jet, Exp Fluids 25:89-95

Albers B, Agrawal AK (1999) Schlieren analysis of flicker in an oscillating gas-jet diffusion flame, Combust Flame 119:84-94

Ben-Yaker A, Hanson RK (2002) Ultra-fast framing schlieren system for studies of the time evolution of jets in supersonic coflows, Exp Fluids 32:652-666.

Cetegen BM, Kasper KD (1996) Experiments on the oscillatory behavior of buoyant plumes of helium and helium-air mixtures, Phys Fluids 8:2974-2984

Cetegen BM (1997) Measurements of instantaneous velocity field of a non-reacting pulsating buoyant plume by particle image velocimetry, Combust Sci Tech 123:377-387.

Cetegen BM, Dong Y, Soteriou MC (1998) Experiments on stability and oscillatory behavior of planar buoyant plumes, Phys Fluids 10:1-7.

Hamins A, Yang JC, Kashiwagi T (1992) An experimental investigation of the pulsation frequency of flames, Proc. Combust Inst 24:1695-1705

Kyle DM, Sreenivasan KR (1993) The stability and breakdown of a round variable density jet, Journal of Fluid Mech. 249:619-664

Monkewitz PA, Bechert DW, Bariskow B, Lehmann B (1990) Self-excited oscillations and mixing in a heated round jet, Journal of Fluid Mech 213:611-639

Pasumarthi KS, Agrawal AK (2003) Schlieren measurements and analysis of concentration field in self-excited helium jets, Phys Fluids 15:3683-3692

Raynal L, Harion JL, Favre-Marinet M, Binder G (1996) The oscillatory instability of plane variable-density jets, Phys Fluids 8:993-1006

Richards CD, Breuel BD, Clark RP, Troutt TR (1996) Concentration measurements in a self-excited jet, Exp Fluids 21:103-109

Satti RP, Pasumarthi KS, Agrawal AK (2004) Numerical simulations of buoyancy effects in low density gas jets, AIAA Paper 2004-1317

Screenivasan, KR, Raghu S, Kyle D (1989) Absolute instability in variable density round jets, Exp Fluids 7:309-317

Subbarao ER, Cantwell BJ (1992) Investigation of a co-flowing buoyant jet: experiments on the effect of Reynolds number and Richardson number, Journal Fluid Mech 245:69-90

Takahashi F, Mizomoto M, Ikai S (1982) Transition from laminar to turbulent free jet diffusion flames, Combust Flame 48:85-95

Takeno T, Kotani Y (1978) Transition and structure of turbulent jet diffusion flames, Prog Astronautics and Aeronautics, AIAA Inc., New York, 58:19-35.

Yep TW, Agrawal AK, Griffin DW (2003) Gravitational effects on near-field flow structure of low-density gas jets, AIAA Journal 41:1973-1979

LIST OF FIGURES

Figure 14. Time-traces of helium mole percentage at different axial planes for Re=800, Ri=4.4×10^{-2}, and d=19.05mm

Figure 15. Instantaneous helium mole percentage contours during an oscillation cycle for Re=1200, Ri=1.9×10^{-2}, and d=19.05mm

Figure 16. Time-traces of helium mole percentage at different axial planes for Re=1200, Ri=1.9×10^{-2}, and d=19.05mm

Figure 17. Path of a large scale structure in the transitional/turbulent flow regime for Re=1200, Ri=1.9×10^{-2}, and d=19.05mm

Table 1. Experimental test conditions

Test Case	Reynolds Number	Richardson Number	Tube Diameter (mm)	Frequency (Hz)	Strouhal Number
1	800	$44x10^{-3}$	19.05	109	0.41
2	800	$19\ x10^{-3}$	14.5	172	0.37
3	800	$7.33\ x10^{-3}$	10.5	266	0.30
4	1000	$28\ x10^{-3}$	19.05	141	0.42
5	1000	$12\ x10^{-3}$	14.5	203	0.35
6	1000	$4.7\ x10^{-3}$	10.5	391	0.35
7	1200	$19\ x10^{-3}$	19.05	172	0.43
8	1200	$8.58\ x10^{-3}$	14.5	234	0.34
9	1200	$3.53\ x10^{-3}$	10.5	438	0.33
10	1600	$4.83\ x10^{-3}$	10.5	344	0.37
11	1600	$1.83\ x10^{-3}$	14.5	547	0.31
12	2000	$1.17\ x10^{-3}$	10.5	813	0.37
13	530	$100\ x10^{-3}$	19.05	70	0.43
14	350	$100\ x10^{-3}$	14.5	78	0.38
15	910	$34\ x10^{-3}$	19.05	125	0.41
16	605	$34\ x10^{-3}$	14.5	109	0.31
17	1250	$18\ x10^{-3}$	19.05	180	0.43
18	830	$18\ x10^{-3}$	14.5	172	0.36
19	510	$18\ x10^{-3}$	10.5	156	0.28

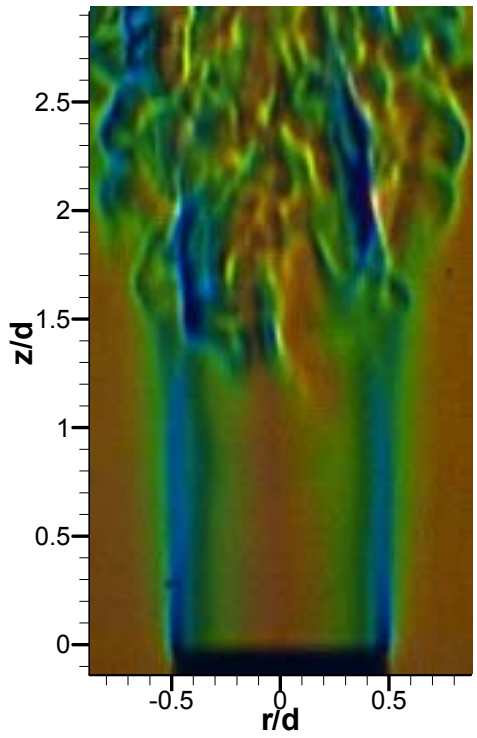

Figure 1. A typical rainbow schlieren image for Re=1200, Ri=8.58×10^{-3}, and d=14.5 mm

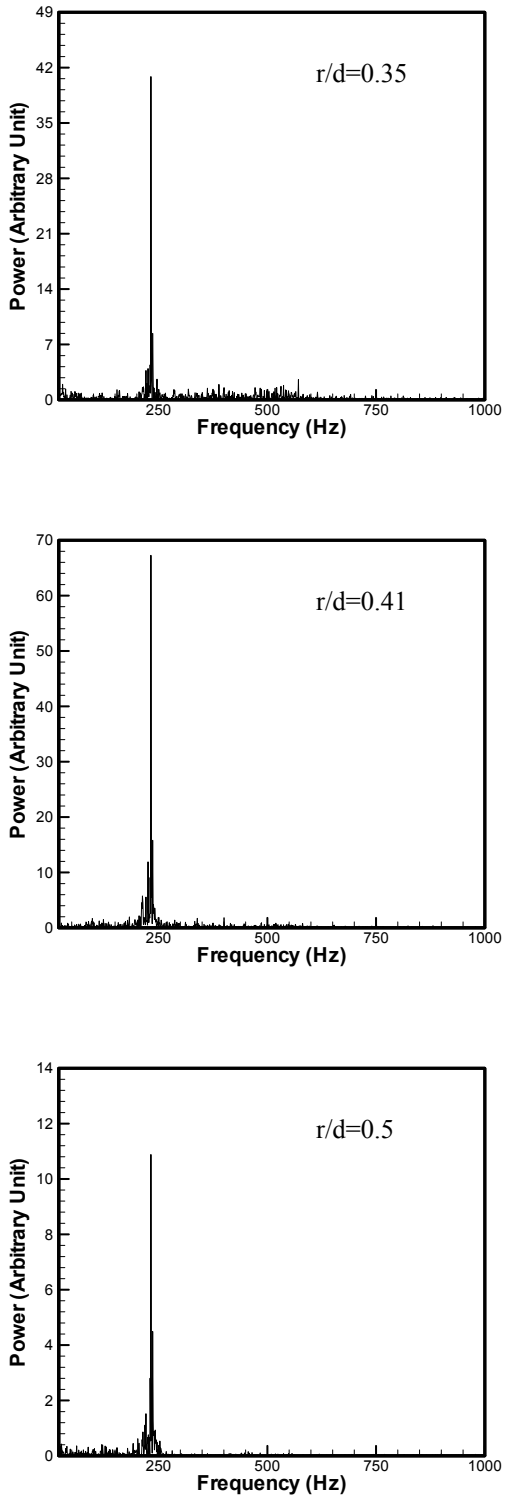

Figure 2. Power spectra in the laminar flow regime at z/d=1.0 for Re=1200, Ri=8.58×10^{-3}, and d=14.5 mm

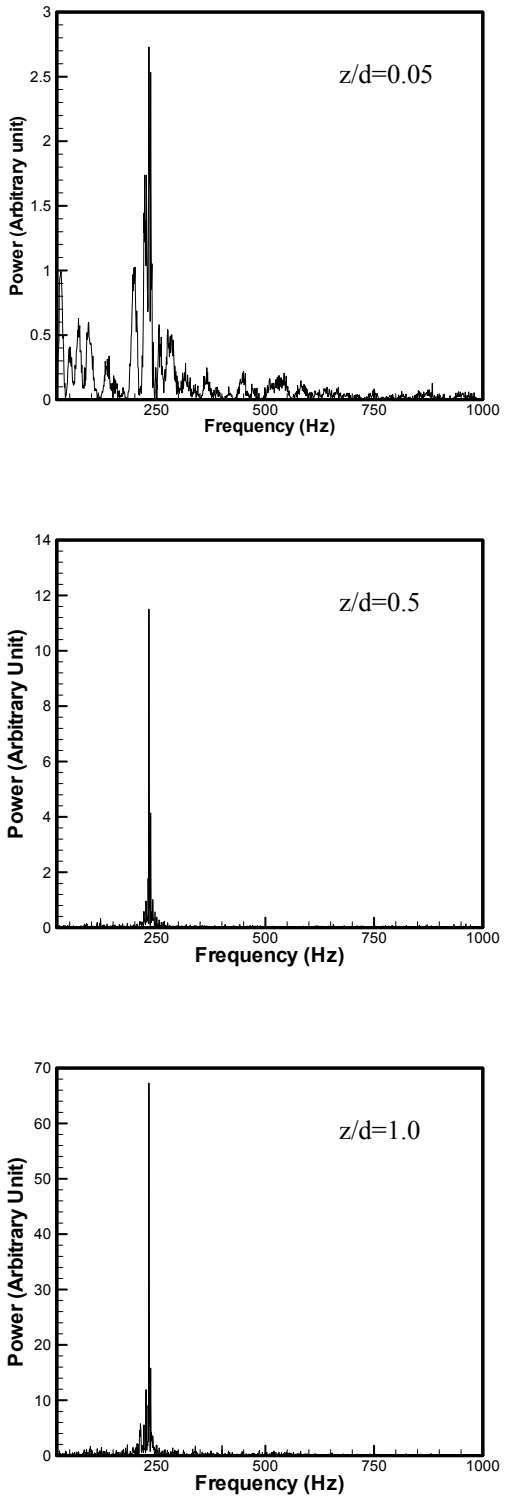

Figure 3. Power spectra in the laminar flow regime at r/d=0.41 for Re=1200, Ri=8.58×10^{-3}, and d=14.5 mm

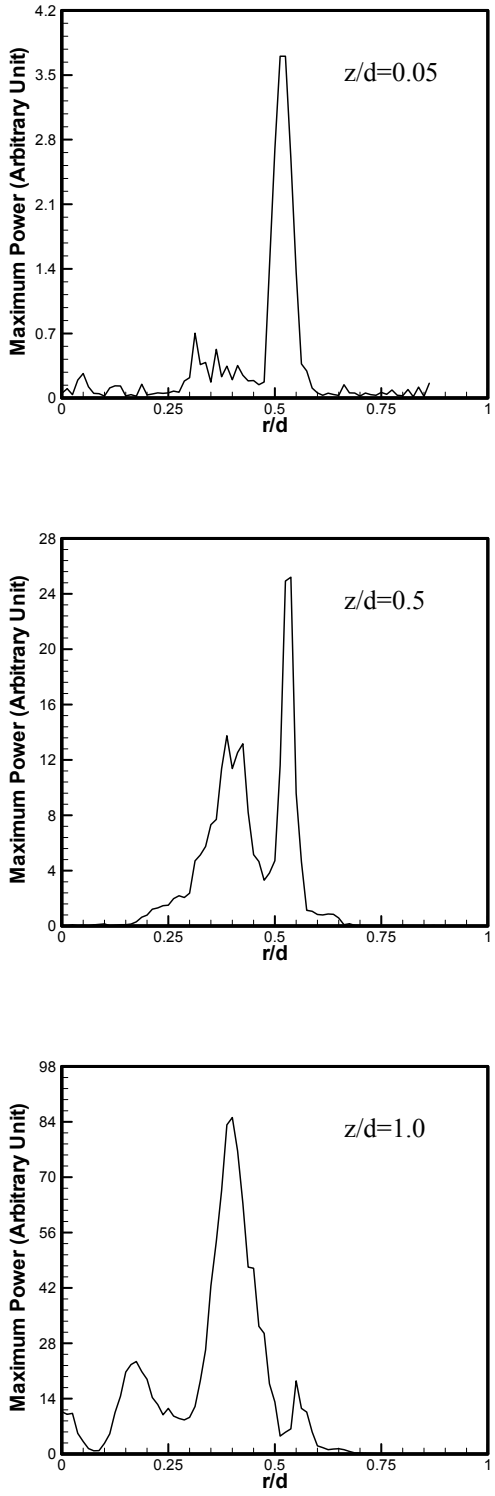

Figure 4. Maximum spectral power at r/d=0.41 for Re=1200, Ri=8.58x10^{-3}, and d=14.5 mm

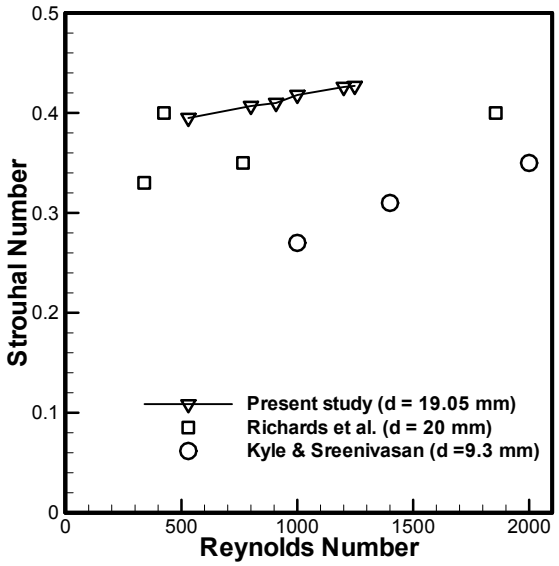

Figure 5. Strouhal number versus Reynolds number for a fixed tube diameter

(a)

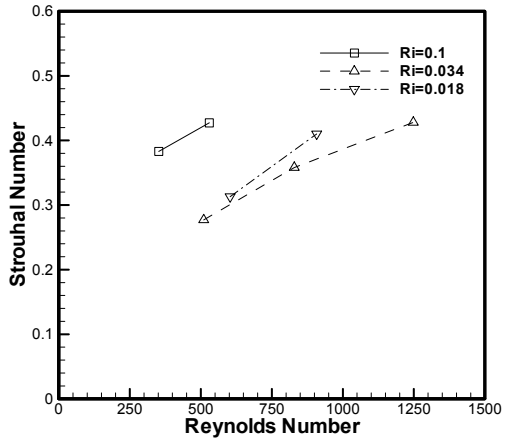

(b)

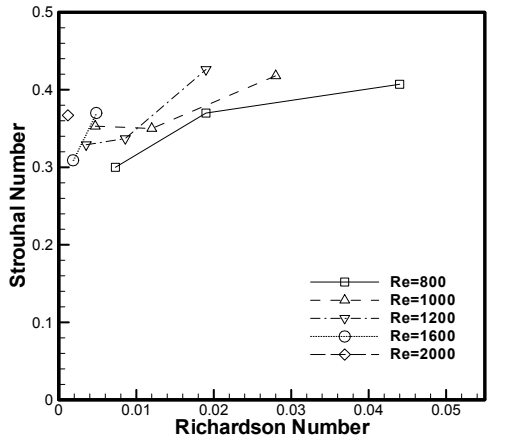

Figure 6 (a) Strouhal number versus Reynolds number, (b) Strouhal number versus Richardson number

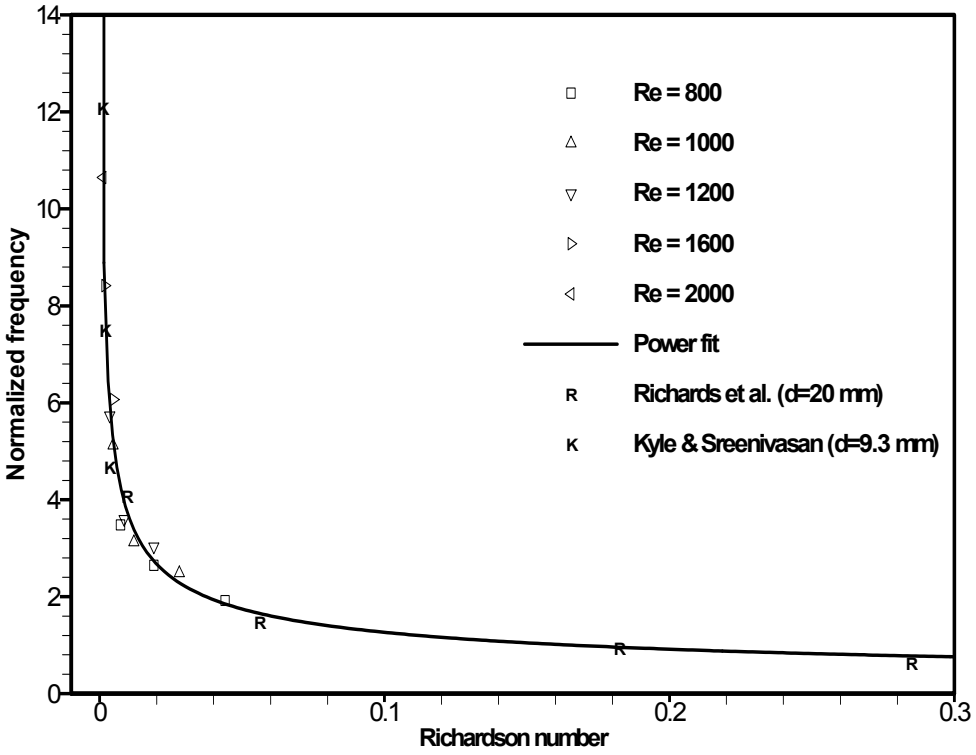

Figure 7. Flow oscillation frequency versus Richardson number for fixed Reynolds numbers

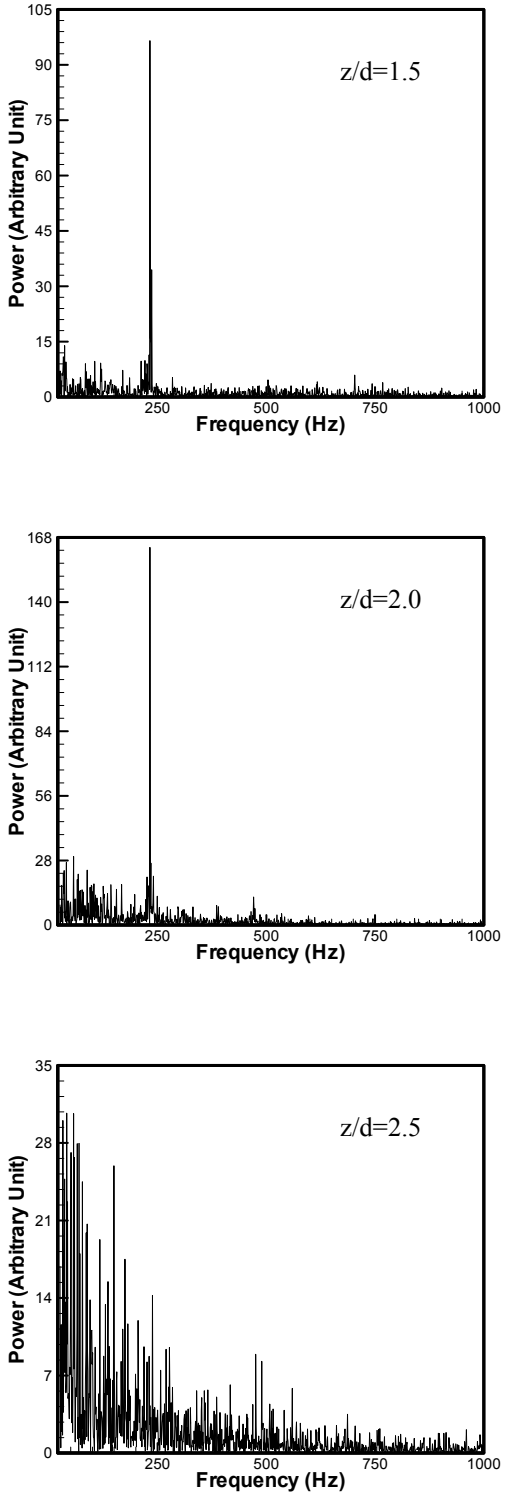

Figure 8. Power spectra in the transitional/turbulent flow regime at r/d=0.41 for Re=1200, $Ri=8.58x10^{-3}$, and d=14.5 mm

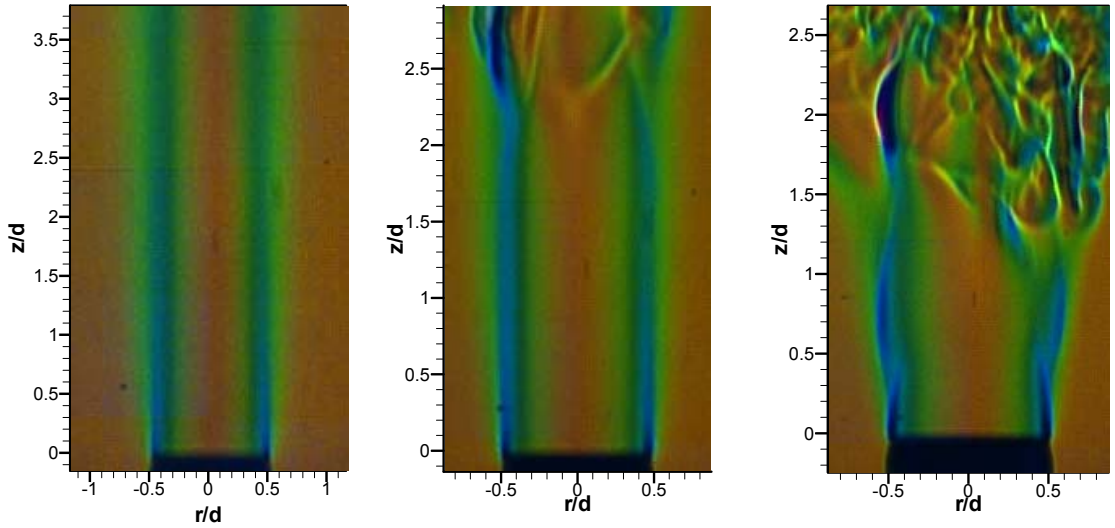

Ri=18x10^{-3}
Re=510

Ri=18x10^{-3}
Re=830

Ri=18x10^{-3}
Re=1250

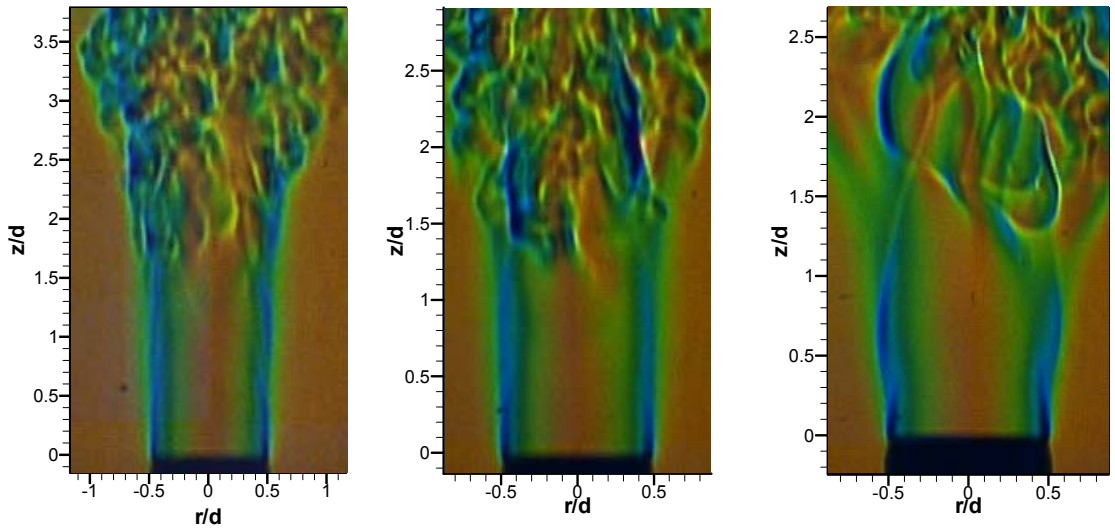

Re=1200
Ri=3.53x10^{-3}

Re=1200
Ri=8.58x10^{-3}

Re=1200
Ri=19x10^{-3}

Figure 9. Effect of Reynolds number and Richardson number on transition from laminar to turbulent flow

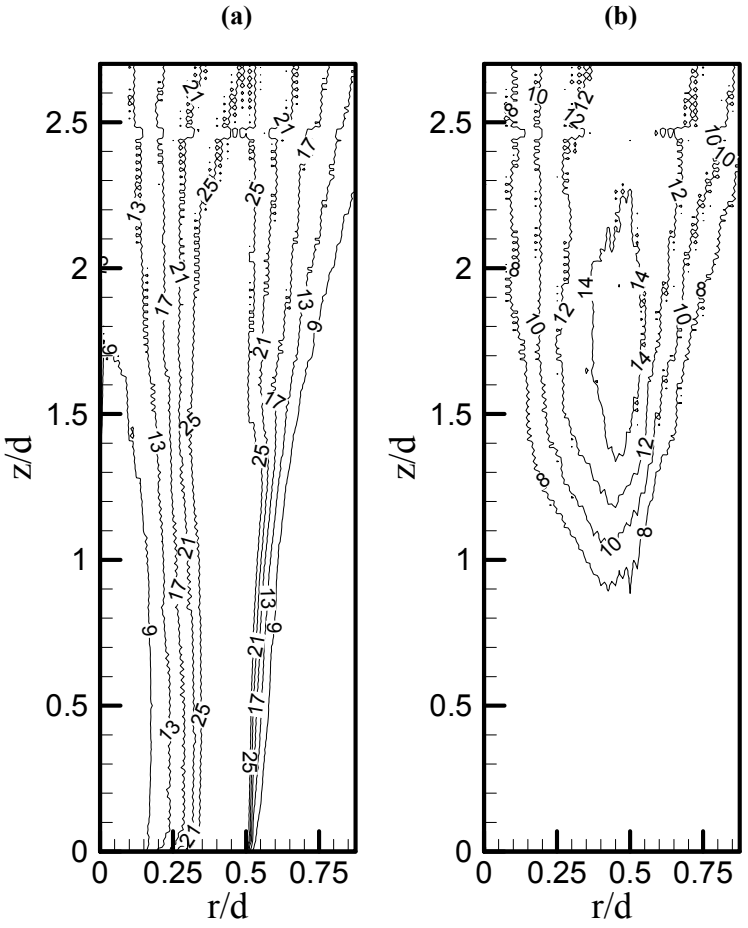

Figure 10. Mean and rms angular deflection for Re=1600, Ri=4.83x10^{-3}, and d=14.5 mm, (a) mean angular deflection (b) rms angular deflection; Contour levels are in milli degrees

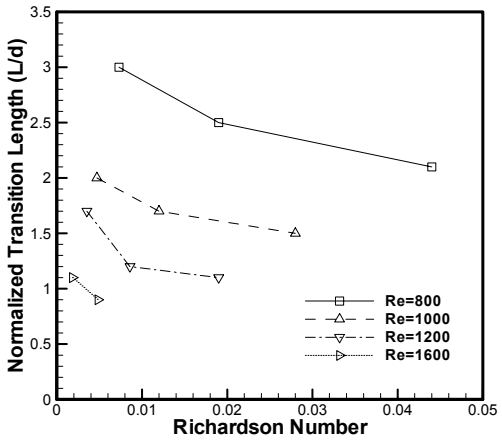

Figure 11. Normalized flow transition length versus Richardson number for fixed Reynolds numbers

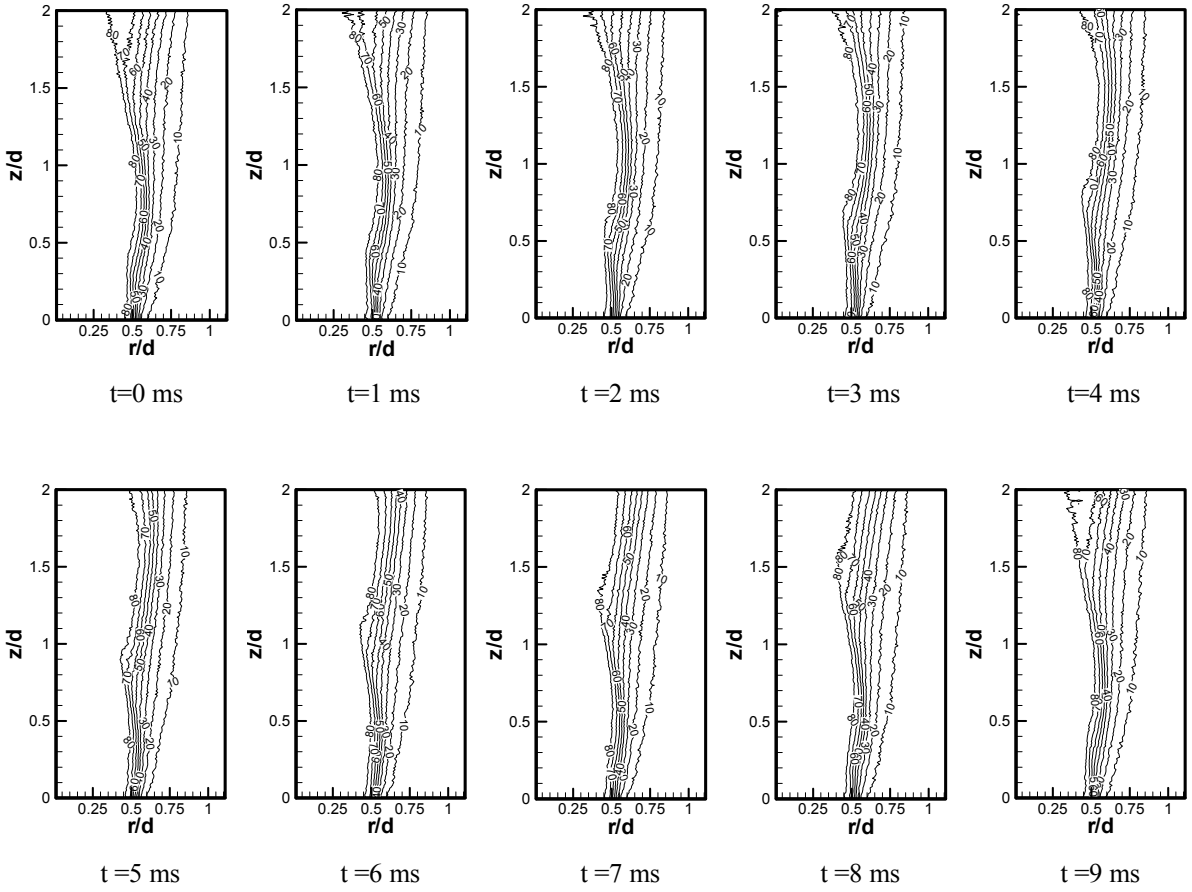

Figure 12. Instantaneous helium mole percentage contours during an oscillation cycle for Re=800, Ri=4.4×10^{-2}, and d=19.05 mm

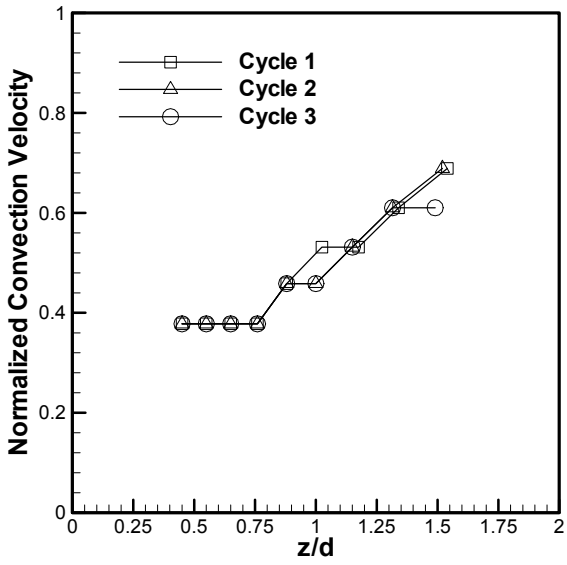

Figure 13. Vortex convection velocity for Re=800, Ri=4.4×10^{-2}, and d=19.05 mm

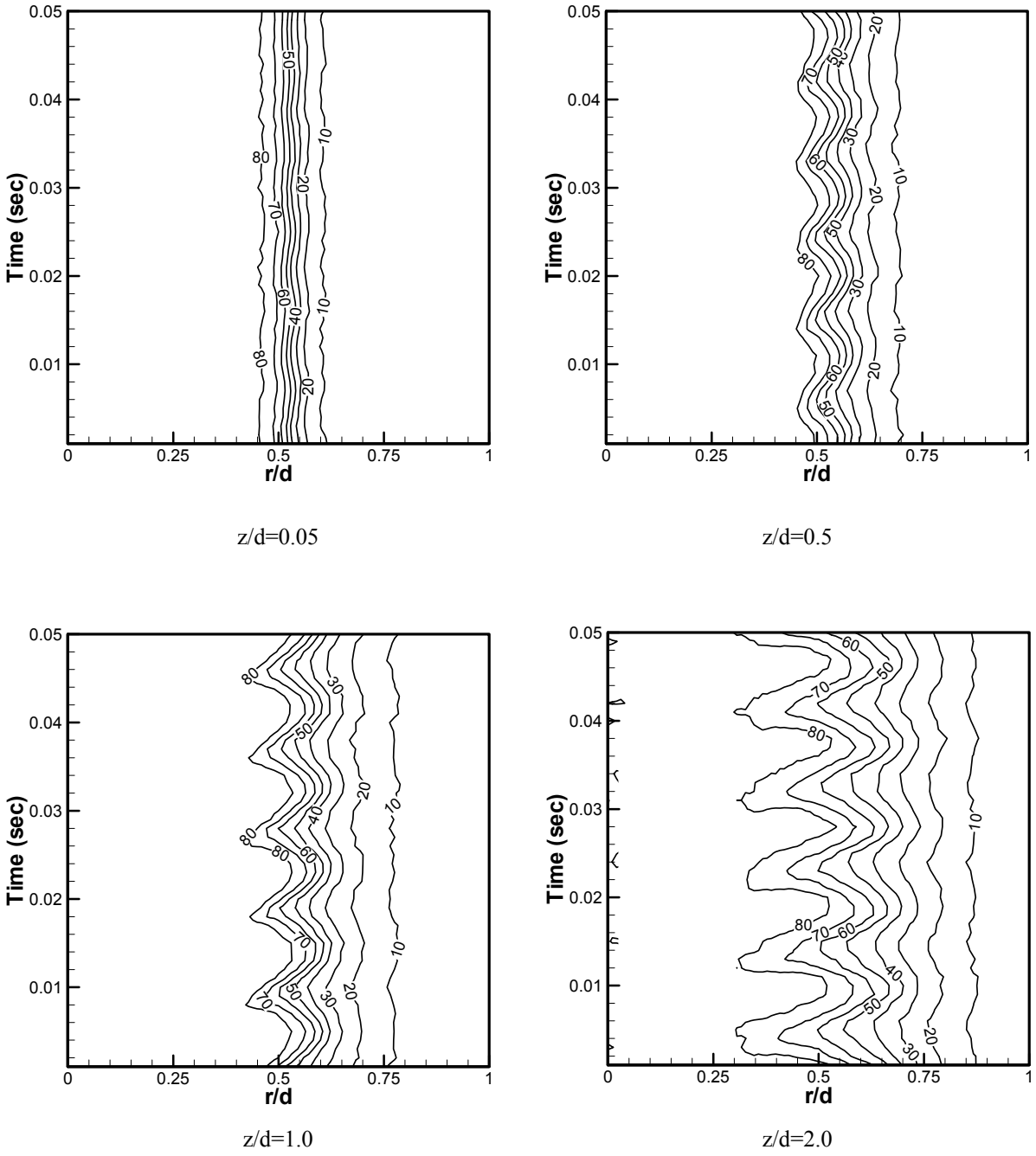

Figure 14. Time-traces of helium mole percentage at different axial planes for Re=800, Ri=4.4×10^{-2}, and d=19.05 mm

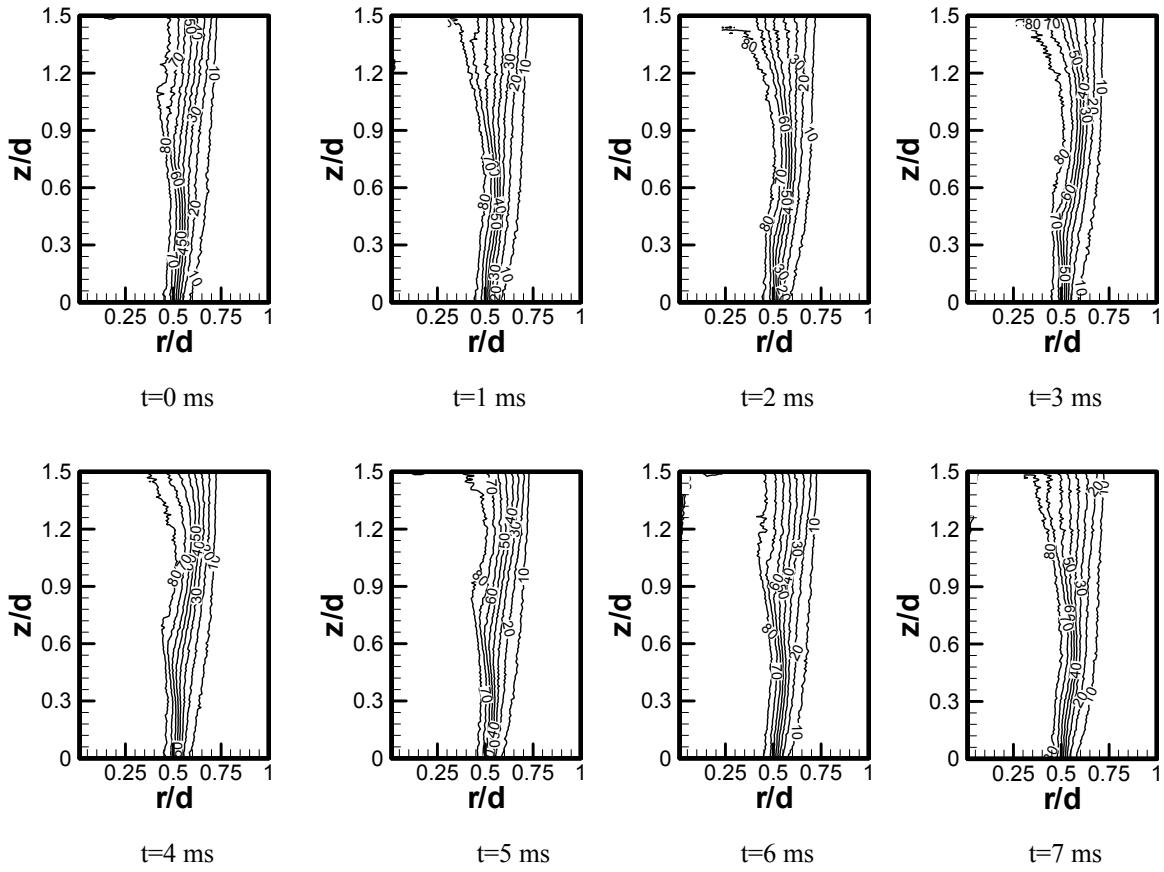

Figure 15. Instantaneous helium mole percentage contours during an oscillation cycle for Re=1200, Ri=1.9x10^{-2}, and d=19.05 mm

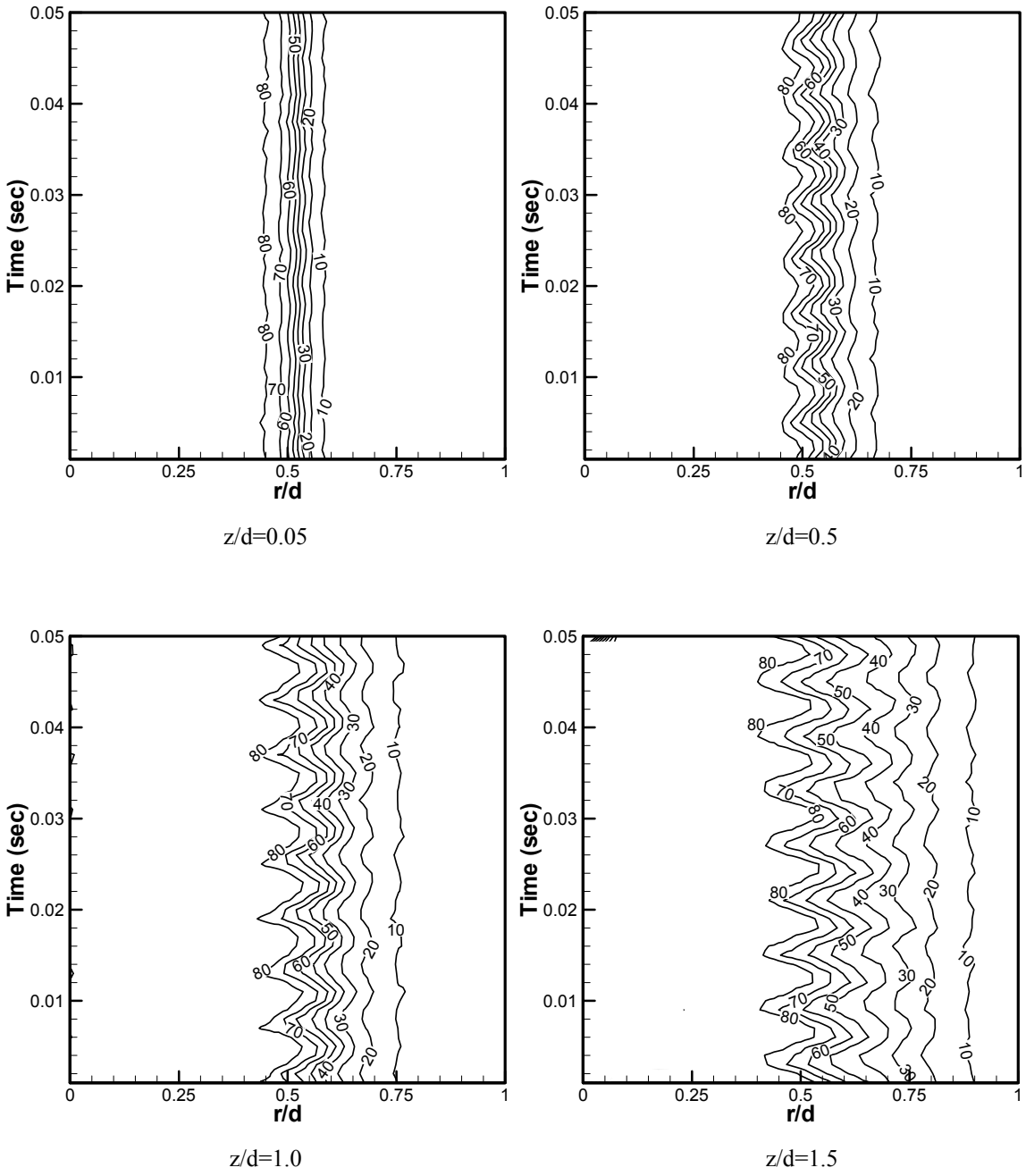

Figure 16. Time-traces of helium mole percentage at different axial planes for Re=1200, Ri=1.9x10^{-2}, and d=19.05 mm

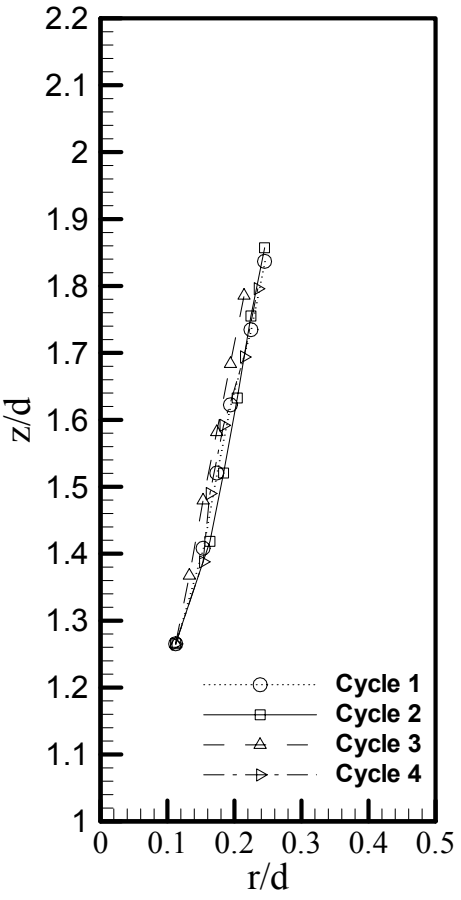

Figure 17. Path of a large scale structure in the transitional/turbulent flow regime for Re=1200, Ri=1.9×10^{-2}, and d=19.05 mm

BUOYANCY EFFECTS ON FLOW TRANSITION IN LOW-DENSITY INERTIAL GAS JETS

Kasyap S. Pasumarthi and Ajay K. Agrawal[1]
School of Aerospace and Mechanical Engineering
University of Oklahoma,
Norman, OK, USA 73019

ABSTRACT

Effects of buoyancy on transition from laminar to turbulent flow are presented for momentum-dominated helium jet injected into ambient air. The buoyancy was varied in a 2.2-sec drop tower facility without affecting the remaining operating parameters. The jet flow in Earth gravity and microgravity was visualized using the rainbow schlieren deflectometry apparatus. Results show significant changes in the flow structure and transition behavior in the absence of buoyancy.

[1] Corresponding Author
Lloyd G. & Joyce Austin Presidential Professor and Associate Professor
School of Aerospace and Mechanical Engineering
865 Asp Avenue, Room 208
University of Oklahoma, Norman, OK 73019
Phone: (405) 325-1754, Fax: (405) 325-1088, E-mail: aagrawal@ou.edu

INTRODUCTION

Transition from laminar to turbulent flow in gas jets is a subject of considerable interest. A transitional jet consists of a laminar potential core near the injector, separated from a downstream turbulent region at the transition plane. The distance from the injector exit to the transition plane or transition length (z) decreases asymptotically with an increase in the jet Reynolds number defined as $\mathrm{Re} = \mathrm{U_j d}/\upsilon$, where $\mathrm{U_j}$ is the mean jet exit velocity, d is the injector inside diameter, and υ is the kinematic viscosity of the injector fluid. Subbarao and Cantwell (1992) found that the flow transition in a helium jet injected into a coflow of air was also affected by the jet Richardson number, $\mathrm{Ri} = \mathrm{gd}\left(\rho_\infty - \rho_\mathrm{j}\right)/\rho_\mathrm{j}\mathrm{U_j}^2$, where g is the gravitational acceleration, ρ_∞ and ρ_j are, respectively, the free-stream and jet densities. For a given Re, the transition length decreased asymptotically with increasing jet Richardson number. This effect was attributed to the buoyancy-induced acceleration of the jet fluid, giving rise to faster core velocities and hence, a more unstable flow at higher Ri. They proposed that the sudden breakdown to turbulence was governed by highly structured and repeatable vortices formed in the upstream laminar region.

Periodic oscillations resulting in the breakdown to turbulence have also been observed in low-density gas jets at Ri<<1.0 (Kyle and Sreenivasan, 1993; Richards et al., 1996). In these studies, the buoyancy effects were considered negligible because of the small Ri. However, the buoyancy may be important locally, for example, in the low-momentum region of the jet shear layer. Buoyant acceleration of the low-density fluid in localized regions of the jet may trigger the instability causing periodic flow oscillations and eventually, the breakdown to turbulence. This explanation is supported by the recent

experiments of Yildirim and Agrawal (2004), who found that the flow oscillation frequency normalized by the buoyancy time scale correlated with the jet Richardson number in inertial low-density jets for Ri<0.1. Furthermore, the transition length normalized by injector inside diameter correlated with the jet Richardson number for a given Re, an observation similar to that of Subbarao and Cantwell (1992) in buoyant jets. Yildirim and Agrawal (2004) utilized different diameter injector tubes to vary the jet Richardson number for a given Re. Besides the limited range of the jet Richardson number achieved, the similarity parameters are not perfectly matched using this approach. In the present study, the microgravity environment of a drop tower facility is used to vary Ri by several orders of magnitude. The operating parameters such as the jet Reynolds number, the jet to ambient density ratio, and the jet momentum thickness (Kyle and Sreenivasan, 1993) remain unchanged in the drop tower and hence, the buoyancy effects can be isolated. The specific objective of this study is to identify if buoyancy affects transition from laminar to turbulent flow in inertial low-density gas jets.

EXPERIMENTAL SETUP

Experiments utilizing a compact rig were conducted at NASA John H. Glenn Research Center's 2.2s drop tower facility to simulate microgravity. The flow system comprised of on-board compressed helium gas cylinders, a calibrated mass flow meter, a needle valve to set the flowrate, a solenoid valve to initiate and terminate the flow, and a vertically oriented stainless steel tube to serve as the injector. Yildirim and Agrawal (2004) have provided details of the schlieren apparatus. The color schlieren images are acquired by a high-speed digital camera operated at exposure time of 297-μs and acquisition rate of 1000 images per second, providing spatial resolution of 0.2 mm.

The jet flow is initiated and allowed to develop into oscillatory mode in Earth gravity. After storing 0.4-sec of Earth gravity images, the drop rig is released to simulate microgravity during the free fall. The camera stores schlieren images during the 2.2-sec drop. After the drop, the rig is retrieved and the image data from camera memory are transferred to an external hard drive for analysis. Details of the experimental and data analysis procedures are provided by Pasumarthi (2004).

RESULTS AND DISCUSSION

Although six different experiments were conducted, results are presented only for two test cases at jet Reynolds number of 800 to depict the overall trends. Jet tubes with d=14.5mm (case 1) and 10.5mm (case 2) were used to obtain jet Richardson number of 0.02 and 0.008, respectively, in Earth gravity. The buoyancy is generally neglected for non-dimensional parameter $P = [(\frac{gd}{U_j^2})^{0.5} (\frac{\rho_j}{\rho_\infty})^{-0.25} \frac{z}{d}] < 0.5$ (Ricou and Spalding, 1961; Takahashi et al., 1982). In this study, P was computed using the normalized transition length measured in Earth gravity to represent z/d. For Ri=0.02, z/d=4.0 and hence, P=0.37. For Ri=0.008, z/d was 4.8, resulting in P=0.28. Thus, according to the literature, both jets of this study are considered momentum-dominated (or inertial) with negligible effects of buoyancy. Results presented next will show that this is not the case because both the flow structure and transition behavior are affected by buoyancy.

Flow Visualization

Figure 1 shows rainbow schlieren images (reproduced in black and white) for the two test cases in Earth gravity and microgravity. The injector wall and exit are visible as a black region in the upstream portion of images. For case 1, the flow transition in Earth gravity, indicated by the appearance of smaller scale structures at the jet center, is evident

in Fig. 1.1(a) approximately at z/d=3.8. According to Fig. 1.1(b), the transition is not visible in the field-of-view in microgravity. The jet remains laminar in the absence of gravitational forcing, providing direct evidence of buoyancy effects in an inertial jet. Figures 1.2(a) and (b) for case 2 show that transition occurs approximately at z/d=4.8 in Earth gravity and at z/d=5.5 in microgravity. Again, the lack of buoyancy has extended the laminar coherent region in microgravity. Comparing Earth gravity images in Figure 1, an increase in transition length at the lower jet Richardson number is observed. Results clearly show that buoyancy is important in low-density gas jets at Ri<0.02.

Space-Time Images

The transient flow behavior is visualized from space-time images in Fig. 2, developed by concatenating 0.1-sec of data at specified axial planes from a sequence of 100 schlieren images. Images are shown for case 1 at z/d=4.4 and case 2 at z/d = 5.4 to represent the transitional/turbulent regions in Earth gravity. For case 1, the periodicity of the flow and breakdown of the potential core in Earth gravity is evident in Fig. 2.1(a). Note that the smaller scale structures have reached the jet center. In microgravity (Fig. 2.1b), the jet center is uncontaminated although periodic oscillations are observed for 0.4<r/d<0.8. The transition is absent since the flow is laminar at this axial location in microgravity. For case 2, the Earth gravity image in Fig. 2.2(a) shows repeatable structures contaminating the jet center. The structures in microgravity are significantly different as shown by the image in Fig. 2.2(b). Overall, the images in Fig. 2 reveal differences in the temporal behavior of Earth gravity and microgravity jet flows to highlight the underlying effects of buoyancy.

Oscillating Flow Characteristics

Fast Fourier Transform (FFT) analysis of angular deflection data obtained from an ensemble of 256 images each in Earth gravity and microgravity was performed to quantitatively assess buoyancy effects on jet oscillations. Figure 3.1(a) shows the power spectra in the transition region (z/d = 4.4, r/d = 0.5) for case 1 in Earth gravity. The dominant frequency of 120Hz was the same as that measured in the upstream laminar regime. Two smaller peaks representing sub-harmonics at 240Hz and 360Hz are also present, signifying the breakdown of large-scale structures in the transition region. In microgravity (Fig. 3.1b), the oscillation frequency is the same (i.e., 120Hz) although the spectral power has decreased. Matching spectral behavior in Earth and microgravity indicates that the flow may not have fully adjusted to microgravity within the 2.2-sec drop period. Longer duration microgravity (or zero gravity) experiments are desired to eliminate residual effects of Earth gravity, especially in the low-momentum regions of the jet. Figure 3.2(a)-(b) show the power spectra in the transition region (z/d = 5.4, r/d = 0.5) for case 2. A dominant frequency of 215 Hz is observed both in Earth gravity and microgravity. Sub-harmonics at higher frequencies were not captured because of the temporal resolution limitation. The spectral power has diminished in microgravity, signifying the importance of buoyancy on flow transition.

CONCLUSIONS

Experiments were performed in Earth gravity and microgravity to evaluate buoyancy effects on inertial helium jets at Richardson numbers of 0.02 and 0.008 and jet Reynolds number of 800. Schlieren images show visual differences in the flow transition behavior in Earth gravity and microgravity. Lack of buoyancy delayed flow transition in

microgravity. Space-time images and spectral plots provide evidence of significant buoyancy effects on flow oscillation and transition in inertial, low-density gas jets.

ACKNOWLEDGEMENTS

This work was supported by Physical Sciences Division of NASA's Office of Biological and Physical research under grant NAG 3-2388.

REFERENCES

Kyle DM, Sreenivasan KR (1993) The instability and breakdown of a round variable-density Jet, J Fluid Mech. 249:619-664.

Pasumarthi KS (2004) Buoyancy effects on flow structure and instability of low-density gas jet, PhD Dissertation, University of Oklahoma.

Richards CD, Breuel BD, Clark RP, Troutt TR (1996) Concentration measurements in a self-excited jet, Exp Fluids 21:103-109.

Ricou FP, Spalding DB (1961) Measurement of entrainment by axisymmetrical turbulent jets, J Fluid Mech. 11:21-32.

Subbarao ER, Cantwell BJ (1992) Investigation of a co-flowing buoyant jet: experiments on the effects of Reynolds number and Richardson number, J Fluid Mech. 245:69-90.

Takahashi F, Mizomoto M, Ikai S (1982) Transition from laminar to turbulent free jet diffusion flames, Combust Flame 48:85-95.

Yildirim BS, Agrawal AK (2004) Full field measurements of self-excited oscillations in momentum-dominated helium jets, Exp Fluids, in review.

LIST OF FIGURES

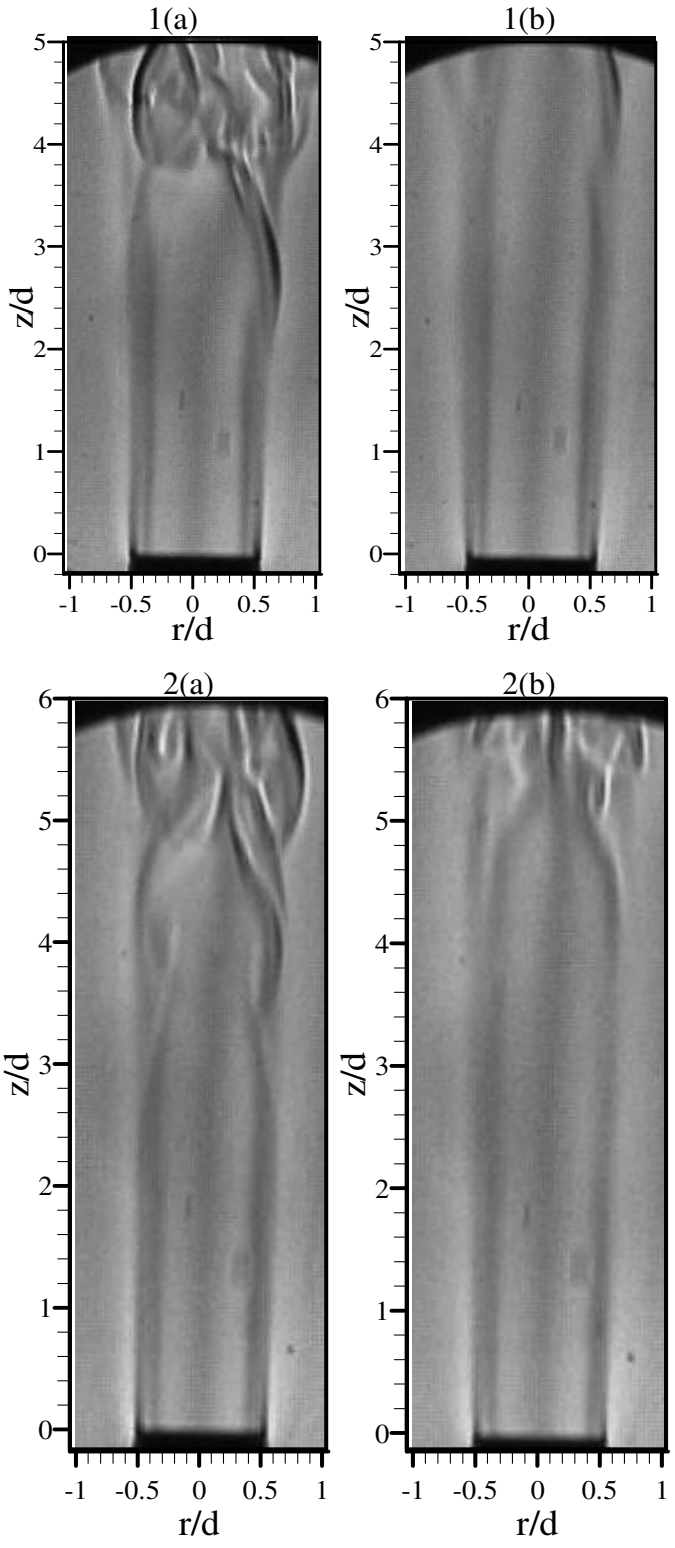

Figure 1.

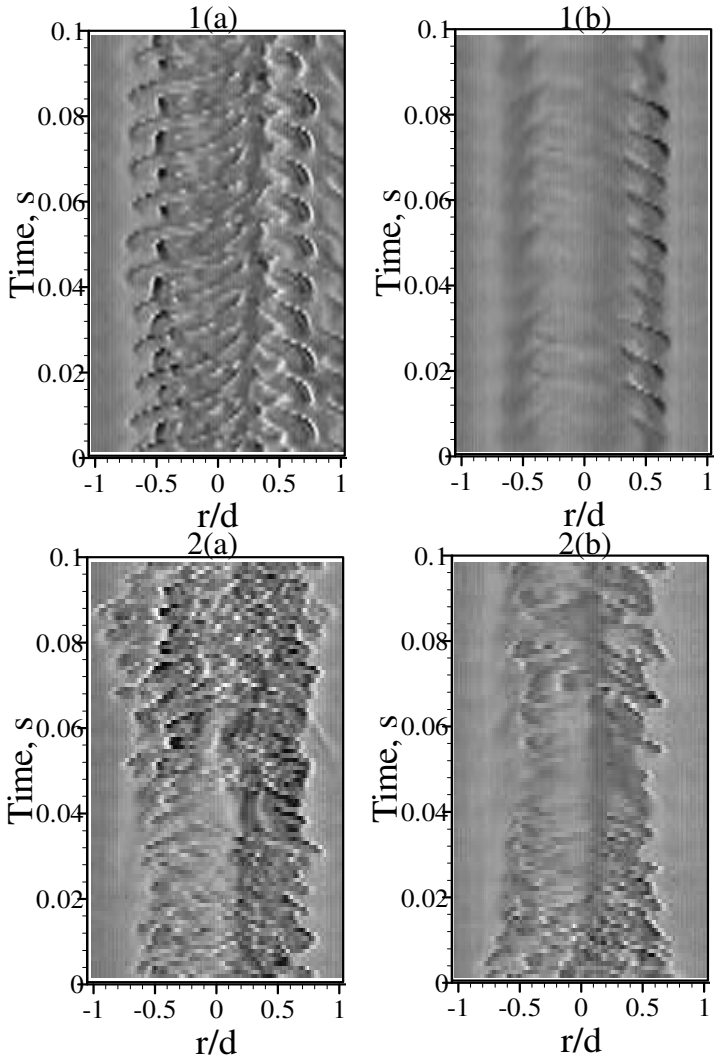

Figure 2.

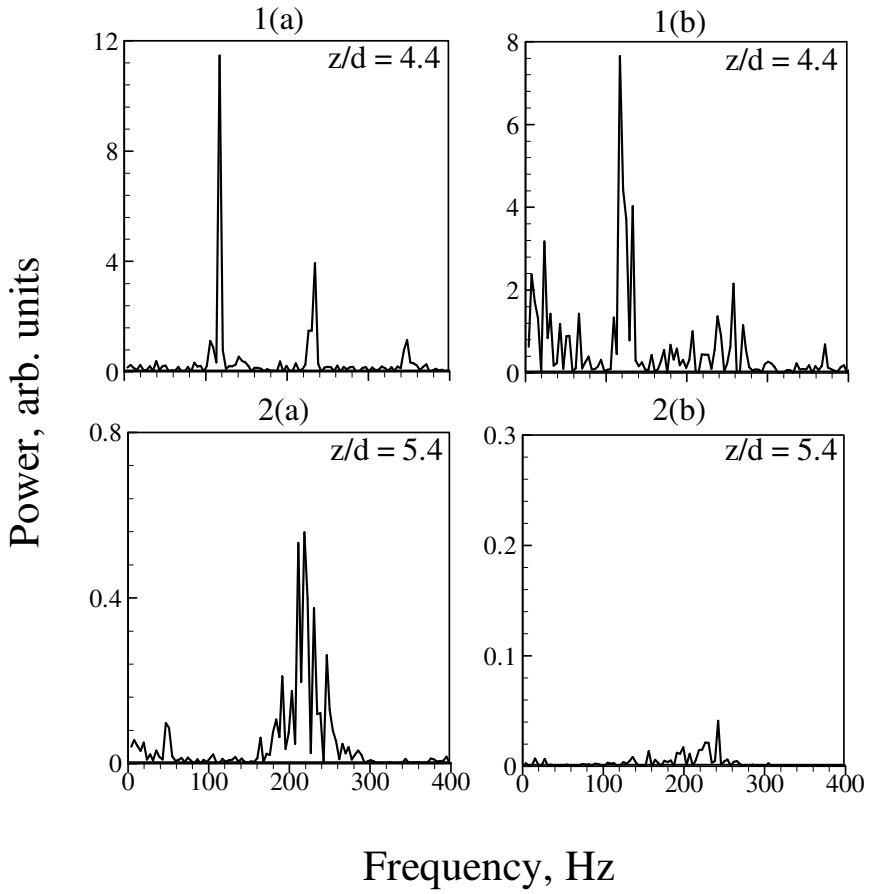

Figure 3.

High-Speed Rainbow Schlieren Visualization of an Oscillating Helium Jet Undergoing Gravitational Change

Peter A. Leptuch[*1] and Ajay K. Agrawal[*2]

*1 Graduate Research Assistant, School of Aerospace and Mechanical Engineering, University of Oklahoma, Norman, OK 73019, USA

*2 Lloyd G. & Joyce Austin Presidential Professor and Associate Professor, School of Aerospace and Mechanical Engineering, University of Oklahoma, Norman, OK 73019, USA, email: aagrawal@ou.edu

Abstract: Rainbow schlieren deflectometry combined with high-speed digital imaging was used to study buoyancy effects on flow structure of a helium jet discharged vertically into air. The experimental data were taken using the 2.2-sec drop tower facility at the NASA John H. Glenn Research Center in Cleveland, Ohio. The test conditions pertained to jet Reynolds number of 490 and jet Richardson number of 0.11, for which buoyancy is often considered unimportant. Experimental results show global oscillations at a frequency of 27 Hz in Earth gravity. In microgravity, the jet oscillations vanished and the jet width increased. Results provide a direct physical evidence of the importance of buoyancy on the flow structure of low-density gas jets at a Richardson number considered too small to account for gravity.

Keywords: Color Schlieren, Low-Density Jets, Flow Oscillations, High-Speed Imaging

1. Introduction

Flow structure of gas jets has been extensively investigated because of their wide-ranging applications. An important focus of these studies involves the formation of instabilities in the near field and the evolution of developed structures in the downstream region. Some of these studies have used the concept of introducing flow oscillations in the jet tube, which are examined subsequently in the downstream flow field. In contrast, the present study considers a flow configuration with oscillations occurring naturally in the Earth gravity environment. It consists of a low-density gas jet (helium) injected into a high-density atmosphere (air). Self-excited oscillations in low-density jets have been observed for jet Reynolds numbers, Re [$=U_j d/\upsilon_j$, where U_j is the average jet velocity, d is the tube inside diameter, and υ_j is kinematic viscosity of the jet fluid] varying from a few hundreds (Hamins et al, 1992; Subbarao and Cantwell, 1992; Richards et al, 1996; Cetegen, 1997) to several thousands (Monkewitz et al, 1990; Kyle and Sreenivasan, 1992). The instability is found to produce distinctly periodic oscillations in the near field, leading to an early and abrupt breakdown of the potential core. The jet is characterized as momentum-dominated for Richardson number, Ri<<1.0, where Ri= $gd(\rho_a-\rho_j)/\rho_j U_j^2$; g is the gravitational acceleration, ρ_a and ρ_j are, respectively, the ambient and jet densities. The jet is considered buoyant for Ri>1, although buoyancy may still be important at lower Ri.

Subbarao and Cantwell (1992) observed highly periodic oscillations in the entire near field of helium jets issued in a co-flow of air for Ri varying between 0.5 and 6.0. The oscillation frequency (f) represented by Strouhal number, St=[fd/Uj] correlated with Richardson number for Ri≥1.0, indicating a buoyancy-dependent instability mode. For Ri<0.5, the Strouhal number was independent of the Richardson number and hence, the flow oscillations were considered to be independent of the gravity. The buoyancy was also considered negligible in momentum-dominated low-density jets of

Kyle and Sreenivasan (1993) at Ri on the order of 10^{-3} and those of Richards et al (1996) for Ri=0.3 to $8*10^{-3}$, bridging the buoyancy-dominated to momentum-dominated jet flow regimes. Evidently, origin of the instability in low-density gas jets leading to global oscillations in the near field has not been established for Ri<0.5. Specifically, the role of gravity has not been delineated in this flow regime.

The above studies conducted in Earth gravity pose experimental limitations in isolating buoyancy effects on the flow structure of low-density jets. First, the experimental variables, i.e., Reynolds number and Richardson number depend upon each other, and therefore, they cannot be varied independently. Subbarao and Cantwell (1992) controlled the operating pressure to circumvent this problem, although for a narrow range of operating conditions. Secondly, even though the buoyancy may be rendered negligible globally in a momentum-dominated jet, it cannot be eliminated. Buoyancy may be significant locally in the low-momentum regions of the flow, e.g., the jet shear layer and thereby, affect the jet instability leading to significant changes in the flow field. Eliminating buoyancy throughout the flow field requires experiments in zero or microgravity environment, which also provides the flexibility to vary the Richardson number by several orders of magnitude for a given Reynolds number.

Yep et al (2003) used the microgravity environment of a drop tower to show that the flow oscillations in a low-density jet in Earth gravity at Ri=1.44 were buoyancy induced. Self-excited oscillations in Earth-gravity disappeared as the jet flow adjusted to microgravity conditions in the drop tower. They also provided quantitative details of buoyancy-induced changes in the helium concentration field using the rainbow schlieren deflectometry technique. The present study extends the investigation by Yep et al. (2003) to a self-excited low-density jet in Earth gravity at a smaller Richardson number (Ri=0.11), for which the origin of the instability has not yet been established. The 60Hz imaging system used by Yep et al (2003) was incapable of resolving the high oscillation frequencies observed at low Richardson numbers. Consequently, the rainbow schlieren apparatus was modified by integrating it with a high-speed digital imaging system, and used for the first time in the 2.2-s drop tower to visualize and quantify effects of gravity in a low-density jet bridging the buoyancy dominated and momentum-dominated flow regimes. Unlike Yep et al (2003), the present experiment however did not seek to quantify the concentration field.

2. Experimental Approach

The experiment was conducted at the NASA John H. Glenn Research Center's 2.2s drop tower facility. Upon release, the experimental package undergoes free fall in the drop tower and experiences microgravity after an initial period of 0.1s during which the acceleration decreases linearly from Earth gravity to microgravity (Lekan, 2004). The drop rig shown in Figure 1 was a battery powered testing device contained within a sturdy aluminum frame of approximate dimensions: 0.84m high, 0.97m wide and 0.41m deep. A thick curtain covering the rig isolated the jet flow from external disturbances. All aspects of system design were constrained to withstand impact decelerations of up to 100g. The flow system comprised of the following components: 1) two compressed gas reservoirs with helium stored at a pressure of 14bar, 2) a mass flowmeter calibrated for helium in the range of 0.0 to 60.0 standard liters per minute, 3) a control valve to specify the helium gas flow rate, 4) a solenoid valve to instantaneously initiate and terminate the flow, 5) a heavy duty, clear, plastic, flexible hose, filled with steel wool to stabilize the flow, 6) a U-tube segment to direct the flow from the flexible tube to the inlet of a straight jet tube, and 7) the straight, polished, jet tube to vertically discharge the flow into quiescent air. The length and diameter of the jet tube were, respectively, 300-mm and 18.7-mm. Because of the spatial constraints of the drop rig, the tube length was insufficient to attain fully-developed laminar flow conditions at the exit.

The components of the rainbow schlieren deflectometry system, positioned on an optical breadboard, included 1) the light source aperture (3mm high and 0.1mm wide) connected through an optical fiber cable to an external 160W halogen light source, 2) the collimating lens (80mm diameter with focal point 310mm upstream at the source aperture), 3) the decollimating lens (80mm diameter

with focal point 1000mm downstream at the filter plane), 4) two aluminum coated, flat surface, reflecting mirrors, 5) a 3.5mm symmetric rainbow filter positioned at the focal point of the decollimating lens and 7) the camera lens, sensor, and data storage. A high-speed digital camera, model Motion Xtra HG-TX by Redlake, was employed to capture and digitally store color schlieren images at exposure time of 663-μs and acquisition rate of 1000 frames per second.

The test sequence consisted of 1) activating the solenoid valve to turn on the flow in Earth gravity, 2) allowing time to establish the oscillating flow, 3) triggering storage of digital schlieren images in the on-board camera memory, 4) initiating the drop, 5) deactivating the solenoid valve to turn-off the flow, 6) retrieving the rig, and (7) transferring image data from camera memory to the hard disk media. The drop procedure was automated using a programmable logic controller (PLC). The image date were processed to (1) create time-space images to depict temporal evolution of the flow at specified axial locations, (2) determine the oscillation frequency at various locations using fast Fourier analysis, and (3) generate hue distributions to study detailed flow structure of the jet.

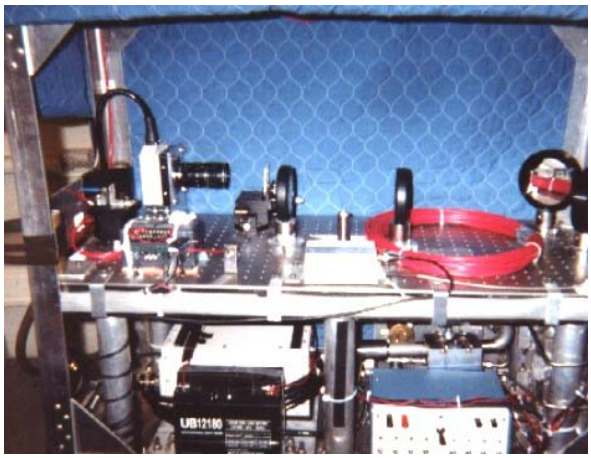

Figure 1. Photograph of the drop rig. Clearly A two-level design with the flow components and power system on the bottom and the optical system on the upper level was used. A battery and the camera controller body are visible on the lower level, while the fuse box and some piping components are visible on the bottom right. The camera lens, mirrors, collimating and decollimating lenses, test section, light source, and PLC are visible on the upper level. Note that a fiber optic cable for light input is coiled and taped in place on the upper floor of the drop rig. It would be connected to an external light source during the drop.

3. Results and Discussion

3.1 Rainbow Schlieren Images

The test conditions reported in this study pertain to jet Reynolds number of 490 and jet Richardson number of 0.11. Figure 2 shows schlieren images at various phases to depict an oscillation cycle in Earth gravity. The jet tube is visible as the black region at the bottom of each image. Figure 2 shows the primary jet bulging near the exit and contracting gradually in the downstream direction, where a separate outer structure is observed. The region between primary jet and outer flow, signifying a toroidal structure, moves downstream during the oscillation cycle. Concurrently, the primary jet contracts near the exit and separates from the outer flow to create a new toroidal structure. Thereafter, a new bulge develops near the jet exit as the oscillation cycle repeats itself. The flow structure observed in Fig. 2 was found to be highly repeatable. The oscillating flow in Earth gravity undergoes a significant change in microgravity. Figure 3 shows a sequence of schlieren images at 20-ms interval, beginning with the onset of free fall. Evidently, the flow oscillations continue for a brief period, as the outer toroidal structure formed in Earth gravity is swept downstream.

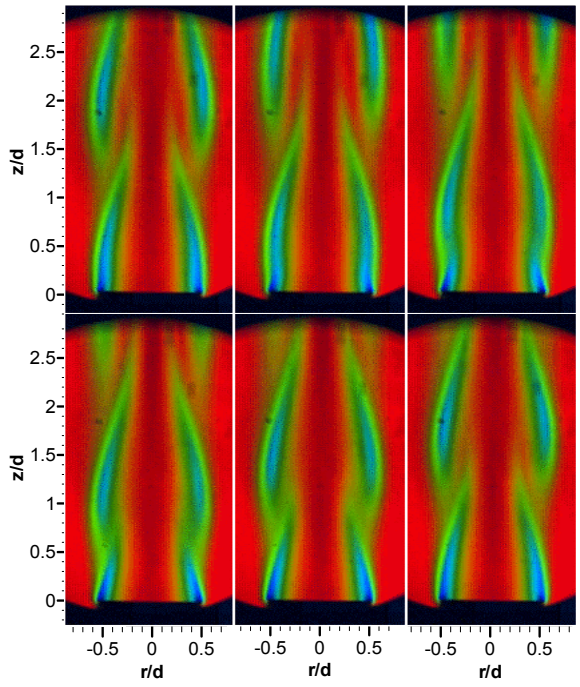

Figure 2. Rainbow schlieren image to depict a typical oscillation cycle in Earth gravity. Images progress at 7ms interval, from left to right starting in the upper left corner.

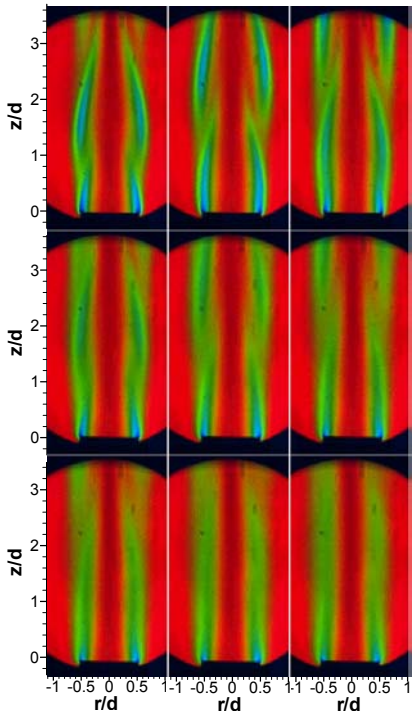

Figure 3. Rainbow schlieren images depicting flow structure during change from Earth gravity to microgravity. The images begin at the onset of free fall and continue from left to right, top to bottom at 20ms interval.

Periodic bulging and contacting of the primary jet leading to the formation of the outer toroidal structure in Earth gravity is absent in microgravity. Results show that the flow approaches steady conditions after a brief period of free fall.

3.1 Space-Time Images

Although nearly 2700 color schlieren images were obtained in the experiment, only a few are shown in Figs. 2 and 3. Thus, schlieren data from successive images were concatenated to create space-time images at selected axial locations. Figure 4 shows a portion of space-time images constructed from 700 schlieren images to span about 700ms; 260ms in Earth gravity and 440ms in free fall. These images are shown for z/d=0.01, 0.5, 1.0, 1.5, and 2.5, where z represents the distance downstream of the tube exit.

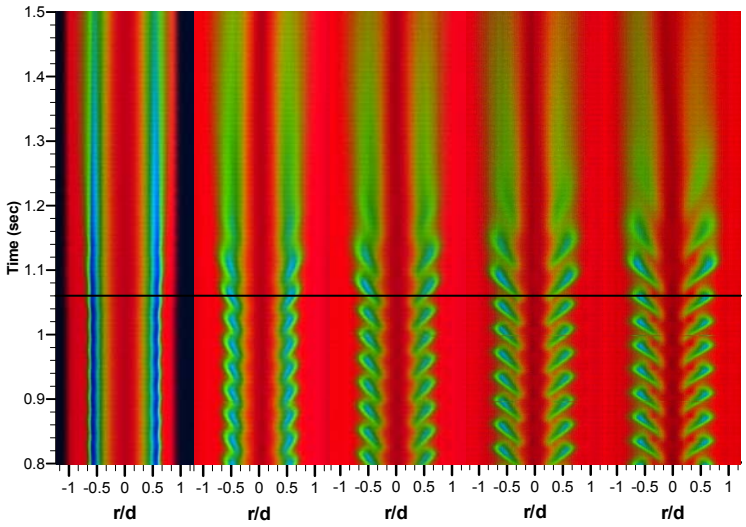

Figure 4. Space-time images at z/d=(a) 0.01, (b) 0.5, (c) 1.0, (d) 1.5, and (e) 2.5, from left to right, respectively. The black line at t=1.06-s indicates start of microgravity.

The horizontal black line in each image denotes the approximate release time (t=1.06s) of the experiment in the drop tower. Thus, the jet flow experiences Earth gravity for $t \leq 1.06$s and free fall for t>1.06s. Figure 4 provides detailed visualization of how the jet flow evolves temporally and spatially. In Earth gravity, the flow oscillations are observed at all axial locations shown in Fig. 4. The oscillation amplitude at z/d=0.01 is small (discernable upon magnification) and it increases with downstream locations. Oscillations penetrated farther into the jet center region at downstream locations. The wavy structure at z/d=0.5 represents the cyclic bulging and contracting of the primary jet. However, at z/d=1.0 and further downstream, the primary jet appears to separate from the outer flow to signify the presence of an outer toroidal structure. Figure 4 reveals a highly repeatable flow structure between consecutive cycles in Earth gravity. At all axial locations, about 7 cycles are completed in 260ms duration of Earth gravity suggesting that the flow oscillates globally at a frequency of approximately 27Hz. The resulting Strahoul number of 0.16 is the same as that obtained from the correlation of Cetegen and Kasper [1996] i.e., $St = 0.8[Ri\rho_a / \rho_j]^{0.38}$.

The image portion above the black line in Fig. 4 represents temporal evolution of the flow structure during change from Earth gravity to microgravity in the drop tower. Results show oscillations persisting during a brief initial period of free fall. The increased time between successive structures at the onset of free fall signifies a decrease in the oscillation frequency. The decay in jet oscillations appears to start from the jet exit and works it way downstream. For example, at t=1.2s,

oscillating structure is observed at z/d=2.5 although the flow at z/d=0.5 appears steady. The flow oscillations at all locations have seized after about 200ms of free fall or t=1.25s. Two factors account for the persistence of oscillations after the drop is initiated; the time required for attaining microgravity conditions in the drop tower and the flow adjustment time. The microgravity conditions are reached after 100ms of free fall [Lekan, 2004] and the flow convection time based on the average jet exit velocity is about 15ms. Thus, oscillations continue mainly because of the finite gravitational level existing during the initial period of free fall. Results show that the jet in microgravity is wider than that in Earth gravity. Lack of buoyancy in microgravity causes the jet to spread mainly by the molecular diffusion. Accordingly, the density varies gradually to produce smaller angular deflections in the radial direction, reflected by fewer color gradations in schlieren images in microgravity. Results in Fig 4 provide direct physical evidence that the flow oscillations in Earth gravity are buoyancy induced.

3.3 Fast Fourier Transform (FFT) Analysis

In this section, an analysis of the power spectra of the flow field is presented. The analysis is based on Fast Fourier Transform (FFT) of hue values at a specified point in the flow field, obtained from 512 successive (in time) images, at a resolution of 1Hz. Three partially overlapping 512-image subsections of data were used in the FFT analyses to represent the early, mid, and late duration of microgravity. Figure 5 shows the power spectra at z/d=0.5 and 1.5 for r/d=0.5.

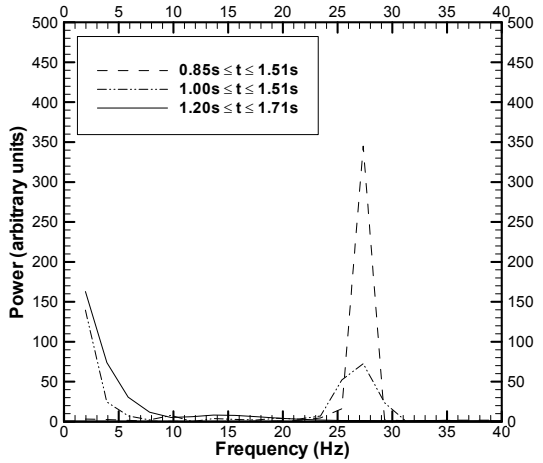

Figure 5a. Power spectra at r/d = 0.5, z/d = 0.5.

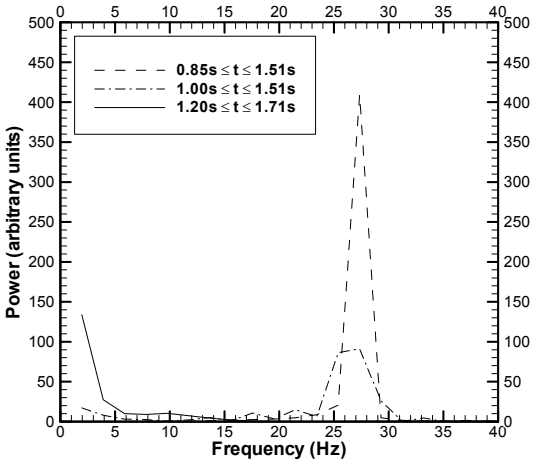

Figure 5b. Power Spectra at r/d = 0.5, z/d = 1.5.

In Fig. 5a, a characteristic peak in the power spectra is observed at a frequency of 27Hz for the "early" period 0.85s ≤ t ≤ 1.51s, where the free fall begins at t=1.06s and microgravity conditions are reached at t=1.16s. Evidently, the FFT analysis captures the dominant frequency of Earth gravity oscillations persisting during the early microgravity period. Note that Earth gravity oscillation frequency of approximately 27Hz was also determined from visual observations in the previous section. The curve for the "mid" period 1.00s ≤t ≤ 1.51s in Fig 5a also shows a peak near 27Hz, signifying Earth gravity as the source of oscillations. A peak is also observed near 0 Hz. The 27Hz peak has disappeared and the 0 Hz peak has intensified for the "late" period 1.20s ≤ t ≤ 1.71s spanning only the microgravity data. Similar results are obtained at a downstream location (z/d=1.5) as shown in Fig. 5b. Clearly, the self-excited oscillations in Earth gravity diminish in microgravity.

3.4 Hue Distribution Plots

Plots of hue distribution at various axial planes were generated to show temporal evolution of the flow structure. In a rainbow schlieren apparatus, the change in hue represents the angular deflection of light rays caused by density gradients in the flow field (Alammar et al., 1998). Hue profiles at z/d=0.5 and 1.5 in Fig. 6 show that the oscillation amplitude in Earth gravity increases in the axial direction. A constant oscillation frequency of 27Hz was obtained by measuring the time between peaks and valleys of various hue contour levels in Fig. 6. The measured oscillation frequency matches with that computed using the FFT analysis. In agreement with results presented earlier, hue oscillations subside in microgravity. The outer edges of the schlieren image provide direct measure of the jet width based on the concentration field. The jet width thus obtained is approximately twice of

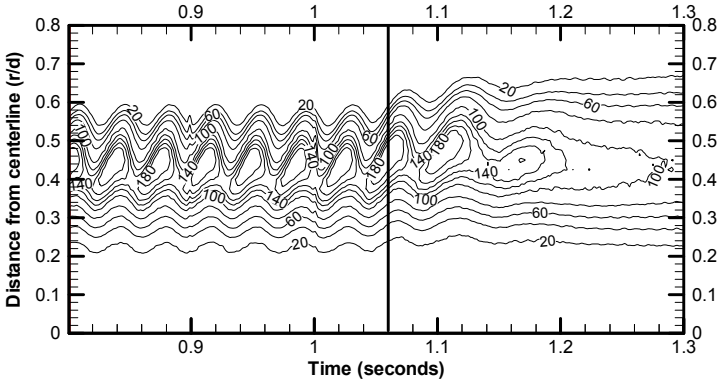

the jet half width (related to the radial location where the velocity or concentration value is half of that at the centerline) typically reported in the literature. In this experiment, the schlieren boundary is approximated by the hue value of 20 degrees, which is close to the background hue of the color schlieren image. Figure 6 shows that the outer edge of the jet (or the 20 degree hue contour) in Earth gravity oscillated between r/d of 0.54 and 0.60. In microgravity, the jet outer edge was located at r/d=0.67, signifying an increase of jet width in microgravity. Similarly, at z/d = 1.5, the jet outer edge in Earth gravity oscillated between r/d of 0.52 and 0.64 and it was located approximately at r/d=0.67 in microgravity. These results concur with the earlier evidence for buoyancy-dominated jets (Yep et al., 2003) showing oscillations decaying and jets widening as microgravity conditions are reached.

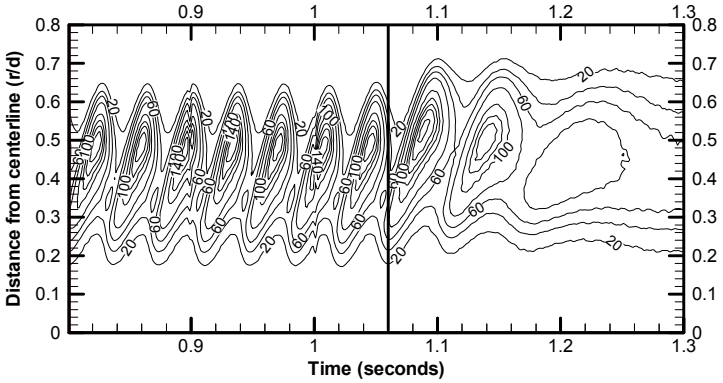

Figure 6b. Hue profiles at z/d=1.5.

4.0 Conclusions

High-speed rainbow schlieren deflectometry technique was used to visualize and quantify buoyancy effects on the flow fields of a helium jet discharged vertically into ambient air at a Richardson number of 0.11, bridging the buoyancy-dominated and momentum-dominated flow regimes. Flow structure details were investigated using space-time images, power spectra and profiles of hue obtained from rainbow schlieren images. Results show highly periodic oscillations in the Earth gravity. A constant oscillation frequency of 27Hz was obtained throughout the flow field using different analysis techniques. Earth gravity oscillations subsided after a brief period of free fall during which the gravitational level decreased from Earth gravity to microgravity. The jet width increased in microgravity. Results provide direct physical evidence that the flow oscillations at the small Richardson number considered in this study were buoyancy induced. Results suggest that the Richardson number based on global parameters is not sufficient to fully characterize buoyancy effects in low-density gas jets. Finally, high-speed rainbow schlieren apparatus was developed and demonstrated by obtaining temporally and spatially resolved measurements in the microgravity environment of the drop tower.

Acknowledgements

This work was supported by the Physical Sciences Division of NASA's Office of Biological and Physical research under grant NAG 3-2388.

References

Al-Ammar, K., Agrawal, A.K., Gollahalli, S.R., and Griffin, D.W., 1998, "Application of Rainbow Schlieren Deflectometry for Concentration Measurements in an Axisymmetric Helium Jet," *Exp. Fluids*, vol. 25, 89.

Cetegen, B.M., and Kasper, K.D., 1996, "Experiments on the Oscillatory Behavior of Buoyant Plumes of Helium and Helium-Air Mixtures," Physics of Fluids, vol. 8, 2974.

Cetegen, B. M., 1997 "Behavior of Naturally Unstable and Periodically Forced Axisymmetric Buoyant Plumes of Helium and Helium-Air Mixtures," *Phys. Fluids*, vol. 9, 1.

Greenberg, P.S., R.B. Klimek and D. R. Buchele, 1995, "Quantitative Rainbow Schlieren Deflectometry," *App. Opt.*, vol. 34, 3819.

Hamins, A., Yang, J.C., and Kashiwagi, T., 1992, "An Experimental Investigation of the Pulsating Frequency of Flames," *Proc. Combust. Inst.*, vol. 24, 1695.

Kyle D. M. and K. R. Sreenivasan, 1993, "The Instability and Breakdown of a Round Variable-Density Jet," J. Fluid Mech., vol. 249, 621.

Lekan, J.H, 2004, Private Communication, NASA Glenn Research Center.

Monkewitz, P.A., Bechert, D.W., Barsikow, B., and Lehmann, B., 1990, "Self-Excited Oscillations and Mixing in a Heated Round Jet," *J. Fluid Mech.,* vol. 213, 611.

Richards, C.D., Breuel, B.D., Clark, R.P., and Troutt, T.R., 1995, "Concentration Measurements in a Self-Excited Jet," *Exp. Fluids*, vol. 21, 103.

Subbarao, E. R., and B. J. Cantwell, 1992, "Investigation of a Co Flowing Buoyant Jet: Experiments on the Effect of Reynolds Number and Richardson Number," *J. Fluid Mech.*, vol. 245, 69.

Yep, T.W., Agrawal, A.K., and Griffin, D.W., 2003, "Gravitational Effects on Near Field Flow Structure of Low-Density Jets," *AIAA Journal*, vol. 41, 1973.

Authors Profile

Peter A. Leptuch: He received his Master of Science degree in Mechanical Engineering in 2002 and Bachelor of Science degree in Meteorology in 1998; both from the University of Oklahoma. His research interests include fluid flows in microgravity and software development.

Ajay K. Agrawal: He is Lloyd G. & Joyce Austin Presidential Professor and Associate Professor in the School of Aerospace and Mechanical Engineering at the University of Oklahoma. Professor Agrawal received his doctoral degree from the University of Miami in 1988. Prior to joining University of Oklahoma in 1993, he was visiting faculty at Michigan Technological University (1988-89) and Clemson University (1989-1993). His research interests include flow and combustion in microgravity, and environmentally benign energy utilization.

Manuscript Submitted to AIAA Journal on August 13, 2004

COMPUTATIONAL ANALYSIS OF GRAVITATIONAL EFFECTS IN LOW-DENSITY GAS JETS

Rajani P. Satti and Ajay K. Agrawal[1]

School of Aerospace and Mechanical Engineering

University of Oklahoma, Norman, OK-73019

ABSTRACT

This study deals with the computational analysis of buoyancy-induced instability in the near-field of an isothermal helium jet injected into quiescent ambient air environment. Laminar, axisymmetric, unsteady flow conditions were considered for the analysis. The transport equations of helium mass fraction coupled with the conservation equations of mixture mass and momentum were solved using a staggered grid finite volume method. The jet Richardson numbers of 1.5 and 0.018 were considered to encompass both buoyant and inertial jet flow regimes. Buoyancy effects were isolated by initiating computations in Earth gravity and subsequently, reducing gravity to simulate the microgravity conditions. Computed results concur with experimental observations that the periodic flow oscillations observed in Earth gravity subside in microgravity.

Keywords: Buoyancy, Inertial, Flow computations, Flow Instability

[1] Corresponding Author
Senior Member of AIAA, Lloyd G. and Joyce Austin Presidential Professor and Associate Professor
865 Asp Avenue, Room 212, School of Aerospace and Mechanical Engineering
University of Oklahoma, Norman, OK 73019
Phone: (405) 325-1754, Fax: (405)325-1088, email: aagrawal@ou.edu

1. INTRODUCTION

Low-density gas jets are characterized by the injection of a lighter fluid into a dense ambient environment. The resulting flow structure is susceptible to buoyancy arising because of the difference in densities of jet and surrounding fluids. In general, jets are considered buoyant for Richardson number, $Ri = gd(\rho_\infty - \rho_j)/\rho_j U_j^2 > 1.0$ and inertial for $Ri << 1.0$, where g is the gravitational acceleration, d is the injector tube inside diameter, ρ_∞ and ρ_j are, respectively, the ambient and jet fluid densities, and U_j is the average jet exit velocity. The present study examines low-density gas jets in both buoyant and inertial flow regimes, with the goal of delineating gravitational effects on the flow structure in the near-field.

Several studies[1-6] have focused on the far-field behavior of low-density jets, which is influenced by the instabilities arising in the near-field. Low-density gas jets are known to exhibit self-excited periodic oscillations in both buoyant and the inertial flow regimes. In the buoyant flow regime, Subbarao and Cantwell[7] conducted experiments with helium jets injected into a co-flow of air for Ri varying from 0.5 to 6.0. The frequency (f) of the periodic oscillations expressed by the Strouhal number, St=fd/Uj correlated with Richardson number for Ri>1.0 indicating buoyancy dependent instability. Hamins et al.[8] observed periodic oscillations in a helium jet injected into air, and reported that a minimum jet exit velocity was required to initiate the oscillations. Similar experiments were conducted by Cetegen and co-workers[9-11] for axisymmetric and planar plumes, whereby buoyancy induced toroidal vortical structures contaminating the primary jet flow were observed. Diagnostics involved flow measurements using laser Doppler velocimetry and particle image velocimetry. Pasumarthi and Agrawal[12] conducted experiments to characterize jet flow in terms of concentration measurements across

the whole field of a helium jet injected into quiescent air. Experiments by Yep et al.[13] demonstrated that the self-excited flow oscillations in Earth gravity were absent in the microgravity environment of the 2.2s drop tower.

Self-excited oscillations have also been reported in low-density inertial jets at $Ri<<1.0$[14-17]. In these studies, buoyancy effects were considered negligible because of the small Richardson number. Although this assumption is justified in the jet core, buoyancy may be significant in the jet shear layer where density and velocity gradients are large. Recently, Pasumarthi[18] conducted experiments at $Ri<1.0$ using helium jet injected into quiescent air in the microgravity environment of the 2.2s drop tower. Concentration measurements revealed global oscillations in the near-field in Earth gravity. In microgravity, the oscillation amplitude decreased significantly for $Ri<0.01$ and no oscillations were observed for $Ri>0.1$. These experiments provided direct physical evidence for the first time that the flow oscillations in inertial low-density gas jets are buoyancy-induced, a well known phenomenon in buoyant jets.

Past experiments have characterized buoyancy effects using either concentration or velocity measurements. However, simultaneous visualization of velocity and concentration fields is desired to fully understand the dynamics of the oscillating flow structure. Experimental difficulties in obtaining simultaneous vector-scalar measurements, especially in the low-gravity environment, have prompted studies of gas jets using computational fluid dynamic (CFD) analysis. Mell et al.[19] performed numerical simulations of a helium jet injected into air and found that the computed oscillation frequency matched with experiments of Hamins et al[8]. Recently, Soteriou et al.[20] investigated the near-field dynamics of planar buoyant plumes incorporating a Lagrangian transport element method. Computations qualitatively captured the plume instantaneous behavior observed experimentally. The mechanism of vorticity generation

and relative roles played by buoyancy and viscous forces in explaining the plume instability were discussed. However, a description of the flow field and its interaction with the scalar structure is desired to explain the instability in low-density gas jets. On a related note, several numerical studies have been conducted to understand the dynamics of flickering jet diffusion flames[21,22]. Thus, the objective of the present study is to delineate the effects of buoyancy in low-density gas jets. The CFD analysis is utilized to concurrently visualize the velocity and concentration fields. Both buoyant and inertial jets are examined in Earth gravity, microgravity, and during change from Earth to microgravity.

2. NUMERICAL FORMULATION

2.1 Governing Equations

Consistent with experimental studies[12, 13], the numerical formulation is based on unsteady, laminar, and axisymmetric flow behavior. The following additional approximations were made to simplify the analysis: (i) the flow is incompressible, (ii) temperature and pressure variations are negligible and (iii) the flow is a binary fluid system with air treated as a single species. Accordingly, the governing equations are expressed as follows:

$$\frac{\partial \rho}{\partial t} + \frac{1}{r}\frac{\partial}{\partial r}\left(\rho v r\right) + \frac{\partial}{\partial z}\left(\rho w\right) = 0 \qquad (1)$$

$$\frac{\partial (\rho r \phi)}{\partial t} + \frac{\partial}{\partial r}\left(\rho v r \phi\right) + \frac{\partial}{\partial z}\left(\rho r w \phi\right) = \frac{\partial}{\partial r}\left(\Gamma^{\phi} r \frac{\partial \phi}{\partial r}\right) + \frac{\partial}{\partial z}\left(\Gamma^{\phi} r \frac{\partial \phi}{\partial z}\right) + S^{\phi} \qquad (2)$$

Equation (1) represents the continuity equation and Equation (2) is the generalized transport equation, which represents the momentum, or species conservation equation depending on the

variable ϕ. Γ^{ϕ} and S^{ϕ} are, respectively, the transport coefficient and source term of the variable ϕ, as listed in Table 1.

Table 1. Transport coefficients and source terms in Equation 2

Variable	ϕ	Γ^{ϕ}	S^{ϕ}
Axial Velocity	w	μ	$-r\frac{\partial p}{\partial z}+r(\rho_{\infty}-\rho)g+\frac{\partial}{\partial z}\left(r\mu\frac{\partial w}{\partial z}\right)+\frac{\partial}{\partial r}\left(r\mu\frac{\partial v}{\partial z}\right)-\frac{2}{3}\left[\frac{\partial}{\partial z}\left(r\mu\frac{\partial v}{\partial r}\right)+\frac{\partial}{\partial z}\left(r\mu\frac{\partial w}{\partial z}\right)\right]$
Radial Velocity	v	μ	$-r\frac{\partial p}{\partial r}-\frac{2}{3}\mu\frac{v}{r}+\frac{\partial}{\partial z}\left(r\mu\frac{\partial w}{\partial r}\right)+\frac{\partial}{\partial r}\left(r\mu\frac{\partial v}{\partial r}\right)-\frac{2}{3}\left[\frac{\partial}{\partial r}\left(r\mu\frac{\partial v}{\partial r}\right)+\frac{\partial}{\partial r}\left(r\mu\frac{\partial w}{\partial z}\right)\right]$
Helium mass fraction	f	ρD_b	0

Density was computed from the equation of state for incompressible ideal gas. The dynamic viscosity was calculated using Wilke's mixture averaged formula[23]. The binary diffusion coefficient of helium into air, D_b was specified as a constant.[24] In microgravity, the gravitational acceleration was specified as 100μg, where g is the gravitational acceleration on Earth.

2.2 Boundary Conditions

The computational domain extended 15d in the axial direction and 6d in the radial direction where "d" is the tube inside diameter. These dimensions were established after trials indicating that the near-field flow behavior was independent of the domain size. The upstream boundary was placed at a distance of 1d from the jet exit plane to account for the diffusion upstream of the jet exit observed in experimental studies[12]. Symmetric boundary condition was imposed along the jet centerline. At the tube inlet, the velocity profile was fully developed and the helium mole fraction was unity. No slip and zero mass diffusion conditions were imposed at the tube walls. At the exit boundary, pressure outlet condition was implemented where flow properties are

extrapolated from the interior[24]. Pressure inlet and outlet conditions were specified, respectively, at the upstream and far-field radial boundaries. All flow properties were set to zero at the start of the computations. The operating pressure and temperature were specified, respectively, as 1 atm and 300K.

2.3 Computational Procedure

An orthogonal non-uniform grid system was used to split the computational domain into five sub regions. The grid elements in the radial direction were concentrated in the flow oscillation region. The grid size was increased gradually in the axial direction. The governing equations were solved sequentially using a segregated approach[24]. The pressure-velocity coupling was achieved using the SIMPLEC algorithm. Grid sensitivity analysis was performed to obtain grid-independent solution. Striking a balance between computational time and accuracy, a grid with 31093 and 80021 nodes was used, respectively, for buoyant and inertial jet analysis. The time step for buoyant and inertial jet computations was 1.6ms and 0.3ms, respectively. The small time step was needed to resolve the high-frequency oscillations in the inertial jet. The numerical code was validated with experimental data[12, 13] and experimental-numerical comparisons are presented for Earth gravity conditions in Ref. 26 and for change from Earth gravity to microgravity in later sections of this paper.

3. RESULTS AND DISCUSSION

Time-dependent simulations of the isothermal helium jet injected into the ambient air environment were performed with the objective of quantifying buoyancy effects in the near-field. Although computations were performed for several cases, detailed results are presented for only one buoyant jet and one inertial jet at operating conditions listed in Table 1. First, details

pertaining to the flow behavior of a buoyant helium jet in Earth gravity and during change from Earth gravity to microgravity are presented. Similar information is provided for the inertial jet. Finally, flow behavior of buoyant and inertial jets is compared in Earth gravity and microgravity.

Table 1. Summary of Test Conditions

Case	*Re*	*Ri*	*d, mm*	*U_j, m/s*	*f, Hz (Computed)*	*f,Hz (Measured)*
Case 1(Buoyant)	*300*	*1.52*	*31.8*	*1.15*	*14.5*	*12.5*
Case 2(Inertial)	*800*	*0.018*	*14.05*	*6.75*	*150*	*120*

3.1 Buoyant Jet

3.1.1 Flow and Concentration Fields in Earth Gravity

Figure 1 shows a sequence of helium mole percentage contours superimposed with velocity vectors for the buoyant jet (case 1). At t=0.0ms, buoyancy accelerates the jet core, which contracts to conserve the mass. This results in entrainment of ambient fluid producing a toroidal vortex represented by the flow recirculation. Note that the vortex core represented by a black dot is located at z/d=0.12 in Fig.1. In the next plot at t=13.6ms, the vortex is characterized by a larger recirculation region accompanied with greater contraction of the jet core, evident from the inward indentations in the concentration field near z/d=0.2. Subsequently, between t=27.3ms and 54.7ms, the vortex grows in size and convects downstream to contaminate a greater portion of the jet core. The vortex gains its strength by momentum transfer from the jet core. This feature is evident in Fig. 1 wherein the velocity vectors downstream of the vortex core are larger than those upstream before interacting with the jet core. As the vortex propagates downstream, the jet expands near the tube exit inducting buoyant fluid to initiate another vortex at t=68.4ms to repeat the oscillation cycle. These results illustrate self-excited periodicity in the jet at a frequency of 14.6Hz, in excellent agreement with the oscillation frequency of 12.5Hz measured by Yep et al.[13]

3.1.2 Flow and Concentration Fields during Change from Earth gravity to Microgravity

Computations were performed to visualize the jet flow during change from Earth gravity to microgravity and to depict how the jet flow adjusts itself in the absence of buoyancy. As a first step, the simulation results were compared with experiments[13] to validate the computational model. Figure 2 shows a series of computational-experimental helium mole fraction contour plots during change from Earth gravity to microgravity. At the onset of microgravity denoted as T=0.0s, the indentations in the helium concentration level higher than 50% signify a vortex located at z/d=0.7. After change to microgravity at T=16.66ms, the vortex convects downstream as the jet expands in the near exit region. At T=50.0ms, the jet has expanded at the exit to r/d= 0.7. The indentations in the concentration contours have weakened, signifying the diminishing nature of the vortex. Subsequently, the jet widens gradually throughout the near-field with diminishing oscillations as steady conditions are reached in microgravity. The helium mole fraction contours in microgravity are straight lines reminiscent of a non-buoyant jet. The above-mentioned features replicate similar phenomena observed in experiments[13] showing self-excited oscillations gradually subsiding after microgravity was initiated. Judging from the plots in Figure 2, it is inferred that computations reproduced experimental observations, proving model's capability in predicting the flow structure during change from Earth gravity to microgravity.

Figure 3 shows contours of helium mole percentage overlapped by velocity vectors during change from Earth gravity to microgravity to highlight the interaction of the flow field with the concentration field. At T=0.0ms, a vortex with core located at z/d=0.7 characterizes the entrainment of ambient fluid into the jet. At this instant the jet flow is similar to that at T=27.3ms in Fig. 1(c). The jet width characterized by the 10% helium concentration contour extends to r/d=0.6 near the exit. In microgravity at T=33.33ms, the jet at the exit has expanded to

r/d=0.7. The vortex has convected downstream with its core located at z/d=1.8. Velocity vectors show a weakening of the vortical structure at this instant. At T=66.6ms, the weakened vortex has moved downstream of the field-of-view while another vortex is formed near the jet exit at z/d=0.3. At T=133.3ms, flow recirculation has diminished as the jet expands to r/d=0.78 near the exit. Similar features are exhibited at t=166.6ms with the flow approaching steady conditions in microgravity. Finally, at T=2000ms the jet has assumed a steady columnar shape. The flow velocity decreases in the radial direction as the jet fluid mixes with ambient air. Further details about the flow structure are provided by spatio-temporal plots during the change from Earth gravity to microgravity.

3.1.3 Temporal Evolution of Axial Velocity and Concentration Fields

Figure 4 depicts temporal evolution of the concentration field during the change from Earth gravity to microgravity. Computed and measured[13] time traces of helium mole fraction at z/d=1.0 illustrate that the oscillating jet flow expands radially after the change in gravity. Results show that the oscillations sustain during a brief initial period of microgravity, with steady conditions reached within T=0.75s. Again, the experimental trends are predicted well by the computations. Figure 5 shows time trace plots of helium mole percentage and axial velocity at selected locations during the change from Earth gravity to microgravity. Near the jet exit at z/d=0.15, the helium concentration at the jet center (r/d=0) is constant at 100% throughout. In contrast, the axial velocity at the jet center fluctuates between 2.3m/s and 2.6m/s in Earth gravity. In microgravity, the axial velocity initially decreases and then reaches a steady value of 2.2m/s at T=0.1s. In the entrainment region at r/d=0.45, the helium mole percentage in Earth gravity varied between 45% and 94%. During change to microgravity, the helium concentration peaked to 100% within 0.08s. Afterwards, minor oscillations occurred before a steady value of 95% was

reached within T=0.3s. Correspondingly, the axial velocity reached a steady value of 0.4m/s in microgravity. Near the jet boundary at r/d=0.6, low amplitude oscillations in the concentration field are observed in Earth gravity. In microgravity, the helium mole percentage rose to 70% prior to reaching a steady value of 52% within T=1.0s. In Earth gravity, the axial velocity profile at this radial location shows troughs with negative velocity indicating flow recirculation.

At a downstream location, z/d=2.0, pure helium is present throughout at the jet center. The axial velocity and its oscillation amplitude have increased at this location, signifying buoyant acceleration in Earth gravity. The flow oscillations diminish within 0.5s of microgravity as steady value of 2.1m/s is reached. At r/d=0.45, high amplitude concentration oscillations are observed in Earth gravity. At r/d=0.6, helium reaches peak concentration level of 60% during change from Earth gravity to microgravity and reaches a steady value of 56% at T=0.6s. The axial velocity profiles at the above radial locations depict flow behavior similar to that observed upstream. These features agree with time traces of concentration field measured by Yep et al.[13]

3.2 Inertial Jet

3.2.1 Flow and Concentration Fields in Earth Gravity

Figure 6 shows a sequence of helium mole percentage contours superimposed with velocity vectors to depict an oscillation cycle. In this case, the computed results are presented only between r/d=0.3 and 0.65 to visualize the flow oscillation region in greater detail. At t=0.0s, buoyant acceleration contracts the jet core leading to entrainment and formation of a toroidal vortex. The flow structure during the oscillation cycle is similar to that of the buoyant jet. The nature and propagation of the toroidal vortex are the same as already explained.

Although self-excited flow oscillations were observed in both buoyant and inertial jets, some aspects of the flow field were found to be different. First, based on the concentration field, the

inertial jet is wider compared to the buoyant jet. This implies that helium diffuses farther in an inertial jet. This effect is opposite to constant density jets where the jet width decreases with increasing initial jet momentum. Contraction and mixing by entrainment are confined to a narrow region in the inertial case compared to the buoyant case. The oscillation frequency for the inertial jet (150 Hz) is much higher than that for the buoyant case (14.5Hz). The above results illustrate self-excited periodicity in the flow field irrespective of the initial jet momentum, which agrees qualitatively and quantitatively with experiments[13, 18].

3.2.2 Flow and Concentration Fields during change from Earth gravity to Microgravity

Figure 7 shows the contours of helium mole percentage overlapped by velocity vectors during change from Earth gravity to microgravity and then to zero gravity to highlight the interaction of flow field with concentration field. At the onset of microgravity (T=0.0ms), a toroidal vortex is located at $z/d \cong 0.75$. The vortex convects downstream and a new one is formed near the exit as shown in Fig. 7(b) for T=24ms. Subsequently, the jet flow maintains a periodic structure in microgravity as by Figs. 7(c)-(e) representing an oscillation cycle. The curvature of concentration contours is less severe and the vortex is narrower in microgravity compared to those in Earth gravity. This result is consistent with experiments by Pasumarthi[18] showing flow oscillations subsiding to smaller amplitudes in microgravity for $Ri<0.01$. The last plot in Fig 7 pertains to the results obtained in zero gravity, simulated by completely turning off the gravity. In this case, the jet assumes a steady non-oscillatory state to support buoyancy as the cause of the instability. Results show that minor buoyant acceleration destabilizes the inertial jet.

3.2.3 Temporal Evolution of Axial Velocity and Concentration Fields

Figure 8 shows time trace plots of helium mole percentage and axial velocity at selected locations during change from Earth gravity to microgravity. At z/d=0.5, helium concentration at

the jet centerline remained 100% throughout. Concentration fluctuations for the inertial case are smaller compared to the buoyant case. Axial velocity at the jet center oscillates between 13 and 14 m/s in Earth gravity and between 12.5 and 13.5 m/s in microgravity. These oscillations ceased when the gravity was completely turned off in zero gravity. At the downstream location, z/d=2.0, the axial velocity fluctuates between 12 and 15 m/s in Earth gravity. These fluctuations are slightly smaller in microgravity but absent in zero gravity. The concentration and velocity fields in Fig.8 reveal that the flow oscillations subside in microgravity and disappear in zero gravity. These results ascertain that buoyancy plays an important role in both buoyant and inertial low-density gas jets.

3.3 Comparison of Flow Behavior in Buoyant and Inertial Jets

In this section, buoyant and inertial jet flows are compared to identify similarities and differences in the flow behavior.

3.3.1 Vortex Convection Velocity

Figure 9 shows the vortex convection velocity (U_v) normalized by the averaged jet exit velocity in Earth gravity. This plot was generated by tracking the position of the vortex core at different times. Results show a gradual increase of vortex convection velocity in the flow direction. The plots are similar for buoyant and inertial jets although higher values are reached for the buoyant case.

3.3.2 Axial Velocity Profiles

As already stated, buoyancy plays an important role in describing the instability phenomena. In case of the buoyant jet, buoyancy effects are prominent in the jet core. However, in the inertial jet, buoyancy affects the low-momentum region of the jet shear layer. This phenomenon is illustrated by the profiles of instantaneous axial velocity at various radial locations as shown in

Fig.10. The axial velocity was normalized by the jet exit velocity (U_e) at that particular radial location. The profiles show the axial velocity varying with axial coordinate and time corresponding to the phases in Figs. 1 and 6.

The normalized axial velocity profiles for the buoyant case (Figs. 10a-c) show periods of acceleration and deceleration at any given phase. The phases reveal the periodic flow behavior of the near-field region. Along the jet centerline, at phase A, slight deceleration occurs up to z/d=0.8 followed by a rapid acceleration between z/d=1.0 and 2.0. Note that the velocity peak at z/d=2.0 occurs slightly upstream of the vortex core at z/d=2.15. Near the jet exit, the decelerating flow at phase A accelerates at Phase B as a new vortex is formed. At phase C, rapid acceleration is observed near the exit, with peak normalized axial velocity reaching a value of 1.25 at z/d=0.5 or slightly upstream of the vortex core at z/d=0.80. Subsequently, the flow decelerates because of the transfer of the energy from the jet core to the vortex. At later phases (D and E), the flow decelerates near the exit but accelerates at downstream locations. Note that the normalized peak axial velocity has increased to about 1.7 at phase D and to 2.0 at phase E. A common feature is that the flow accelerates upstream of the vortex core and decelerates downstream of it. The inertial jet shows a similar behavior. However, the normalized axial velocity profiles are elongated implying that the peak occurs farther downstream. The peak normalized axial velocity is within 1.1 for all phases. These results clearly show that the buoyancy induced acceleration at the jet center is more prominent for the buoyant case compared to the inertial case.

At r/d=0.3, both buoyant and inertial jets exhibit flow acceleration and deceleration because of the interaction with the outer vortex. However, the peak normalized axial velocity has decreased from 2.0 to 1.4 for the buoyant jet and it has increased from 1.1 to 1.2 for the inertial jet. Thus buoyancy is more important at this radial location for the inertial jet. At r/d=0.45, both

buoyant and inertial jets show large variations in the normalized axial velocity because of the small initial momentum in the shear layer region. Note that the flow acceleration is greater for the inertial jet compared to that for the buoyant case.

3.3.3 Mean and RMS Flow Structure

The oscillating flow of buoyant and inertial jets is compared in Fig. 11 using the mean and RMS profiles of helium mole percentage and axial velocity at several axial locations. Near the jet exit at z/d=0.05, the mean concentration shows a top hat profile with finite shear layer thickness for both buoyant and inertial jets. Pure helium is present till r/d=0.38 for the buoyant case compared to r/d=0.46 for the inertial case. A steep reduction in helium concentration occurs thereafter. The scalar jet width extends to $r/d \cong 0.8$ for the buoyant case and to r/d>0.8 for the inertial case, indicating greater radial expansion at the higher Reynolds number.

At z/d=0.5, the mean concentration at the tube inside the boundary plane (r/d=0.5) has reduced to 50% for the buoyant case compared to 75% for the inertial case, suggesting greater radial mixing for the buoyant case. Further downstream at z/d=1.5, the concentration profiles show an inflection point located at r/d=0.29 for the buoyant case and r/d=0.33 for the inertial case, attributed to the entrainment by the vortex. The concentration gradient in the inflection region is higher for the buoyant case compared to the inertial case. The scalar jet width is nearly independent of the axial location for the buoyant case because the entrainment has restricted radial expansion of the jet. In contrast, for the inertial case, the scalar jet width increases in the flow direction because of the higher jet momentum limiting the entrainment.

The RMS concentration profiles show large fluctuations near the jet exit for the buoyant case. The peak RMS concentration of 14% at z/d=0.05 increased to 25% at z/d=0.5 and to 29% at z/d=1.5. The location of the peak RMS concentration shifts inwards with the axial direction,

which is consistent with the contraction of the jet as the vortex propagates downstream. The concentration fluctuations confined to a wake region ($0.4<r/d<0.6$) near the jet exit broaden in the flow direction and contaminate a greater portion of the flow at $z/d>1.0$. These observations agree with experimental results presented by Pasumarthi.[13] For the inertial case, fluctuations are negligible at $z/d=0.05$. Peak RMS concentration of 10% at $z/d=0.5$ increased to 12% at $z/d=1.5$. Lower fluctuations in the inertial jet compared with buoyant jet signify low level of mixing in the inertial jet.

Mean axial velocity at $z/d=0.05$ shows a typical parabolic profile at the tube exit for buoyant and inertial cases. For the buoyant case, the axial velocity at the jet centerline has increased from 2.4m/s at $z/d=0.05$ to 2.6 m/s at $z/d=0.5$ and to 3.1 m/s at $z/d=1.5$, indicating strong buoyancy induced acceleration. However, the buoyant acceleration is confined mainly to $r/d<0.3$. For the inertial jet case, the mean axial velocity is nearly the same at all axial locations. The RMS axial velocity profiles show negligible fluctuations near the jet exit ($z/d=0.05$) for both cases. The peak fluctuations increase with axial distance. For the buoyant case, peak RMS velocity of 0.3m/s at $z/d=0.5$ increased to 0.75m/s at $z/d=1.5$. Note that the peak RMS axial velocity shows a decreasing trend from the jet centerline towards the jet boundary plane for the buoyant case. In contrast, the RMS axial velocity peaked at $r/d \cong 0.4$ for the inertial case.

3.3.4 Flow Behavior in Microgravity

Radial profiles of axial velocity and concentration field in microgravity are presented in Fig. 12 for buoyant and inertial cases. These profiles were obtained after the jet adapted to the change in gravity. In microgravity, the jet assumed steady, non-oscillatory structure for the buoyant case and it maintained flow oscillations for the inertial jet. For both cases, the jet width increased in microgravity. For buoyant jet, the helium concentration at $r/d=0.7$ is less than 5% in Earth

gravity and approximately 30% in microgravity. The corresponding values for the inertial jet are between 10-30% in Earth gravity and between 25-50% in microgravity. Figure 12 shows that the oscillation amplitude for the inertial jet is significantly smaller in microgravity compared to that in Earth gravity.

CONCLUSIONS

A laminar, time-dependent, axisymmetric numerical model was developed to simulate helium-air jets previously studied experimentally. The CFD-based model accurately simulated the experiments in Earth gravity and microgravity involving buoyant and inertial jets. The major conclusions of the study are summarized in the following:

- The buoyant jet exhibited self-excited oscillations in Earth gravity at a frequency of 14.5Hz. The inertial jet exhibited similar self-excited oscillations in Earth gravity at a frequency of 150Hz. However, the oscillation amplitude was smaller and oscillations were confined to a narrow region in the inertial jet compared to the buoyant jet.
- The buoyant jet attained a steady, columnar structure in microgravity. Temporal plots of velocity and concentration fields depict that the flow oscillations persisted for a brief period during the change from Earth gravity to microgravity.
- The inertial jet exhibited self-excited oscillations in microgravity, although the oscillation amplitude was lower. Simulations illustrated that the inertial jet reached a steady, non-oscillatory flow when the gravity was completely turned off (zero gravity). These results show that the inertial jet becomes unstable in the presence of small amount of buoyant acceleration.

- In Earth gravity, the scalar jet width was found to increase with increasing Reynolds number. This near-field behavior of low-density jets is opposite to that of constant density jets where the jet width decreases at higher Reynolds numbers.
- The scalar jet width increased in microgravity for both buoyant and inertial jets.

ACKNOWLEDGEMENTS

This work was supported by Physical Sciences Division of NASA's office of Biological and Physical research under grant NAG 3-2388.

REFERENCES

[1]Fay, J.A., "Buoyant Plumes and Wakes," *Annual Review of Fluid Mechanics*, Vol. 5, 1973, pp. 151-160.

[2]Morton, B.A., "Forced Plumes," *Journal of Fluid Mechanics*, Vol. 5, 1959, pp. 151-159.

[3]List, E.L., "Turbulent Jets and Plumes," *Annual Review of Fluid Mechanics*, Vol. 14, 1982, pp. 189-212.

[4]Papanicolaou, P.A., and List, E.L., "Investigations of Round Vertical Turbulent Buoyant Jets," *Journal of Fluid Mechanics*, Vol. 195, 1988, pp. 342-391.

[5]Dai, Z., Tseng, L.K., and Faeth G.M., "Structure of Round, Fully Developed, Buoyant Turbulent Plumes," *Journal of Heat Transfer,* Vol. 116, 1994, pp. 409-417.

[6]So, R.M.C., Zhu, J.Y., Otugen, M.V., and Hwang, B.C., "Some Measurements in a Binary Gas Jet," *Experiments in Fluids*, Vol. 9, 1990, pp. 273-284.

[7]Subbarao, E.R., and Cantwell B.J., "Investigation of a Co-Flowing Buoyant Jet: Experiments on the Effects of Reynolds number and Richardson number," *Journal of Fluid Mechanics*, Vol.245, 1992, pp. 69-90.

[8]Hamins, A., Yang, J.C., and Kashiwagi, T., "An Experimental Investigation of the Pulsating Frequency of Flames," *Proceedings of the Combustion Institute* Vol. 24, 1992, pp. 1695-1705.

[9]Cetegen, B.M., and Ahmed, T.A., "Experiments on the Periodic Instability of Buoyant Plumes and Pool Fires," *Combustion and Flame*, Vol. 93, 1993, pp. 157-184.

[10]Cetegen, B.M., and Kasper, K.D., "Experiments on the Oscillatory Behavior of Buoyant Plumes of Helium and Helium-Air Mixtures," *Physics of Fluids,* Vol. 8, 1996, pp. 2974-2984.

[11]Cetegen, B.M., "Measurements of Instantaneous Velocity Field of a Non-Reacting Pulsating Buoyant Plume by Particle Image Velocimetry," *Combustion Science and Technology*, Vol. 123, 1997, pp. 377-387.

[12]Pasumarthi, K.S., and Agrawal, A.K., "Schlieren Measurements and Analysis of Concentration Field in Self-Excited Helium Jets," *Physics of Fluids,* Vol. 15, 2003, pp. 3683-3692.

[13]Yep, T.W., and Agrawal, A.K., "Gravitational Effects on Near-Field Flow Structure of Low Density Gas Jets," *AIAA Journal*, Vol. 41, 2003, pp. 1973-1979.

[14]Sreenivasan, K.R., Raghu, S., and Kyle, D.M., "Absolute Instability in Variable Density Round Jets," *Experiments in Fluids,* Vol. 7*,* 1989, pp. 309-317.

[15]Monkewitz, P.A., Bechert, D.W., Bariskov, B., and Lehmann, B., "Self Excited Oscillations and Mixing in a heated Round Jet," *Journal of Fluid Mechanics,* Vol. 213, 1990, pp. 611-639.

[16]Kyle, D.M., and Sreenivasan, K.R., "The Stability and Breakdown of a Round Variable Density Jet," *Journal of Fluid Mechanics,* Vol. 249*,* 1993, pp. 619-664.

[17]Richards,C.D.,Breuel,B.D.,Clark, R.P., and Troutt, T.R., "Concentration Measurements in a Self-Excited Jet," *Experiments in Fluids,* Vol. 21,1996, pp. 103-109.

[18]Pasumarthi, K.S and Agrawal, A.K., "Buoyancy Effects on Flow Structure and Instability of Low-Density Gas Jets," Doctoral Dissertation, University of Oklahoma, 2004.

[19]Mell, W.E., McGrattan, W.B., and Baum, H.R., "Numerical Simulation of Combustion in Fire Plumes," *Proceedings of the Combustion Institute*, Vol. 26, 1996, pp. 1523-1530.

[20]Soteriou, M.C., Dong, Y., and Cetegen, B.M., "Lagrangian Simulation of the Unsteady Near-field Dynamics of Planar Buoyant Plumes," *Physics of Fluids,* Vol. 14, 2002, pp. 3118-3140.

[21]Katta, V.R., and Goss, L.P., "Numerical Investigations of Transitional H_2/N_2 Jet Diffusion Flames," *AIAA Journal*, Vol. 32, 1994, pp. 84-94.

[22]Sato, H., Kushida, G., Amagai, K., and Arai, M., "Numerical Analysis of the Gravitational Effect on the Buoyancy-Driven Fluctuations in Diffusion Flames," *Proceedings of the Combustion Institute*, Vol. 29, 2002, pp. 1671-1678.

[23]Bird, R.B., Stewart, W.E., Lightfoot, E.N., "Transport Phenomena, 1st edition, 1960, Wiley, New York.

[24] Fluent 6.0, User's Guide, *Fluent Inc.* Lebanon, NH 1-4 (2003).

[25]Gambit 2.1, User's Guide, *Fluent Inc.* Lebanon, NH 1-4 (2003).

[26]Satti, R.P., and Agrawal, A.K., "Numerical Analysis of Flow Evolution in a Helium Jet injected into Ambient Air," *ASME Paper No. HTFED-2004-56811*.

[27]Satti, R.P., Pasumarthi, K.S., and Agrawal, A.K., "Numerical Simulations of Buoyancy Effects in Low Density Gas Jets," *AIAA Paper-2004-1317*

LIST OF FIGURES

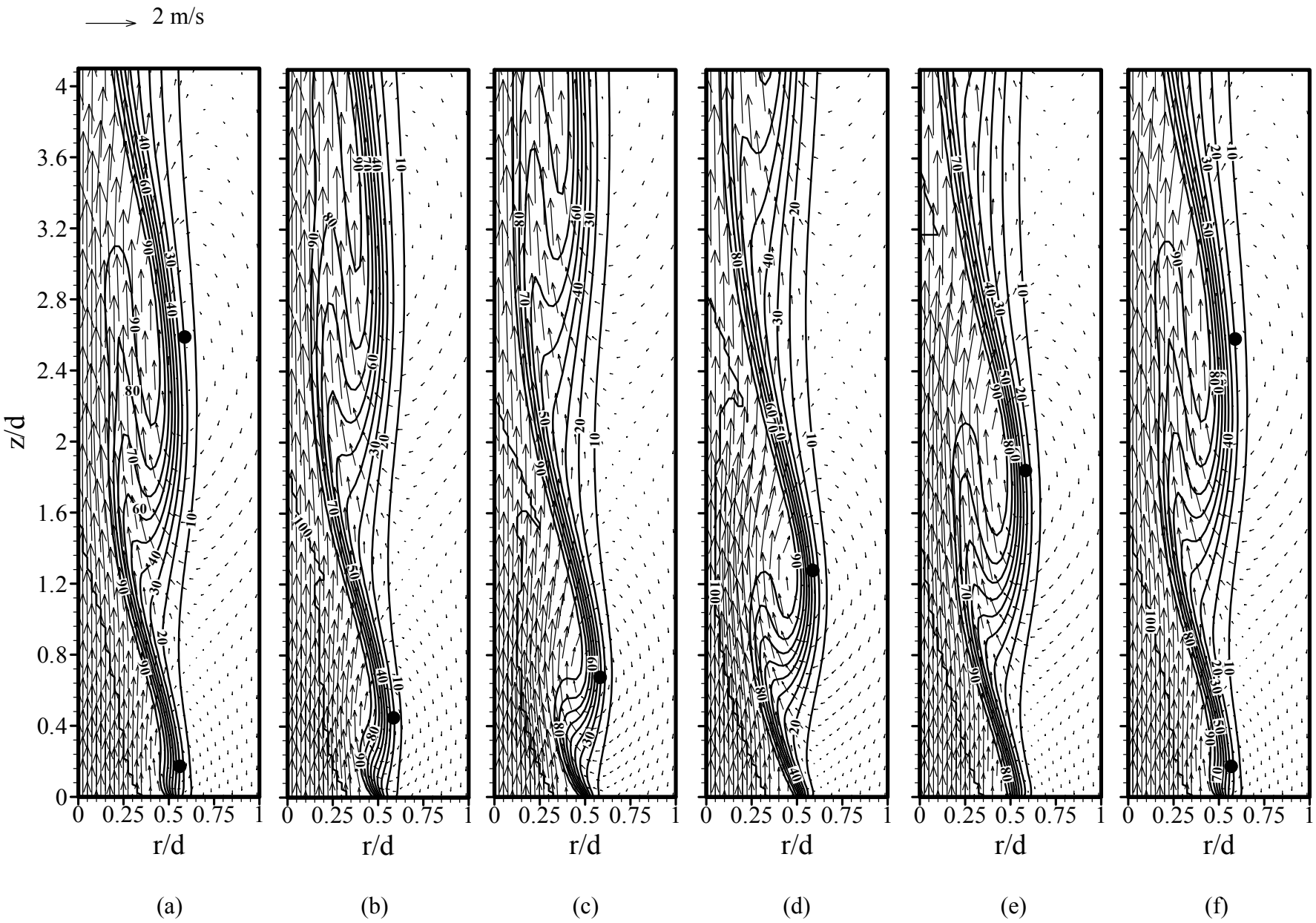

Fig.1, AIAA

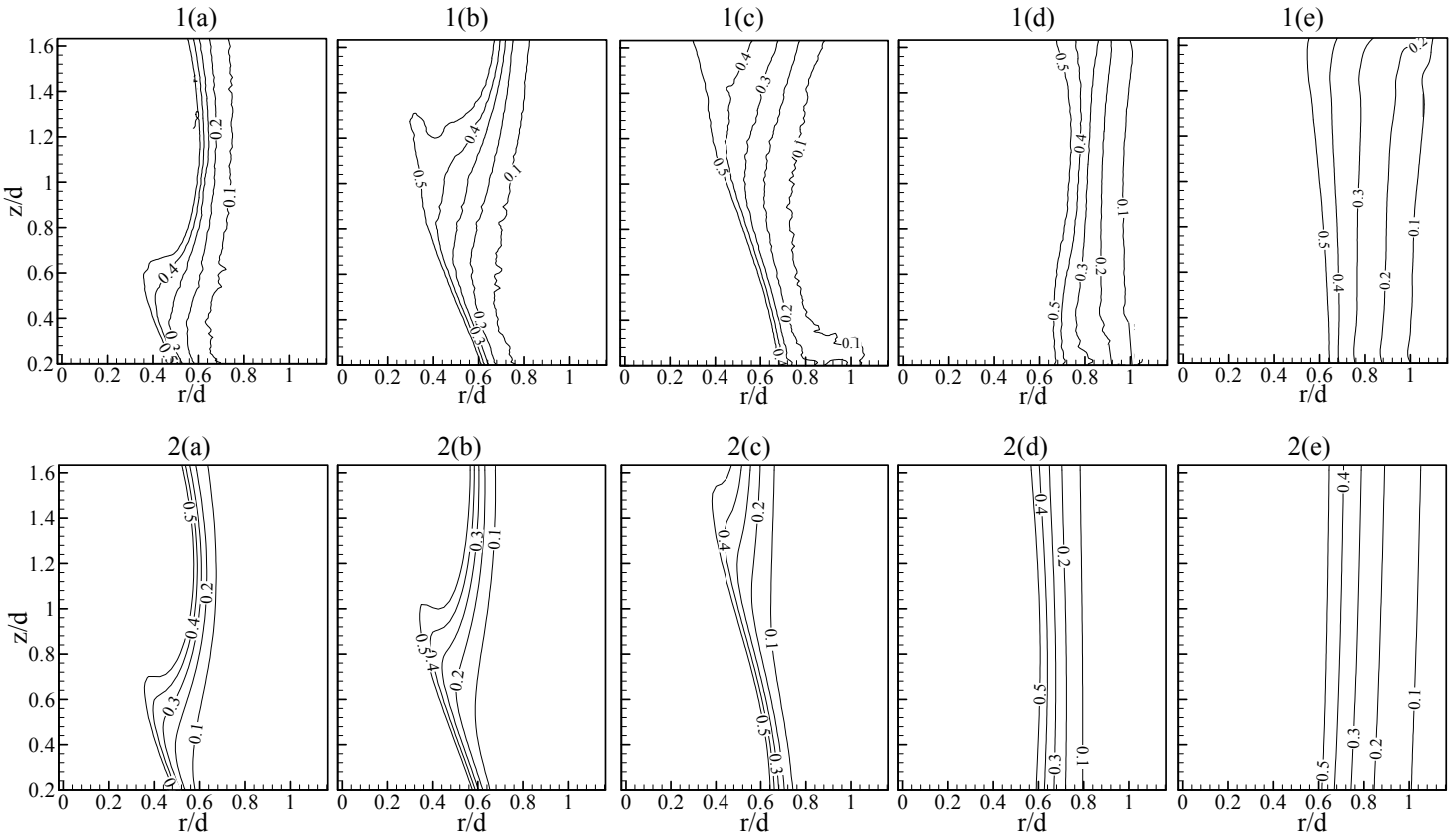

Fig. 2, AIAA

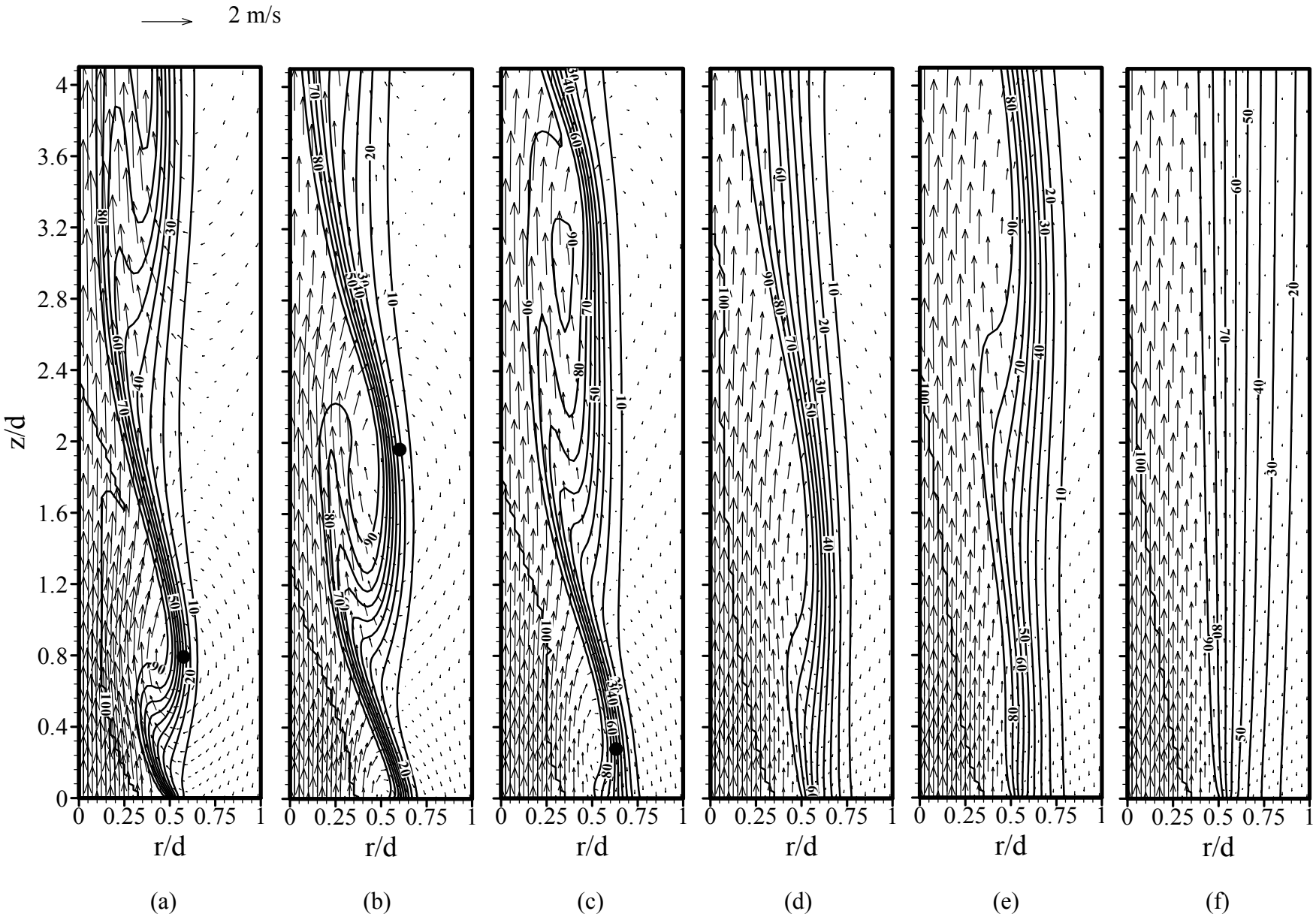

Fig .3, AIAA

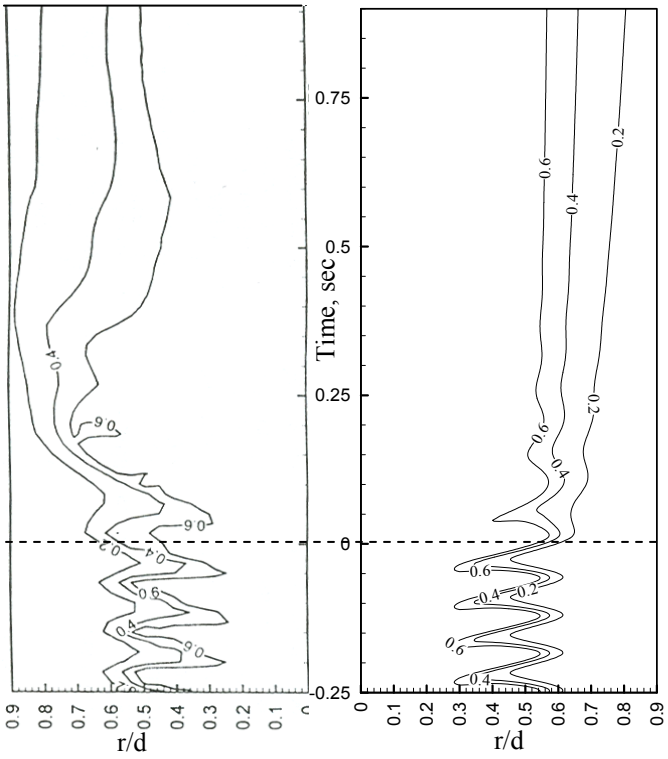
0.75
0.5
0.25
0
-0.25
Time, sec
0.9 0.8 0.7 0.6 0.5 0.4 0.3 0.2 0.1
r/d
0 0.1 0.2 0.3 0.4 0.5 0.6 0.7 0.8 0.9
r/d

(a) ***(b)***

Fig. 4, AIAA

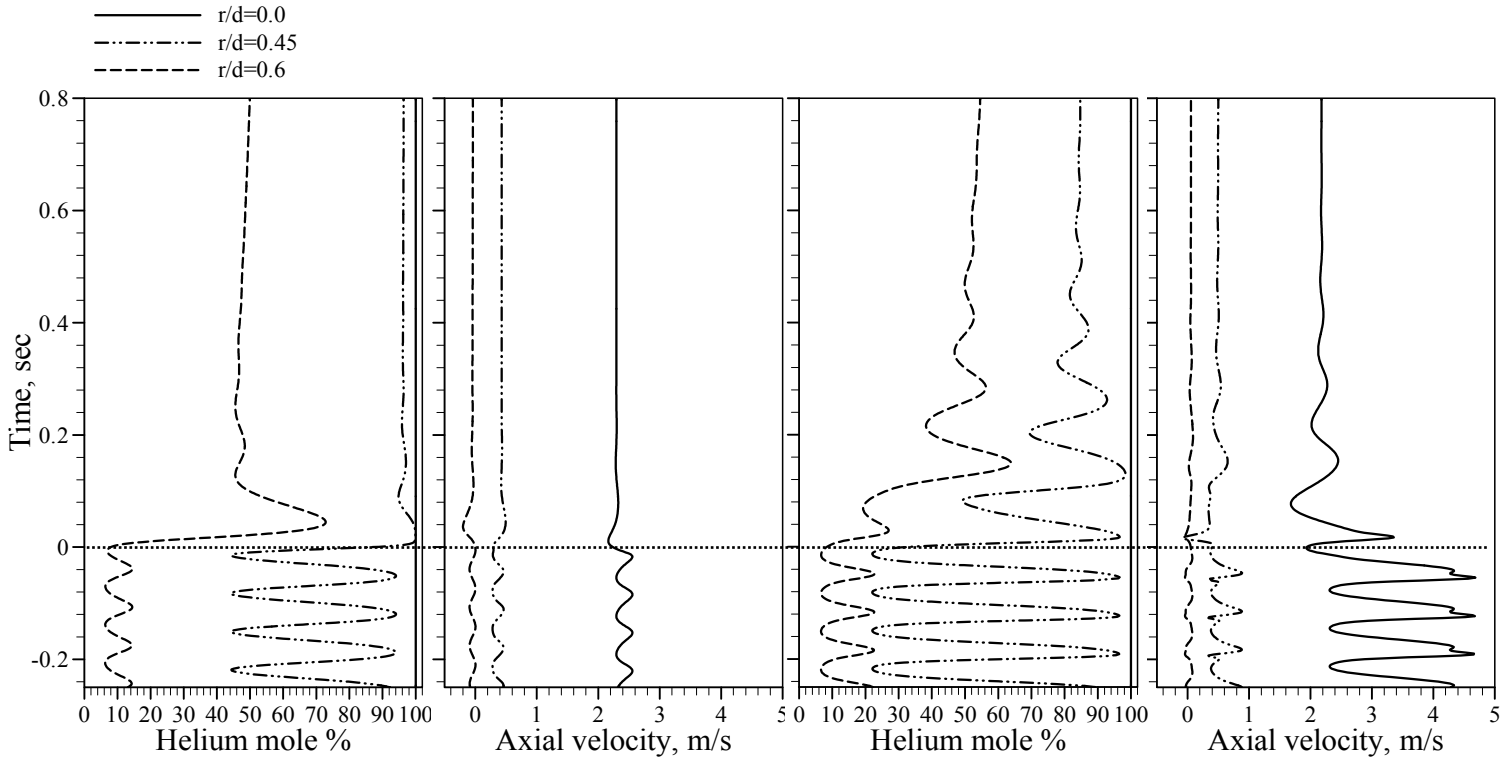

1 (a) **2 (a)** **1 (b)** **2 (b)**

Fig. 5, AIAA

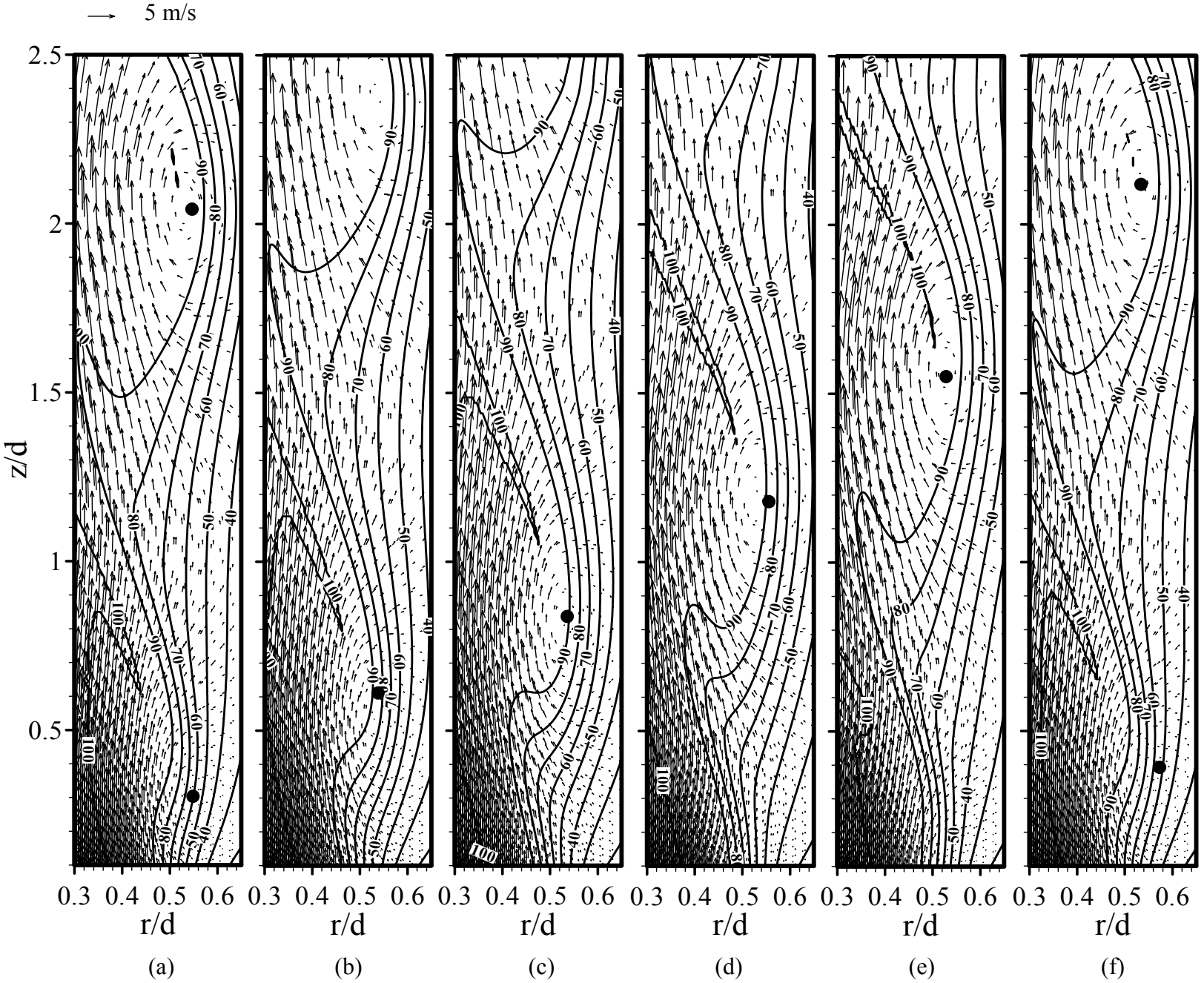

Fig. 6, AIAA

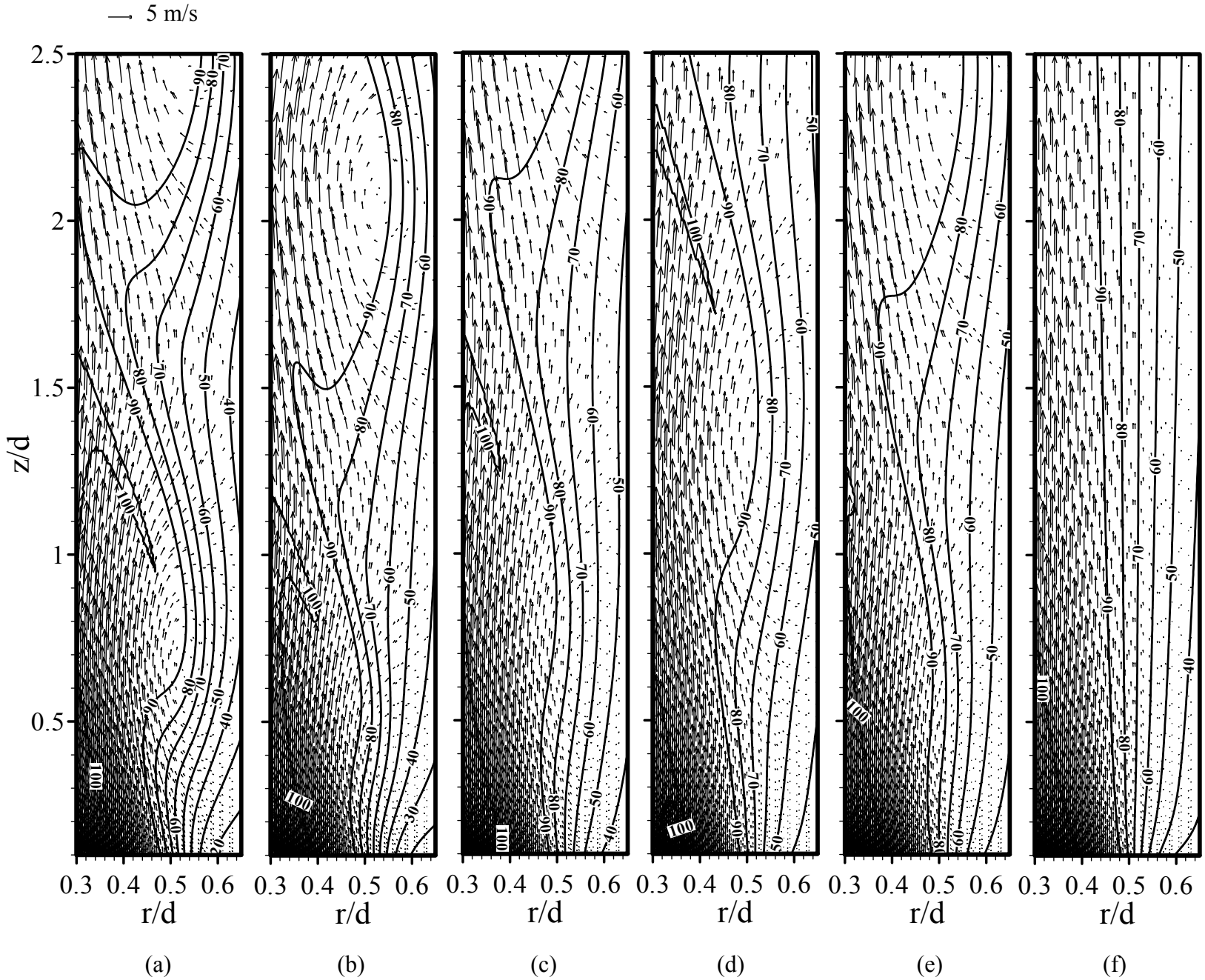

Fig. 7, AIAA

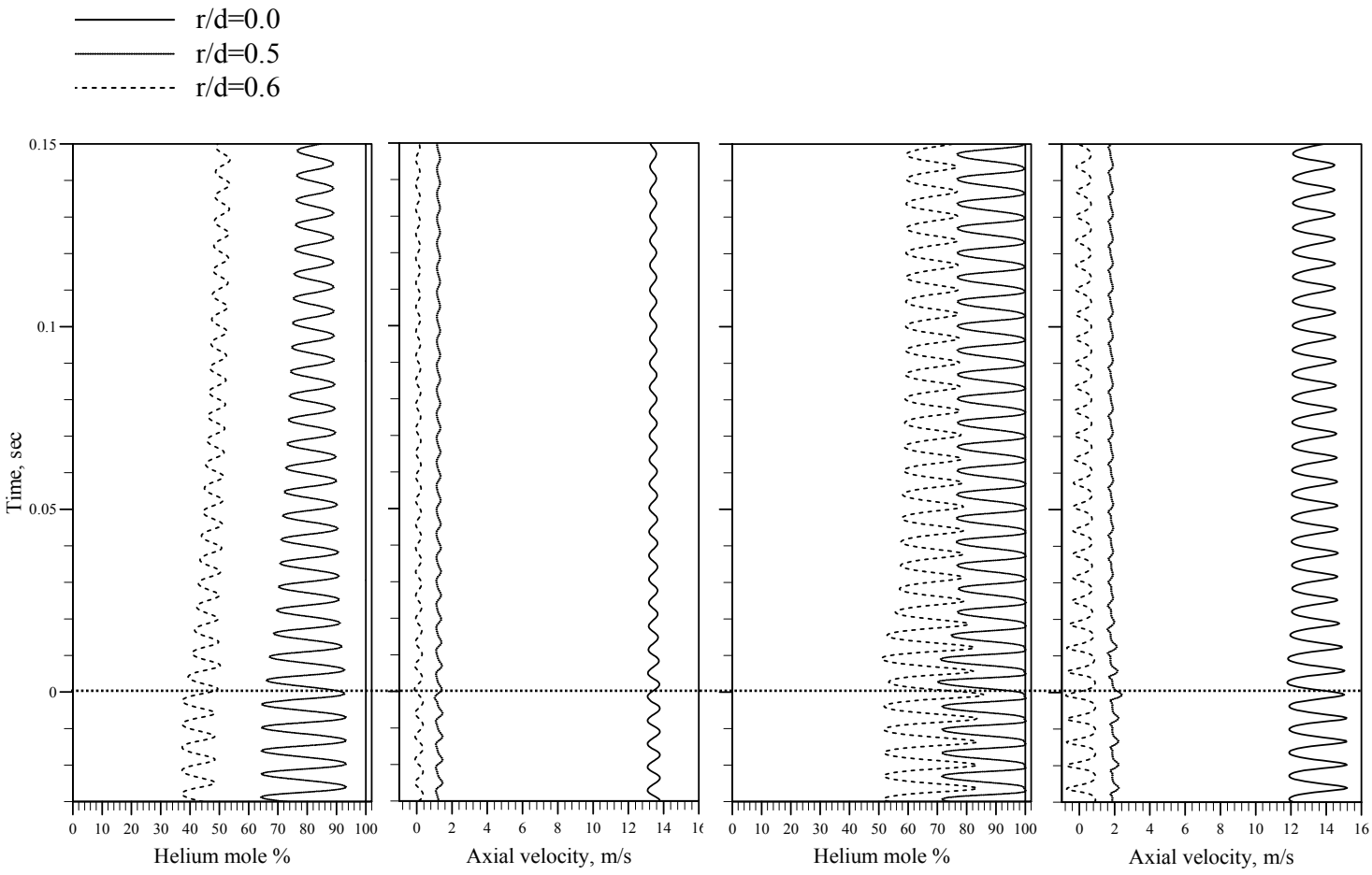

1 (a) **2 (a)** **1 (b)** **2 (b)**

Fig. 8, AIAA

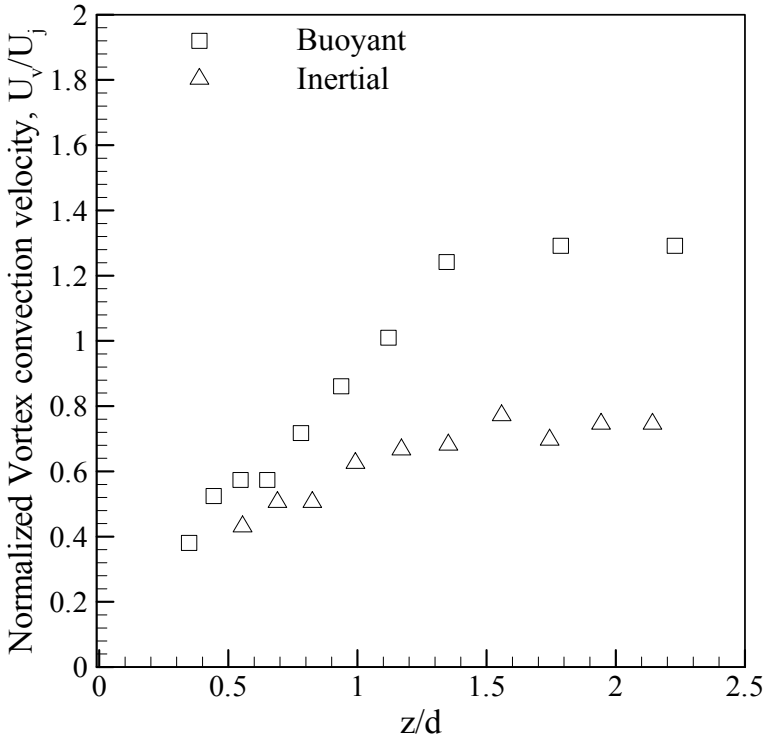
Buoyant
Inertial
Normalized Vortex convection velocity, U_v/U_j
z/d
0
0.2
0.4
0.6
0.8
1
1.2
1.4
1.6
1.8
2
0
0.5
1
1.5
2
2.5

Fig. 9, AIAA

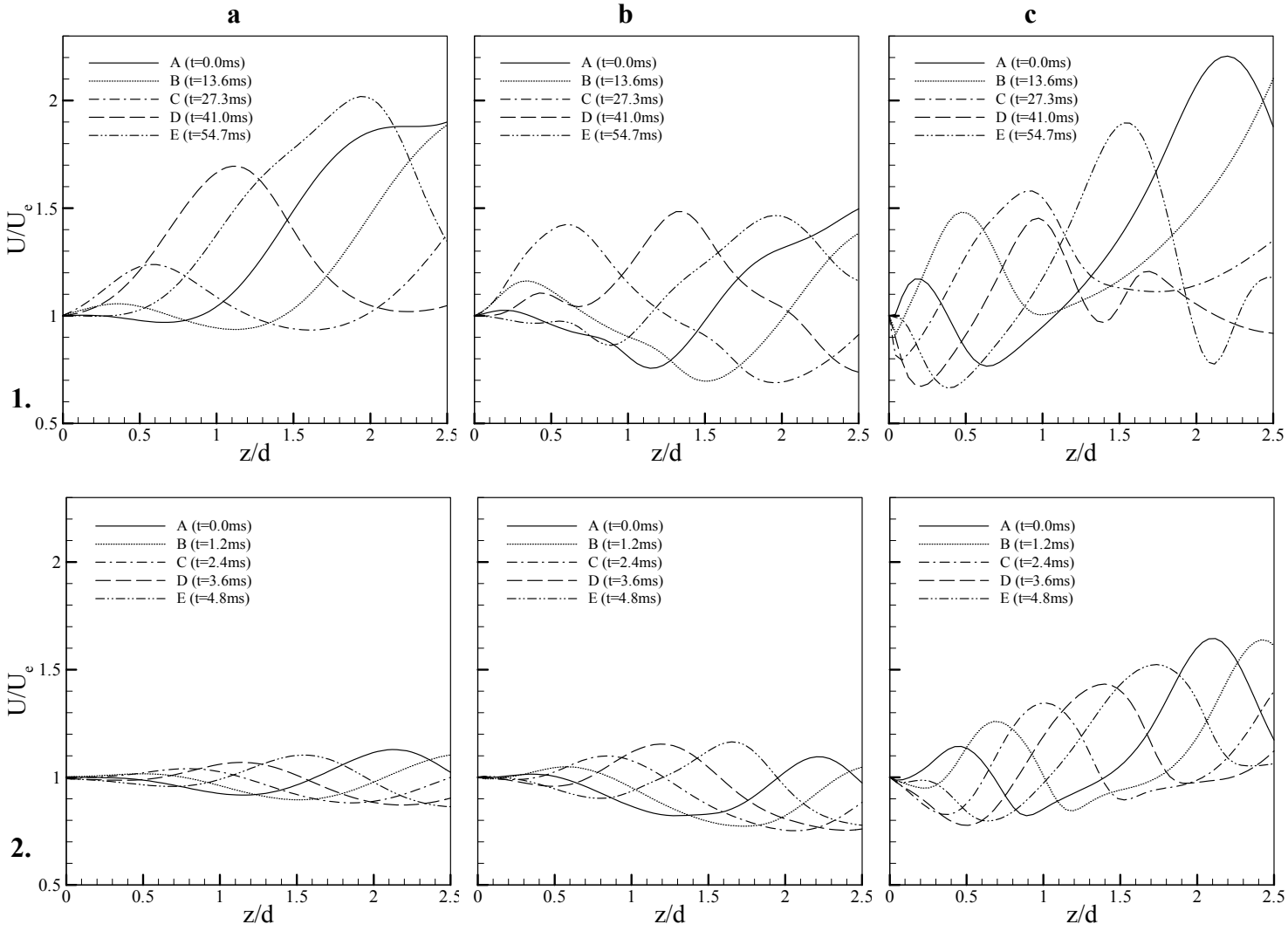
a
b
c
A (t=0.0ms)
B (t=13.6ms)
C (t=27.3ms)
D (t=41.0ms)
E (t=54.7ms)
U/U_e
z/d
1.
A (t=0.0ms)
B (t=1.2ms)
C (t=2.4ms)
D (t=3.6ms)
E (t=4.8ms)
U/U_e
z/d
2.

Fig.10, AIAA

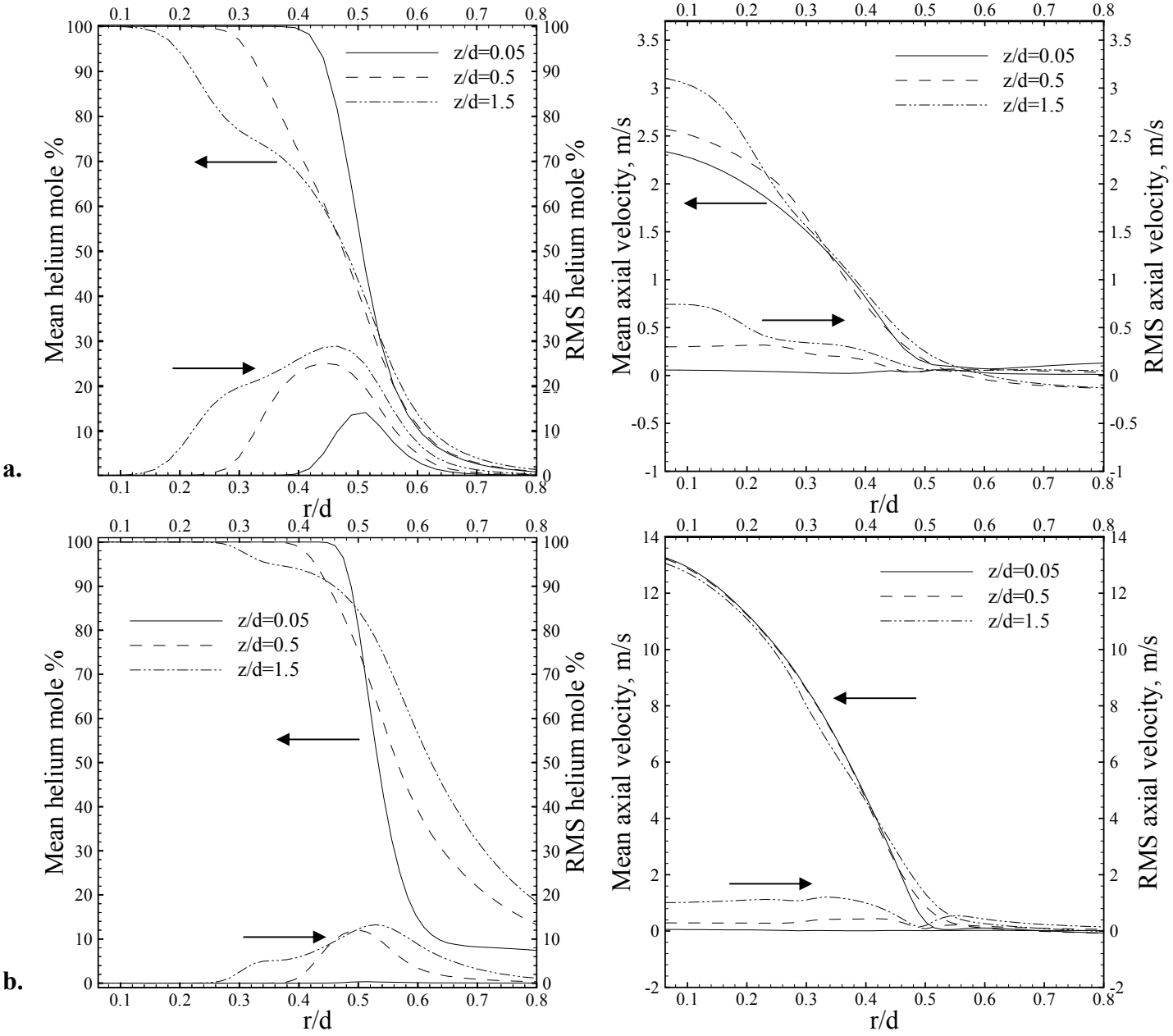
a.
b.
Mean helium mole %
RMS helium mole %
Mean axial velocity, m/s
RMS axial velocity, m/s
r/d
z/d=0.05
z/d=0.5
z/d=1.5

Fig.11, AIAA

a.

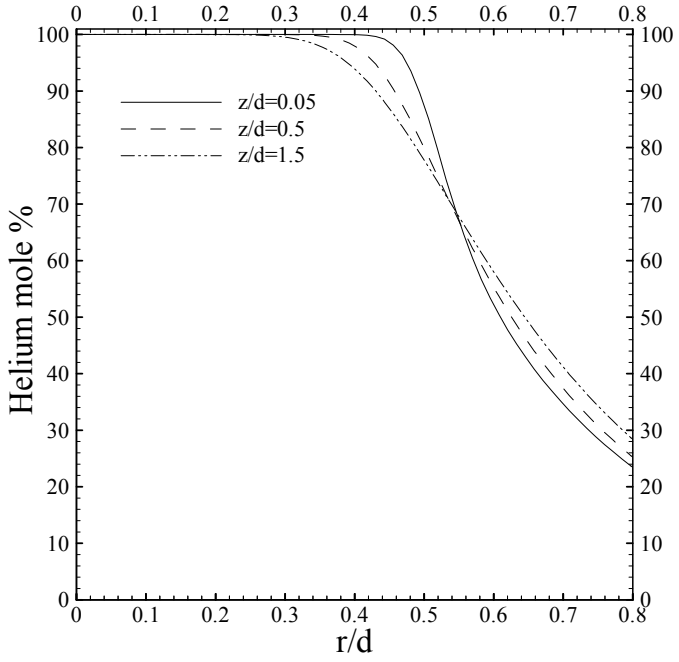

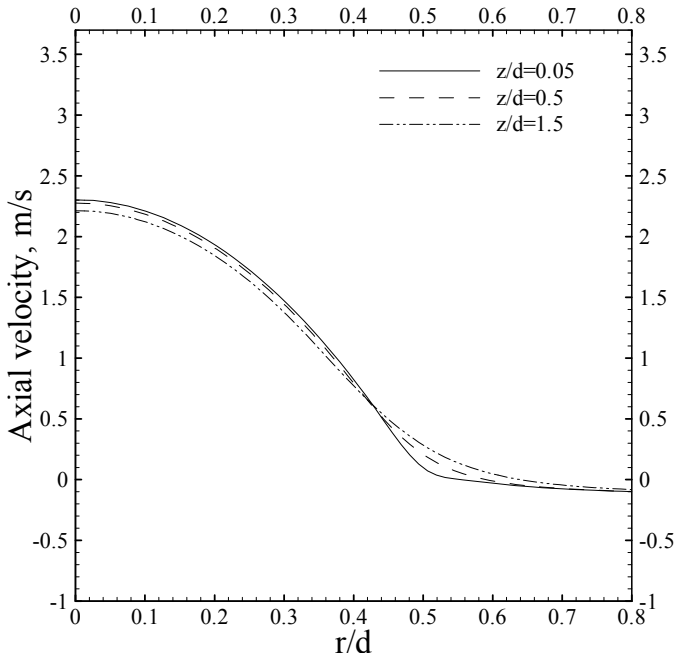

b.

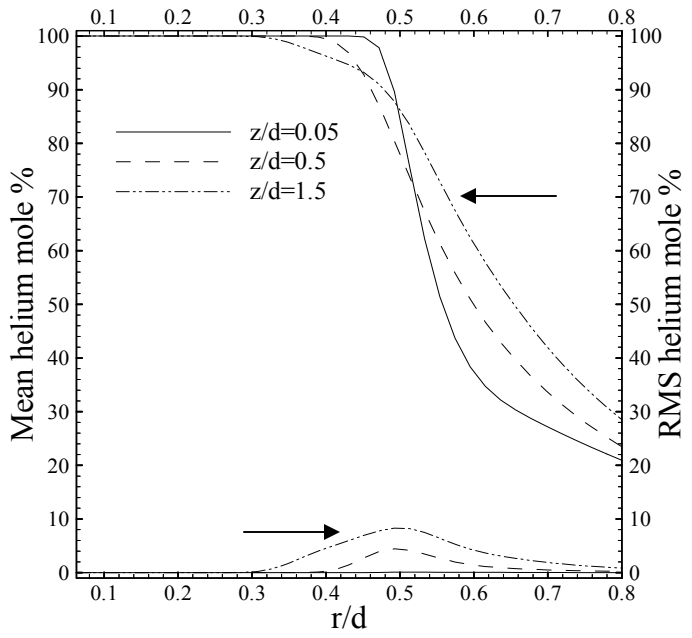

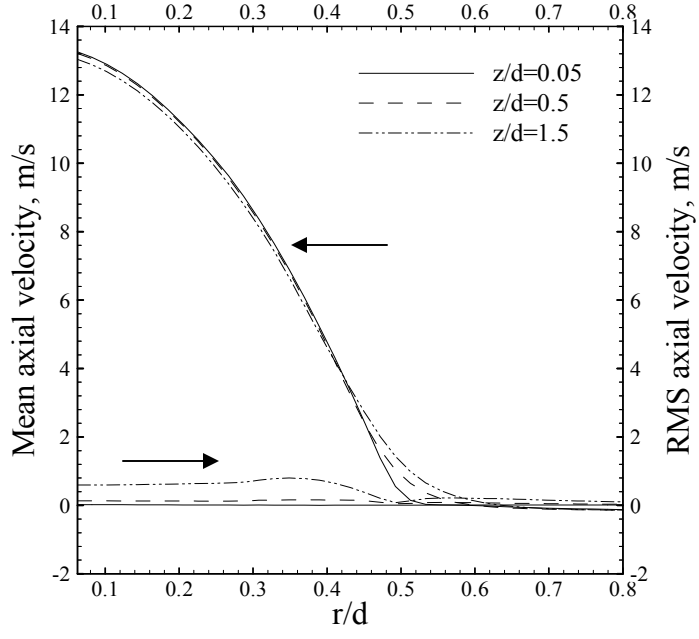

Fig. 12, AIAA

LINEAR STABILITY ANALYSIS OF GRAVITATIONAL EEFFECTS ON A LOW-DENSITY GAS JET INJECTED INTO A HIGH-DENSITY MEDIUM

Anthony L. Lawson and Ramkumar N. Parthasarathy

School of Aerospace and Mechanical Engineering

The University of Oklahoma

Norman, Oklahoma 73019

rparthasarathy@ou.edu

ABSTRACT

The objective of this study was to determine the effects of buoyancy on the absolute instability of low-density gas jets injected into high-density gas mediums. Most of the existing analyses of low-density gas jets injected into a high-density ambient have been carried out neglecting effects of gravity. In order to investigate the influence of gravity on the near-injector development of the flow, a spatio-temporal stability analysis of a low-density round jet injected into a high-density ambient gas was performed. The flow was assumed to be isothermal and locally parallel; viscous and diffusive effects were ignored. The variables were represented as the sum of the mean value and a normal-mode small disturbance. An ordinary differential equation governing the amplitude of the pressure disturbance was derived. The velocity and density profiles in the shear layer, and the Froude number (signifying the effects of gravity) were the three important parameters in this equation. Together with the boundary conditions, an eigenvalue problem was formulated. Assuming that the velocity and density profiles in the shear layer to be represented by hyperbolic tangent functions, the eigenvalue problem was solved for various values of Froude number. The Briggs-Bers criterion was combined with the spatio-temporal stability analysis to determine the nature of the absolute instability of the jet – whether absolutely or convectively unstable. The roles of the density ratio, Froude number, Schmidt number, and the lateral shift between the density and velocity profiles on the absolute instability of the jet were determined. Comparisons of the results with previous experimental studies show good agreement when the effects of these variables are combined together. Thus, the combination of these variables determines how absolutely unstable the jet will be.

NOMENCLATURE

English Symbols

C_1 constant of integration of equation (15)

C_2 constant of integration of equation (16)

d nozzle diameter in Cetegen (1997-2)

D jet diameter

D_b binary diffusivity coefficient

Fr Froude number; $Fr^2 = \dfrac{U_j^2}{gR}\dfrac{\rho_j}{\left(\rho_\infty - \rho_j\right)}$

g acceleration due to gravity

G non-dimensional coefficient of the buoyancy term in the pressure disturbance equation; $G = \dfrac{1}{Fr^2 \dfrac{R}{\theta}\left(\dfrac{\rho_\infty}{\rho_j} - 1\right)}$

i $\sqrt{-1}$

k wavenumber

Δk step-size of the real and imaginary parts of the wavenumber

m azimuthal wavenumber

N parameter that controlled the jet mixing layer thickness in Monkewitz and Sohn (1988)

P Prandtl number

p pressure

r radial coordinate

r_o low-density jet exit radius

Δr lateral shift between the inflexion points of velocity and density profiles

R radius of the jet shear layer

R_e radius of the jet exit

Ri Richardson number; $Ri = \frac{gD}{U_j^2}\frac{\left(\rho_\infty - \rho_j\right)}{\rho_j}$

Ri_1 Richardson number; $Ri_1 = \frac{\rho_j}{\rho_\infty} Ri$

S Density ratio

Sc Schmidt number; $Sc = \frac{\upsilon}{D_b}$

t time

T temperature

u jet axial velocity component

U jet base velocity

U_c jet base centerline velocity

v jet radial velocity component

w jet azimuthal velocity component

x axial coordinate

Y_j local mass fraction of injected gas

Greek Symbols

δ_{ij} Kronecker delta

∇ del operator

ϕ azimuthal coordinate

λ wavelength

Λ velocity ratio in Monkewitz and Sohn (1988); $\Lambda = \dfrac{U_j - U_\infty}{U_j + U_\infty}$

μ fluid viscosity

υ fluid kinematic viscosity

ρ fluid mass density

ρ_j fluid mass density of low-density gas

ρ_∞ fluid mass density of high-density ambient gas

θ shear layer momentum thickness

Ω angular frequency

Superscripts

( )' fluctuations

($\bar{}$) averaged variable

(^) amplitude of variable

(˜) dimensional variable

Subscripts

∞ ambient gas property

j low-density gas property

1. Introduction

Plumes of diffusion flames, fuel leaks, engine and industry exhaust, propulsion in space, materials processing, and natural phenomena such as fires and volcanic eruptions are a few examples of low-density gas jets injected into higher density ambient gases encountered in many engineering and technical applications. A number of experimental studies[1-4] indicate that at certain conditions, low-density gas jets injected into high-density gases may sustain an absolute instability leading to highly periodic oscillations. A similar phenomenon is observed in the flickering of diffusion flames that is attributed to buoyancy[5,6]. Recent experimental studies in drop-towers[7,8] also indicate that the observed periodic oscillations vanish when effects of gravity are removed. This served as the motivation for the present investigation to study the influence of gravity on the disturbances in the near-injector region of low-density jets. This study aims to highlight and improve our understanding of the nature of flow instability in low-density round gas jets injected into high-density gases.

Round jets with homogeneous shear layers have been studied extensively in the past. The near-injector region of a round jet, as influenced by disturbances, has a direct influence on the flow development in the far-field of the jet. Several authors[9-11] have shown that linear stability analysis models the large-scale structures of the near-injector region well. Batchelor and Gill[12] studied the stability of steady unbounded axisymmetric single-phase jet flows of the wake-jet type with nearly parallel streamlines and obtained the critical Reynolds number of the jet. Mollo-Christensen[13] and Crow and Champagne[14] found that the near-injector large-scale structure of jet turbulence was well

modeled by linear stability theory. Gaster et al.[15] applied the inviscid stability theory to model the large-scale vortex structures that occurred in a forced mixing layer. The comparison between experimental data and computational models showed that the agreement in both amplitude and phase velocity of the disturbances across the various sections of the flow was excellent on a purely local basis. Michalke[16] reviewed early studies of jet instability. These studies were carried out to understand the transition from laminar flow to turbulence and to describe the evolution of the large-scale coherent structures in the near-injector field. The analysis was based on the locally parallel flow assumption and the neglect of fluid viscosity, heat conduction and dissipation, and gravitational effects. Small disturbances in the form of normal modes were introduced in the equations of motion and the equations were linearized. The critical Reynolds number denoting the transition from laminar to turbulent flow was found. Also, the streak line patterns obtained using the results of the linear stability analysis were in good agreement with the first-stage of the vortex rolling-up process that was observed experimentally in the near-injector field. Cohen and Wygnanski[17] concluded that the linear stability analysis was able to correctly predict the local distribution of amplitudes and phases in an axisymmetric jet that was excited by external means. The analysis was also capable of predicting the entire spectral distribution of velocity perturbations in an unexcited jet over a short distance in the streamwise direction.

Monkewitz and Sohn[18] re-examined the linear inviscid stability analysis of compressible heated axisymmetric jets with particular attention to the impulse response of the flow. Two different responses were identified based on the results. In one case, the flow was absolutely unstable, when a locally generated small disturbance grew

exponentially at the site of the disturbance and eventually affected the entire flow region. In the other case termed convective instability, the disturbance was convected downstream leaving the mean flow undisturbed. It was shown that heated (low-density) jets injected into ambient gas of high density developed an absolute instability and became self-excited when the jet density was less than 0.72 times the ambient gas density. The critical density ratio (demarcating absolute and convective stability) was much lower, about 0.35, for the first azimuthal wavenumber mode than that for the axisymmetric wavenumber mode. This indicated the dominance of the axisymmetric mode during jet instability for high-density ratios. Yu and Monkewitz[19] carried out a similar analysis for two-dimensional inertial jets and wakes with non-uniform density and axial velocity profiles. Again, gravitational effects were neglected and the flow was assumed to be locally parallel. It was found that the absolute frequencies and wavenumbers of small disturbances in the near-injector region scaled with the jet/wake width and not on the thickness of the individual mixing layers, suggesting that the absolute instability was brought about by the interaction of the two mixing layers. Jendoubi and Strykowski[20] considered the stability of axisymmetric jets with external co-flow and counterflow using linear stability analysis. The boundaries between absolute and convective instability were distinguished for various parameters: jet-to-ambient velocity ratio, density ratio, jet Mach number, and the shear layer thickness in the absence of gravitational effects. Raynal et al.[21] carried out experiments with variable-density plane jets issuing into ambient air. A range of density ratios (0.14 to 1) and a range of Reynolds numbers based on the slot width and the jet fluid viscosity (250 to 3000) were studied. It was found that when the jet to ambient fluid density ratio was less

than 0.7, the jets exhibited self-excited oscillations. Theoretical results based on the analysis of Yu and Monkewitz[19] indicated the presence of absolute instability for density ratios less than 0.94 for plane jets, which was different from the value of 0.7 observed in experiments. Raynal et al.[21] attempted to explain this discrepancy by taking into account the differences in the location of the inflection points in the density and velocity profiles for the cases of heated jets injected into air and the isothermal helium-air jets injected into air.

Note that gravitational effects have been neglected in all of the analyses listed above. The neglect of gravitational effects has been justified by the authors because of the small magnitude of the Richardson number based on the jet velocity and jet diameter. However, within the shear layer where the density and velocity change from jet to ambient values, the gravitational effects may not be negligible. The present study extends the work of Michalke and Hermann[22]to consider the effects of gravity on the instability of a low-density gas injected into a high-density ambient. The specific objectives of the study were:

(a) to determine the effects of buoyancy on the absolute stability of low-density round jets injected into high-density ambient gases by performing a linear spatio-temporal stability analysis; and

(b) to determine the nature of the instabilities, whether absolute or convective, and to demarcate the boundary separating the two modes of instability.

2. Theory

A round low-density gas jet (radius R and density ρ_j) is discharged into a high-density ambient gas medium (density ρ_∞) at atmospheric pressure. The basic jet flow is assumed to be a locally inviscid parallel flow with an axial velocity component varying radially. The flow is assumed to be isothermal to simplify the analysis. The radial velocity of the jet is considered small and, therefore, neglected. This corresponds to the "locally-parallel" assumption normally used in the linear stability analysis.

Representing the velocity components by $(\tilde{u},\tilde{v},\tilde{w})$, in cylindrical coordinates $(\tilde{x},\tilde{r},\phi)$ centered at the origin of the jet, the conservation equations governing the flow are :

$$\frac{\partial\tilde{\rho}}{\partial t}+\frac{\partial(\tilde{\rho}\tilde{u})}{\partial\tilde{x}}+\frac{1}{\tilde{r}}\frac{\partial(\tilde{r}\tilde{\rho}\tilde{v})}{\partial\tilde{r}}+\frac{1}{\tilde{r}}\frac{\partial(\tilde{\rho}\tilde{w})}{\partial\phi}=0 \qquad (1)$$

$$\tilde{\rho}\left[\frac{\partial\vec{v}}{\partial t}+\vec{v}\bullet\nabla\vec{v}\right]=-\nabla p+g(\rho_\infty-\tilde{\rho})\delta_{i1}+\nabla\bullet(\mu\nabla\vec{u}) \qquad (2)$$

where g is the acceleration due to gravity and δ_{i1} is the Kronecker delta function with i = 1 representing the axial direction. The binary mass diffusion equation for the diffusion of the injected gas in the ambient gas medium is given in terms of the local mass fraction of the injected gas[23]:

$$\tilde{\rho}\left[\frac{\partial Y_j}{\partial t}+\vec{v}\bullet\nabla Y_j\right]=\nabla\bullet\left[\tilde{\rho}D_b\nabla Y_j\right] \qquad (3$$

In the linear stability analysis, the variables are represented as the sum of the base state value and a fluctuation. Substitution of these variables into equations (1) and (2), linearization, and the neglect of viscous and diffusive terms, yields

$$\frac{\partial \rho'}{\partial t} + \bar{u}\frac{\partial \rho'}{\partial \tilde{x}} + \bar{\rho}\frac{\partial u'}{\partial \tilde{x}} + \frac{1}{\tilde{r}}\frac{\partial\left(\tilde{r}\bar{\rho}v'\right)}{\partial \tilde{r}} + \frac{\bar{\rho}}{\tilde{r}}\frac{\partial w'}{\partial \phi} = 0 \tag{5}$$

$$\bar{\rho}\left[\frac{\partial u'}{\partial t} + \bar{u}\frac{\partial u'}{\partial \tilde{x}} + v'\frac{d\bar{u}}{d\tilde{r}}\right] = -\frac{\partial p'}{\partial \tilde{x}} - g\rho' \tag{6}$$

$$\bar{\rho}\left[\frac{\partial v'}{\partial t} + \bar{u}\frac{\partial v'}{\partial \tilde{x}}\right] = -\frac{\partial p'}{\partial \tilde{r}} \tag{7}$$

$$\bar{\rho}\left[\frac{\partial w'}{\partial t} + \bar{u}\frac{\partial w'}{\partial \tilde{x}}\right] = -\frac{1}{\tilde{r}}\frac{\partial p'}{\partial \phi} \tag{8}$$

The density of the mixture is related to the mass fraction by

$$\tilde{\rho} = \frac{\rho_j}{Y_j + \left(1 - Y_j\right)S} \tag{9}$$

Substituting for Y_j in equation (3), linearizing and neglecting the diffusive term, we obtain

$$\frac{\partial \rho'}{\partial t} + \bar{u}\frac{\partial \rho'}{\partial \tilde{x}} + v'\frac{d\bar{\rho}}{d\tilde{r}} = 0 \tag{10}$$

Using equation (10), equation (5) reduces to

$$\bar{\rho}\left[\frac{\partial u'}{\partial \tilde{x}} + \frac{1}{\tilde{r}}\frac{\partial\left(\tilde{r}v'\right)}{\partial \tilde{x}} + \frac{1}{\tilde{r}}\frac{dw'}{d\phi}\right] = 0 \tag{11}$$

The fluctuations are assumed to be normal mode disturbances given by

$$\left(u', v', w', p', \rho'\right) = \left[\hat{u}\left(\tilde{r}\right), \hat{v}\left(\tilde{r}\right), \hat{w}\left(\tilde{r}\right), \hat{p}\left(\tilde{r}\right), \hat{\rho}\left(\tilde{r}\right)\right]e^{i\left(\tilde{k}\tilde{x} - \tilde{\Omega}t + m\phi\right)} \tag{12}$$

Substituting the expressions (12) in equations (6), (7), (8), (9) and (10), we obtain the pressure disturbance equation:

$$\frac{d^2\hat{p}}{d\tilde{r}^2}+\left[\frac{1}{\tilde{r}}-\frac{2\dfrac{d\bar{u}}{d\tilde{r}}}{\bar{u}-\dfrac{\tilde{\Omega}}{\tilde{k}}}-\frac{1}{\bar{\rho}}\frac{d\bar{\rho}}{d\tilde{r}}\left(1+\frac{ig}{\tilde{k}\left(\bar{u}-\dfrac{\tilde{\Omega}}{\tilde{k}}\right)^2}\right)\right]\frac{d\hat{p}}{d\tilde{r}}-\left(\tilde{k}^2+\frac{m^2}{\tilde{r}^2}\right)\hat{p}=0 \quad (13)$$

Nondimensionalizing equation (12) using ρ_∞, U_j, and θ (the momentum thickness of the jet boundary layer); and setting m = 0 gives the nondimensionalized pressure disturbance equation - for the varicose mode:

$$\frac{d^2P}{dr^2}+\left[\frac{1}{r}-\frac{2\dfrac{dU}{dr}}{U-\dfrac{\Omega}{k}}-\frac{1}{\rho}\frac{d\rho}{dr}\left(1+i\frac{1}{Fr^2\dfrac{R}{\theta}\left(\dfrac{\rho_\infty}{\rho_j}-1\right)k\left(U-\dfrac{\Omega}{k}\right)^2}\right)\right]\frac{dP}{dr}-k^2P=0 \quad (14)$$

With no density gradient equation (14) reduces to the equation governing the instability of constant-density jets[22]. Also, as $r\to\infty$, and if gravitational effects are neglected, equation (14) is identical to the equation used by Yu and Monkewitz[19] and Raynal et al.[21] in the analysis of plane jets. Inclusion of buoyancy effects indicates that the stability characteristics are altered by the additional term present in equation (14). Thus, an eigenvalue problem is posed, for specified mean velocity and density profiles, by equation (14) along with the boundary conditions:

$$\begin{aligned} &P(\infty)\to 0 \\ &P(0) \text{ is finite} \\ &\frac{dP(0)}{dr}=0 \quad \text{due to symmetry} \end{aligned} \qquad (15)$$

As $r\to 0$ and $r\to\infty$, $\dfrac{dU}{dr}$ and $\dfrac{d\rho}{dr}$ equal zero and the pressure disturbance equation (13) reduces to the modified Bessel equation. The solutions of the modified Bessel equation satisfying the boundary conditions (14), as $r\to 0$ and $r\to\infty$, are

$$P^{(i)} = C_1 I_m\left(kr\right) \qquad P^{(o)} = C_2 K_m\left(kr\right) \tag{16}$$

respectively, where the superscripts *i* and *o* represent the inner and outer solutions respectively. I_m and K_m are the modified Bessel functions of the order m and C_1 and C_2 are arbitrary constants.

The basic jet velocity profile, $\bar{u}(r)$, is given by that used by Michalke and Hermann[22],

$$\frac{\bar{u}(\tilde{r})-U_\infty}{U_j-U_\infty} = 0.5\left\{1-\tanh\left[0.25\frac{R}{\theta}\left(\frac{\tilde{r}}{R}-\frac{R}{\tilde{r}}\right)\right]\right\} \tag{17}$$

where U_j is the injected jet uniform velocity and U_∞ is the uniform co-flow velocity. For this study the co-flow velocity was set to zero for a quiescent ambient gas and *R* is the radius of the jet defined as the radial location corresponding to the center of the shear layer. As shown by Crighton and Gaster[24],

$$\frac{R}{\theta} = \frac{100}{3\frac{\tilde{x}}{R}+4} \tag{18}$$

for no co-flow. The values of the jet parameter used in this study are 25, 10 and 5 corresponding to $\tilde{x}/(2R)$ = 0, 1 and 2.67. This is within the near-injector region of the jet and allows for the effects of buoyancy to manifest as the jet proceeds downstream. Figure 1 illustrates the basic jet velocity profiles at these three locations. The shear layer widens as the jet proceeds downstream from R/θ = 25 to R/θ = 5 indicating the downstream development of the jet. A hyperbolic tangent profile is also assumed for the basic density profile in the shear layer,

$$\frac{\bar{\rho}(r)}{\rho_\infty} = 1+\left(\frac{\rho_j}{\rho_\infty}-1\right)\left\{0.5\left(1-\tanh\left[0.25\frac{R}{\theta}\left(\frac{\tilde{r}}{R}-\frac{R}{\tilde{r}}\right)\right]\right)\right\} \tag{19}$$

Figure 2 illustrates the density profiles at R/θ = 10 for ρ_j/ρ_∞ = 1, 0.6, and 0.14.

The effects of buoyancy on the jet were studied by investigating the variation of the real and imaginary parts of both the complex wavenumber and frequency with the Froude number. The Froude number is the ratio of the inertia force to buoyancy force and is defined as

$$Fr^2 = \frac{U_j^2}{gR}\frac{\rho_j}{\rho_\infty - \rho_j} \tag{20}$$

To solve the disturbance equation (14), a fourth-order Runge-Kutta scheme with automatic step-size control is used to integrate the equation (14). The infinite integration domain, $0 < r < \infty$ is divided into two finite domains: an inner domain $R \geq r \geq 0$ and an outer domain $r_\infty \geq r \geq R$, where R is the jet radius and r_∞ is a specified large radius where the gradients of the velocity and density are small. A shooting method is used to determine $\Omega(k)$ such that both P and $\frac{dP}{dr}$ are continuous at $r = R$. A parabolic complex zero-search procedure was used to vary Ω for a specified k until the matching conditions were satisfied to a minimum accuracy within 10^{-10}.

For the spatio-temporal linear stability analysis, both the frequency and wavenumber are considered complex. The spatio-temporal linear stability along with the Briggs-Bers criterion[25, 26] was used to determine the absolute stability and the nature of the absolute stability of the jet. The jet is said to be absolutely unstable when the complex frequency eigenvalue is a saddle point and its imaginary part is greater than zero. If its imaginary part is less than zero, the jet is convectively unstable. Therefore, the saddle points in the complex (Ω, k) domain were determined and the satisfaction of the pinching requirements was verified using the mesh-searching technique described by Li and

Shen[27].

3. Results and Discussion

Preliminary calculations confirmed the conclusion of Monkewitz and Sohn[18] that the varicose mode (m = 0) is more absolutely unstable than the sinuous mode (m = 1) in the near-injector region of round jets. This is illustrated in Figure 3. Figure 3 depicts the variation of the absolute temporal growth rate Ω_i^o with density ratio of an inviscid top-hat jet bounded by a cylindrical vortex sheet at m = 0 and m = 1. At all density ratios studied, Ω_i^o values are higher for the varicose mode than for the sinuous mode. Also, the density ratio at which Ω_i^o first becomes positive, as density ratio is reduced, is higher for the varicose mode (at a density ratio of 0.66) than for the sinuous mode (at a density ratio of 0.35). Therefore, the following results on the instability of a low-density round gas jet injected into a high-density ambient gas concentrate on the varicose mode (m = 0).

Results of the temporal stability analysis of low-density jets injected into a high-density ambient gas were first carried out[28]. A non-dimensional parameter, G, was found to play an important role in the temporal instability:

$$G = \frac{1}{Fr^2 \frac{R}{\theta}\left(\frac{\rho_\infty}{\rho_j} - 1\right)} \qquad (21)$$

G is a non-dimensional number that compares the acceleration of the large-scale structures of the jet due to buoyancy to that due to inertial forces. It was found that the effect of buoyancy at low Fr values was to cause the jet instabilities to increase exponentially.

The focus of this paper is the effects of the inhomogeneous shear-layer and buoyancy on the nature of the absolute instability. This was done by first studying the effect of varying the density ratio from 0.99 to 0.14, while varying the Froude number from infinity to 0.5. The complex frequency Ω and the complex wavenumber k are normalized in the present results using the shear-layer momentum thickness θ and the velocity difference $\Delta U = U_j - U_\infty$. First, the present results were compared with those of Monkewitz and Sohn[19] and a favorable agreement was obtained[28].

Effect of density ratio

The imaginary part Ω_i^o of the complex absolute frequency, in this study, denotes the absolute temporal growth rate of the disturbances. When Ω_i^o is positive (and the Briggs-Bers criterion is satisfied) the jet is absolutely unstable while for a negative Ω_i^o the jet may be convectively unstable. A constant-density jet (such as an air-in-air jet) is convectively unstable; as the density ratio is reduced (a low-density jet injected into a high-density gas medium), the nature of instability of the jet is changed from convective instability to absolute instability. This density ratio, at which the jet first becomes absolutely unstable, is referred to as the critical density ratio (S_c). In Figure 3, for example, this is the density ratio at which $\Omega_i^o = 0$. The real part Ω_r^o of the absolute complex frequency is the frequency corresponding to the absolute temporal growth rate of the disturbance. The imaginary part k_i^o of the complex wavenumber is the absolute spatial growth rate of the disturbances. Figure 4 depicts the variation of the absolute temporal growth rate of the disturbances with the density ratio at $R/\theta = 10$ and 5 with Froude number fixed at infinity (no buoyancy effects). At $R/\theta = 10$, the growth rate is increased by about 201%, as the density ratio is reduced from 0.99 to 0.14 . The critical

density ratio, S_c, at this location is 0.525. The absolute growth rates of the jet disturbance are positive for density ratios below 0.525 indicating that the jet is absolutely unstable. However, for density ratios above 0.525 the absolute growth rates are negative meaning the jet is convectively unstable.

As the jet proceeds downstream from an axial location corresponding to $R/\theta = 10$ to $R/\theta = 5$, the absolute temporal growth rates decrease for all density ratios. The absolute temporal growth rates are decreased by about 76% at a density ratio of 0.14 and by about 316% at a density ratio of 0.99 (the other extreme of the range of density ratios studied). The percentage decrease in the growth rates for density ratios between 0.14 and 0.99 is increased from 76% to 316%. Trends similar to those observed at $R/\theta = 10$ for the growth rates are also observed at $R/\theta = 5$, but the critical density ratio is decreased to 0.17. Figure 4 illustrates the change in critical density ratio as the jet proceeds from $R/\theta = 10$ to $R/\theta = 5$.

The variation of the real part of the absolute frequency Ω_r^o as the density ratio is increased from 0.14 to 0.99 for $R/\theta = 10$ and 5 is illustrated in Figure 5. At $R/\theta = 10$ and 5, Ω_r^o is increased by about 107% and 62%, respectively, as the density ratio increased from 0.14 to 0.99. Ω_r^o is increased as the flow proceeds from $R/\theta = 10$ to 5 at all density ratios. At extremes of the range of density ratios investigated (0.14 and 0.99) Ω_r^o is increased by about 83% and 43%, respectively, as the flow proceeds from $R/\theta = 10$ to 5.

The absolute spatial growth rates $-k_i^o$ are plotted against density ratio for $R/\theta = 10$ and 5 in Figure 6. At $R/\theta = 10$, the absolute spatial growth rate is increased by about 76% as the density ratio is increased from 0.14 to 0.99. At $R/\theta = 5$, the absolute spatial growth

rate is increased by about 71% as the density ratio is increased from 0.14 to 0.99. And, as the jet proceeds downstream from $R/\theta = 10$ to $R/\theta = 5$, the absolute spatial growth rates are increased by about 65% at density ratio = 0.14 and by about 60% at density ratio = 0.99.

Figure 7 illustrates the variation of the real part of the absolute wavenumber k_r^o as the density ratio is increased from 0.14 to 0.99 for R/θ values of 10 and 5. At $R/\theta = 10$, k_r^o is increased by about 47% as the density ratio is increased from 0.14 to 0.99 while at $R/\theta = 5$, k_r^o is increased by about 27% as the density ratio is increased from 0.14 to 0.99. And, as the jet proceeds from $R/\theta = 10$ to $R/\theta = 5$, k_r^o is increased by about 70% and 47% at density ratios of 0.14 and 0.99 respectively.

The above trends of the real and imaginary parts of the saddle points (Ω^o, k^o) are similar to those presented by Monkewitz and Sohn[19] in their study on the absolute instability of hot jets at an axial location of $x/R = 2$ ($R/\theta = 10$), with buoyancy effects neglected. Next, buoyancy effects are introduced and the influence of buoyancy on the jet instability is discussed.

Effect of buoyancy

Figures 8 and 9 illustrate the variation of the absolute temporal growth rate of the disturbances with the density ratio for several Froude numbers at $R/\theta = 10$ and 5 respectively. At both $R/\theta = 10$ and 5, as the Froude number is reduced from infinity the absolute temporal growth rate varies with the density ratio only, but below a Froude number of 2 the absolute temporal growth rate varies with both the density ratio and Froude number. For $R/\theta = 10$, the absolute temporal growth rate is increased as the

density ratio is reduced for large Froude numbers. As the density ratio is reduced from 0.14 to 0.99, the absolute temporal growth rate is increased by about 200% at Fr = ∞ and 10. At Fr = 5, the absolute temporal growth rate is increased by about 188%. For Fr = 2, 1.58, and 1, the absolute temporal growth rates are enhanced by about 131%, 99%, and 20% respectively. Below a Froude number of unity, this trend is reversed.. At Fr = 0.75 and 0.5, the absolute temporal growth rates are increased by about 28% and 76% respectively, as the density ratio is increased from 0.14 to 0.99. The absolute temporal growth rates are higher at each density ratio as the Froude number alone is decreased below Fr = 5. For Fr ≥ 5, there is no significant change in the absolute temporal growth rates due to changes in the Froude number, indicating that the jet is momentum-driven at Fr ≥ 5 and that effects of buoyancy are small. At R/θ = 5, the trend is reversed at Froude numbers below 0.75 and the same trends observed at R/θ = 10 are observed at this downstream location also.

As noted earlier, the critical density ratio below which the jet is absolutely unstable for a given Froude number is of interest. Figures 10 and 11 depict the variation of the critical density ratio with Froude number at R/θ = 10 and 5 respectively. At R/θ = 10, at large Froude numbers, the critical density ratio tends to 0.525, and the “critical Froude number” below which the jet is absolutely unstable for all density ratios studied is 1.58. Thus, at density ratios less than 0.525 the jet is absolutely unstable at this location and for Fr < 1.58 any low-density gas jet injected into a high density ambient gas becomes absolutely unstable at R/θ = 10. For R/θ = 5, as the Froude number tends to a large value, the critical density ratio tends to 0.17 and the “critical Froude number” is

1.015. Thus the critical density ratio and critical Froude number appear to be functions of the shear layer width and thus the axial location downstream of the jet.

The real part of frequencies corresponding to the absolute temporal growth rates of the saddle points discussed above are depicted in Figures 12 and 13 for R/θ = 10 and 5 respectively. Note that the real part of the normalized frequency Ω_r^o might be interpreted as the Strouhal number expressed in terms of the shear-layer momentum thickness, θ and the velocity difference, $\Delta U = U_j - U_\infty$. At R/θ = 10, Ω_r^o is increased by about 105% at Fr ≥ 1.58 as the density ratio is increased from 0.14 to 0.99. Below the critical Fr = 1.58, at this axial location, Ω_r^o is increased by about 102%, 105%, and 112% at Fr = 1, 0.75 and 0.5 respectively as the density ratio is increased from 0.14 to 0.99. Above the critical Fr, Ω_r^o does not change significantly with Fr, although it is a function of density ratio; whereas, below the critical Fr at this location Ω_r^o depends on both the density ratio and Fr, suggesting that the critical Fr demarcates two jet flow regimes. For values less than the critical Fr, the flow is momentum-driven, while at values greater than the critical Fr the flow is within the buoyancy-driven regime. The same trends are noticed at the axial location corresponding to R/θ = 5, and again the dependence on Fr is noticed below the critical Fr, at this location, of 1.015.

From the discussions above it is clear that there is a critical Froude number, which depends on axial location, below which Ω_r^o exhibits a dependence on the Froude number. This is also the Froude number below which the flow is absolutely unstable for all density ratios studied.

Effect of co-flow

Figure 14 illustrates the effect of co-flow on the absolute temporal growth rates of the jet flow at $R/\theta = 10$ for $\rho_j/\rho_\infty = 0.14$ and Fr = ∞, 10, 5, 2, 1, 0.75 and 0.5. Results are presented for co-flow velocity ratios of $U_\infty/\Delta U = 0$, 0.5 (corresponding to $U_\infty = 0.33U_j$), and 1 (corresponding to $U_\infty = 0.5U_j$). As the co-flow is increased ($U_\infty/\Delta U$ is increased from 0 to 1), it is observed that the absolute temporal growth rates of the disturbances decrease linearly at each Fr. An increase in co-flow leads to a decrease in the magnitude of mean shear that serves as the driving force for the instability, thus, resulting in a decrease in the growth rates. As $U_\infty/\Delta U$ is increased from 0 to 1, at this axial location, the absolute growth rates are reduced by about 414% for Fr > 2, and about 359%, 257%, 204%, and 137% at Fr = 2, 1, 0.75 and 0.5 respectively. Though the effect of co-flow is felt less as Fr is decreased, it is obvious from Figure 14 that the presence of co-flow tends to make the previously absolutely unstable flow become convectively unstable. The variation of the real part of the complex absolute frequency Ω_r^o at the saddle points with co-flow is illustrated in Figure 15 for $\rho_j/\rho_\infty = 0.14$ and Fr = ∞, 10, 5, 2, 1, 0.75 and 0.5 at an axial location corresponding to $R/\theta = 10$. An increase in co-flow causes Ω_r^o to increase. As $U_\infty/\Delta U$ is increased from 0 to 1, Ω_r^o is increased by about 53% at all Fr. Note again the reducing effect of co-flow as Fr decreased below 10.

4. Conclusions

In this study, the absolute stability characteristics of a low-density round gas jet injected into a high-density ambient gas were investigated. A linear spatio-temporal stability analysis was performed to solve for eigenvalues of the pressure disturbance equation obtained from the simultaneous solution of the continuity equations and the equations of motion. The equation was solved numerically and a mesh-searching technique was used to determine the saddle points. The limits of the *k*-plane for the mesh-searching technique employed obtained from the results of a linear temporal analysis of a previous paper by the authors. The effects of buoyancy and density ratio on the absolute instability of the jet were investigated using the linear spatio-temporal stability analysis.

Reducing the density ratio steepens the density gradient in the shear layer causing additional disturbance. At a Froude number value of Fr = ∞, as the density ratio reduces, the low-density jet injected into a high-density gas medium becomes absolutely unstable at a critical density ratio of 0.525 and 0.17 at axial locations corresponding to R/θ = 10 and 5 respectively. Below this critical density ratio, reducing the density ratio further causes the jet to become more absolutely unstable. As the Froude number decreases to account for increasing effect of buoyancy, the critical density ratio of the jet increases. Thus, reducing the Froude number has the effect of causing the jet to become absolutely unstable at higher density ratios. At low Froude numbers, buoyancy causes the jet instabilities to increase exponentially which accounts for the abrupt breakdown of the jet large-scale structures observed in experiments at low Froude numbers. There is a critical Froude number below which the jet is absolutely unstable at all density ratios less than

unity. This critical Froude number also demarcates the jet flow into the momentum-driven regime and the buoyancy-driven regime similar to the experimentally-observed Strouhal number regimes. Increasing the co-flow velocity reduces the shear layer thickness and thus the energy available for the growth of the instabilities in the jet. Thus increasing co-flow velocity makes the jet less absolutely unstable. causes the jet to be less absolutely unstable. At lower Froude number values decreasing the relative radial location (negative lateral shift) of the density profile with respect to the velocity profile causes the jet to be more absolutely unstable.

Acknowledgments

This work was supported by a NASA Grant under the Microgravity Fluid Physics Program.

References

[1]Monkewitz, P. A., Bechert, D. W., Barsikow, B. and Lehmann, B. (1990) "Self-excited Oscillations and Mixing in a Heated Round Jet," *Journal of Fluid Mechanics*, Vol. 213, pp. 611-639.

[2]Subbarao, E. R. and Cantwell, B. J., (1992) "Investigation of a Co-Flowing Buoyant Jet: Experiments on the Effects of Reynolds Number and Richardson Number," *Journal of Fluid Mechanics*, Vol. 245, pp. 69-90.

[3]Kyle, D. M. and Sreenivasan, K. R., (1993) "The Instability and Breakdown of a Round Variable-Density Jet," *Journal of Fluid Mechanics*, Vol. 249, pp. 619-664.

[4]Cetegen, B. M. and Kasper, K. D., (1996) “Experiments on the Oscillatory Behavior of Buoyant Plumes of Helium and Helium-Air Mixtures,” *Physics of Fluids*, Vol. 8, No 11, pp. 2974-2984.

[5]Yep, T. W., Agrawal, A. K. and Griffin, D. V. (2003) “Gravitational Effects on Near Field Flow Structure of Low Density Gas Jets,” *AIAA Journal*, Vol. 41, No. 10, pp. 1973-1979.

[6]Pasumarthi, K. (2004) “Buoayncy Effects on Flow Structure and Instability of Low-Density Gas Jets,” *PhD Dissertation*, University of Oklahoma.

[7]Buckmaster, J. and Peters, N., (1986) “The Infinite Candle and its Stability – A Paradigm for Flickering Diffusion Flames,” *Twenty-First Symposium (International) on Combustion*, pp. 1829-1836.

[8]Chen, L. D., Seaba, J. P., Roquemore, W. M., and Goss, L. P. (1988) “Buoyant Diffusion Flames,” *Twenty-Second Symposium (International) on Combustion*, The Combustion Institute, pp. 677-684.

[9]Crow, S. C., (1972) “Acoustic Gain of a Turbulent Jet,” *Paper IE6, Annual Meeting of the Division of Fluid Dynamics of the American Physics Society, Boulder, CO, Nov. 20-22, 1972.*

[10]Moore, C. J., (1977) “The Role of Shear-Layer Instability Waves in Jet Exhaust Noise,” *Journal of Fluid Mechanics*, Vol. 80, Pt. 2, pp. 321-367.

[11]Ffowcs-Williams, J. E. and Kempton, A. J., (1978) “The Noise from the Large-Scale Structure of a Jet,” *Journal of Fluid Mechanics*, Vol. 84, Pt. 4, pp. 673-694.

[12]Batchelor, G. K. and Gill, A. E. (1962) "Analysis of the Stability of Axisymmetric Jets," *Journal of Fluid Mechanics*, Vol. 14, pp. 529-551.

[13]Mollo-Christensen, E. (1967) "Jet Noise and Shear Flow Instability seen from an Experimenter's Viewpoint," Trans. A.S.M.E. E, *Journal of Applied Mechanics*, Vol. 89, pp. 1-7.

[14]Crowe, S. C. and Champagne, F. H. (1971) "Orderly Structure in Jet Turbulence," *Journal of Fluid Mechanics*, Vol. 48, pp. 547-591.

[15]Gaster, M., Kit, E., and Wygnanski, I. (1985) "Large-scale Structures in a Forced Turbulent Mixing Layer," *Journal of Fluid Mechanics*, Vol. 150, pp. 23.

[16]Michalke, A. (1984) "Survey on Jet Instability Theory," *Progress in Aerospace Sciences*, Vol. 21, pp. 159-199.

[17]Cohen, J. and Wygnanski, I. (1987) "The Evolution of the Instabilities in the Axisymmetric Jet. Part 2. The Flow Resulting from the Interaction between Two Waves," *Journal of Fluid Mechanics*, Vol. 176, pp. 221.

[18]Monkewitz, P. A. and Sohn, K. D. (1988) "Absolute Instability in Hot Jets," *AIAA Journal*, Vol. 26, pp. 911-916.

[19]Yu, M.-H. and Monkewitz, P. A. (1990) "The Effect of NonUniform Density on the Absolute Instability of Two-Dimensional Inertial Jets and Wakes," *Physics of Fluids A*, Vol. 2, No. 7, pp. 1175-1181.

[20]Jendoubi, S. and Strykowski, (1994) "Absolute and Convective Instability of Axisymmetric Jets with External Flow," *Physics of Fluids*, Vol. 6, No. 9, pp. 3000-3009.

[21]Raynal, L., Harion, J.-L., Favre-Marinet, M. and Binder, G. (1996) "The Oscillatory Instability of Plane Variable-Density Jets," *Physics of Fluids*, Vol. 8, No. 4, pp. 993-1006.

[22]Michalke, A. and Hermann, G. (1982) “On the Inviscid Instability of a Circular Jet with External Flow,” *Journal of Fluid Mechanics*, Vol. 114, pp. 343-359.

[23]Gebhart, B. (1993) “Heat Conduction and Mass Diffusion,” *McGraw-Hill*, New York.

[24]Crighton, D. G. and Gaster, M. (1976) "Stability of Slowly Diverging Jet Flow" *Journal of Fluid Mechanics*, Vol. 77, pp. 397-413.

[25]Bers, A., (1983) “Space-time Evolution of Plasma Instabilities,” *Handbook of Plasma Physics*, Vol. I, pp. 452-517.

[26]Briggs, R. J., (1964) *Electron Stream Interaction with Plasmas*, MIT Press, Cambridge, Massachusetts.

[27]Li, X. and Shen, J. (1996) “Breakup of Cylinderical Liquid Jets in Co-Flowing Gas Streams,” *ASME*, pp. 22-31.

[28]Lawson, A. L. and Parthasarathy, R. N. (2002) “Linear Temporal Stability Analysis of a Low-Density Round Gas Jet Injected into a High-Density Gas,” *Paper ETCE 2002/CAE-29010, Proceedings of the ASME Engineering Technology Conference on Energy, Houston, TX, Feb. 4-6, 2002.*

[29]Lawson, A. L. (2001) “Instability Analysis of a Low-Density Gas Jet Injected into a High-Density Gas,” *PhD Dissertation*, University of Oklahoma.

LIST OF FIGURES

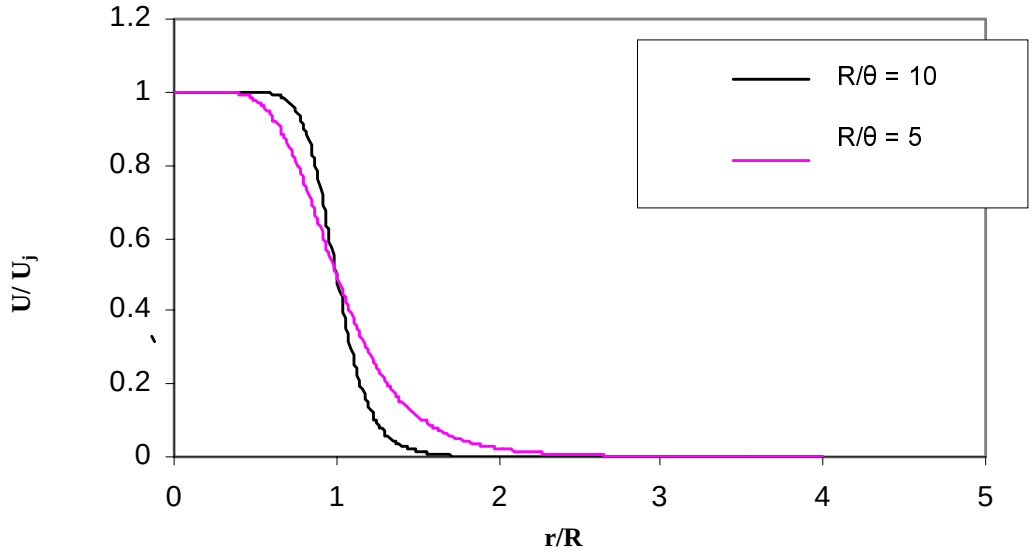
1.2
1
0.8
0.6
0.4
0.2
0
0
1
2
3
4
5
U/ U_j
r/R
R/θ = 10
R/θ = 5

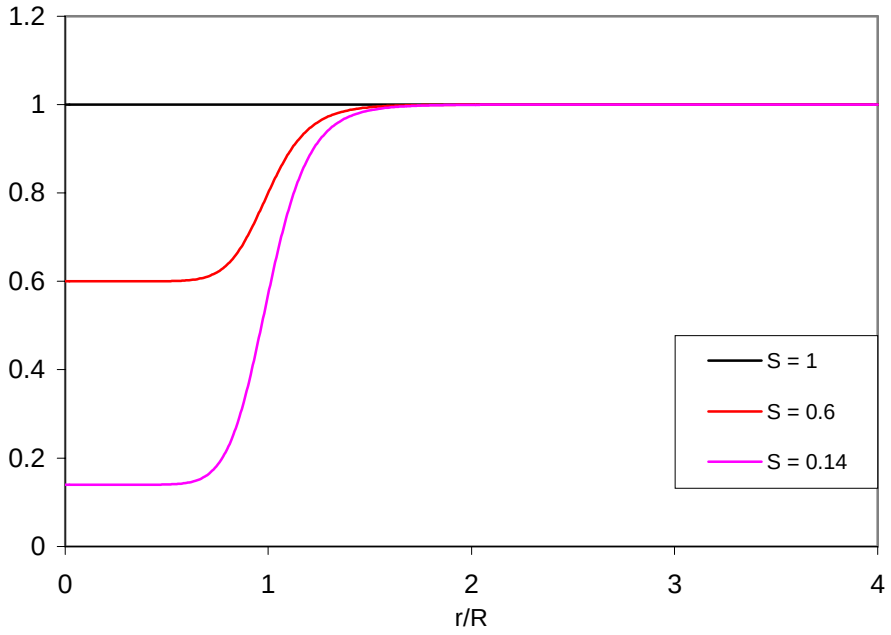
1.2
1
0.8
0.6
0.4
0.2
0
0
1
2
3
4
r/R
S = 1
S = 0.6
S = 0.14

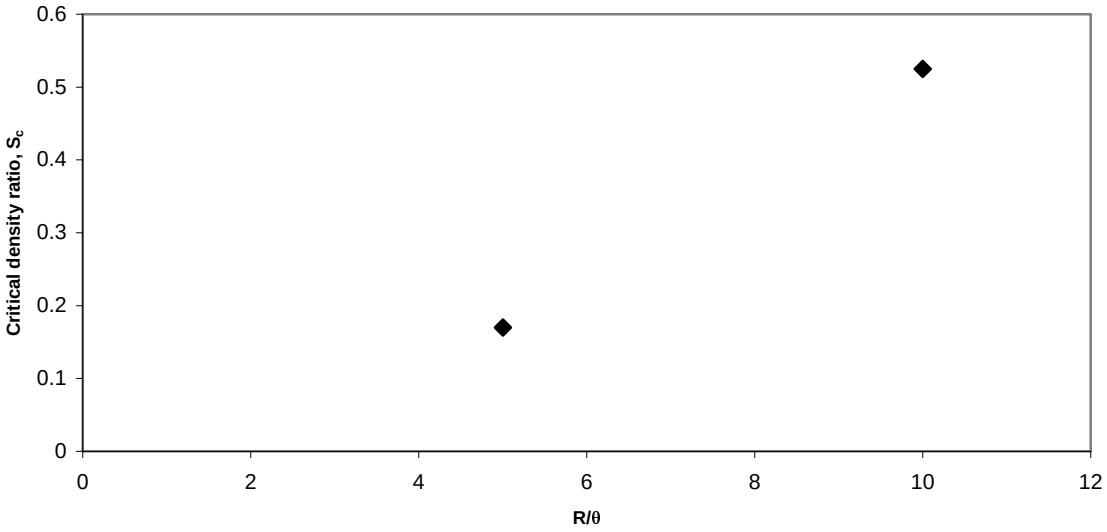
0.6
0.5
0.4
0.3
0.2
0.1
0
Critical density ratio, S_c
0
2
4
6
8
10
12
R/θ

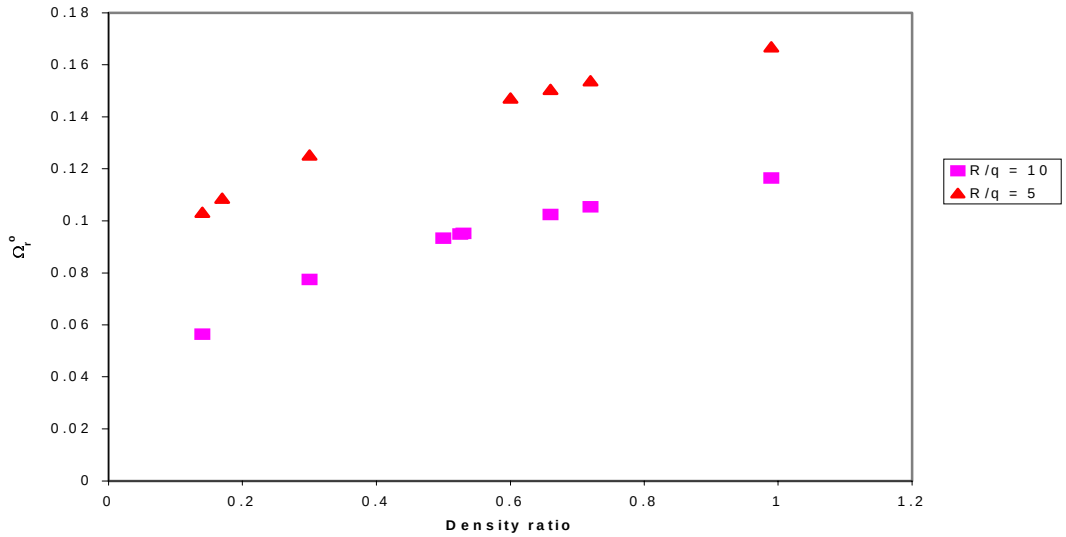
0.18
0.16
0.14
0.12
0.1
0.08
0.06
0.04
0.02
0
Ω_r^o
0
0.2
0.4
0.6
0.8
1
1.2
Density ratio
R/q = 10
R/q = 5

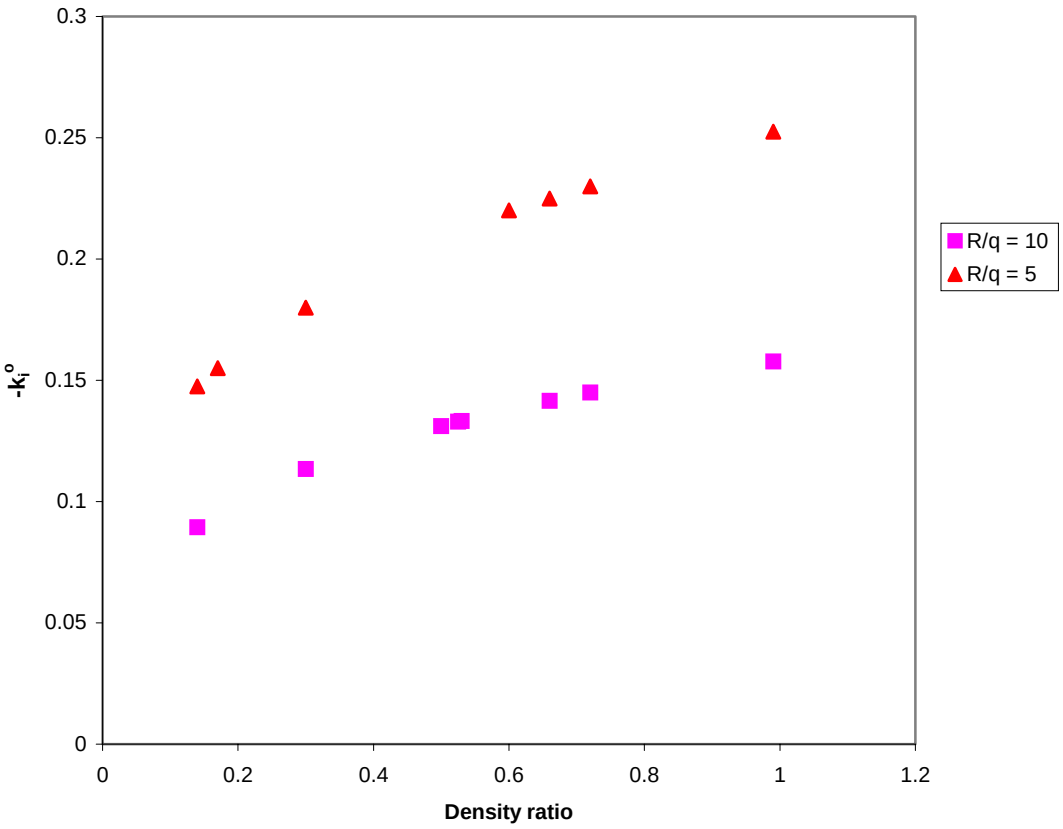
0.3
0.25
0.2
0.15
0.1
0.05
0
-k_i^o
0
0.2
0.4
0.6
0.8
1
1.2
Density ratio
R/q = 10
R/q = 5

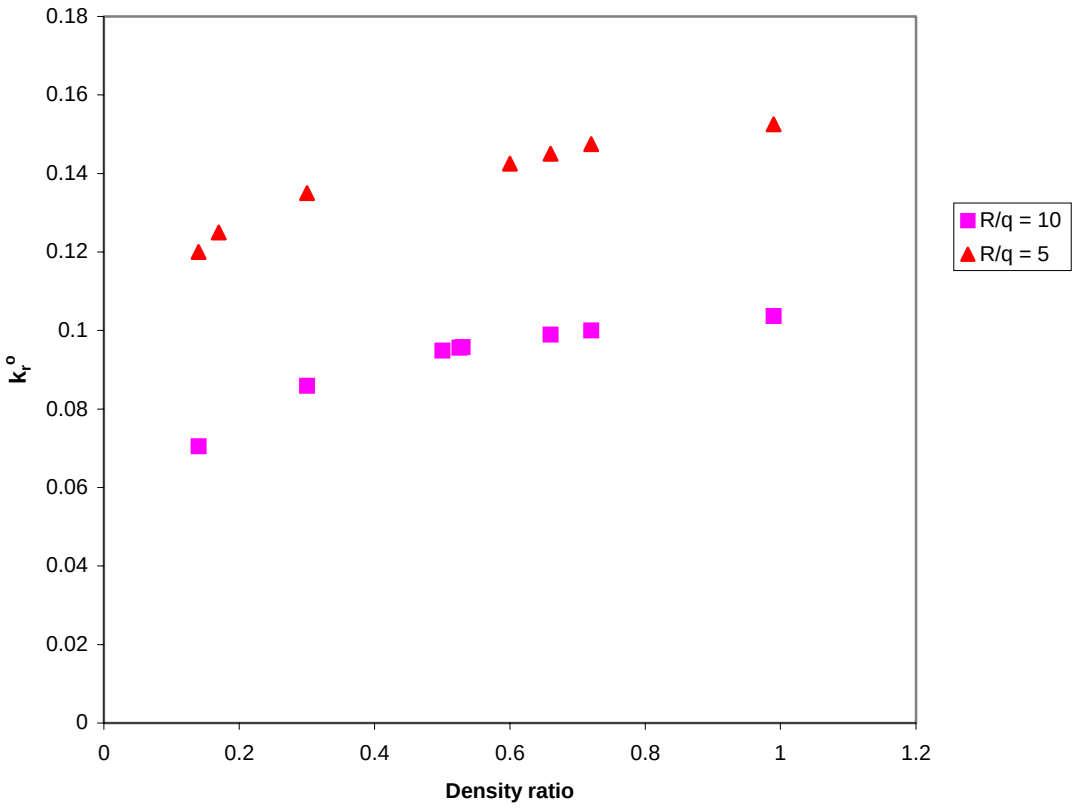
0.18
0.16
0.14
0.12
0.1
0.08
0.06
0.04
0.02
0
k_r^o
0
0.2
0.4
0.6
0.8
1
1.2
Density ratio
R/q = 10
R/q = 5

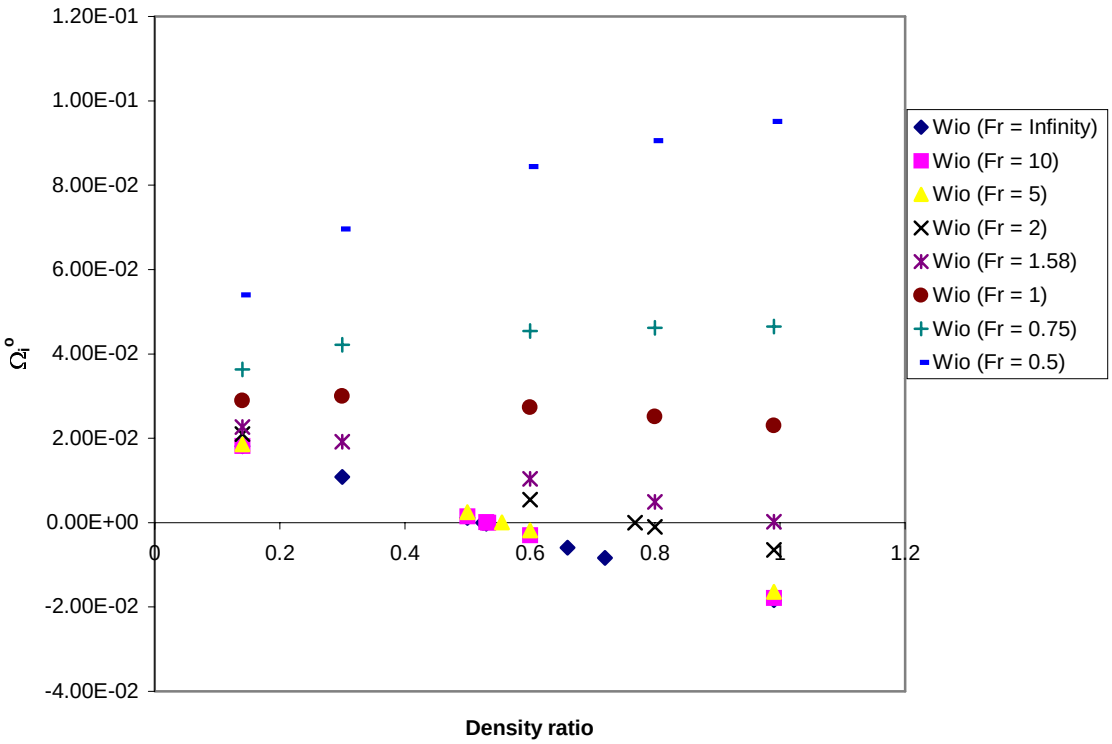
1.20E-01
1.00E-01
8.00E-02
6.00E-02
4.00E-02
2.00E-02
0.00E+00
-2.00E-02
-4.00E-02
Ω_i^o
0
0.2
0.4
0.6
0.8
1
1.2
Density ratio
Wio (Fr = Infinity)
Wio (Fr = 10)
Wio (Fr = 5)
Wio (Fr = 2)
Wio (Fr = 1.58)
Wio (Fr = 1)
Wio (Fr = 0.75)
Wio (Fr = 0.5)

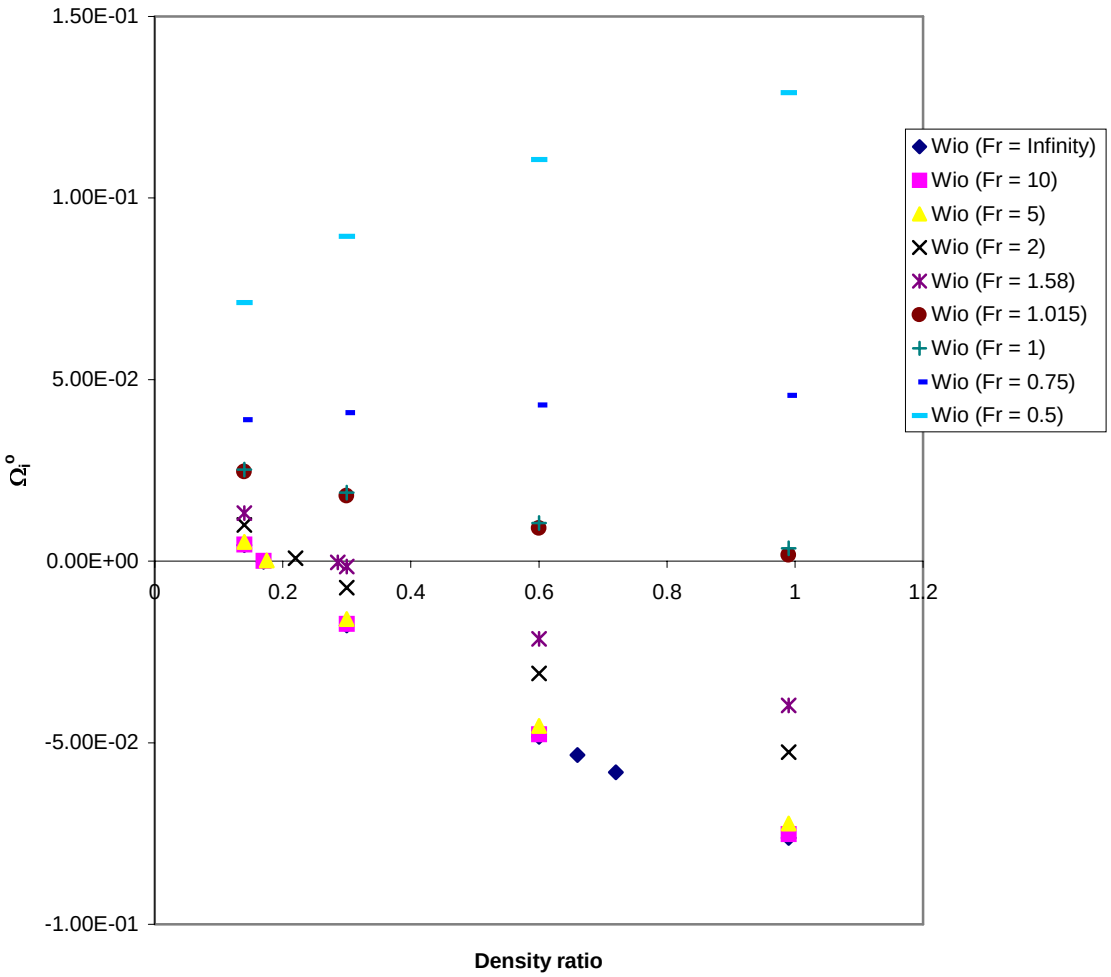
1.50E-01
1.00E-01
5.00E-02
0.00E+00
-5.00E-02
-1.00E-01
0
0.2
0.4
0.6
0.8
1
1.2
Ω_i^o
Density ratio
Wio (Fr = Infinity)
Wio (Fr = 10)
Wio (Fr = 5)
Wio (Fr = 2)
Wio (Fr = 1.58)
Wio (Fr = 1.015)
Wio (Fr = 1)
Wio (Fr = 0.75)
Wio (Fr = 0.5)

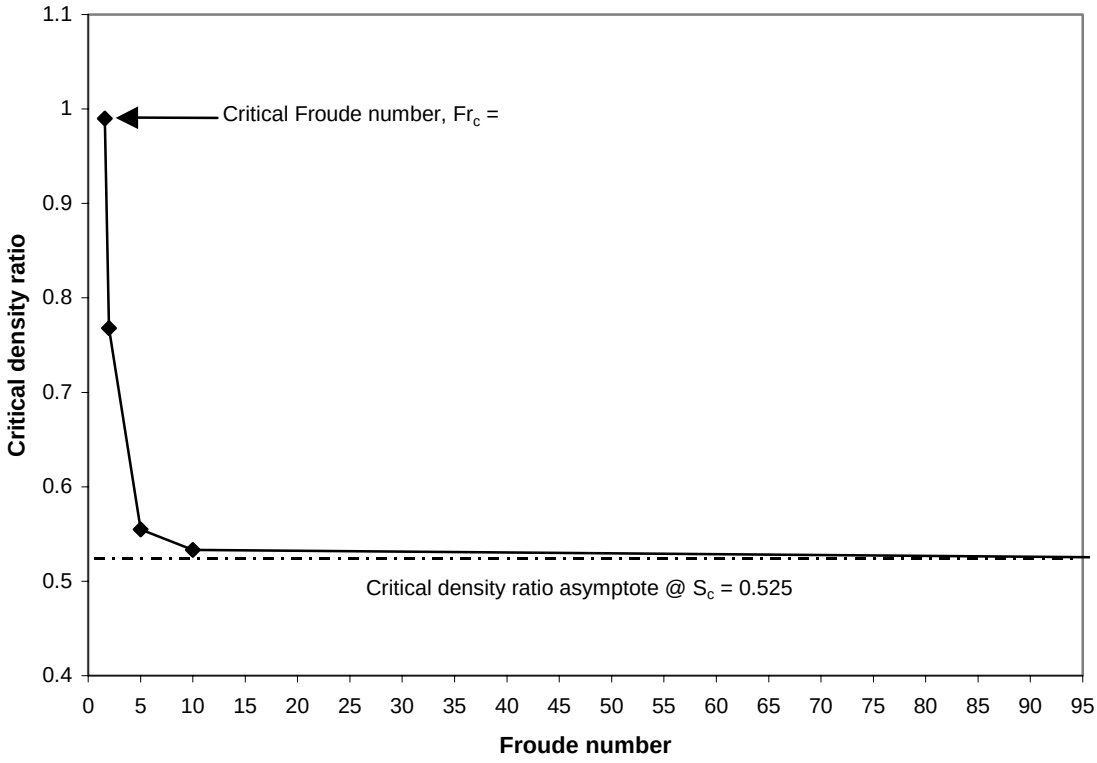
1.1
1
0.9
0.8
0.7
0.6
0.5
0.4
Critical density ratio
Critical Froude number, Fr$_c$ =
Critical density ratio asymptote @ S$_c$ = 0.525
0
5
10
15
20
25
30
35
40
45
50
55
60
65
70
75
80
85
90
95
Froude number

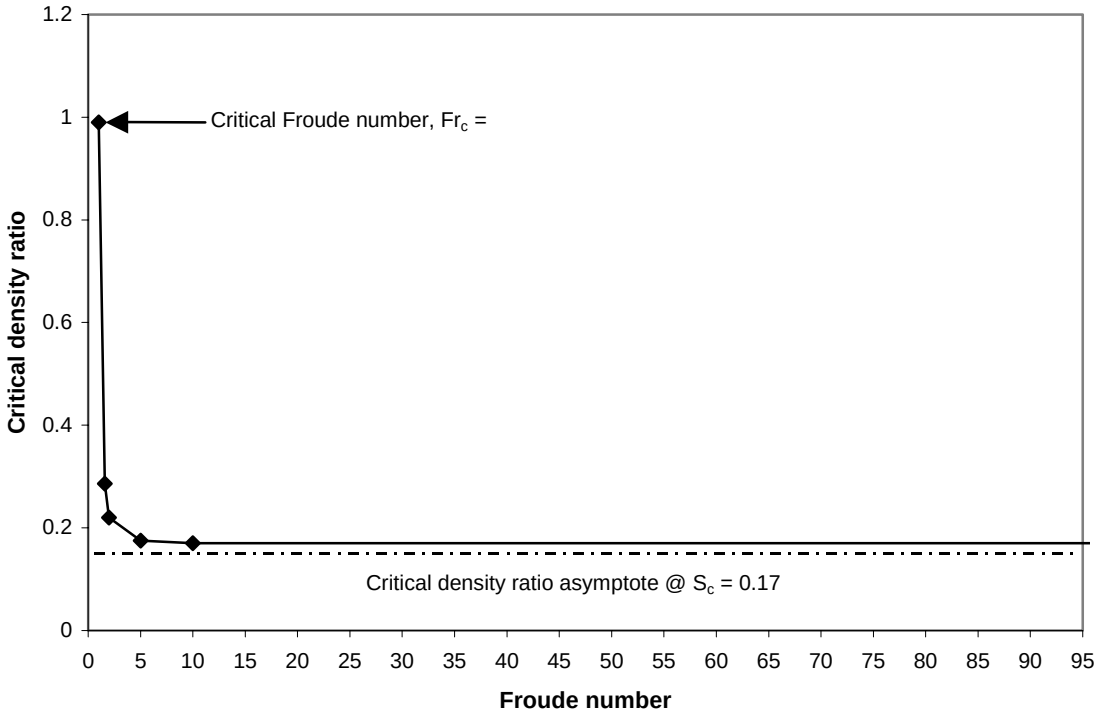
1.2
1
0.8
0.6
0.4
0.2
0
Critical density ratio
Critical Froude number, Fr$_c$ =
Critical density ratio asymptote @ S$_c$ = 0.17
0 5 10 15 20 25 30 35 40 45 50 55 60 65 70 75 80 85 90 95
Froude number

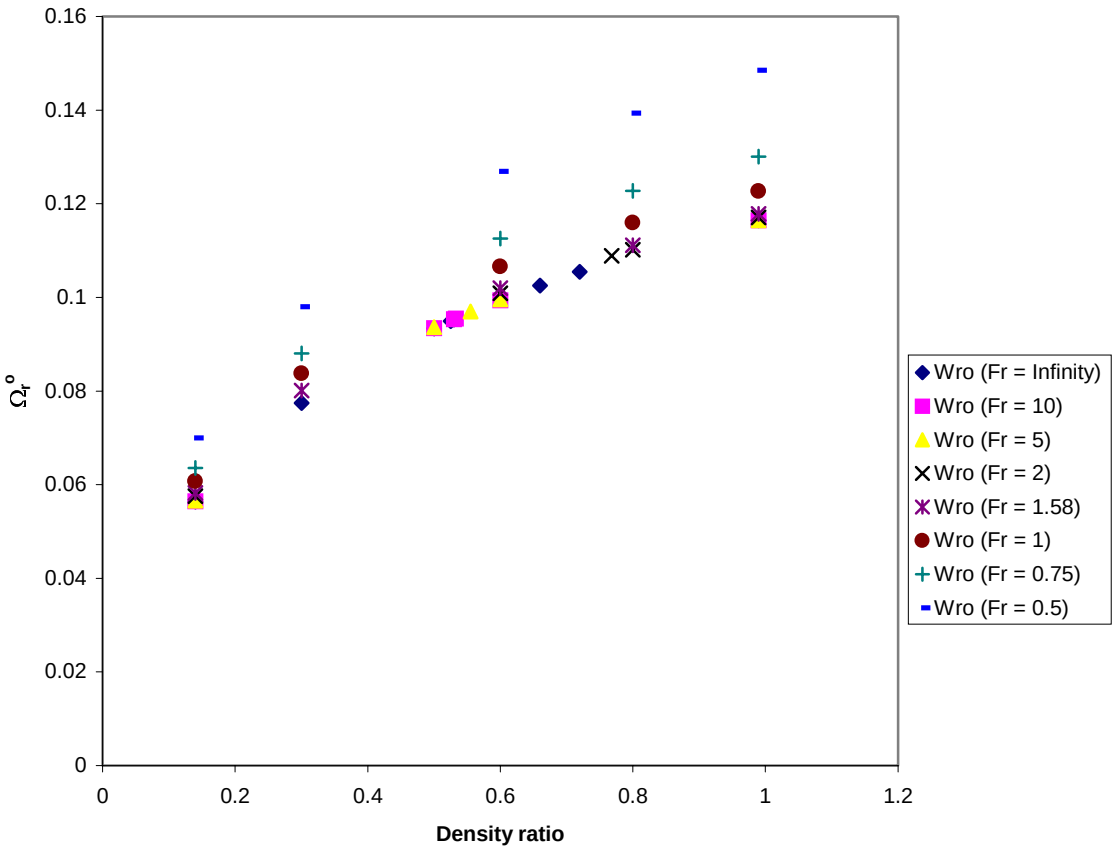
0.16
0.14
0.12
0.1
0.08
0.06
0.04
0.02
0
Ω_r^o
0
0.2
0.4
0.6
0.8
1
1.2
Density ratio
Wro (Fr = Infinity)
Wro (Fr = 10)
Wro (Fr = 5)
Wro (Fr = 2)
Wro (Fr = 1.58)
Wro (Fr = 1)
Wro (Fr = 0.75)
Wro (Fr = 0.5)

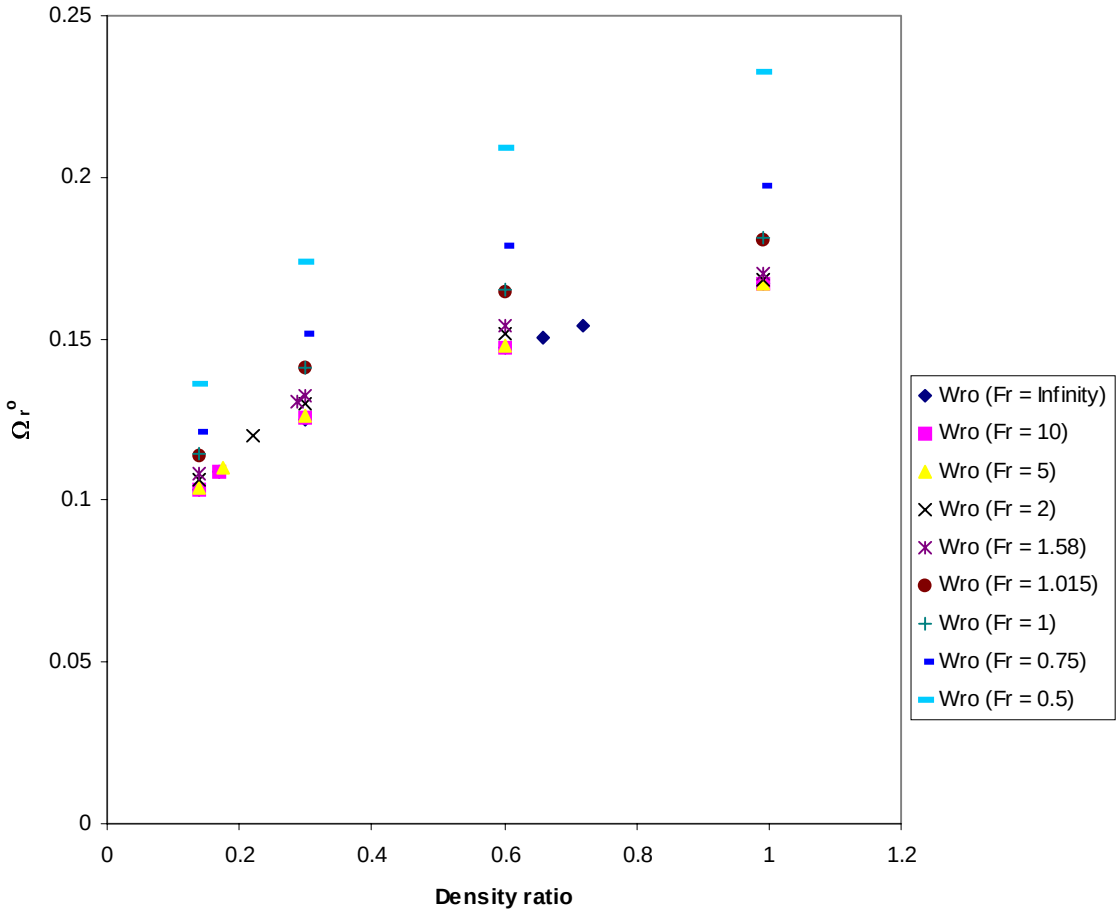
0.25
0.2
0.15
0.1
0.05
0
Ω r°
0
0.2
0.4
0.6
0.8
1
1.2
Density ratio
Wro (Fr = Infinity)
Wro (Fr = 10)
Wro (Fr = 5)
Wro (Fr = 2)
Wro (Fr = 1.58)
Wro (Fr = 1.015)
Wro (Fr = 1)
Wro (Fr = 0.75)
Wro (Fr = 0.5)

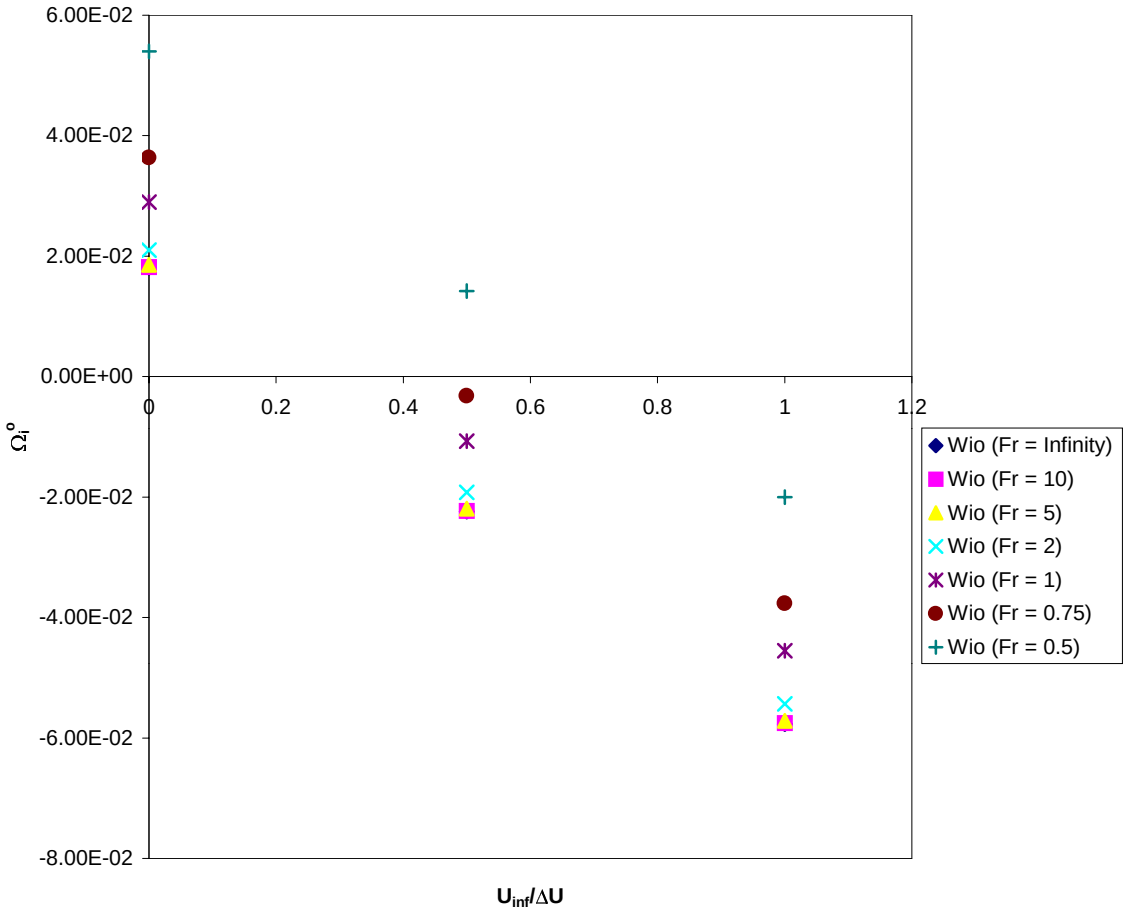
6.00E-02
4.00E-02
2.00E-02
0.00E+00
-2.00E-02
-4.00E-02
-6.00E-02
-8.00E-02
0
0.2
0.4
0.6
0.8
1
1.2
Ω°
U_inf/ΔU
Wio (Fr = Infinity)
Wio (Fr = 10)
Wio (Fr = 5)
Wio (Fr = 2)
Wio (Fr = 1)
Wio (Fr = 0.75)
Wio (Fr = 0.5)

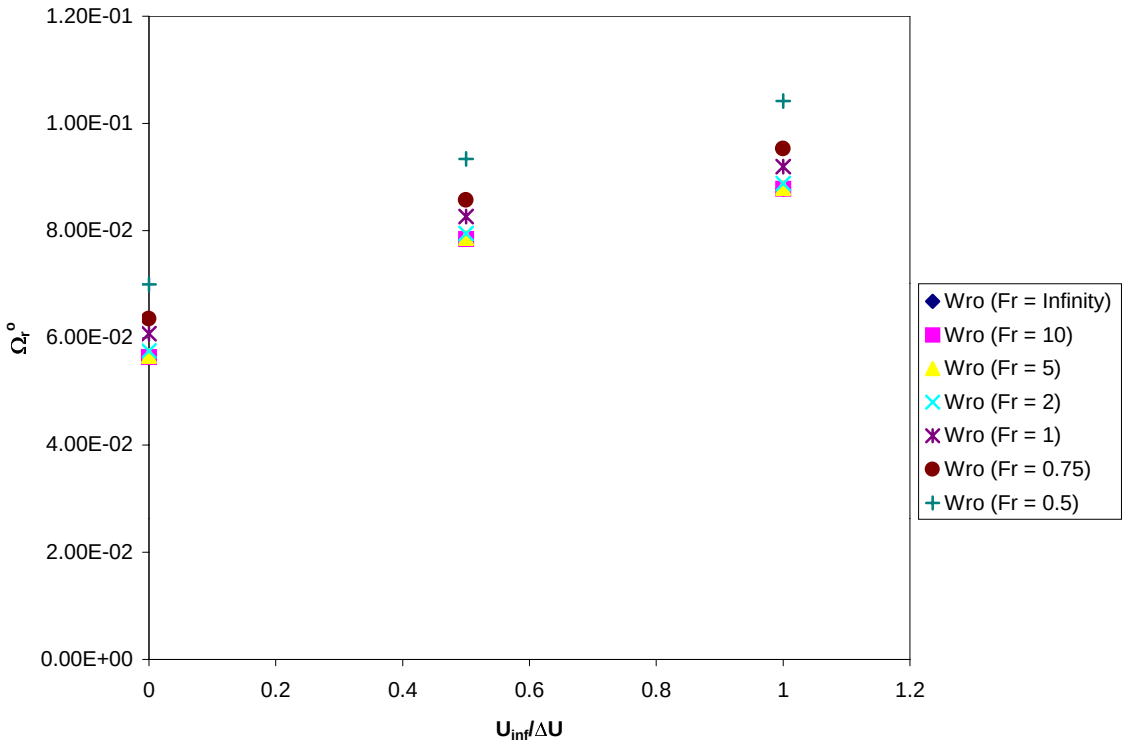
1.20E-01
1.00E-01
8.00E-02
6.00E-02
4.00E-02
2.00E-02
0.00E+00
Ω_r°
0
0.2
0.4
0.6
0.8
1
1.2
$U_{inf}/\Delta U$
Wro (Fr = Infinity)
Wro (Fr = 10)
Wro (Fr = 5)
Wro (Fr = 2)
Wro (Fr = 1)
Wro (Fr = 0.75)
Wro (Fr = 0.5)

Conference Papers (Published)

1. Pasumarthi, K., and Agrawal, A.K., 2004, "Schlieren Measurements of Buoyancy Effects on Flow Transition in Low-Density Gas Jets," ASME Heat Transfer-Fluid Engineering Conference, *ASME HT-FED2004-56810*, July 2004.

2. Satti, R.P., and Agrawal, A.K., 2004, "Numerical Analysis of Flow Evolution in a Helium Jet Injected into Air," ASME Heat Transfer-Fluid Engineering Conference, *ASME HT-FED2004-56811*, July 2004.

3. Vedantam, N. K. and Parthasarathy, R. N. 2004, "Effects of Mean Flow Profiles on the Instability of a Low-Density Gas Jet Injected into a High-Density Gas," ASME Heat Transfer-Fluid Engineering Conference, *ASME HT-FED2004-56794*.

4. Yildrim, B.S., Pasumarthi, K.S., and Agrawal, A.K., 2004, "Concentration Measurements in Self-Excited Momentum-Dominated Low-Density Gas Jets," AIAA Paper-2004-1279.

5. Satti, R., Pasumarthi, K.S., and Agrawal, A.K., 2004, "Numerical Simulations of Buoyancy Effects in Low-Density Gas Jets," AIAA Paper-2004-1317.

6. Yep, Tze-Wing, Agrawal, A.K., and Griffin, D.W., 2002, "Gravitational Effects on Near Field Flow Structure of Low-Density Gas Jets," *AIAA Paper 2002-0761*.

7. Lawson, A. L. and Parthasarathy, R. N. 2002, "Linear Temporal Instability Analysis of a Low-Density Round Gas Jet Injected into a High-Density Gas," *ASME 2002 Energy Technology Conference and Exposition*, ASME Paper ETCE2002/CAE-29010.

Proceedings of HT-FED2004:
2004 ASME Heat Transfer/Fluids Engineering Summer Conference
July 11-15, Charlotte, North Carolina, USA

HT-FED2004-56810

SCHLIEREN MEASUREMENTS OF BUOYANCY EFFECTS ON FLOW TRANSITION IN LOW-DENSITY GAS JETS

Kasyap. S. Pasumarthi and Ajay. K. Agrawal
University of Oklahoma
School of Aerospace and Mechanical Engineering
Norman, Oklahoma 73019
USA
Telephone: (405) 325-1754
Fax: (405) 325-1088
E-mail: aagrawal@ou.edu

ABSTRACT

The transition from laminar to turbulent flow in helium jets discharged into air was studied using Rainbow Schlieren Deflectometry technique. In particular, the effects of buoyancy on jet oscillations and flow transition length were considered. Experiments to simulate microgravity were conducted in the 2.2s drop tower at NASA Glenn Research Center. The jet Reynolds numbers varied from 800 to1200 and the jet Richardson numbers ranged between 0.01 and 0.004. Schlieren images revealed substantial variations in the flow structure during the drop. Fast Fourier Transform (FFT) analysis of the data obtained in Earth gravity experiments revealed the existence of a discrete oscillating frequency in the transition region, which matched the frequency in the upstream laminar regime. In microgravity, the transition occurred farther downstream indicating laminarization of the jet in the absence of buoyancy. The amplitude of jet oscillations was reduced by up to an order of magnitude in microgravity. Results suggest that jet oscillations were buoyancy induced and that the brief microgravity period may not be sufficient for the oscillations to completely subside.

INTRODUCTION

Low-density gas jets ejecting into high density ambient exhibit oscillatory instability under certain operating conditions. The buoyancy-driven oscillatory mode is predominantly present in the laminar flow region of the jet. The instability existing in the laminar region contaminates the jet potential core, leading to the transition from laminar to turbulent flow regime. Even in the transition regime, the periodic characteristics of the oscillating instability are retained to some extent. Low-density jets are characterized by the jet exit Richardson number, $\mathrm{Ri} = \frac{\mathrm{gd}}{\mathrm{U_j}^2}\frac{\left(\rho_\infty - \rho_\mathrm{j}\right)}{\rho_\mathrm{j}}$, where g is the gravitational acceleration, d is the jet diameter, ρ_∞ and ρ_j are, respectively, the free-stream and jet densities, and $\mathrm{U_j}$ is the mean jet exit velocity; the jet exit Reynolds number, $\mathrm{Re} = \frac{\mathrm{U_j d}}{\upsilon}$, where υ is the kinematic viscosity, and the Strouhal number, $\mathrm{St} = \frac{\mathrm{fd}}{\mathrm{U_j}}$ where f is the oscillation frequency.

Subbarao and Cantwell [1] conducted experiments in buoyant helium jets discharged from a circular tube into a co-flow of air. The Reynolds number was varied from 300 to 1500 and the Richardson numbers ranged between 0.5 and 6.0. The jet Richardson number was independently controlled in a variable-pressure facility as Re was varied during the experiments. Results showed that the Strouhal number was nearly independent of the Reynolds number. For Ri>1.0, St scaled with Ri, suggesting a buoyancy-dependent oscillating mode. The transition length defined as the distance between jet exit and flow transition plane decreased as Ri was increased, indicating the importance of buoyancy. Transition from laminar to turbulent flow was highly structured and repeatable. Similar observations were made by Richards et al. [2] for Ri=0.3 to $8\text{x}10^{-3}$ in helium jets. Vortex pairing was reported in the transition regime with the appearance of a subharmonic in the measured power spectra of helium concentration. Yep et al. [3] demonstrated buoyancy effects on oscillating flow structure by conducting experiments in Earth gravity and microgravity. Oscillations disappeared in

microgravity conditions, proving that the oscillations were buoyancy induced.

Kyle and Sreenivasan [4] examined the near field of momentum-dominated helium/air jets from contoured nozzles and found a global oscillatory instability when the jet to ambient fluid density ratio (S) was less than 0.5. The oscillatory instability characterized by large amplitude vortex rings dominated the flow in the entire near field and affected entrainment and mixing rates significantly. A distinguishing feature of the instability was the spectacular spreading near the end of the potential core, related to the generation of strong side jets emanating from the jet column. The jet structure in the transition region exhibited remarkable repeatability indicating that the potential core breakdown occurred in an organized manner.

Recently, Yildrim and Agrawal [5] utilized quantitative high-speed Rainbow Schlieren Deflectometry (RSD) to measure concentration across the whole field in momentum-dominated helium jets for Ri varying from 0.1 to 0.001 and Re ranging from 350 to 2000. They reported a unique oscillation frequency in the transition flow regime which matched with the global oscillation frequency in the upstream laminar regime. Measurements indicated that the flow transition length was affected by buoyancy even though the Richardson number was small (Ri<0.1).

Although experiments have identified self-excited global oscillations in the laminar region of low-density jets, an understanding of buoyancy effects on transition from laminar to turbulent flow is lacking in the current literature. Experiments by [5] reveal that buoyancy plays an important role in determining the structure of the transition region. However, the exact nature of this effect cannot be known without studies of equivalent jets under microgravity conditions. Thus, the present study was conducted to non-intrusively study the flow transition in self-excited helium jets. The diagnostic involves quantitative rainbow schlieren deflectometry, an optical technique applied previously for scalar measurements in non-reacting [3, 5, 6] and reacting flows [7, 8]. Brief descriptions of the experimental setup and the schlieren analysis technique are presented in the next section. Buoyancy effects will be explained using rainbow schlieren images, power spectra of angular deflection and spatio-temporal images in Earth and microgravity conditions.

EXPERIMENTAL SETUP

Experiments were conducted at NASA John H. Glenn Research Center's 2.2s drop tower facility. A compact rig was utilized for tests in the drop tower to simulate microgravity conditions. This was accomplished by re-designing an existing setup and by integrating the rainbow schlieren apparatus with a high-speed imaging system.

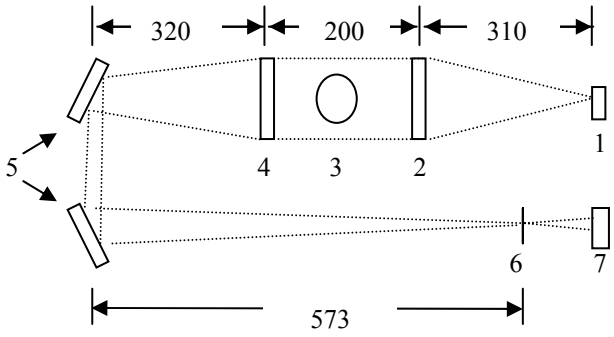

All dimensions are in mm

Fig. 1. Optical Layout
1 - Source aperture, 2 - Collimating lens, 3 – Test Media, 4 -Decollimating lens, 5 - Flat surface mirrors, 6 – Rainbow Filter, 7 – Camera lens

The flow system included two compressed helium gas cylinders, a pressure regulator, a calibrated mass flow meter (0-100 slpm), a needle valve, a solenoid valve to initiate and terminate the flow, and the tubing system. The tubing system consisted of a plastic hose, U-tube segment and a straight, polished stainless steel tube. Three 300mm long straight tubes with inside diameters of 19.1mm, 14.5 mm and 10.5mm were used. The tube outer surface was chamfered at 30 degree to reduce the wall thickness to 1.0 mm at the exit. The helium gas was discharged vertically into the quiescent air.

The RSD apparatus was configured on a horizontal optical breadboard. The optical layout of the rainbow schlieren apparatus is shown in Fig 1. The major components include a 100-μm wide, 3-mm high source aperture placed at the focal point of an 80mm diameter, 310mm focal length achromatic lens serving as the collimating lens. The light input to the source aperture is provided by a 1000-μm diameter fiber optic cable connected to a 300-W halogen light source with a light focusing assembly. The light rays deflected by the test media are decollimated by an 80-mm diameter, 1000-mm focal length achromatic lens. A pair of 100-mm diameter, aluminum coated flat surface mirrors is used to fold the rays by 180 degrees. A displaced image of the source aperture is formed at the focal point of the decollimating lens, wherein a 3-mm wide calibrated symmetric rainbow filter with hue varying between 30 and 300 degrees is placed.

The filtered schlieren image is acquired by a high-speed digital camera, model Motion Xtra HG-TX by Redlake, operated at exposure time of 297-us and acquisition rate of 1000 images per second. The spatial resolution of each acquired image was 512×385 pixels measuring 512KB in size. The camera has a buffer memory of 1.5GB, making it possible to store 2728 images. This enables acquisition of 2.728 seconds of image data, making it possible to store ~0.4 seconds of data in Earth gravity and 2.2 seconds of data in microgravity for each test case. Test procedure involved activating the solenoid valve initiate the flow in Earth gravity. Sufficient time is allowed for the flow to develop and stabilize into an oscillatory mode at the required flow rate. Then, the camera is triggered to store schlieren images in the camera memory. After 0.4 seconds of image capture in Earth gravity, the drop is executed. At the end of the drop, the

solenoid valve is deactivated to terminate the flow. The operations to execute the drop sequence were performed by programmable logic controller. After retrieving the drop rig, the images were transferred from camera memory to hard disk memory of a computer.

In RSD, the deflected light rays by the test media are decollimated and filtered by a continuously graded color filter of known transmissivity to create a color schlieren image. The transverse ray displacement at the filter plane is found from measurement of hue (color) in the schlieren image together with the filter calibration curve. Details of quantitative RSD are given by Greenberg et. al [9]. The transverse displacement at the filter plane is related to the deflection angle by

$$D(y) = \tan\left[\varepsilon(y)\right].f_c \approx \varepsilon(y).f_c$$

where f_c is the focal length of the decollimating lens, and $\varepsilon(y)$ is the deflection angle of a ray at the projected location 'y'.

RESULTS AND DISCUSSION

Table 1 lists the operating test conditions for the three test cases discussed in this section.

Table 1

Case	d, mm	U_j, m/s	Re	Ri	f, Hz
Case I	10.5	9.3	800	0.008	215
Case II	14.5	8.4	1000	0.013	160
Case III	14.5	6.7	800	0.02	120

First, we present schlieren images in Earth gravity and microgravity for all three cases. Next, power spectra of angular deflection data detailing the buoyancy effects on the flow transition are discussed. Figure 2 shows the rainbow schlieren images for Case I acquired in Earth gravity and towards the end of the drop in microgravity. Transition from laminar to turbulent flow is observed at z/d>4.0 in Earth gravity. In microgravity, transition is not visible in the field of view. The jet remains laminar up to z/d=6.0.

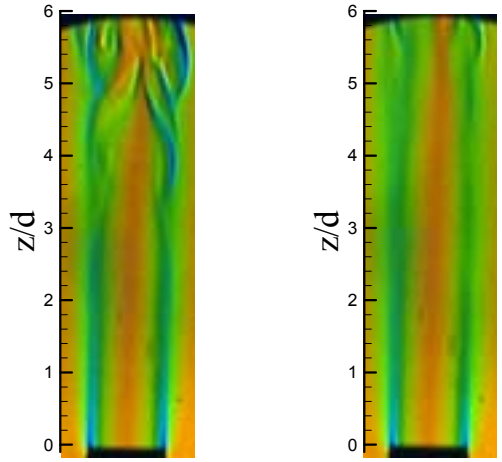

Fig. 2. Rainbow schlieren images for Case I in Earth gravity (left) and microgravity (right).

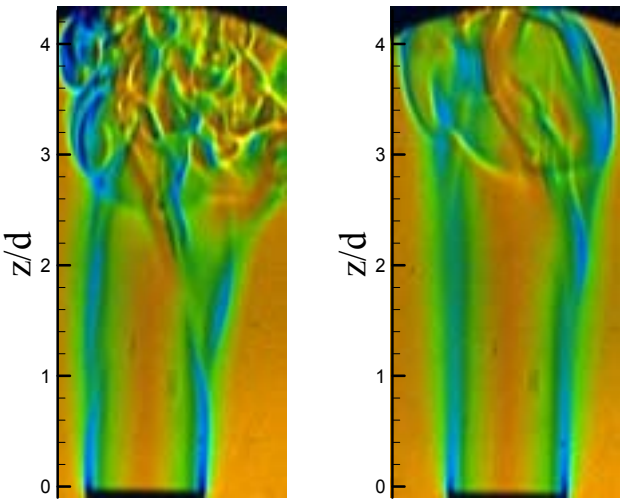

Fig. 3. Rainbow schlieren images for Case II in Earth gravity (left) and microgravity (right).

The results provide direct evidence that buoyancy affects flow transition in a momentum-dominated jet. Figure 3 shows schlieren images in Earth gravity and microgravity for Case II. In Earth gravity, transition occurs at z/d =2.0 marked by a visible breakdown of the potential core characterized by bifurcation of the jet and intense mixing downstream (z/d>2.2). However, in microgravity, the transition plane has shifted downstream to about z/d = 2.8. Furthermore, mixing in the jet core at z/d>2.8 is less intense than that in Earth gravity.

Figure 4 shows schlieren images in Earth gravity and microgravity for Case III. Transition from laminar to turbulent flow occurs at z/d = 3.2 in Earth gravity while it is absent in the field of view in microgravity. Again, a delay in flow transition has extended the laminar coherent region in microgravity.

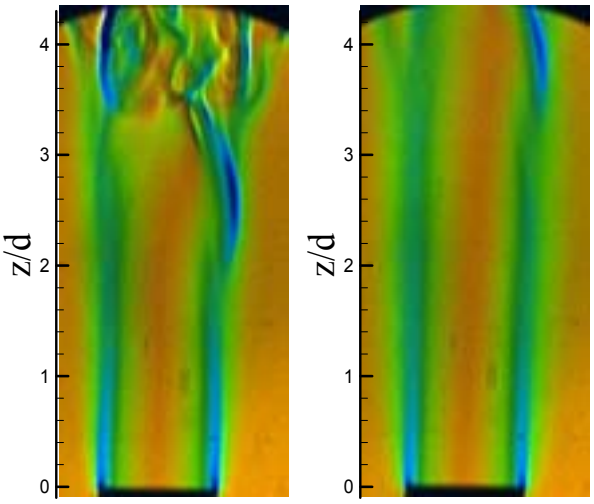

Fig. 4. Rainbow schlieren images for Case III in Earth gravity (left) and microgravity (right).

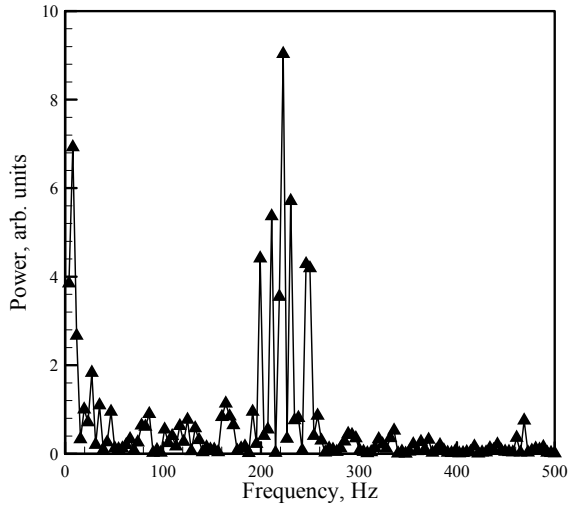

Fig. 5(a). Power spectra of angular deflection data for Case I in Earth gravity at z/d = 3.0 and r/d = 0.5.

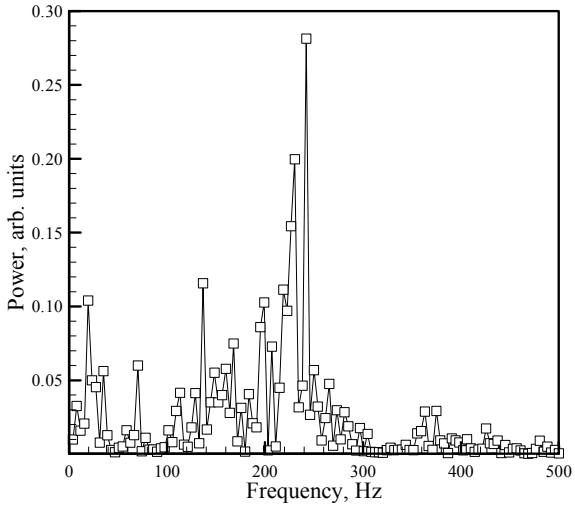

Fig. 5(b). Power spectra of angular deflection data for Case I in microgravity at z/d = 3.0 and r/d = 0.5.

To assess the buoyancy effects on the jet oscillations, Fast Fourier Transform (FFT) analysis was conducted on the angular deflection data obtained from an ensemble of 256 images, each in Earth gravity and microgravity. The data in the microgravity were taken from images acquired towards the end of the drop to ensure that the jet had adjusted to the absence of buoyancy. Figure 5 (a) shows the power spectra in Earth gravity for Case I at z/d = 3.0 and r/d=0.5, for a location upstream of the flow transition plane. Results show a dominant peak at a frequency of 215 Hz.

Figure 5 (b) shows that in microgravity, the oscillatory mode still persists but the spectral power has decreased by two orders of magnitude. The remarkable decrease in spectral power points toward damping of flow oscillation in the absence of buoyancy.

Next, Figure 6(a) shows the power spectra in the transition region (z/d = 4.0) for Case I in Earth gravity**.** The dominant frequency of 215Hz in the transition region is the same as that in the upstream laminar regime. However, the spectral power has decreased considerably compared to that in the upstream laminar region indicating the breakdown of large-scale structures into smaller ones. In microgravity, the spectral power is decreased by an order of magnitude as shown in Figure 6(b).

Figure 7(a) shows the power spectra in laminar region at z/d=1.5 and r/d =0.5 for Case II in Earth gravity. We observe a unique dominant peak in spectral power at a frequency of 160 Hz. Unlike Case I, the spectral density plot for Case II is devoid of any spectral noise. Also with increase in jet Richardson number from 0.008 for Case I to 0.013 for Case II, a reduction in the oscillation frequency is observed.

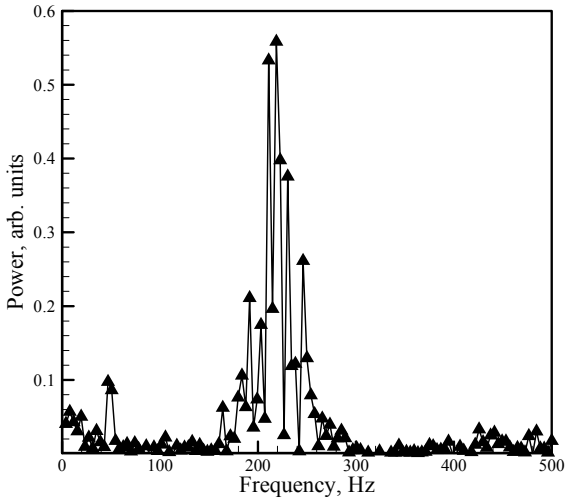

Fig. 6(a). Power spectra of angular deflection data for Case I in Earth gravity at z/d = 4.0 and r/d = 0.5.

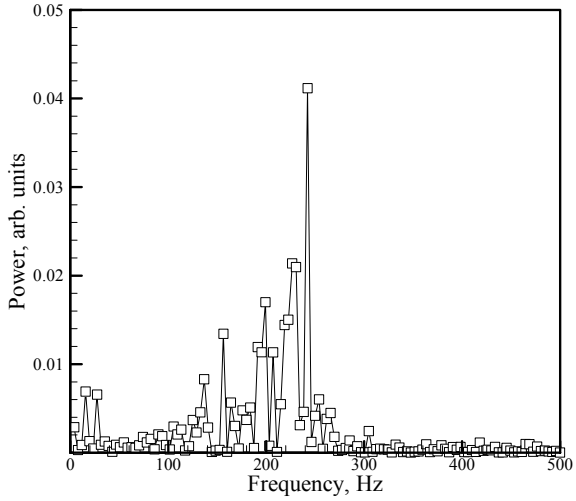

Fig. 6(b). Power spectra of angular deflection data for Case I in microgravity at z/d = 4.0 and r/d = 0.5.

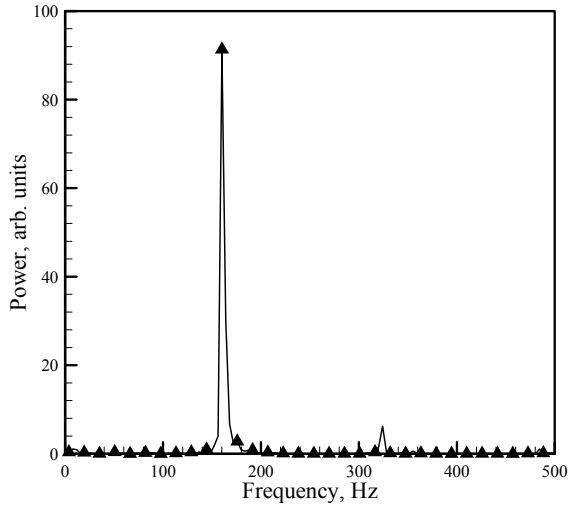

Fig. 7(a). Power spectra of angular deflection data for Case II in Earth gravity at z/d = 1.5 and r/d = 0.5.

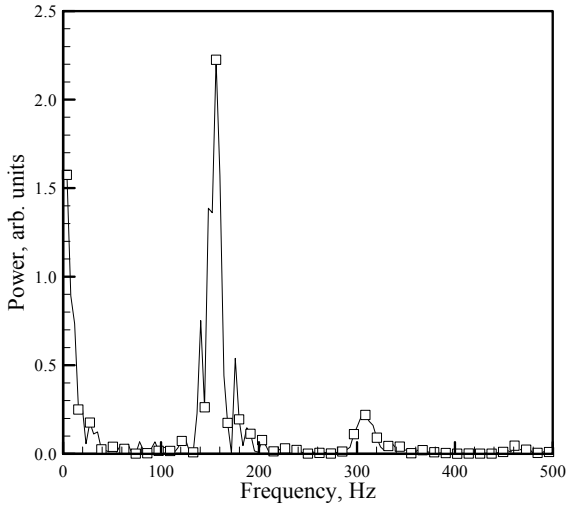

Fig. 7(b). Power spectra of angular deflection data for Case II in microgravity at z/d = 1.5 and r/d = 0.5.

Figure 7 (b) shows the power spectra in microgravity in the laminar region at z/d=1.5 and r/d =0.5. We still observe the peak at a frequency of 160 Hz, but at reduced spectral power than in Earth gravity. The power spectra for Case II in the transition region (z/d = 2.5) are shown in Figure 8(a) in Earth gravity. The dominant frequency of 160Hz in the transition region matches with the upstream frequency measurement. However, the decrease in spectral power compared to that in the laminar region is not that steep as observed for Case I. In microgravity, the oscillatory mode still exists but at a lower spectral power shown by Figure 8(b).

Even though the spectral power is lower than the power observed in Figure 8(a), it is qualitatively comparable. The slower decay of the amplitude of the oscillatory mode is attributed to the increased time required for the breakdown of large-scale structures for Case II (d=14.5mm) in microgravity. Figure 9(a) shows the power spectra at z/d=2 and r/d =0.5 in the laminar region for Case III in Earth gravity. A dominant peak is observed at a frequency of 120 Hz. The peak power has increased with increase in Richardson number.

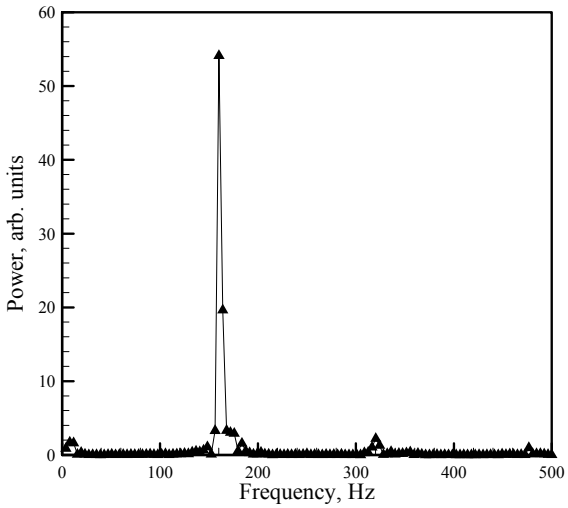

Fig. 8(a). Power spectra of angular deflection data for Case II in Earth gravity at z/d = 2.5 and r/d = 0.5.

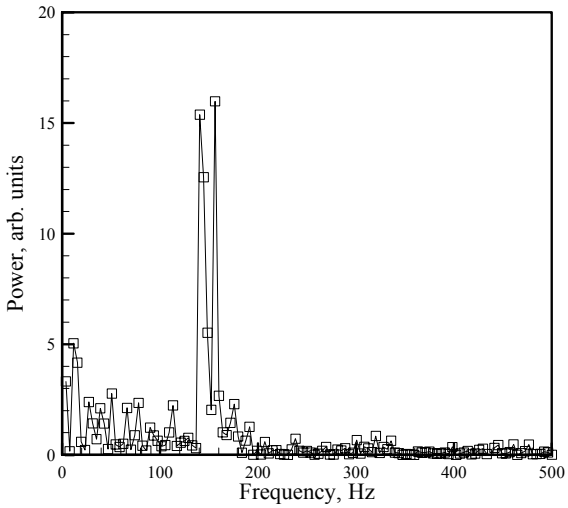

Fig. 8(b). Power spectra of angular deflection data for Case II in microgravity at z/d = 2.5 and r/d = 0.5.

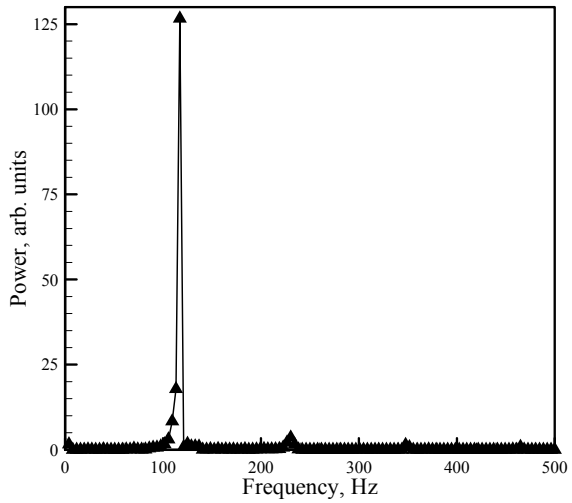

Fig. 9(a). Power spectra of angular deflection data for Case III in Earth gravity at z/d = 2.0 and r/d = 0.5.

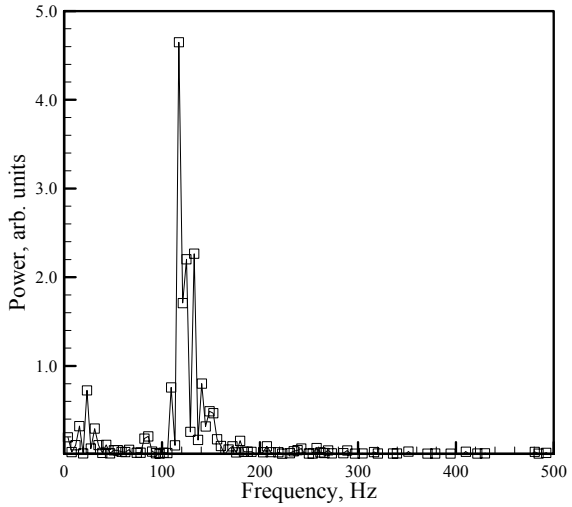

Fig. 9(b). Power spectra of angular deflection data for Case III in microgravity at z/d = 2.0 and r/d = 0.5.

Figure 9(b) shows the power spectra at z/d=2 and r/d =0.5 in the laminar region for Case III in microgravity. The oscillatory mode is damped with peak power decreasing by more than an order of magnitude in absence of buoyancy. The power spectra in the transition region are shown at z/d=3 and r/d=0.5 in Figure 10(a) for Case III in Earth gravity. As observed for Case II, the decrease in spectral power from laminar to transition region is very nominal in Earth gravity. In microgravity, the jet has laminarized and flow transition is absent in the field of view. The power spectra in microgravity are shown in Figure 10(b). The amplitude of oscillatory mode is further reduced in the absence of buoyancy as observed from the steep drop in spectral power compared to that in Earth gravity.

One of the effective ways to visualize flow oscillations is by observing spatio-temporal images at specified axial locations. The space-time images were developed by concatenating radial scan lines at specified axial planes from a sequence of 2728 images. Figure 11 show spatio-temporal image in Earth gravity and microgravity for Case III at z/d =3. As shown in Figure 4, this axial location corresponds to transition regime in Earth gravity and laminar regime in microgravity. These images reveal significant differences and the underlying effect of buoyancy on the jet oscillations. In Earth gravity, the oscillating jet structure is highly repeatable in transition region. In microgravity, repeatable oscillations are present although the amplitude of oscillations has clearly decreased.

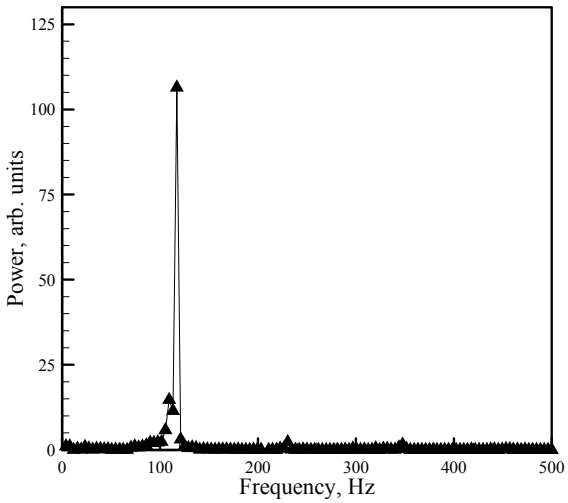

Fig. 10(a). Power spectra of angular deflection data for Case III in Earth gravity at z/d = 3.0 and r/d = 0.5.

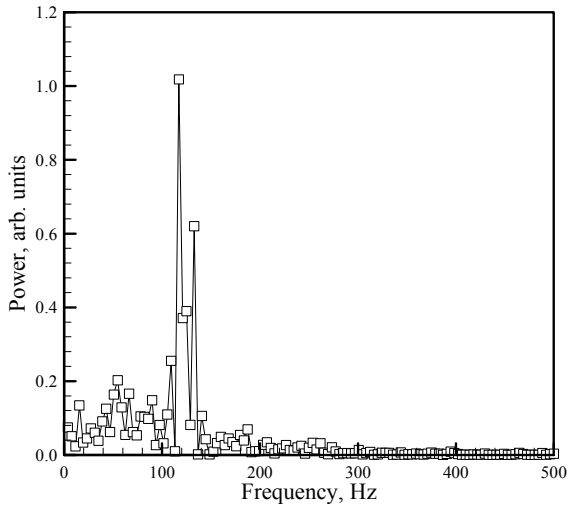

Fig. 10(b). Power spectra of angular deflection data for Case III in microgravity at z/d = 3.0 and r/d = 0.5.

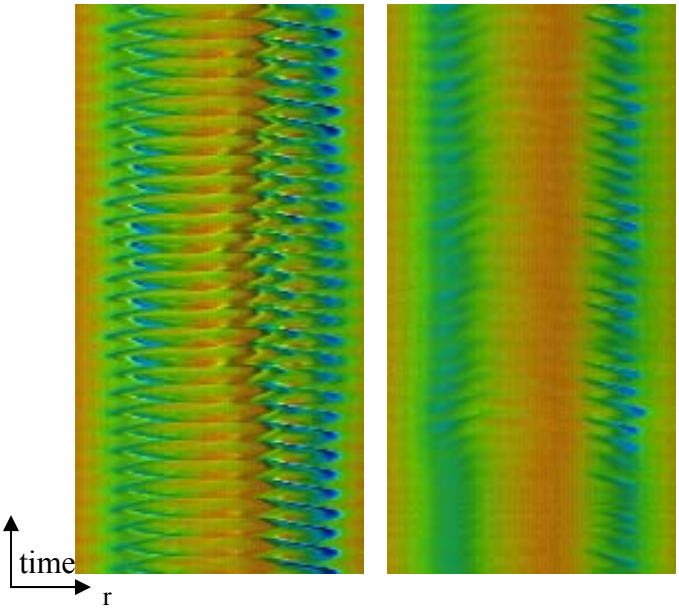

Fig. 11 Spatio-temporal images for Case III in Earth gravity (left) and microgravity (right) at z/d = 3.

CONCLUSIONS

Experiments were performed in Earth gravity and microgravity to evaluate buoyancy effects on momentum-dominated helium jets undergoing transition from laminar to turbulent flow. Instantaneous schlieren images in the whole field revealed a repeatable oscillatory mode in both laminar and transition regimes. The jet flow structure and transition length varied with change in the gravitational level. In microgravity, the laminar region was extended to delay flow transition for the three cases shown. Power spectra in the transition region revealed an oscillatory mode with a frequency matching with the oscillation frequency of the upstream laminar flow regime. Spectral power of flow oscillations was significantly reduced in microgravity for all the cases. These results provided direct physical evidence that flow transition in momentum-dominated low-density jets is affected by buoyancy.

ACKNOWLEDGEMENTS

This work was supported by Physical Sciences Division of NASA's Office of Biological and Physical research under grant NAG 3-2388.

REFERENCES

[1] Subbarao, E. R., and Cantwell, B. J., 1992, "Investigation of a Co-Flowing Buoyant Jet: Experiments on the Effects of Reynolds Number and Richardson Number," *Journal of Fluid Mechanics*, Vol.**245**, pp. 69-90.

[2] Richards, C.D., Breuel, B.D., Clark, R.P., and Troutt, T.R., 1996, "Concentration Measurements in a Self-Excited Jet," *Experiments in Fluids*, Vol.**21**, pp. 103-109.

[3] Yep, T.W., Agrawal, A.K., and Griffin, D., 2003, "Gravitational Effects on Near-Field Flow Structure of Low-Density Gas Jets," *AIAA Journal*, Vol.**41**, pp. 1973-1979.

[4] Kyle, D.M., and Sreenivasan, K.R., 1993, "The Instability and Breakdown of a Round Variable-Density Jet," *Journal of Fluid Mechanics*, Vol. **249**, pp. 619-664.

[5] Yildrim, B.S., and Agrawal A.K., 2004, "Full Field Measurements of Self-Excited Oscillations in Momentum-Dominated Helium Jets," *Experiments in Fluids*, *In review*.

[6] Al-Ammar, K., Agrawal, A.K., Gollahalli, S.R., and Griffin, D., 1998, "Application of Rainbow Schlieren Deflectometry for Concentration Measurements in an Axisymmetric Helium Jet," *Experiments in Fluids*, Vol.**25**, pp. 89-95.

[7] Agrawal, A.K., Butuk, N., Gollahalli, S.R. and Griffin, D., 1998, "Three-Dimensional Rainbow Schlieren Tomography of Temperature Field in Gas Flows," *Applied Optics*, Vol.**37**, pp. 479-485.

[8] Albers, B.W., and Agrawal, A.K., 1999, "Schlieren analysis of an Oscillating Gas-Jet Diffusion Flame," *Combustion and Flame*, Vol.**119**, pp. 89-94.

[9] Greenberg, P.S., Klimek, R.B., Buchele, D.R., 1995, "Quantitative Rainbow Schlieren Deflectometry," *Applied Optics*, Vol.**34**, No. 10, pp. 3810-3822.

Proceedings of HT-FED 2004:
2004 ASME Heat Transfer/ Fluids Engineering Summer Conference
July 11-15, Charlotte, North Carolina, USA

HT-FED 2004-56811

NUMERICAL ANALYSIS OF FLOW EVOLUTION IN A HELIUM JET INJECTED INTO AMBIENT AIR

Rajani P. Satti and Ajay K. Agrawal
School of Aerospace and Mechanical Engineering
University of Oklahoma
Norman, OK-73019, USA
E-mail: aagrawal@ou.edu

ABSTRACT

A computational model to study the stability characteristics of an evolving buoyant helium gas jet in ambient air environment is presented. Numerical formulation incorporates a segregated approach to solve for the transport equations of helium mass fraction coupled with the conservation equations of mixture mass and momentum using a staggered grid method. The operating parameters correspond to the Reynolds number varying from 30 to 300 to demarcate the flow dynamics in oscillating and non-oscillating regimes. Computed velocity and concentration fields were used to analyze the flow structure in the evolving jet. For Re=300 case, results showed that an instability mode that sets in during the evolution process in Earth gravity is absent in zero gravity, signifying the importance of buoyancy. Though buoyancy initiates the instability, below a certain jet exit velocity, diffusion dominates the entrainment process to make the jet non-oscillatory as observed for the Re=30 case. Initiation of the instability was found to be dependent on the interaction of buoyancy and momentum forces along the jet shear layer.

Keywords: Buoyancy, Flow Instability, Evolution, Jets.

INTRODUCTION

The basic flow of a jet issuing into quiescent environment has applications in a vast array of engineering problems, ranging from pollutant dispersal to combustor design. Of particular interest are the low density jets found in applications involving fuel leaks, aerosol sprays, diffusion flames, jet propulsion, smokestack discharges, volcanic eruptions, etc. The present work investigates the near-field stability characteristics of an evolving helium jet injected into ambient air. The jet flow characteristics are investigated at different inflow and gravitational forcing conditions.

In the past few decades, many studies [1-4] have focused on studying the fully turbulent far-field jet region. The near-field influence owing to buoyant flow instabilities has also been a subject of interest to many researchers. Self-excited oscillations leading to the formation and propagation of large-scale vortical structures have been investigated in detail by Subbarao and Cantwell [5], Cetegen [6], Richards et al. [7], Agrawal and his co-workers [8-9]. The first two studies [5-6] explained the periodic oscillatory behavior in helium jets injected into air using velocity measurements. In the latter studies [7-9], mass transfer measurements characterized the flow instability for helium jets in quiescent air. Experiments by Yep et al. [8] demonstrated that flow oscillations were absent in the microgravity environment of the 2.2 s drop tower.

While the above studies serve to develop a basic understanding of the instability phenomena, it is also of fundamental importance to investigate the flow structure of a jet during its evolution period. Smith et al. [10] and Irshi et al. [11] performed studies on the evolution of synthetic jets and circular pulse jets to examine the formation of vortex pairs. Velocity and scalar field measurements were obtained in a laminar starting plume by Shlien and his co-workers [12,13] to visualize the spiral structure in the plume cap. Similar studies by Shusser and Gharib [14] on vortex ring formation in a starting buoyant plume explained the formation dynamics of vortex rings.

The jet literature is also abundant with studies relating to the mechanism of instability. Some early experiments with helium have shown that oscillations are solely a consequence of buoyancy near the source of a plume [15]. Cetegen and Kasper [16] conducted experiments on non-reacting buoyant plumes and related the instability to the highly unstable density stratification in the sharply contracting region of the flow just above the injector. Investigations of Monkewitz and Sohn [17] and Kyle and Sreenivasan [18] on round jets established the onset of local absolute instability to a critical density ratio below 0.6. Though it was found that the unstable mode was dependent on buoyancy, there also existed a threshold jet exit velocity, which governed the onset of the oscillatory mode. Hamins et al. [19] investigated the stability limits, and the

critical jet velocity needed to initiate pulsations in flames was measured as a function of burner diameter.

Few computational studies on the stability and unsteady flow dynamics of helium jets have been reported in the literature. Mell et al. [20] performed numerical simulations of helium jets in air and found that the computed oscillation frequency matched with experimentally obtained value by Hamins et al [19]. Soteriou [21] provided a vorticity dynamics based model and revealed that instability is inviscid in nature and arises due to the mechanism of vorticity generation by buoyancy. More recently, Satti et al. [22] conducted numerical simulations on isothermal helium jets during the change from Earth gravity to zero gravity. Their results explained that buoyancy induced global flow oscillations present in Earth gravity are absent in zero gravity. The dependence of oscillation frequency and amplitude on gravitational forcing was presented. However, the flow physics of the jet during the initial evolutionary stages characterized by the formation of vortex rings and the mushroom-like cap structure was not detailed.

Though the above experimental/numerical literature explains the physics of the flow structure of low-density jets, studies of an evolving jet eventually showing stable/unstable mode are virtually non-existent in the literature. Recently, Pasumarthi [23] conducted experiments depicting evolution of low-density jets in Earth and micro gravity. Preliminary results show that the jet maintained axisymmetric structure in the near field. To our knowledge, no detailed study has been conducted showing the effect of buoyancy on an evolving jet with concurrent visualizations of mass and momentum transport processes. Concurrently, it needs to be quantified that not only buoyancy, but also sufficient jet momentum is required to initiate self-excited oscillations in low-density jets. Motivated by these ideas, using computational fluid dynamic analysis, we seek to provide insight into the evolution dynamics of a helium-air jet leading to steady/unsteady behavior. In the following section, we provide details relating to the governing equations, boundary and initial conditions, and the computational procedure. Results indicating the oscillating/non-oscillating jets are explained subsequently.

THEORETICAL FORMULATION

Concurring with experiments [8-9], the governing equations for laminar, unsteady and axisymmetric flow are expressed in the cylindrical coordinate system as follows:

$$\frac{\partial \rho}{\partial t}+\frac{1}{r}\frac{\partial}{\partial r}(\rho v r)+\frac{\partial}{\partial z}(\rho w)=0 \qquad (1)$$

$$\frac{\partial(\rho r\phi)}{\partial t}+\frac{\partial}{\partial r}(\rho v r\phi)+\frac{\partial}{\partial z}(\rho r w\phi)=\frac{\partial}{\partial r}\left(\Gamma^{\phi} r\frac{\partial \phi}{\partial r}\right)+\frac{\partial}{\partial z}\left(\Gamma^{\phi} r\frac{\partial \phi}{\partial z}\right)+S^{\phi} \qquad (2)$$

where ρ represents density; and w and v are, respectively, the axial and radial components of the velocity. Note that possible three-dimensional effects in the downstream region are ignored in this paper. Equation 1 represents the continuity equation and Equation 2 is the general transport equation, which represents momentum, or species conservation equation depending on the variable ϕ. The terms Γ^{ϕ} and S^{ϕ} in the transport equation represent respectively, the diffusion coefficient and source term of the variable ϕ. Density was computed from the incompressible ideal gas law and viscosity calculations used Wilke's mixture averaged formula. Further details about the source terms and equations involved in defining physical properties are given in ref.22.

COMPUTATIONAL MODEL

The two-dimensional geometry under consideration is illustrated in Fig. 1, where d=31.8mm is the tube inside diameter. The grid was generated by splitting the computational domain into five sub regions. An orthogonal non-uniform grid system was used. The grid elements in the radial direction were concentrated in the oscillatory zone. The grid size was increased gradually in the axial direction. The upstream boundary was placed at a distance of 1d from the jet exit plane. The operating pressure and temperature were specified, respectively as 1atm and 300K. Fig. 1 shows the boundary conditions used for the analysis. A parabolic velocity profile was used at the inlet. No slip and zero mass diffusion conditions were imposed on both surfaces of the tube wall. The exit and lateral boundaries were specified as pressure outlet where flow properties are extrapolated from the interior. Pressure inlet condition was imposed at the radial boundary.

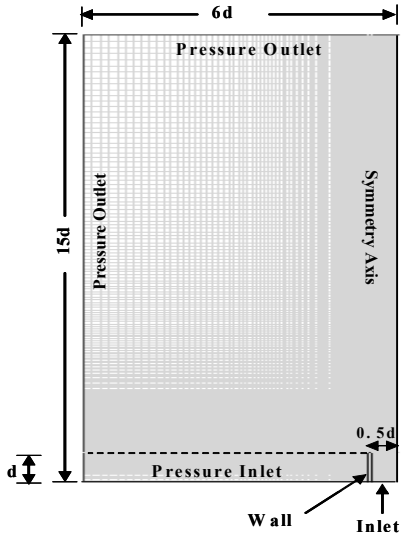

Fig 1: Schematic of the computational domain.

SOLUTION STRATEGY

The governing equations were solved sequentially using a segregated approach [24]. An implicit, second order time dependent formulation was incorporated into the numerical model. Since the governing equations are coupled, several iterations of the solution loop were performed before a converged solution was obtained. The convective terms were discretized using the QUICK scheme and the SIMPLEC algorithm was used to achieve the pressure–velocity coupling. Iterations were started with an initial guess of zero everywhere. Sufficient time was given for the flow to develop using a constant time step of 1.667ms. A convergence criterion of 10^{-3} was used for continuity and 10^{-5} for transport equations of momentum and species conservation.

RESULTS AND DISCUSSION

The two-dimensional unsteady simulations were primarily aimed at investigating the flow-field evolution of the laminar helium jet injected into the ambient air. Computed results address the spatial and temporal development of the jet providing concurrent visualizations of mass and momentum transport processes. In particular, the effect of buoyancy and inflow conditions on the stable/unstable modes was studied. Table 1 summarizes the test conditions considered for the numerical analysis using the commercial CFD code, **FLUENT**.

Table 1. Summary of test conditions.

Case	Reynolds Number	Richardson Number	Frequency, Hz		Gravitational Acceleration, m/s^2
			Exp	Comp	
1	300	1.52	12	14	9.81
2	300	0.0	Non-osc	Non-osc	0.0
3	150	6.25	17	13	9.81
4	30	152	Non-osc	Non-osc	9.81

The numerical results are presented in the following order. First, the code validation and grid independence studies are discussed. Next, the oscillating/non-oscillating modes arising because of gravity are examined from Cases 1 and 2. For Case 3, simulations are performed at Earth gravity to study flow features similar to Case 1. For Case 4, the effect of inflow conditions on an evolving buoyant jet was investigated.

Grid Convergence Study

Computational models with different grid sizes were analyzed for the Re=150 case. The grid refinement was performed selectively in the near field region i.e z/d=0.0 to 3.0. Grid convergence check was implemented at several locations throughout the near field and the results demonstrated that the solution was grid independent. For brevity, grid independence study performed for r/d=0.5 and z/d=0.6 is presented in Fig. 2.

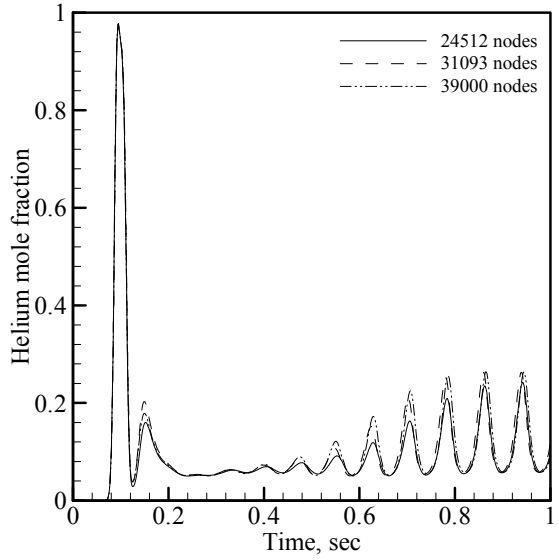

Fig 2: Temporal evolution of helium mole fraction for various grid sizes.

At this location, the helium mole fraction increases and then decreases rapidly followed by the gradual onset of flow oscillations at about t=0.7s. As seen from the plot, the solution was found to be grid independent. Considering a balance between computational time and accuracy of the solution, the grid size of approximately 31093 nodes with a time step size of 0.0016s was chosen for further analysis.

Validation

The numerical model was validated by comparing results with the experimental data of Pasumarthi [9] as shown in Fig. 3. Results showed that good qualitative agreement was reached between simulated and experimental instantaneous helium concentration fields. It can be seen that computations replicated the experiments proving the model's reliability and competency in predicting the flow features characterizing the vortex and its propagation, entrainment characteristics and above all, the flow repeatability observed at Earth gravity conditions. Even during the change from Earth to zero gravity, the phenomena of gradual diminishing of flow oscillations observed experimentally were effectively captured by the computational model as documented in ref. 22.

Effects of Buoyancy on Near-Field Flow Evolution

The space-time evolution of buoyant/non-buoyant helium jets was investigated systematically to gain insight into the conditions leading to the stable/unstable modes and the basic convective mixing patterns that result from entrainment and/or diffusion. The flexibility of varying the buoyancy forces in computations was utilized to examine the structural development of the jet for the Re=300 case in Earth and zero gravity environments. Figs. 4 and 5 show a sequence of images of the helium concentration field superimposed with velocity vectors. Images are shown at a time interval of 0.0167s for Earth gravity in Fig. 4 and zero gravity in Fig. 5 until the stable/unstable modes were observed. Note that the larger black dot in the images represents the vortex core and the smaller dot represents the approximate point of entrainment.

At Earth gravity conditions, the image sequence started with the ejection of jet fluid inside the tube as seen at t=0.016s. A hemi-spherical dome structure representing the initial mass of the jet fluid was evident at this instant. Though the jet fluid has not reached the tube exit plane, recirculating flow is observed at the tube exit owing to the displacement of the heavy ambient fluid from the tube. Subsequently, at t=0.033s the fluid exits the tube because of the jet momentum. The hemispherical jet front deforms itself into a flattened one and the formation of the initial vortex ring is evident.

As the lighter jet fluid encountered the heavy ambient surroundings at t=0.050s, the jet flow structure was primarily affected by three physical mechanisms: 1. The stream wise motion of the jet driven by momentum/buoyancy. 2. The hydrodynamic downward force acting on the advancing front due to the suspension of the heavy fluid on light fluid. 3. The lateral contraction effects due to density differences. Under the effect of these forces and energy transfer from the upstream region (stem), the advancing front transforms itself into a mushroom shaped cap structure by t=0.066s. Contraction of the

Track-1 TOC

Proceedings of HT-FED04
2004 ASME Heat Transfer/Fluids Engineering Summer Conference
July 11-15, 2004, Charlotte, North Carolina USA

HT-FED04-56794

EFFECTS OF MEAN FLOW PROFILES ON THE INSTABILITY OF A LOW-DENSITY GAS JET INJECTED INTO A HIGH-DENSITY GAS

NandaKishore Vedantam and Ramkumar. N. Parthasarathy
University of Oklahoma
School of Aerospace and Mechanical Engineering
Norman, Oklahoma 73019
USA
Telephone: (405) 325-1735
Fax: (405) 325-1088
E-mail: rparthasarathy@ou.edu

ABSTRACT

The effects of the mean velocity profiles on the instability characteristics in the near-injector region of axisymmetric low-density gas jets injected vertically upwards into a high-density gas medium were investigated using linear inviscid stability analysis. The flow was assumed to be isothermal and locally parallel. Three velocity profiles, signifying different changes in the mean velocity in the shear layer, were used in the analysis. The effects of the inhomogeneous shear layer and the Froude number (signifying the effects of gravity) on the instability for each set of mean profiles were delineated. At a large Froude number (negligible gravity), a critical density ratio was found for the three profiles at which the jet became absolutely unstable. The critical density ratio for each velocity profile was increased as the Froude number was reduced. A critical Froude number was found for the three sets of profiles, below which the jet was absolutely unstable for all the density ratios less than unity, which demarcated the jet flow into the momentum-driven regime and the buoyancy-driven regime.

NOMENCLATURE

English Symbols

C_1	constant of integration
C_2	constant of integration
Fr	Froude number
g	acceleration due to gravity
k	wavenumber
L	potential core length
m	azimuthal wavenumber
N	parameter that controls the jet mixing layer thickness for Sohn's profiles
P	turbulent Prandtl number
p	pressure
r	radial coordinate
R	half jet width
S	Density ratio
t	time
u	jet axial velocity component
U	jet base velocity
v	jet radial velocity component
w	jet azimuthal velocity component
x	axial coordinate

Greek Symbols

ϕ	azimuthal coordinate
λ	wavelength
Λ	velocity ratio
ρ	fluid mass density
θ	shear layer momentum thickness
Ω	angular frequency

Superscripts

$( )'$	fluctuations
$(\bar{\ })$	averaged variable
(^)	amplitude of variable

Subscripts

∞	ambient gas property
j, c	low-density gas property

INTRODUCTION

The stability characteristics of low-density gas jets discharged into a high-density ambient gas medium are of considerable practical interest because of their occurrence in a wide variety of applications such as fuel leaks, engine and industry exhaust, space propulsion, plumes, and natural phenomena such as fires and volcanic eruptions. Experimental studies by Monkewitz et al [1], Subbarao and Cantwell [2], Kyle and Sreenivasan [3], and Cetegen and Kasper [4] revealed that under certain conditions, the inhomogeneous (variable density) gas jets exhibited self-excited oscillations, which appear to be a direct consequence of the instability of the jet shear layer. Linear stability analysis has been an effective tool for the study of instability characteristics of such shear flows due to its relative computational simplicity.

Michalke and Hermann [5] investigated the influence of co-flow velocity on the stability of a constant density jet using inviscid linear stability theory. The flow was assumed to be isothermal, and viscous and diffusion effects were ignored. A hyperbolic tangent mean velocity profile was assumed across the jet cross-section. The results indicated that with increasing downstream distance, the jet velocity profiles became less unstable; the peak of the turbulence spectrum was shifted to lower frequencies. Inspection of the instability characteristics showed that the spatial growth rate of the axisymmetric and azimuthal disturbances was reduced by the coflow, but the range of unstable wave frequencies and the phase velocity were increased. The results were in good agreement with experimental results of Michalke and Michel [6]. Most of the earlier theoretical investigations by Michalke [7], Crighton and Gaster [8], Morris [9] and many others were concentrated on round homogeneous gas jets.

Monkewitz and Sohn [10] studied the linear impulse response of the flow by re-examining the linear inviscid stability of heated compressible axisymmetric jets. The flow was assumed to be locally parallel with an infinite Froude number and zero Eckert number. A two-parameter family of mean velocity and density profiles with a variable ratio of mixing layer thickness to jet diameter was assumed. The instability results indicated that, for axisymmetric disturbances in the potential core region, the heated jet became absolutely unstable for exit density ratios (ratio of density of the jet to the density of the ambient gas) less than 0.72. This study raised the possibility that the heated jets could be subjected to self-excited oscillations under certain operating conditions. Yu and Monkewitz [11] performed a linear stability analysis of two-dimensional inertial jets and wakes in a similar fashion. The density variation was achieved by specifying a mean temperature profile similar to the mean velocity profile. It was found that the low-density of the high-speed fluid promoted absolute instability, while low-density of the low-speed fluid had an opposite effect. The absolute frequencies and wavenumbers scaled with the jet/wake width and not on the thickness of the individual mixing layers, which indicated that the absolute instability was brought about mainly by the interaction of the two mixing layers.

In all the theoretical work cited above, the effects of buoyancy were completely neglected. Extensive research in the past decade has led to the recognition of the fact that buoyancy plays a considerable role in the instability mechanism of the jet even for low Richardson number flows. Lawson [12] investigated the effects of buoyancy on the near-injector instability characteristics of a low-density gas jet emanating into a high-density gas by applying inviscid linear stability analysis. A hyperbolic tangent velocity profile, and a similar hyperbolic tangent density profile were assumed to account for the inhomogeneous shear layer. The presence of variable density within the shear layer resulted in an increase in the temporal amplification rate of the disturbances, an increase in the range of unstable frequencies, and a reduction in the phase velocity of the disturbances. A critical density ratio of 0.52 was found at which the jet first became absolutely unstable for large Froude numbers. Yep et al. [13] conducted experiments on helium jets injected into air both in Earth gravity and microgravity. The jet flow was visualized using quantitative rainbow schlieren deflectometry. The results revealed that global flow oscillations observed under terrestrial conditions were absent in microgravity, providing direct physical evidence that the flow oscillations were buoyancy-induced.

There is a discrepancy between the theoretical results obtained by Lawson [12] and experimental results of Yep et al. [13]. Lawson [12] obtained a critical density ratio of 0.52; i.e., even with negligible buoyancy effects, the jet became absolutely unstable for density ratios less than 0.52, whereas, the results of Yep et al. [13] indicated no instability for a density ratio of 0.14. One of the reasons for this discrepancy could be the mean velocity and density profiles assumed in the analysis. The present study aims at investigating the effects of mean velocity and density profiles on the linear instability characteristics of a low-density gas jet injected into a quiescent high-density ambient gas.

LINEAR STABILITY ANALYSIS

Mean Flow

A round jet of a low-density gas injected vertically upwards into a high-density quiescent ($U_\infty = 0$) gas is considered, with ρ_j and ρ_∞ being the densities of low-density and high-density gas respectively. The centerline velocity of the jet is U_j and R is the half jet width. Since the jet is round and axisymmetric, cylindrical coordinates centered at the origin of the jet are chosen for convenience. The fluid properties of the jet such as viscosity and density are expressed in terms of the mixture fraction, *f,* which is the mass fraction of the injected gas in unit mixture of the injected gas and the ambient gas. Viscous effects are neglected; the usual parallel flow assumption is made.

The jet flow is divided into two components using Reynolds decomposition. The mean flow is specified as

$$\begin{aligned} &\bar{u} = \bar{u}(r), \quad \bar{v} = 0, \quad \bar{w} = 0, \quad \bar{p} = \bar{p}(r), \\ &\bar{f} = \bar{f}(r), \quad \text{and} \quad \bar{\rho} = \bar{\rho}(r) \end{aligned} \tag{1}$$

and the disturbed components of the fluid quantities admit the following normal mode exponential form:

$$\left(u', v', w', p', \rho'\right) = \left[\hat{u}(r), \hat{v}(r), \hat{w}(r), \hat{p}(r), \hat{\rho}(r)\right] e^{i(kx - \Omega t + m\varphi)} \tag{2}$$

where $\hat{u}(r),\hat{v}(r),\hat{w}(r),\hat{p}(r)$ and $\hat{\rho}(r)$ are the velocity, pressure and density amplitudes of the disturbance wave. m is the azimuthal mode or azimuthal wavenumber (m=0 is the axisymmetric mode which is considered in this study). And, $k = k_r + ik_i$ and $\Omega = \Omega_r + i\Omega_i$ are the complex wavenumber and the complex frequency, respectively. The real wavenumber k_r is related to the wavelength λ by $k_r = 2\pi/\lambda$, and the real circular frequency Ω_r is proportional to the Strouhal number based on the jet exit velocity and half jet-width. The imaginary quantities k_i and Ω_i are the spatial and temporal amplification rates of disturbances, respectively.

Introducing Eq. (1) and Eq. (2), in the basic conservation equations, a second-order linear differential equation in $\hat{p}$ is obtained as given in Eq. (3). The details of the derivation are given in detail by Vedantam [14].

$$\frac{d^2\hat{p}}{dr^2}+\left[\frac{1}{r}-\frac{2\frac{d\bar{u}}{dr}}{\bar{u}-\frac{\Omega}{k}}-\frac{1}{\rho}\frac{d\bar{\rho}}{dr}\left(1+\frac{ig}{k\left(\bar{u}-\frac{\Omega}{k}\right)^2}\right)\right]\frac{d\hat{p}}{dr}-k^2\hat{p}=0 \qquad (3)$$

If the density gradient is zero, Eq. (3), reduces to the disturbance equation used by Michalke and Hermann [5] for constant-density jets. Further, if $r\to\infty$ and the effects of gravity are neglected, Eq. (3) turns into the disturbance equation used by Yu and Monkewitz [11] for the instability analysis of inertial jets. The present analysis differs from that of Michalke and Hermann [5] and Monkewitz and Sohn [10] by considering the effects of buoyancy in the form of an additional term in the disturbance equation.

In the present analysis, all lengths are normalized by the half jet-width R, the density is normalized by the ambient fluid density ρ_∞, the velocity is normalized by the exit velocity Uj and the pressure is normalized by $\rho_j U_j^2$. The acceleration due to gravity g in the Eq. (3), when normalized, yields the Froude number, Fr, defined as the ratio of inertial forces to buoyancy forces.

$$Fr^2=\frac{U_j^2}{gR}\frac{\rho_j}{\rho_\infty-\rho_j} \qquad (4)$$

Mean Velocity and Density Profiles

In order to solve the disturbance equation (3), mean velocity and density profiles need to be assumed. For the present analysis, three sets of mean velocity and density profiles are assumed to perform the linear stability analysis. Figures 1 and 2 illustrate the three velocity and density profiles assumed.

First Set of Mean Flow Profiles

The first set of mean velocity and density profiles used for this study are the ones used by Michalke and Hermann [5], Crighton and Gaster [8], Lawson [12]:

$$\frac{\bar{u}(r)}{U_j}=0.5\left\{1-\tanh\left[0.25\frac{R}{\theta}\left(\frac{r}{R}-\frac{R}{r}\right)\right]\right\} \qquad (5)$$

where, R/θ is the jet parameter that characterizes the jet velocity profile at various axial locations. Crighton and Gaster [8] specified a relation between the jet parameter R/θ and the normalized axial distance x/R.

$$\frac{R}{\theta}=\frac{100}{3\frac{x}{R}+4} \qquad (6)$$

Equation (6) is valid only for the case of zero co-flow velocity. Different values of R/θ used for this study lies between R/θ = 25 and 10, which corresponds to x/R = 0 and 2.0, respectively.

The density profile in the shear layer is assumed to be similar:

$$\bar{\rho}(r)=0.5\rho_\infty\left\{2+\left(\frac{\rho_j}{\rho_\infty}-1\right)\left(1-\tanh\left[0.25\frac{R}{\theta}\left(\frac{r}{R}-\frac{R}{r}\right)\right]\right)\right\} \qquad (7)$$

From this point onward, this set of mean flow profiles is referred to as the *hypertan profiles*.

Second Set of Mean Flow Profiles

The second set of mean velocity and density profiles used are those assumed by Monkewitz and Sohn [10]:

$$\frac{2\bar{u}(r)}{U_j}=1-\Lambda+2\Lambda F(r) \qquad (8)$$

$$F(r)=\left[1+\left[\exp\left(r^2\ln 2\right)-1\right]^N\right]^{-1}$$

$$N^{-1}=\begin{cases}0.02+0.869\left(x/L\right)-0.031(x/L)^{6.072}, & x<1.35L\\ 1, & x\geq 1.35L\end{cases}$$

$$L=\left[8.0+2.5\ln\left(S_e\right)\right]$$

In the present analysis, the velocity ratio Λ=1, and the value of jet parameter x/L is varied from 0 to 0.65 which is well within the near-injector region allowing for the effects of buoyancy to manifest as the jet proceeds downstream from x/L = 0. Depending upon the value of N, the velocity profiles lie between a cylindrical vortex sheet ($N\to\infty$) and a Gaussian profile (N=1) suitable for the asymptotic region.

Based on the experimental results of Reichardt discussed by Schlichting [15], a relation is specified between the velocity and density profiles as

$$\frac{1/\rho-1}{1/S-1}=\left(\frac{u+R-1}{2R}\right)^P \qquad (9)$$

$$\frac{\bar{\rho}(r)}{\rho_\infty}=\left[1+\left(1/S-1\right)\left[F(r)\right]^P\right]^{-1}$$

$$P=\begin{cases}1 & x\leq 0.64L\\ 0.8+0.2\cos\left[2.49(x/L)-1.60\right] & 0.64L<x<1.90L\\ 0.6 & 1.90L\leq x\end{cases}$$

where the exponent P is the turbulent Prandtl number whose values at various downstream locations are determined from the

experimental data of Brown and Roshko [16] and Corrsin and Uberoi [17]. These profiles will be referred to as the *Sohn's profiles*.

Third Set of Mean Flow Profiles

The third set of mean profiles includes a parabolic velocity profile (for fully-developed pipe flow) and a hyperbolic tangent density profile:

$$\frac{\bar{u}(r)}{2U_j} = \left[1 - \left(\frac{r}{R}\right)^2\right] \tag{10}$$

The jet velocity at various axial locations is characterized by the jet parameter, R/θ. The R/θ values used for this analysis are 25 and 10, which corresponds to the normalized axial distances of x/R=0 and 2, respectively. The density profile assumed is the hyperbolic tangent profile same as that of the hypertan profiles given in Eq. (7).

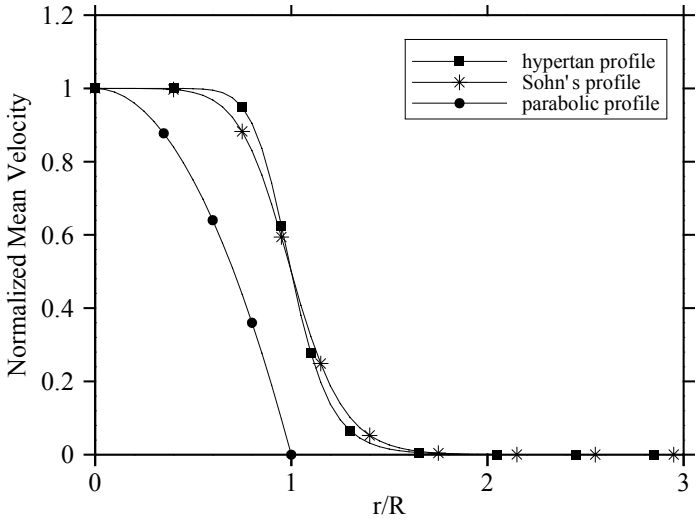

Fig. 1. Normalized mean velocity profiles at a location equivalent to x/R = 2.

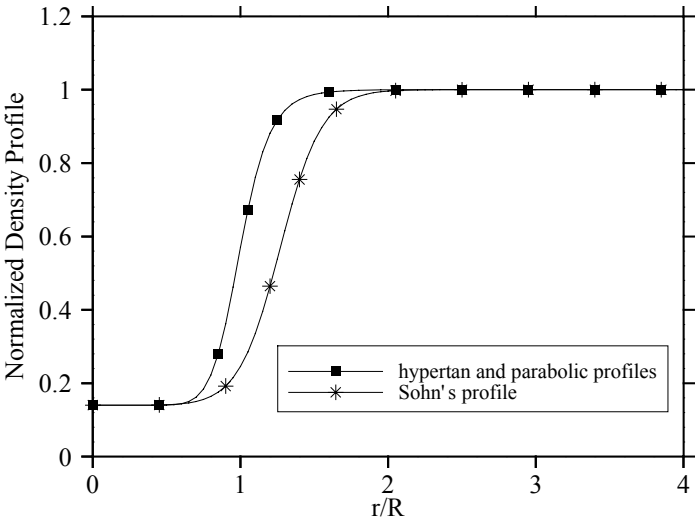

Fig. 2. Normalized mean density profiles at a location equivalent to x/R = 2.

Method of Solution

By specifying the mean velocity and density profiles, Eq. (3) is solved for the eigenvalues that satisfy the boundary condition given in Eq. (11).

$$\hat{p}(0) \text{ is finite} \qquad \text{when } m = 0 \tag{11}$$

Since $d\bar{u}/dr$ and $d\bar{\rho}/dr$ vanish as $r\to 0$ and $r\to\infty$, asymptotic solutions for Eq. (3) are sought. The asymptotic solutions for Eq. (3) that satisfy the boundary condition given in Eq. (11) are

$$\hat{p}^{(i)} = C_1 I_0(kr) \tag{12}$$

$$\hat{p}^{(o)} = C_2 K_0(kr) \tag{13}$$

where the superscripts i and o represent the inner and outer solutions respectively. The inner solution is valid close to the jet centerline and the outer solution is valid in the far-field. Here I_0 and K_0 are the modified Bessel functions of order zero, and C_1 and C_2 are the arbitrary constants. For the parabolic profiles, $d\bar{u}/dr$ vanishes as $r\to\infty$ but it does not vanish as $r\to 0$ (equal to zero only at r=0). Hence, the asymptotic solutions given in Eq. (12) and Eq. (13) does not hold good. Alternately, a Frobenius series solution for Eq. (3), satisfying the boundary condition given in Eq. (11), is obtained for $r\to 0$ as given by Vedantam [14].

A classical fourth-order Runge-Kutta scheme with adaptive step-size control is used to integrate the pressure disturbance equation given in Eq. (3). The infinite integration domain extending from the jet centerline to a far field away from the centerline, $0 < r < \infty$ is divided into two finite domains: an inner domain $0 \le r \le R$ and an outer domain $R \le r \le r_\infty$, where R is the half jet width and r_∞ is a specified large radius. The far field integration limit, r_∞ for this analysis is appropriately chosen as $4R$ at which the velocity and density gradients are small and almost negligible. A shooting method is used to determine $\Omega(k)$ such that both $\hat{p}$ and $d\hat{p}/dr$ are continuous at $r = R$. Two kinds of analysis, namely, temporal and spatio-temporal analysis are conducted. In temporal stability analysis, the complex frequency, Ω is determined as a function of real wavenumber, k. In spatio-temporal stability analysis, both Ω and k are considered complex.

Criteria for Absolute and Convective Instability

According to Briggs [18] and Bers [19], to determine whether the existing spatio-temporal instability is absolute or convective it is important to locate the saddle point in the complex (Ω^0, k^0) domain and to check whether it meets the pinching requirements. The numerical method specified by Li and Shen [20] was used for locating these saddle points and pinch points. A computed pinch point for the case of $Fr\to\infty$, R/θ=10 and density ratio, S=0.14 for the hypertan profiles is illustrated in Fig. 3.

When the jet is absolutely unstable, the initially localized disturbances grow with time and space, and eventually infect the entire flow. Whereas, if the jet is convectively unstable, the disturbances grow as they are convected downstream and at a

particular spatial location these disturbances appear to die with time. The nature of instability is determined depending upon the imaginary part, Ω_i^0 of the complex frequency Ω^0 of the pinch point. The Ω_i^0 represents the temporal amplification rate of the disturbances. If $\Omega_i^0 > 0$, then the flow is absolutely unstable and if $\Omega_i^0 < 0$ then the flow system is convectively unstable. The temporal and absolute instability characteristics are obtained by locating the pinch points for the three sets of mean velocity and density profiles by varying the parameters such as *x/L*, *R/θ*, *Fr* and ratio of density of the jet to the density of the ambient gas, *S*.

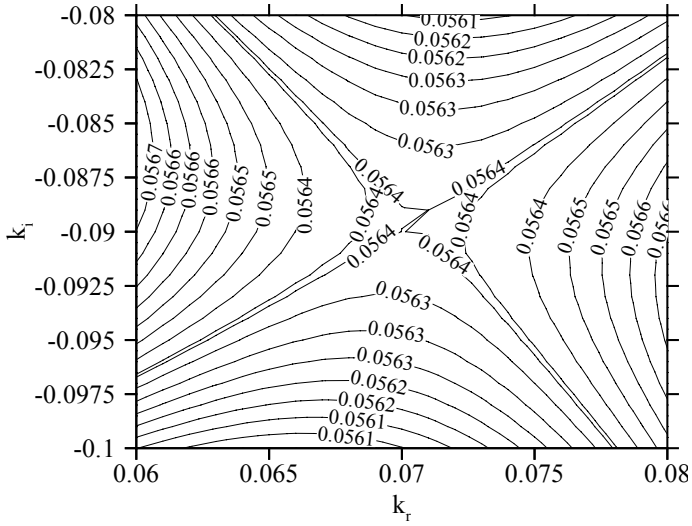

Fig. 3. Contour plot of Ω_r, in the k-plane, for the hypertan profiles at R/θ =10, Fr = ∞ and density ratio ρ_j/ρ_∞=0.14 illustrating a pinch point.

TEMPORAL ANALYSIS RESULTS

In order to determine the limits in the complex *k*-plane, for the mesh searching process used to locate the saddle points and pinch points for the absolute analysis, and also to explore the effects of the inhomogeneous shear-layer and buoyancy on the temporal evolution of the disturbances, a temporal stability analysis is first performed. The temporal analysis is carried out at a normalized axial distance of x/R = 2 from the jet exit, where the jet parameter value for the hypertan and parabolic profiles is R/θ=10 and for the Sohn's profiles, the combination of *x/L* and density ratio *S* (ρ_j/ρ_∞) is equivalent to R/θ = 10.

Effect of Inhomogeneous Shear Layer

The lone effects of inhomogeneous shear-layer on the temporal (time) evolution of instabilities of the jet are investigated by fixing the Froude number *Fr* at a very large value tending to infinity (negligible buoyancy) and varying density ratio from *S* = 1 (air-in-air jet) to *S* = 0.14 (helium-in-air jet). The variation of normalized temporal growth rate of the instabilities, Ω_i, with the normalized wavenumber, *k*, for the hypertan, Sohn's, and the parabolic profiles is depicted in Fig. 4. For the density ratio of 1.0, the temporal growth rate for the parabolic profiles is so low compared to the other density ratios that it is not shown in the figure. Hence, Fig. 4(c) depicts the temporal growth rates for the density ratios 0.9 to 0.14.

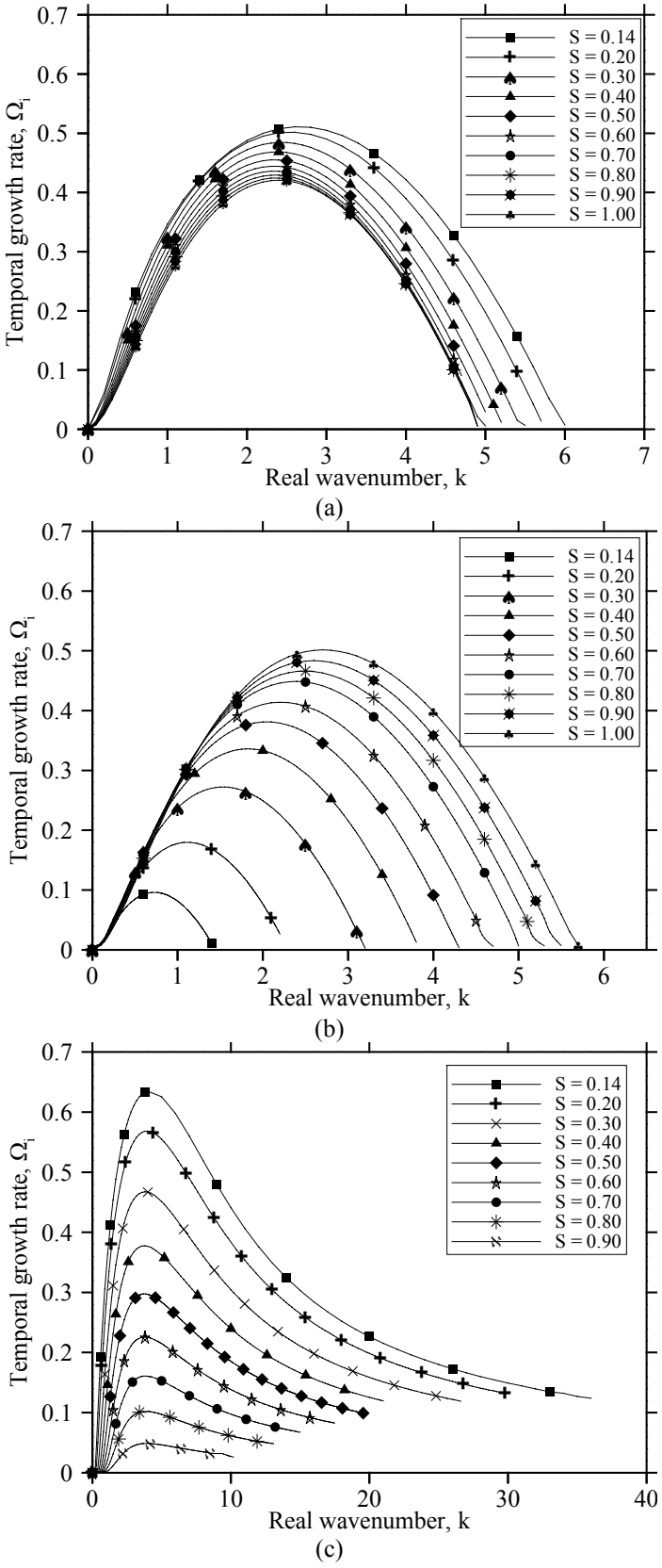

Fig. 4. The variation of temporal growth rate Ω_i with the wavenumber *k* for (a) the hypertan profiles, (b) the Sohn's profiles, and (c) the parabolic profiles at *x/R* = 2, *Fr*=infinity, and *S* = 0.14, 0.2, 0.3, 0.4, 0.5, 0.6, 0.7, 0.8, 0.9, and 1.

For the hypertan and the parabolic profiles, the maximum temporal growth rate and the corresponding wavenumber are increased as the density ratio is reduced from 1.0 to 0.14, as can be seen from Fig. 4(a) and 4(c). The normalized wavenumber is the ratio of circumference of a jet of radius equal to half jet width, R, to the disturbance wavelength. As the density ratio is reduced, the range of unstable wavenumbers is increased indicating that range of unstable wavelengths decreases as the gas jet density is reduced below the value of ambient gas density. The maximum temporal growth rate occurs at a larger wavenumber with a decrease in the density ratio.

As illustrated in Fig. 4(b), the maximum temporal growth rate and the corresponding wavenumber for the Sohn's profiles decrease as the density ratio is reduced from 1.0 to 0.14. A decrease in jet density should cause a steepening of the density gradient in the shear layer, which would lead to additional generation of vorticity, and hence, should cause an increase in the temporal growth rate. But, in this case the temporal growth rate declines with the decrease in the jet density. The reason for this reverse trend is not clear. More work needs to be conducted to find the reason for this abnormal behavior.

Note, however, that the range of unstable wavenumbers is almost same for both Sohn and hypertan profiles. For the density ratio of 0.7, the temporal growth rate curves for both the profiles are almost identical and the value of maximum temporal growth rate is observed to be almost equal (a difference of less than 3% only). Also the value of wavenumber corresponding to the maximum temporal growth rate is almost same for both the profiles (only a difference of 4%). Moreover, for the density ratios of 0.5 to 1.0, the maximum temporal growth rate values and the corresponding wavenumber values differ by only 3% to 16%. This indicates that, the Sohn's profiles yield temporal instability results comparable with the hypertan profiles, for the density ratios between 0.5 and 1.0. The variation of temporal growth rate with the wavenumber, for the parabolic and the hypertan profiles, follows the same trend. At x/R=2, the maximum temporal growth rates for the parabolic profiles are comparable to the maximum temporal growth rates for the hypertan profiles for S >0.5.

Figure 5 depicts the variation of phase velocity with the wavenumber for the three profiles at x/R=2. For all the profiles, the phase velocity of the disturbances decreases at all the unstable wavenumbers as the density ratio is reduced. Also, the phase velocity of the disturbances decreases with increasing wavenumber for each density ratio. The phase velocity of the disturbance is the ratio of the real part of the frequency to the wavenumber of the disturbance. Hence, the unstable frequencies can be determined from the product of the phase velocity and the corresponding wavenumbers. For all the three profiles, the phase velocity of the disturbances exhibit a similar trend and characteristics, with the only disparity being the increase in the range of the unstable frequencies in the case of hypertan and parabolic profiles and decrease in the range of the unstable frequencies in the case of Sohn's profiles with decreasing density ratio. For the parabolic profiles, the phase velocity is greater than 1 for the wavenumbers less than or equal to 1.0 at the density ratio of 0.5; as the density ratio is increased from 0.5 to 0.9, the phase velocity is greater than 1 for the wavenumbers less than or equal to 1.6.

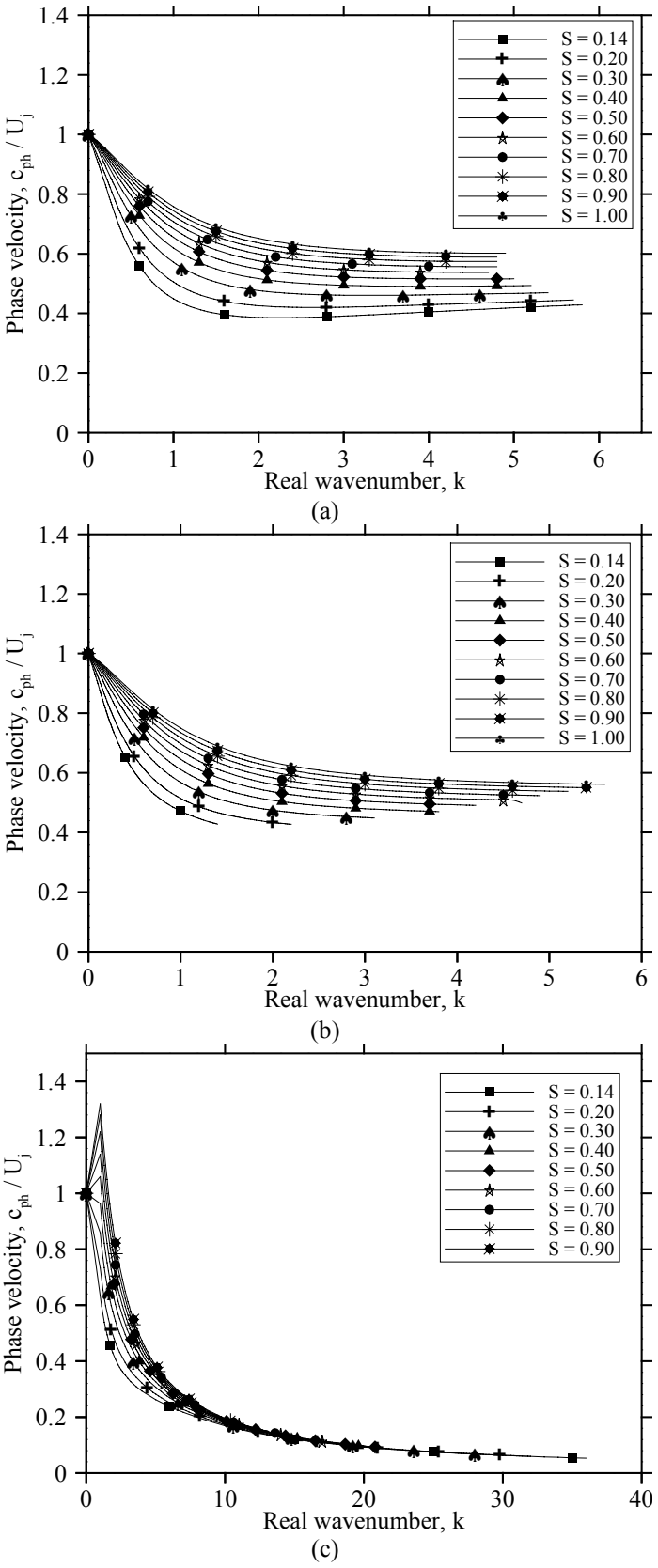

Fig. 5. The variation of phase velocity c_{ph}/U_j with the wavenumber k for (a) the hypertan profiles, (b) the Sohn's profiles, and (c) the parabolic profiles at x/R = 2, Fr=infinity, and S = 0.14, 0.2, 0.3, 0.4, 0.5, 0.6, 0.7, 0.8, 0.9, and 1.

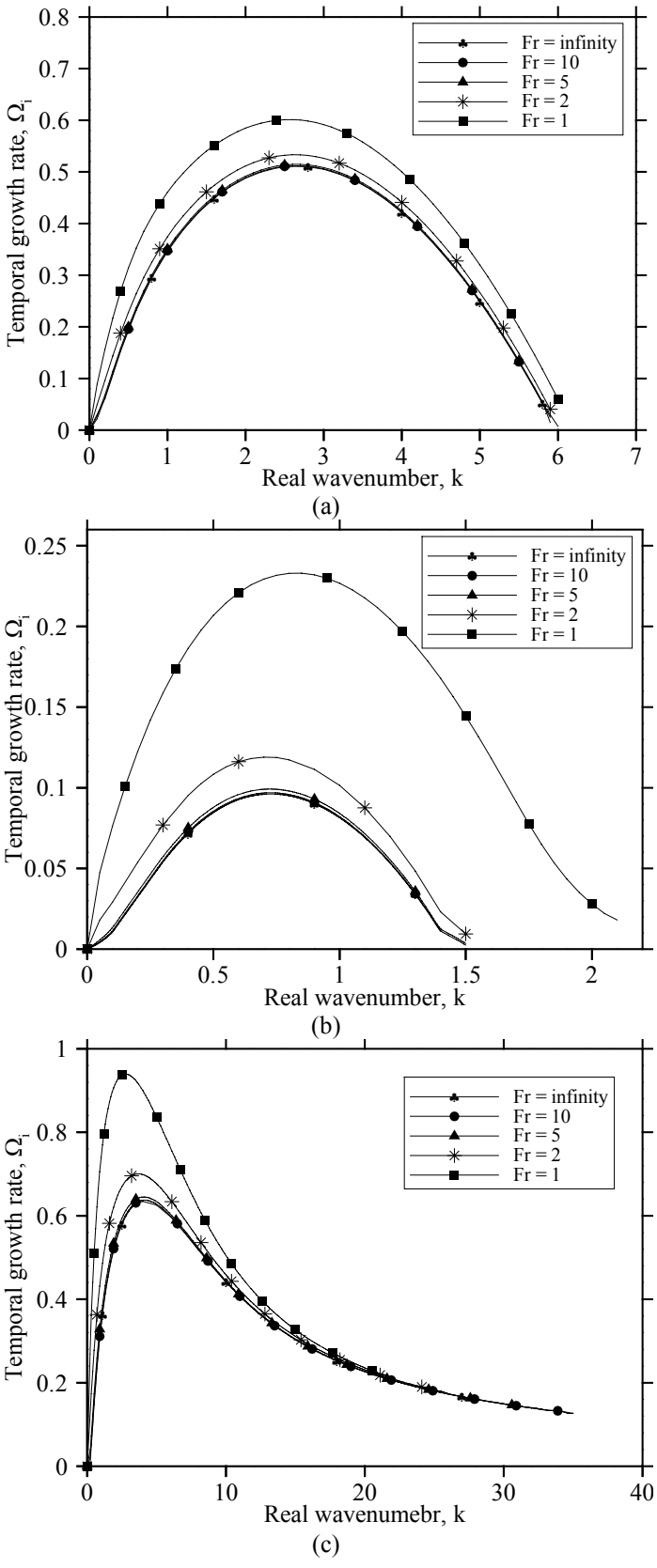

Fig. 6. The variation of temporal growth rate Ω_i with the wavenumber k for (a) the hypertan profiles, (b) the Sohn's profiles, and (c) the parabolic profiles at x/R = 2, S = 0.14, and Fr = ∞, 10, 5, 2, and 1.

Effects of Buoyancy

The effects of the buoyancy on the jet temporal instability are determined by considering finite values of the Froude number. The density ratio is fixed at 0.14 and the Froude number is varied from infinity (very large value) to 1. The lower the value of the Froude number, the more dominant are the effects of buoyancy on the jet instability characteristics.

The variation of the temporal growth rate with the wavenumber for the three profiles, at x/R=2, as the Froude number is reduced from infinity to 1 is illustrated in Fig. 6. The temporal growth rates are increased with the decrease in the Froude number for all the three profiles. The variation of temporal growth rate with the wavenumber for the three profiles exhibits a similar trend with the decrease in the Froude number. As the Froude number is reduced from a very large value (infinity) to 5, the maximum temporal growth rate shows no significant change. A small increase in the maximum temporal growth rate is observed as the Froude number is reduced from 5 to 2. But, as the Froude number is further reduced from 2 to 1, a large increase in the maximum temporal growth rate for all the three profiles is observed. As the Froude number is reduced from infinity to 1, the wavenumber corresponding to the maximum temporal growth rate and the range of unstable wavenumbers for the hypertan profiles remain unchanged. For the Sohn's profiles, the wavenumber corresponding to the maximum temporal growth rate and the range of unstable wavenumbers exhibit no significant change except for Fr=1. For the parabolic profiles, the wavenumber corresponding to the maximum temporal amplification rate remains unchanged for $Fr \geq 5$ and decreases for $Fr \leq 2$, and the range of unstable wavenumbers decreases as the Froude number is reduced.

SPATIO-TEMPORAL ANALYSIS RESULTS

In order to determine the absolute stability characteristics of the jet and to determine the nature of the absolute instability, a spatio-temporal stability analysis is performed. The effects of density ratio and buoyancy on the absolute stability characteristics of the jet are studied. The nature of the absolute instability (whether absolutely unstable or convectively unstable) of the jet for the three profiles is examined.

Effect of Variable Density Ratio

A constant-density ratio jet is convectively unstable. But, as the density ratio is reduced gradually, the nature of instability of the jet is changed from convective instability to absolute instability. The density ratio at which the absolute temporal growth rate changes its sign, i.e. the density ratio at which Ω_i^0=0, where the jet first becomes absolutely unstable, is referred to as the critical density ratio, S_c.

The variation of absolute temporal growth rate of disturbances, Ω_i^0, with the density ratio for the three profiles is depicted in Fig. 7. For the hypertan and the parabolic profiles, the absolute temporal growth rate is negative (convectively unstable) at the density ratio of 0.99 and as the density ratio decreases from 0.99 to 0.14, the absolute growth rate gradually increases to a positive value and further. The critical density ratio, S_c, is found to be 0.525 for the hypertan profiles and 0.843 for the parabolic profiles. For the Sohn's profiles, the absolute temporal growth rate increases as the density ratio decreases from 0.99 to 0.3, and

NUMERICAL SIMULATIONS OF BUOYANCY EFFECTS IN LOW DENSITY GAS JETS

R. P. Satti*, K. S. Pasumarthi* and A. K. Agrawal#

School of Aerospace and Mechanical Engineering

University of Oklahoma, Norman, OK-73019, USA

ABSTRACT

This paper deals with the computational analysis of buoyancy effects in the near field of an isothermal helium jet injected into quiescent ambient air environment. The transport equations of helium mass fraction coupled with the conservation equations of mixture mass and momentum were solved using a staggered grid finite volume method. Laminar, axisymmetric, unsteady flow conditions were considered for the analysis. An orthogonal system with non-uniform grids was used to capture the instability phenomena. Computations were performed for Earth gravity and during transition from Earth to different gravitational levels. The flow physics was described by simultaneous visualizations of velocity and concentration fields at Earth and microgravity conditions. Computed results were validated by comparing with experimental data substantiating that buoyancy induced global flow oscillations present in Earth gravity are absent in microgravity. The dependence of oscillation frequency and amplitude on gravitational forcing was presented to further quantify the buoyancy effects.

Keywords: Buoyancy, Flow computations, Flow Instability.

INTRODUCTION

Low density gas jet flows are encountered in many engineering and technical applications such as smokestack discharge, fuel leak, space propulsion, aerosol spray, jets entering mixing chamber, ventilation jets and many other environmental issues relating to atmosphere and hydrosphere. Jets are termed as buoyant for Richardson number, $Ri = gd(\rho_\infty - \rho)/\rho V^2 > 1.0$ and inertial for $Ri << 1.0$. The present study examines the near field flow structure of a buoyant helium jet injected into quiescent ambient air environment.

Several studies[1-6] have focused on the far field behavior of jets. However, the near field flow stability has direct influence on the entrainment and flow pattern in the far field. Self-excited oscillations in the near injector region of low-density gas jets have been studied extensively. Subbarao and Cantwell[7] observed highly periodic oscillations in the near field of helium jets injected into a co-flow air environment for Ri between 0.5 and 6.0. The Strouhal number, St=fd/V correlated with Richardson number for Ri>1.0 indicating buoyancy dependent instability mode. Similar experiments were conducted by Cetegen[8-10] for axisymmetric and planar plumes, whereby buoyancy induced toroidal vortical structures contaminating the primary jet flow were observed. Agrawal and co-workers[11-12] conducted experiments to characterize the flow instability in terms of concentration measurements across the whole field of a helium jet injected into quiescent air. Experiments by Yep et al.[11] demonstrated that flow oscillations were absent in the microgravity environment of the 2.2 s drop tower.

Few computational studies have also been a part of low-density jet instability literature. Mell et al.[13] performed numerical simulations of helium jet in air and found that the computed oscillation frequency matched with experimentally obtained value by Hamins et al[14]. Recently, Soteriou[15] revealed that the instability characteristics in buoyant planar plumes compared well with experiments, providing insight into the role played by viscous and buoyancy forces in establishing oscillating or non-oscillating modes.

The above studies provided extensive details relating to flow instability, attributed to buoyancy dominating the flow field. Although the instability in high Richardson number helium jets is attributed to buoyancy, direct physical evidence with respect to concurrent visualizations of velocity and concentration fields is lacking in the present literature.

* Graduate Research Assistant

Member AIAA, Associate Professor

If the instability is indeed caused by buoyancy, the near field flow structure of the jet will change significantly when buoyancy is removed. Thus, quantitative data on the spatial and temporal evolutions of the instability, length and time scales of the oscillating mode and its effects on the mean flow are needed in Earth gravity and microgravity conditions to delineate gravitational effects in buoyant jets.

Although microgravity experiments[11] have quantified buoyancy effects and provided details of the concentration field, results are devoid of the flow structure details. Simultaneous visualization of velocity and concentration fields is desired to fully understand the oscillating instability and consequent flow structure of the jet. Owing to the experimental limitations in obtaining such measurements, especially in microgravity, the present study utilizes computational analysis to simulate helium jet in air. Features of the jet are described in both Earth gravity and microgravity. In the following section, we provide details relating to the governing equations, boundary and initial conditions, and the computational procedure. Results obtained at Earth gravity and microgravity conditions are discussed subsequently.

NUMERICAL FORMULATION

Governing Equations

The governing equations for laminar, unsteady and axisymmetric flow are expressed in the cylindrical coordinate system as follows:

$$\frac{\partial \rho}{\partial t}+\frac{\partial}{\partial r}(\rho v r)+\frac{\partial}{\partial z}(\rho r w)=0 \qquad (1)$$

$$\frac{\partial(\rho\phi)}{\partial t}+\frac{\partial}{\partial r}(\rho v r\phi)+\frac{\partial}{\partial z}(\rho r w\phi)=\frac{\partial}{\partial r}\left(\Gamma^{\phi} r\frac{\partial \phi}{\partial r}\right)+\frac{\partial}{\partial z}\left(\Gamma^{\phi} r\frac{\partial \phi}{\partial z}\right)+S^{\phi} \qquad (2)$$

where ρ represents density; and w and v are, respectively, the axial and radial components of the velocity. Equation 1 represents the continuity equation and Equation 2 is the general transport equation, which reduces to momentum, or species conservation equation depending on the variable ϕ. The terms Γ^{ϕ} and S^{ϕ} in the transport equation represent the diffusion coefficient and source term of the variable ϕ. The coefficients and source terms appearing in Equation 2 are listed in Table 1. In this study, the temperature and pressure variations are considered to be negligible and the jet flow is assumed to be a binary fluid system.

Table 1. Coefficients and source terms in Equation 2.

ϕ	Γ^{ϕ}	S^{ϕ}
w	μ	$-r\frac{\partial p}{\partial z}+r(\rho_{\infty}-\rho)g+\frac{\partial}{\partial z}\left(r\mu\frac{\partial w}{\partial z}\right)+\frac{\partial}{\partial r}\left(r\mu\frac{\partial v}{\partial z}\right)-\frac{2}{3}\left[\frac{\partial}{\partial z}\left(r\mu\frac{\partial v}{\partial r}\right)+\frac{\partial}{\partial z}\left(r\mu\frac{\partial w}{\partial z}\right)\right]$
v	μ	$-r\frac{\partial p}{\partial r}-\frac{2}{3}\mu\frac{v}{r}+\frac{\partial}{\partial z}\left(r\mu\frac{\partial w}{\partial r}\right)+\frac{\partial}{\partial r}\left(r\mu\frac{\partial v}{\partial r}\right)-\frac{2}{3}\left[\frac{\partial}{\partial r}\left(r\mu\frac{\partial v}{\partial r}\right)+\frac{\partial}{\partial r}\left(r\mu\frac{\partial w}{\partial z}\right)\right]$
f	D_b	0

Thermo-Physical Properties

The density was computed from the incompressible ideal gas law as follows:

$$\rho=\frac{P_{op}}{RT\sum_i \frac{Y_i}{M_{w,i}}}=\frac{P_{op}}{RT\left[\frac{Y_{he}}{M_{w,he}}+\frac{Y_{air}}{M_{w,air}}\right]} \qquad (3)$$

The dynamic viscosity was calculated using the Wilke's mixture averaged formula[16] as follows:

$$\mu=\sum_{i=1}^{n}\frac{Y_i\mu_i}{\sum_{j=1}^{n}Y_j\phi_{ij}}=\frac{Y_{he}\mu_{he}}{Y_{he}\phi_{11}+Y_{air}\phi_{12}}+\frac{Y_{air}\mu_{air}}{Y_{he}\phi_{21}+Y_{air}\phi_{22}} \qquad (4)$$

with $$\phi_{ij}=\frac{\left[1+\left(\frac{\mu_i}{\mu_j}\right)^{1/2}\left(\frac{M_{w,j}}{M_{w,i}}\right)^{1/4}\right]^2}{\left[8\left(1+\frac{M_{w,i}}{M_{w,j}}\right)\right]^{1/2}}$$

where subscripts 1 and 2 represent helium and air, respectively. The binary diffusion coefficient of helium into air, D_b was specified as a constant.

Operating and Boundary Conditions

Figure 1 shows the computational domain extending 15d in the axial direction and 6d in the radial direction where d=31.8mm is the tube inside diameter. The upstream boundary was placed at a distance of 1d from the jet exit plane. Symmetric boundary condition was imposed along the jet centerline. At the tube inlet, the velocity profile was fully developed and the helium mole fraction was unity. The jet Reynolds number was specified as 300 corresponding to Richardson number of 1.52. No slip and zero mass diffusion conditions were imposed at the tube walls. At the exit boundary, pressure outlet condition was implemented instead of

outflow conditions to account for the backflow. Figure 1 shows pressure conditions imposed at other boundaries. The operating pressure and temperature in the domain were specified, respectively, as 1 atm and 300 K.

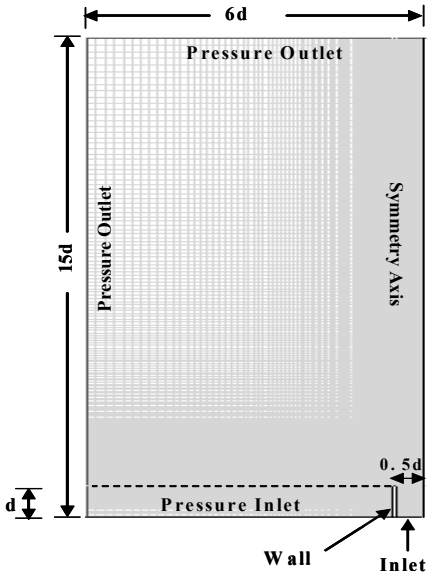

Figure 1. Computational domain.

Computational Details

The grid was generated by splitting the computational domain into five sub regions. An orthogonal non-uniform grid system was used. The grid elements in the radial direction were concentrated in the oscillatory zone. The grid size was increased gradually in the axial direction. The governing equations were solved sequentially using a segregated approach[17]. Since the governing equations are coupled, several iterations of the solution loop were performed before a converged solution was obtained. The pressure velocity coupling was achieved using the SIMPLEC algorithm.

RESULTS AND DISCUSSION

Numerical simulations were performed for the isothermal helium jet injected into the ambient air environment with the objective of isolating gravitational effects in the near field. First, grid sensitivity analysis was performed using different sizes of grids and the solution was found to be independent of the grid structure. Based on the analysis, a 260 x 95 grid was chosen for computations. In the following sections, we provide details pertaining to the self excited instability observed in the helium jet at Earth gravity conditions. Subsequently, the near field flow physics is explained as the jet undergoes change to microgravity conditions. Further insight is gained from the parametric study by varying the gravitational level. The change in the buoyant structure of the jet is illustrated from vortex convection velocity, and flow oscillation frequency and amplitude plots.

Self-Excited Oscillatory Structure in Earth Gravity

Periodic oscillations occur in the near field of the helium jet at Earth gravity conditions owing to buoyancy induced acceleration of the jet fluid. To illustrate this phenomenon, Figure 2 shows a sequence (1/73s apart) of helium mole percentage contours superimposed with velocity vectors. The jet boundary is demarcated by the 60-70% concentration level and the vortex core is represented by a black dot. At t=0.0s, buoyancy accelerates the jet core, which contracts to conserve the mass. The net result is entrainment of ambient fluid illustrated by the flow recirculation representing the vortex. In the next plot at t=1/73s, the vortex is characterized by larger recirculation region accompanied with greater contraction of the jet boundary, evident from the indentation in the concentration field. Subsequently, between t=2/73s and 4/73s, the vortex convects downstream while growing in size to further contaminate the jet core.

The vortex formation is accompanied by momentum transfer from the jet core to the vortex. This feature is evident in Figure 2 wherein vectors downstream of the vortex have higher magnitude than those upstream before interacting with the jet core. As the straining effect of the vortex diminishes in the upstream region, the jet expands at the exit inducting buoyant jet fluid to initiate another vortex at t=5/73s to repeat the oscillation cycle. The above results illustrate self excited periodicity in the jet at a frequency of 14.6 Hz, indicating both qualitative and quantitative agreement with experiments[11]. In the following sub-section, our study is focused on delineating buoyancy effects by simulating the jet flow in the absence of gravity.

Transition from Earth to Microgravity Conditions

Computations were performed to visualize the jet flow during change from Earth to microgravity conditions and to depict how the jet flow structure adjusts itself in the absence of buoyancy driven forces. As a first step, the simulation results were compared with experiments[11] to validate the computational model. Figure 3 shows a series of computational-experimental helium mole fraction contour plots during transition from Earth gravity to microgravity. Note that the experimental data were taken from Yep et al[11].

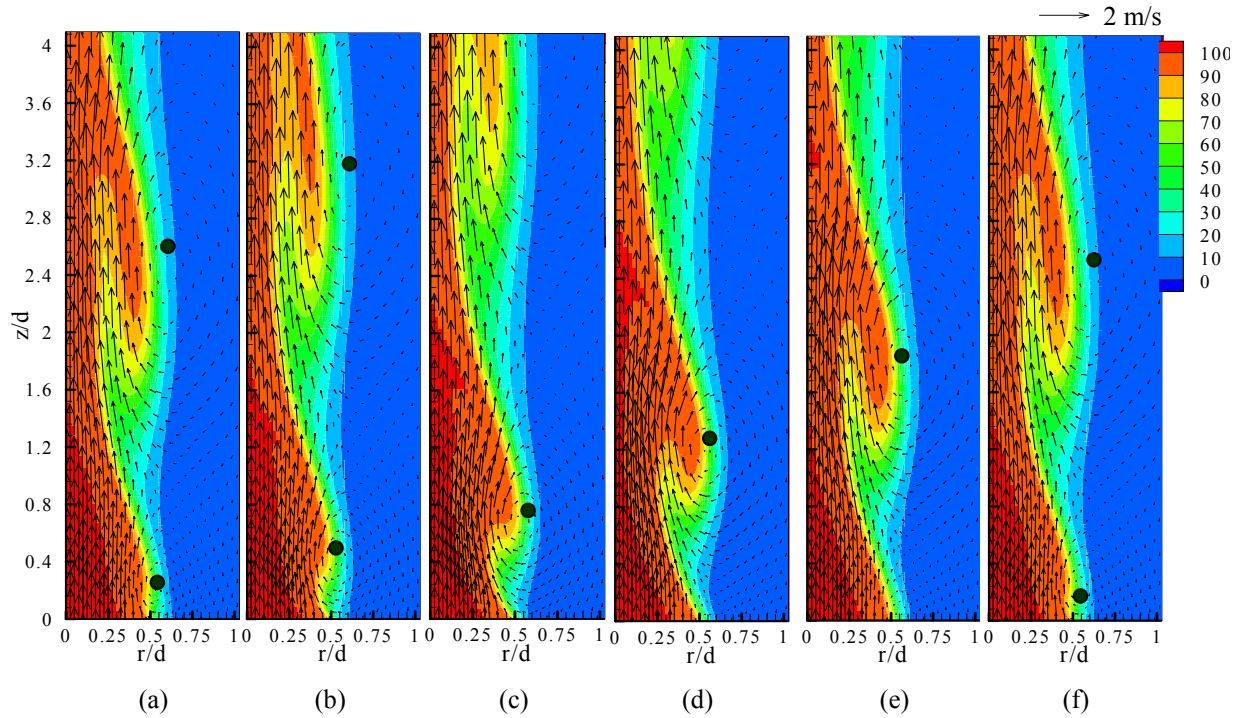

Figure 2. Contours of helium mole percentage superimposed by velocity vectors during an oscillation cycle (left to right) in Earth gravity (a) t=0.0 s; (b) t=1/73 s; (c) t=2/73 s; (d) t=3/73 s; (e) t=4/73 s; (f) t=5/73 s.

At t=0.0s, we observe a vortex located at z/d= 0.7, indicated by the indentation in the concentration level of 50%. With the initiation of microgravity, between t=1/60s and 2/60s, the vortex convects downstream as the jet expands in the near exit region, similar to experiments[11]. At t=3/60s, the jet has expanded at the exit to r/d= 0.7. The vortex located at z/d=1.5 has weakened as seen from the diminishing nature of the indentation and decrease in the curvature of concentration profile. Subsequently, the jet widens gradually throughout the near field with weakening and diminishing of oscillations as steady microgravity conditions are reached. The helium mole fraction contours in microgravity are straight lines reminiscent of a non-buoyant jet. The above mentioned features replicate similar phenomena observed in experiments[11] wherein the self-excited oscillations gradually subsided after microgravity condition was initiated. Judging from the plots in Figure 3, it was inferred that the computations accurately reproduced the experiments proving the model's reliability in predicting the flow physics during change from Earth gravity to microgravity.

Figure 4 shows the contours of helium mole percentage overlapped by velocity vectors during transition from Earth to microgravity to highlight the interaction of the flow field with the concentration field. At t=0.0s, a vortex with the core located at z/d=0.7, characterizes the entrainment of ambient fluid into the helium jet. At this instant, the jet width near the exit extends to r/d=0.6. After the initiation of microgravity, at t=2/60s, the jet has expanded at the exit to r/d=0.7. The vortex convects downstream with its core located at about z/d=1.8. Upstream of the vortex, we observe an irregular distribution of the flow vectors together with distortions around the vortex core region. This behavior is attributed to the flow adjusting to the sudden decay in buoyancy induced acceleration along the jet core region. In the next plot at t=4/60s, the weakened vortex moves away from the field of view as another vortex is initiated at the jet exit. Observe that the vortex core is located close to the 90% concentration level with the jet expanding to r/d=0.75. Though buoyancy forces are absent, we observe vortical motion near the exit possibly because of the residual effects.

At t=8/60s, we observe that the recirculation and entrainment have decreased with the jet continually expanding near the exit. Similar features are exhibited at t=10/60s with flow approaching steady conditions, whereby entrainment is dominated by diffusion. Finally, at t=2.0s, the jet has assumed a steady columnar shape. Higher velocities persist in the jet core and the velocity decreases radially as the jet mixes with the ambient air by molecular diffusion. The vorticity magnitude (not shown) decreases when buoyancy was removed, signifying reduction in mixing of helium and air by entrainment. Further information about the flow structure is provided by the spatio-temporal plots.

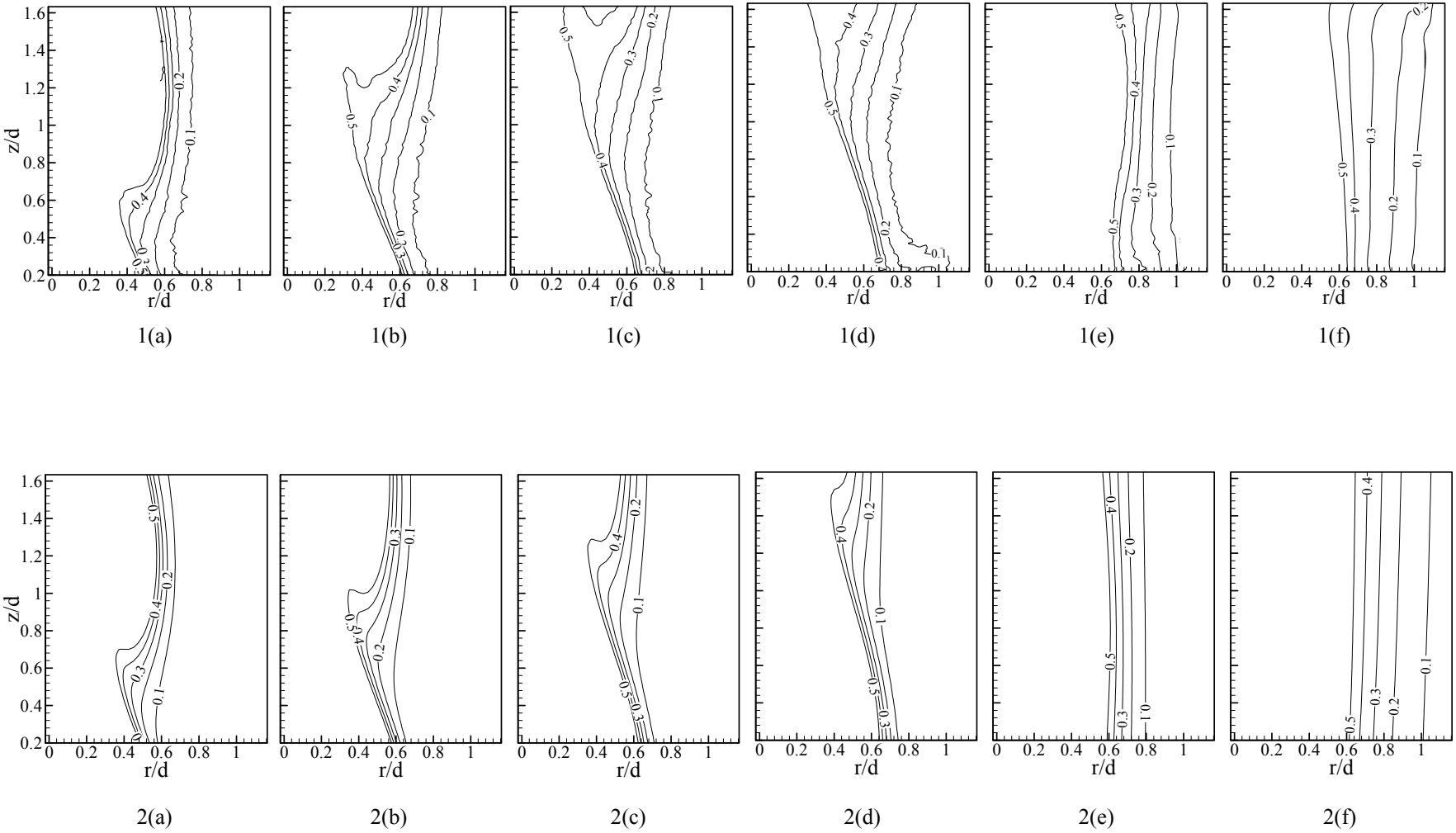

Figure 3. Measured (1) and Computed (2) Helium mole fraction contours during transition from Earth to microgravity at Re = 300, d = 31.8 mm, and Ri = 1.52. (a) t=0.0 s; (b) t=1/60 s; (c) t=2/60 s; (d) t=3/60 s; (e) t=13/60 s; (f) t=2.0 s. Measurements are taken from Yep et al[11].

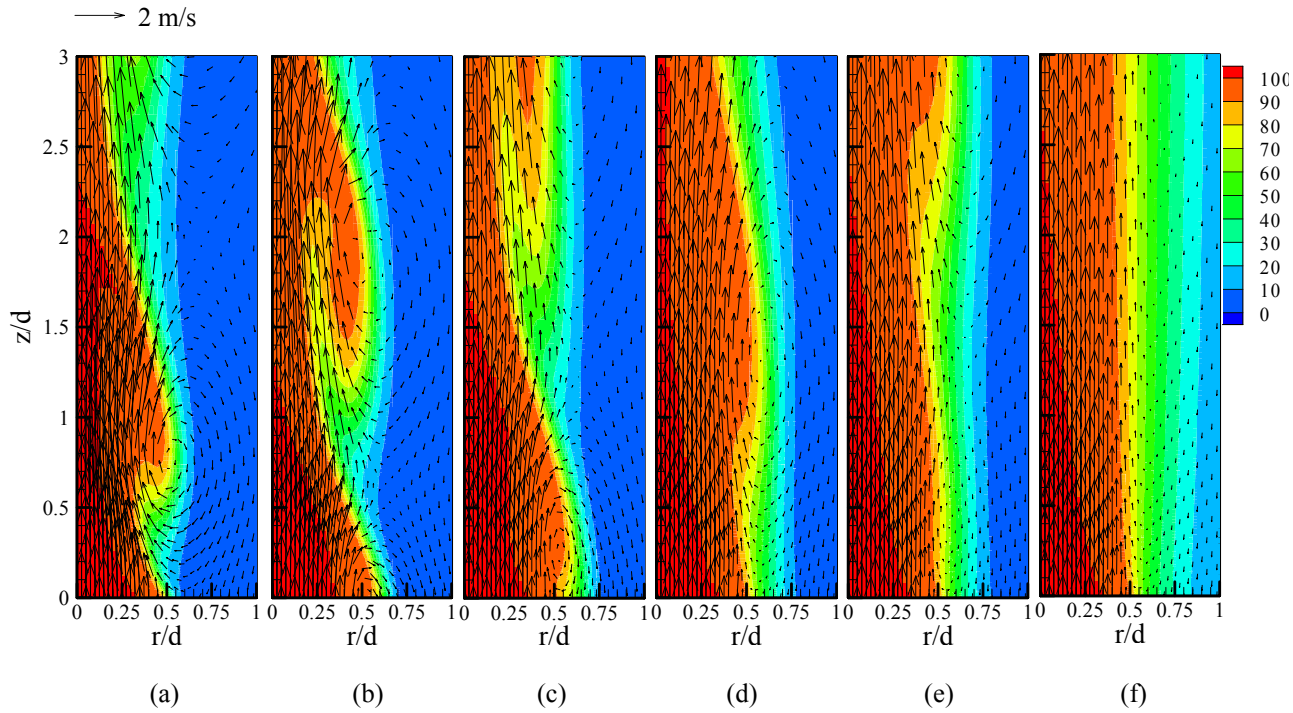

Figure 4. Contours of helium mole percentage superimposed by velocity vectors during transition from Earth gravity to microgravity (left to right) for (a) t=0.0 s; (b) t=2/60 s; (c) t=4/60 s; (d) t=8/60 s; (e) t=10/60 s; (f) t=2.0 s. Note that gravity was removed at t=0.0sec.

Temporal Evolution of Axial Velocity and Concentration fields

Figure 5 shows time trace plots of helium mole percentage and axial velocity at selected axial and radial locations during the change from Earth to micro gravity conditions. Near the jet exit at z/d=0.15, the concentration at the jet center is constant at 100% throughout. In contrast, the axial velocity at the jet center fluctuates between 2.3m/s and 2.6m/s in Earth gravity. With the initiation of microgravity conditions, the axial velocity initially decreases and then reaches a steady value of 2.2m/s within 0.1s of the change in gravity. In the entrainment region at r/d=0.45, the helium mole percentage in Earth gravity varied between 45% and 94%. During transition to microgravity, the concentration peaks to 100% within 0.08s. Afterwards, the flow oscillates until t=0.2s with gradual decrease in the amplitude. Steady state was reached at t=0.3s with helium concentration reaching a value of 95%. Correspondingly, the axial velocity fluctuations in Earth gravity diminish in microgravity, reaching a steady axial velocity of 0.4m/s. Near the jet boundary at r/d=0.6, low amplitude oscillations in the concentration level were observed in Earth gravity. Helium mole percentage reached a peak value of 70% within 0.1s after change of gravity. Subsequently, low Amplitude concentration oscillations were observed till t=0.4s before a steady value of 52% was reached at t = 1.0s. Axial velocity fluctuations at this radial location in Earth gravity show troughs with negative velocity indicating flow recirculation. With the initiation of microgravity, the flow stabilized and reached a near zero axial velocity.

At a downstream location of z/d=2.0, the helium concentration at r/d=0.0 remained constant throughout at 100% level. However, high amplitude oscillations are evident in axial velocity ranging between 2.4m/s and 4.6m/s in Earth gravity. With the initiation of microgravity, the fluctuations diminish within t=0.5s and reach steady conditions with an axial velocity of 2.1m/s. At r/d=0.45, high amplitude concentration oscillations are observed in Earth gravity with helium concentration reaching peak levels of 95% during transition to microgravity and then reaching steady state within 0.6s. At r/d=0.6, helium reaches peak concentration level of 60% during transition to microgravity and reaches steady condition with 56% concentration after 0.6s. The velocity fluctuations at the above radial locations depict a similar flow behavior as already observed at the upstream location.

The above observed features are in excellent agreement with time traces of concentration fields obtained by Yep et al.[11] using the 2.2 sec drop tower. The jet expanded in microgravity and flow oscillations in concentration field existed for a brief period before attaining steady

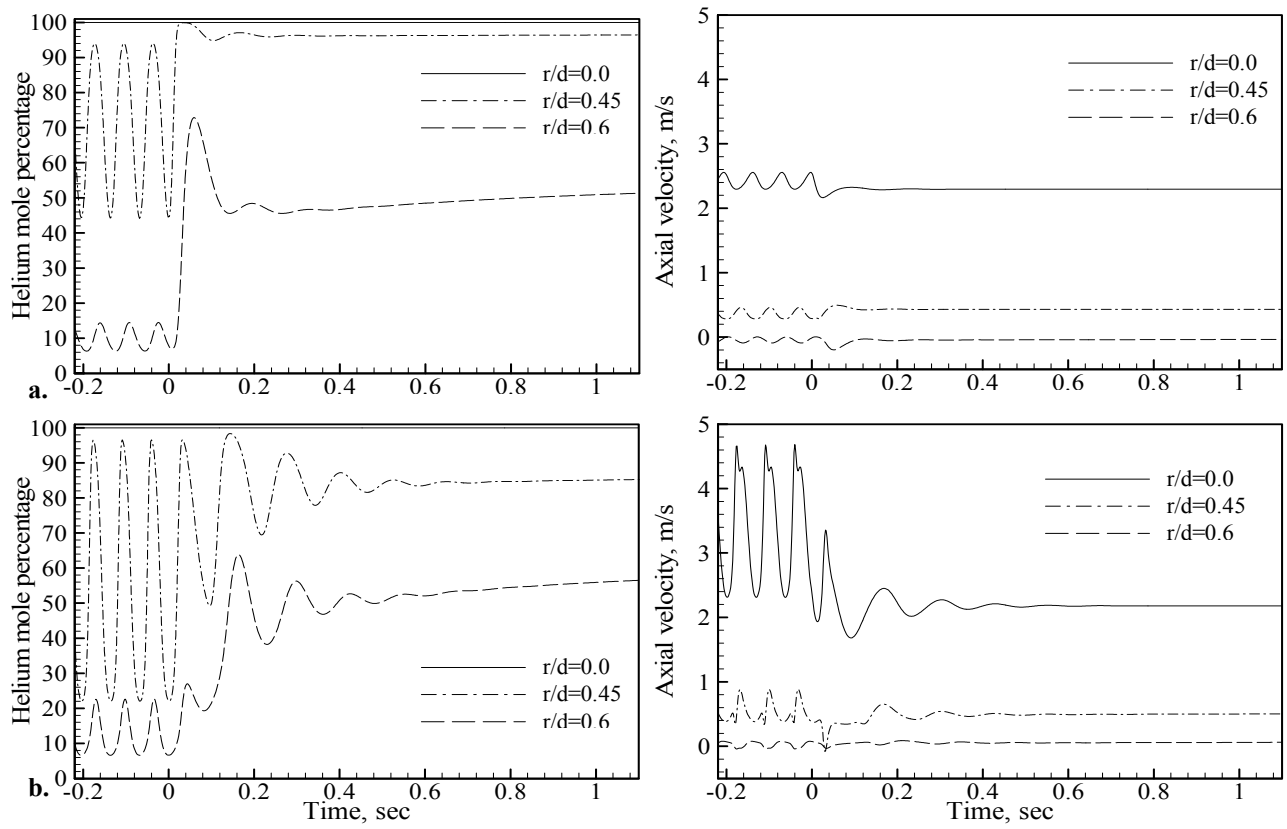

Figure 5. Time traces of helium mole percentage and axial velocity during transition from Earth gravity to microgravity at a) z/d=0.15, and b) z/d=2.0.

state conditions. Observe that an upstream location reaches steady state prior to the downstream location. Coupling between the concentration and velocity fields is explained next using radial profiles near the jet exit (z/d=0.15) at Earth and microgravity conditions to focus on the buoyancy effects in the jet shear layer.

Figures 6 and 7 depict the radial profiles of normalized axial velocity and helium mole percentage at z/d=0.15 for Earth and microgravity conditions. Note that the axial velocity has been normalized with the jet exit velocity at respective radial locations. In Earth gravity, the normalized axial velocity profile shows a gradual increase from the jet core towards the tube wall indicating greater acceleration in the outer region of the jet. The peak normalized axial velocity corresponds to a value of 1.2 at r/d=0.4, a location coinciding with the sudden drop in concentration. Thus, we observe that buoyancy causes large axial velocity gradients and unstable density stratification near the jet shear layer, leading to the entrainment of ambient fluid into the primary jet to produce the oscillatory flow.

In microgravity, a flat normalized axial velocity profile with a minor dip near the tube wall is noticed (Ref. figure 7). The concentration changes gradually as helium diffuses into the ambient environment. Results show that the lack of buoyant acceleration in the jet shear produces a non-oscillatory flow. The next section provides quantitative details relating to the vortex movement and frequency and amplitude of flow oscillations with changes in the gravitational forcing.

Flow Structure: Dependence on Gravitational Forcing

In this section, the analysis has been limited only to the vortex movement and the frequency and amplitude of flow oscillations as functions of the gravitational forcing. Figure 8 illustrates the convection velocity of the vortex core at different gravitational levels. For Martian gravity (g/go=0.37), we observe that the vortex convected at a uniform acceleration with peak velocity of 0.9 m/s at z/d=3.0. Further, in Earth gravity (g/go=1.0), the vortex convection velocity increased at all the axial stations with a peak velocity of 1.0 m/s.

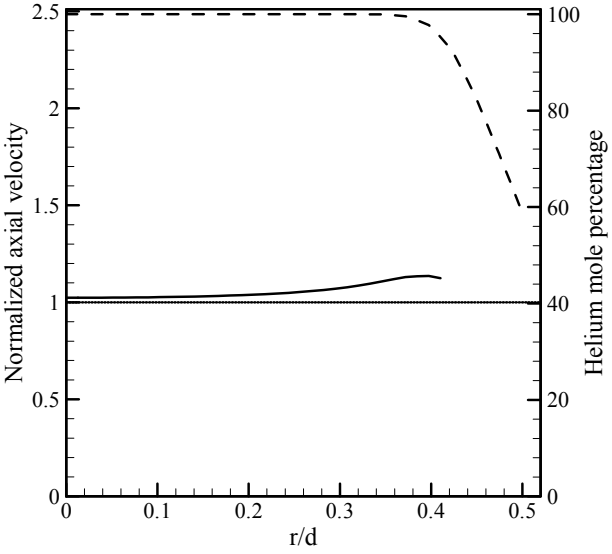

Figure 6. Helium mole percentage and normalized axial velocity profiles in Earth gravity at z/d=0.15.

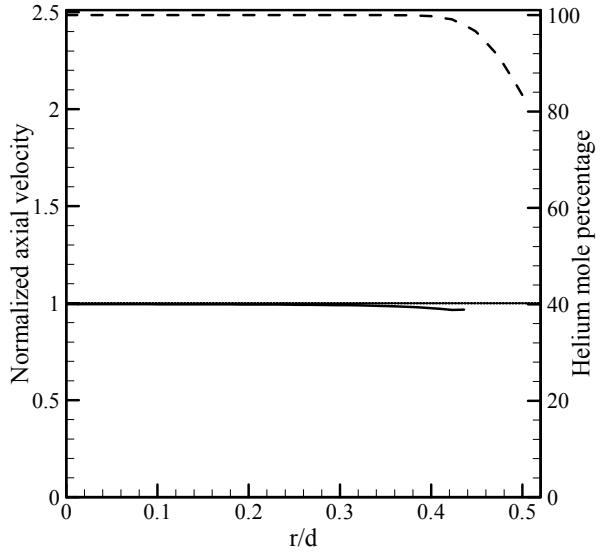

Figure 7. Helium mole percentage and normalized axial velocity profiles in microgravity at z/d=0.15.

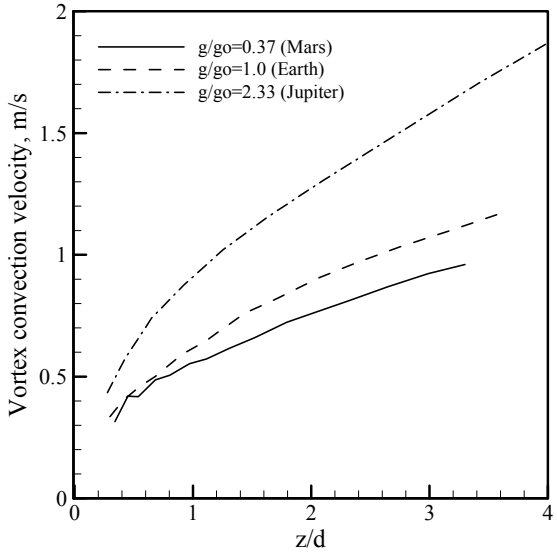

Figure 8. Vortex convection velocity at various gravitational levels.

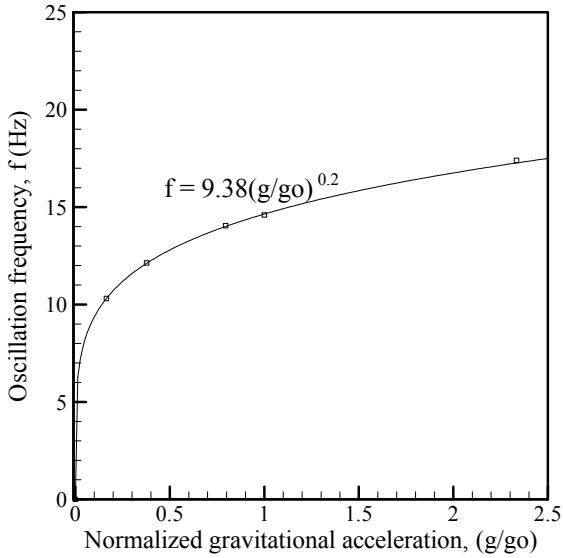

Figure 9. Oscillation frequency Vs normalized gravitational acceleration.

In Jupiter gravity (g/g_o=2.33), the vortex convects with higher acceleration throughout the near field as shown by the steep rise of the curve, with peak velocity reaching about 2.0m/s. Notice that with increase in buoyancy, the vortex convection velocity increases throughout the near field. Accordingly, the entrainment rate, which is a function of the vortex convection velocity, would also increase at higher gravitational levels. Higher entrainment rate leads to enhanced mixing and contamination of the jet core in the downstream region.

Figures 9 and 10 show plots explaining the variation of frequency and amplitude of flow oscillation with the gravitational level. The best fit resulted in the relationship between oscillation frequency and gravitational acceleration as $f = 9.38(g/go)^{0.2}$. The normalized amplitude of the jet oscillatory structure in Figure 10 shows dependence on the gravitational level as well. The amplitude refers to that of the concentration wave and normalization is done using amplitude at Earth gravity. An increase in amplitude with the rise in gravitational level suggests that buoyancy enhances wrapping of the ambient fluid into the jet flow field to affect the entrainment and mixing characteristics in the oscillating shear layer.

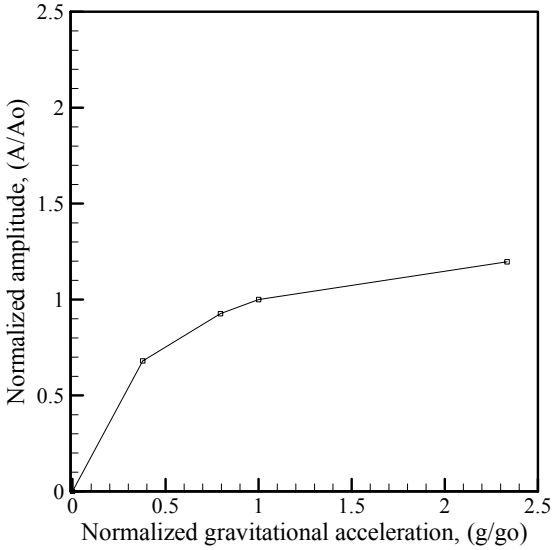

Figure 10. Normalized concentration amplitude Vs normalized gravitational acceleration at z/d=1.0 and r/d=0.45.

CONCLUSIONS

Numerical simulations of a helium jet injected into quiescent air environment were performed to describe the effects of buoyancy in the jet flow field. The interaction of the velocity and the concentration fields was presented by simultaneous visualizations at Earth and microgravity conditions. Results indicated gravity induced global oscillations occurring in the near field of the jet at Earth gravity. Further, the gradual weakening and diminishing of oscillations during transition from Earth to microgravity confirmed that flow oscillations are buoyancy induced. Temporal plots of velocity and concentration fields depict that oscillations existed for a brief period during transition from Earth to microgravity. The jet width increased in microgravity and the upstream locations of the jet reached steady state prior to the downstream locations. Radial profiles of normalized axial velocity and concentration fields near the jet exit illustrated the jet diffusion and entrainment processes characterizing the instability. It was found that the flow oscillation frequency and amplitude increase with the rise in the gravitational level.

ACKNOWLEDGEMENTS

This work was supported by Physical Sciences Division of NASA's office of Biological and Physical research under grant NAG 3-2388.

NOMENCLATURE

d	Tube Inside Diameter (mm)
f	frequency (Hz)
g	Accelaration due to gravity (m/s^2)
M_w	Molecular Weight (Kg/Kmole)
P	Pressure (Pa)
R	Universal Gas Constant (J/KgK)
Re	Jet Reynolds Number
Ri	Jet Richardson Number
T	Absolute Temperature (K)
V	Average jet exit velocity (m/s)
Y	Mole Fraction

Greek Symbols

μ	Viscosity ($Kg/m-s$)
ρ	Density (Kg/m^3)

Subscripts

air	Air
he	Helium
i	Species i
j	Species j
∞	Ambient fluid

REFERENCES

[1]Fay, J.A., (1973), "Buoyant plumes and wakes," *Annual Review of Fluid Mechanics*, Vol. 5, pp. 151-160.

[2]Morton, B.A., (1959), "Forced plumes," *Journal of Fluid Mechanics*, Vol. 5, pp. 151-159.

[3]List, E.L., (1982), "Turbulent Jets and plumes," *Annual Review of Fluid Mechanics*, Vol. 14, pp. 189.

[4]Papanicolaou, P.A., and List, E.L., (1988), "Investigations of Round Vertical Turbulent Buoyant Jets," *Journal of Fluid Mechanics*, Vol. 195, pp. 342-391.

[5]Dai, Z., Tseng, L.K., and Faeth G.M., (1994), "Structure of round, fully developed, buoyant turbulent plumes," *Journal of Heat Transfer,* Vol. 116, pp. 409-417.

[6]So, R.M.C., Zhu, J.Y., Otugen, M.V., and Hwang, B.C., (1990), "Some Measurements in a Binary Gas Jet," *Experiments in Fluids*, Vol. 9, pp. 273-284.

[7]Subbarao, E.R., and Cantwell B.J., (1992), "Investigation of a co-flowing buoyant jet: experiments on the effects of Reynolds number and Richardson number," *Journal of Fluid Mechanics*, Vol.245, pp. 69-90.

[8]Cetegen, B.M., and Ahmed, T.A., (1993), "Experiments on the periodic instability of buoyant plumes and pool fires," *Combustion and Flame*, Vol. 93, pp. 157-184.

[9]Cetegen, B.M., and Kasper, K.D., (1996), "Experiments on the oscillatory behavior of buoyant plumes of helium and helium-air mixtures," *Physics of Fluids,* Vol. 8, pp. 2974-2984.

[10]Cetegen, B.M., (1997), "Measurements of Instantaneous Velocity field of a Non-Reacting Pulsating Buoyant Plume by Particle Image Velocimetry," *Combustion Science and Technology*, Vol. 123, pp. 377-387.

[11]Yep, T.W., and Agrawal, A.K., (2003), "Gravitational Effects on near field flow structure of Low density gas jets," *AIAA Journal*, Vol. 41, pp. 1973-1979.

[12]Pasumarthi, K.S., and Agrawal, A.K., (2003), "Schlieren Measurements and Analysis of Concentration Field in Self-Excited Helium Jets," *Physics of Fluids,* Vol. 15 (In Press).

[13]Mell, W.E., McGrattan, W.B., Baum, H.R., (1996), "Numerical Simulation of Combustion in Fire Plumes," *Proceedings of the Combustion Institute*, Vol. 26, pp. 1523-1530.

[14]Hamins, A., Yang, J.C., Kashiwagi, T., (1992), "An Experimental Investigation of the Pulsating Frequency of Flames," *Proceedings of the Combustion Institute* Vol. 24, pp. 1695-1705.

[15]Soteriou, M.C., Dong, Y., Cetegen, B.M., (2002), "Lagrangian simulation of the unsteady near field dynamics of planar buoyant plumes," *Physics of Fluids* Vol. 14, pp. 3118-3140.

[16]Bird, R.B., Stewart, W.E., Lightfoot, E.N., (1960), "Transport *Phenomena*, 1st edition. Wiley, New York.

[17] Fluent 6.0, User's Guide, *Fluent Inc.* Lebanon, NH 1-4 (2003).

[18]Gambit 2.1, User's Guide, *Fluent Inc.* Lebanon, NH 1-4 (2003).

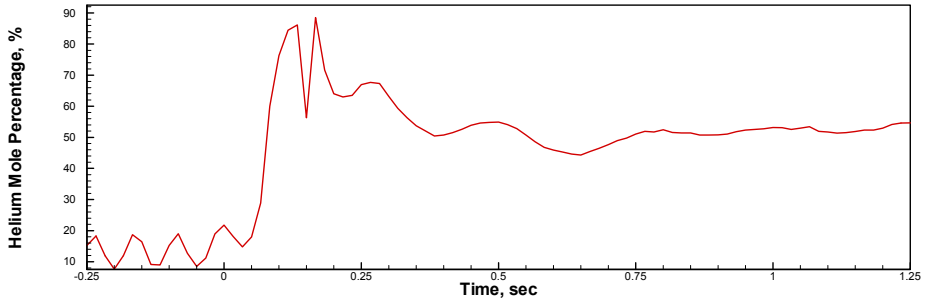

FIG. 15 (a). Helium mole percentage in Earth gravity and microgravity at z/d = 0.5, r/d = 0.6.

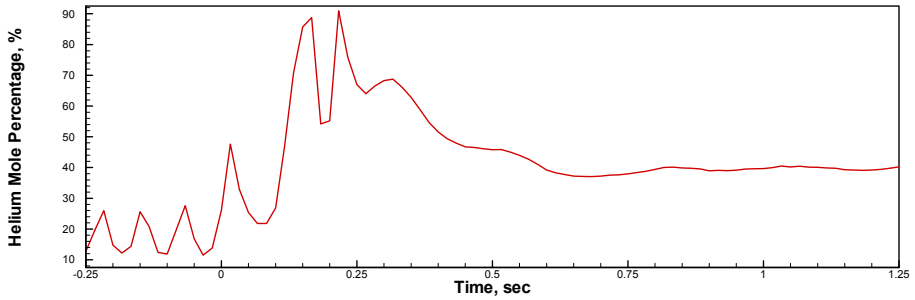

FIG. 15 (b). Helium mole percentage in Earth gravity and microgravity at z/d = 1, r/d = 0.6.

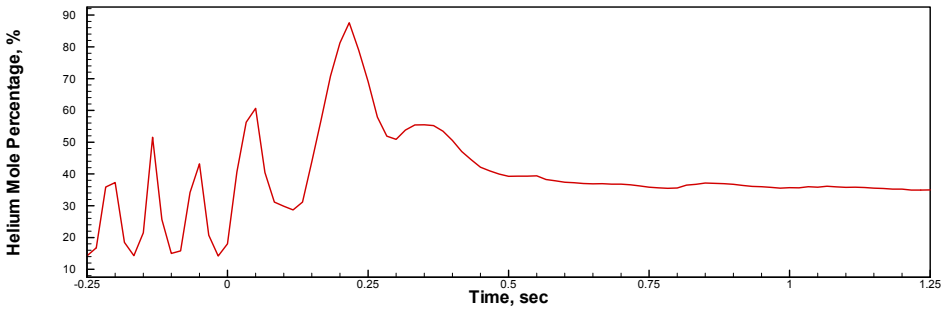

FIG. 15 (c). Helium mole percentage in Earth gravity and microgravity at z/d = 1.5, r/d = 0.6.
(Time t=0 denotes release of the package)

Conclusions

The non-intrusive, line-of-sight, RSD technique was utilized for quantitative flow measurements in the near field of buoyant and non-buoyant helium gas jets. Results show that the radial growth of the jet shear layer in Earth gravity is hindered by the buoyant acceleration. The jet core region is however diluted by air as the flow accelerates by buoyancy. The jet in microgravity is 30 to 70 percent wider than that in Earth gravity. The microgravity jet shows typical growth of a non-buoyant jet shear layer. In case of a self-excited jet in Earth gravity, the flow oscillations continued as the jet flow adjusted to microgravity conditions in the drop tower. The flow oscillations are however not present at the end of the drop when steady flow conditions in microgravity are reached. Results provide direct physical evidence, for the first time, that the flow oscillations in low-density jets are buoyancy-induced and that the flow instability originates in the downstream region of the jet. Finally, the rainbow schlieren apparatus was shown to provide quantitative scalar measurements across the whole field in the microgravity environment.

Acknowledgment

This work was supported by the Physical Sciences Division of NASA's Office of Biological and Physical research under grant NAG 3-2388.

References

1. So, R.M.C., Zhu, J.Y., Otugen, M.V., and Hwang, B.C., "Some Measurements in a Binary Gas Jet," *Experiments in Fluids*, Vol. 9, 1990, pp. 273-284.
2. Richards, C.D., and Pitts, W.M., "Global Density Effects on the Self Preservation Behaviour of Turbulent Free Jets," *Journal of Fluid Mechanics*, Vol. 254, 1993, pp. 417-435.
3. Panchapakesan, N.R., and Lumley, J.L., "Turbulence Measurements in Axisymmetric Jets of Air and Helium. Part 2. Helium Jet," *Journal of Fluid Mechanics*, Vol. 246, 1993, pp. 225-248.
4. Subbarao, E.R., and Cantwell, B.J., "Investigation of a Co-Flowing Buoyant Jet: Experiments on the Effect of Reynolds Number and Richardson Number," *Journal of Fluid Mechanics*, Vol. 245, 1992, pp. 69-90.
5. Hamins, A., Yang, J.C., and Kashiwagi, T., "An Experimental Investigation of the Pulsating Frequency of Flames," *Proceedings of the Combustion Institute*, Vol. 24, 1992, pp. 1695-1705.
6. Cetegen, B.M., and Kasper, K.D., "Experiments on the Oscillatory Behavior of Buoyant Plumes of Helium and Helium-Air Mixtures," *Physics of Fluids*, Vol. 8, 1996, pp 2974-2984
7. Cetegen, B.M., "Measurements of Instantaneous Velocity Field of a Non-Reacting Pulsating Buoyant Plume by Particle Image Velocimetry" *Combustion Science and Technology*, Vol. 123, 1997, pp. 377-387.
8. Monkewitz, P.A., Bechert, D.W., Barsikow, B., and Lehmann, B., "Self-Excited Oscillations and Mixing in a Heated Round Jet," *Journal of Fluid Mechanics*, Vol. 213, 1990, pp. 611-639.
9. Screenivasan, K.R., Raghu, S., and Kyle, D., "Absolute Instability in Variable Density Round Jets," *Experiments in Fluids*, Vol. 7, 1989, pp. 309-317.
10. Kyle, D.M., and Sreenivasan, K.R., "The Instability and Breakdown of a Round Variable-Density Jet," *Journal of Fluid Mechanics*, Vol. 249, 1993, pp. 619-664.
11. Richards, C.D., Breuel, B.D., Clark, R.P., and Troutt, T.R., "Concentration Measurements in a Self-Excited Jet," *Experiments in Fluids*, Vol. 21, 1995, pp. 103-109.
12. Greenberg, P.S., Klimek, R.B., and Buchele, D.R., "Quantitative Rainbow Schlieren Deflectometry," *Applied Optics*, Vol. 34, 1995, pp. 3819-3822.
13. Al-Ammar, K., Agrawal, A.K., Gollahalli, S.R., and Griffin, D.W., "Application of Rainbow Schlieren Deflectometry for Concentration Measurements in an Axisymmetric Helium Jet," *Experiments in Fluids*, Vol. 25, 1998, pp. 89-95.
14. Pasumarthi, K.S., "Full Field Scalar Measurements in a Pulsating Helium Jet Using Rainbow Schlieren Deflectometry," *M.S. Thesis*, University of Oklahoma, 2000.
15. Albers, B.W., and Agrawal, A.K., "Schlieren Analysis of an Oscillating Gas-Jet Diffusion Flame," *Combustion and Flame*, Vol. 119, 1999, pp. 89-94.
16. Shenoy, A.K., Agrawal, A.K., and Gollahalli, S.R., "Quantitative Evaluation of Flow Computations by Rainbow Schlieren Deflectometry," *AIAA Journal*, Vol. 36, 1998, pp. 1953-1960
17. Al-Ammar, K., Agrawal A.K., and Gollahalli, S.R., "Quantitative Measurements of Laminar Hydrogen Gas-Jet Diffusion Flames in a 2.2 s Drop Tower," *Proceedings of the Combustion Institute*, Vol. 28, 2000, pp. 1997-2004.
18. Xiao, X., Puri, I.K., and Agrawal, A.K., "Temperature Measurements in Steady Axisymmetric Partially Premixed Flames using Rainbow Schlieren Deflectometry," in print, *Applied Optics*.
19. Agrawal, A.K., and Albers, A.K., "Abel Inversion of Deflectometric Measurements in Dynamic Flows," *Applied Optics*, Vol. 38, 1999, pp. 3394-3398.
20. Cetezen, B., "Behavior of Naturally Unstable and Periodically Forced Axisymmetric Buoyant Plumes of Helium and Helium-Air Mixtures," *Physics of Fluids*, Vol. 9, No. 12, 1997, pp. 1-11.

Proceedings of ETCE 2002
ASME Engineering Technology Conference on Energy
February 4-6, 2002, Houston, Texas

ETCE2002/CAE-29010

LINEAR TEMPORAL STABILITY ANALYSIS OF A LOW-DENSITY ROUND GAS JET INJECTED INTO A HIGH-DENSITY GAS

Anthony L. Lawson
School of Aerospace and Mechanical Engineering
The University of Oklahoma
Norman, Oklahoma

Ramkumar N. Parthasarathy
School of Aerospace and Mechanical Engineering
The University of Oklahoma
Norman, Oklahoma
rparthasarathy@ou.edu

ABSTRACT

It has been observed in previous experimental studies that round helium jets injected into air display a repetitive structure for a long distance, somewhat similar to the buoyancy-induced flickering observed in diffusion flames. In order to investigate the influence of gravity on the near-injector development of the flow, a linear temporal stability analysis of a round helium jet injected into air was performed. The flow was assumed to be isothermal and locally parallel; viscous and diffusive effects were ignored. The variables were represented as the sum of the mean value and a normal-mode small disturbance. An ordinary differential equation governing the amplitude of the pressure disturbance was derived. The velocity and density profiles in the shear layer, and the Froude number (signifying the effects of gravity) were the three important parameters in this equation. Together with the boundary conditions, an eigenvalue problem was formulated. Assuming that the velocity and density profiles in the shear layer to be represented by hyperbolic tangent functions, the eigenvalue problem was solved for various values of Froude number. The temporal growth rates and the phase velocity of the disturbances were obtained. The temporal growth rates of the disturbances increased as the Froude number was reduced (i.e. gravitational effects increased), indicating the destabilizing role played by gravity.

NOMENCLATURE

English Symbols

d	jet diameter
D_b	binary diffusivity coefficient
Fr	Froude number; $Fr^2 = \frac{U_j^2}{gR}\frac{\rho_j}{\left(\rho_\infty - \rho_j\right)}$
g	acceleration due to gravity
G	non-dimensional coefficient of the buoyancy term in the pressure disturbance equation; $G = \frac{1}{Fr^2 \frac{R}{\theta}\left(\frac{\rho_\infty}{\rho_j} - 1\right)}$
i	$\sqrt{-1}$
k	wavenumber
m	azimuthal wavenumber
p	pressure
r	radial coordinate
r_o	low-density jet exit radius
R	radius of the jet shear layer
S	Density ratio
Sc	Schmidt number; $Sc = \frac{\upsilon}{D_b}$
t	time
u	jet axial velocity component
U	jet base velocity
U_c	jet base centerline velocity
v	jet radial velocity component
w	jet azimuthal velocity component
x	axial coordinate
Y_j	local mass fraction of injected gas

Greek Symbols

δ_{ij}	Kronecker delta
∇	del operator
ϕ	azimuthal coordinate

λ	wavelength
μ	fluid viscosity
υ	fluid kinematic viscosity
ρ	fluid mass density
ρ_j	fluid mass density of low-density gas
ρ_∞	fluid mass density of high-density ambient gas
θ	shear layer momentum thickness
Ω	angular frequency

Superscripts

( )'	fluctuations
$\bar{(\ )}$	averaged variable
(^)	amplitude of variable
(˜)	dimensional variable

Subscripts

∞	ambient gas property
j	low-density gas property

INTRODUCTION

Low-density gas jets injected into higher density ambient gases are encountered in many engineering and technical applications such as plumes of diffusion flames, fuel leaks, engine and industry exhaust, and in natural phenomena such as fires and volcanic eruptions. Recent experimental studies (Monkewitz et al, 1990; Subbarao and Cantwell, 1992; Kyle and Sreenivasan, 1993; Cetegen and Kasper, 1996) indicate that at certain conditions, low-density gas jets injected into high-density gases may sustain an absolute instability leading to highly periodic oscillations. This phenomenon is similar to the buoyancy-induced flickering observed in diffusion flames (Buckmaster and Peters, 1986; Chen et al., 1988; Cetegen and Dong, 2000). It is thus plausible that the periodicity observed in the oscillations of low-density gas jets injected into a high-density medium is related to buoyancy effects. Therefore, an investigation of the influence of gravity on the disturbances in the near-injector region of low-density jets is necessary. This study aims to highlight as well as improve the understanding of the nature of flow instability in low-density round gas jets injected into high-density gases.

Round jets with homogeneous shear layers have been studied extensively in the past. The near-injector region of a round jet, as influenced by disturbances, has a direct influence on the flow development in the far-field of the jet. Early studies of jet instability were reviewed by Michalke (1984). These studies were carried out to understand the transition from laminar flow to turbulence and to describe the evolution of the large-scale coherent structures in the near-injector field. The critical Reynolds number denoting the transition from laminar to turbulent flow was documented. Also, it was found that the streak line patterns obtained using the results of the linear stability analysis were in good agreement with the first-stage of the vortex rolling-up process that was observed experimentally. Cohen and Wygnanski (1987) concluded that the linear stability analysis was able to correctly predict the local distribution of amplitudes and phases in an axisymmetric jet that was excited by external means.

Monkewitz and Sohn (1988) re-examined the linear inviscid stability analysis of compressible heated axisymmetric jets with particular attention to the impulse response of the flow, using assumed forms of the velocity and density profiles in the shear layer. Two different responses were identified based on the results. In one case, the flow was absolutely unstable, when a locally generated small disturbance grew exponentially at the site of the disturbance and eventually affected the entire flow region. In the other case termed convective instability, the disturbance was convected downstream leaving the mean flow undisturbed. Monkewitz and Sohn (1988) documented the boundaries between the absolute and convective instability assuming locally parallel flow, infinite Froude number, and zero Eckert number. It was shown that heated (low-density) jets injected into ambient gas of high density developed an absolute instability and became self-excited when the jet density was less than 0.72 times the ambient gas density. Yu (1990) carried out a similar analysis for two-dimensional inertial jets and wakes with non-uniform density and axial velocity profiles neglecting gravitational effects. It was found that the absolute frequencies and wavenumbers of small disturbances in the near-injector region scaled with the jet/wake width. Jendoubi and Strykowski (1994) considered the stability of axisymmetric jets with external co-flow and counterflow. The boundaries between absolute and convective instability were distinguished for various parameters: jet-to-ambient velocity ratio, density ratio, jet Mach number, and the shear layer thickness. The onset of global self-excitation identified in laboratory jets agreed reasonably well with the predictions.

Kyle and Sreenivasan (1993) performed experiments at low Richardson numbers to study the instability and breakdown of axisymmetric helium/air mixtures emerging into ambient air using high-speed photography and velocity measurements. An intense oscillating instability was observed when the ratio of the jet exit density to the ambient fluid density was less than 0.6. Raynal et al. (1996) carried out experiments with variable-density plane jets issuing into ambient air for a range of density ratios (0.14 to 1) and a range of Reynolds numbers (250 to 3000). It was found that when the jet to ambient fluid density ratio was less than 0.7, the jets exhibited self-excited oscillations. Richards et al. (1996) used Mie scattering to visualize helium-air jets injected into air. Intense mixing and vortex interactions characterized the self-excited helium jets at a density ratio of 0.14.

Note that gravitational effects have been neglected in all of the analyses listed above. The neglect of gravitational effects has been justified by the authors because of the small magnitude of the Richardson number based on the jet velocity

and jet diameter. However, within the shear layer where the density and velocity change from jet to ambient values, the gravitational effects may not be negligible. Literature on the effects of gravity and/or buoyancy on the stability characteristics of low-density gas jets injected in higher density ambient gases is limited.

Hamins et al. (1992) used a shadowgraph technique to observe the near-field behavior of a non-reacting buoyant helium plume discharged from a round tube into air and obtained a complex relation between the Strouhal number and the Froude number. Subbarao and Cantwell (1992) performed experiments on a co-flowing buoyant jet to study the scaling properties and effects of Richardson number and Reynolds number, independently, on the natural frequency of the jet. The Strouhal number was plotted as a function of the square root of the Richardson number and was separated into three regimes. At low Richardson numbers, the flow Strouhal number scaled with an inertial timescale, while at high Richardson numbers the Strouhal number scaled with a buoyancy timescale. Between the Richardson numbers of 0.7 and 1, a transition regime occurred. Cetegen and Kasper (1996) performed experiments on the oscillatory behavior of axisymmetric buoyant plumes of helium and helium-air mixtures. The effects of varying nozzle diameters, source velocities and plume densities were investigated. Cetegen (1997-1) investigated the effect of sinusoidal forcing on an axisymmetric buoyant plume of helium and helium-air mixtures. Mushroom-shaped small-scale vortex pairs were observed in the early part of the forced plumes that were not observed in unforced plumes. Cetegen (1997-2) used digital particle image velocimetry to measure the velocity field of a naturally pulsating plume of helium-air mixture in the presence of co-flowing air. The oscillation frequency of the plume, observed using a movie camera at a frame rate of 30 fps, was between 3 and 4.5 Hz. Pasumarthi (2000) conducted experiments to investigate the flow structure of a pulsating helium jet injected into air using quantitative rainbow schlieren deflectometry. It was found that the Richardson number had a more significant effect on the flow structure than the jet exit Reynolds number.

The present study extends the work of Buckmaster and Peters (1986) to consider the effects of gravity on the instability of a low-density gas injected into a high-density ambient. The specific objectives of the study were to perform a linear temporal stability analysis of low-density round jets injected into high-density ambient gases, and to determine the effects of buoyancy on the instabilities of the jet.

THEORY

The present analysis considers a round jet of low-density gas discharged into a high-density ambient gas medium. The basic jet flow is assumed to be a locally inviscid parallel flow with an axial velocity component varying radially. In order to simplify the analysis, the flow is assumed to be isothermal. The radial velocity of the jet is considered small and, therefore, neglected. An analysis considering the effects of buoyancy, along the lines of Buckmaster and Peters (1986) is performed. The analysis differs from that of Buckmaster and Peters (1986) in several ways. First, the near-injector velocity and density profiles are used in the analysis. Second, an axisymmetric configuration is studied.

Linear stability analysis

Consider a round jet (radius R) of a low-density gas (density ρ_j) injected vertically upward with velocity U_j into an ambient quiescent gas of density ρ_∞ at atmospheric pressure as illustrated in the schematic diagram of Figure 1. Representing the velocity components by $(\tilde{u},\tilde{v},\tilde{w})$, in cylindrical coordinates $(\tilde{x},\tilde{r},\phi)$ centered at the origin of the jet, and the pressure by p the conservation equations governing the flow are:

$$\frac{\partial\tilde{\rho}}{\partial t}+\frac{\partial(\tilde{\rho}\tilde{u})}{\partial\tilde{x}}+\frac{1}{\tilde{r}}\frac{\partial(\tilde{r}\tilde{\rho}\tilde{v})}{\partial\tilde{r}}+\frac{1}{\tilde{r}}\frac{\partial(\tilde{\rho}\tilde{w})}{\partial\phi}=0 \qquad (1)$$

$$\tilde{\rho}\left[\frac{\partial\vec{v}}{\partial t}+\vec{v}\bullet\nabla\vec{v}\right]=-\nabla p+g(\rho_\infty-\tilde{\rho})\delta_{i1}+\nabla\bullet(\mu\nabla\vec{v}) \qquad (2)$$

where g is the acceleration due to gravity and δ_{i1} is the Kronecker delta function with i = 1 representing the axial direction. The binary mass diffusion equation for the diffusion of the injected gas in the ambient gas medium is given in terms of the local mass fraction of the injected gas, Y_j (Gebhart, 1993):

$$\tilde{\rho}\left[\frac{\partial Y_j}{\partial t}+\vec{v}\bullet\nabla Y_j\right]=\nabla\bullet\left[\tilde{\rho}D_b\nabla Y_j\right] \qquad (3)$$

where D_b is the binary diffusivity coefficient.

The flow is assumed to be locally parallel, and the variables are represented as the sum of the base state value and a fluctuation:

$$\begin{aligned}\tilde{u}&=\overline{u}(\tilde{r})+u'\\ \tilde{v}&=v'\\ \tilde{w}&=w'\\ \tilde{p}&=p'\\ \tilde{p}&=\overline{p}(\tilde{r})+p'\end{aligned} \qquad (4)$$

Substitution of equations (4) into equations (1) and (2), linearization, and the neglect of viscous and diffusive terms yields

$$\frac{\partial\rho'}{\partial t}+\overline{u}\frac{\partial\rho'}{\partial\tilde{x}}+\overline{\rho}\frac{\partial u'}{\partial\tilde{x}}+\frac{1}{\tilde{r}}\frac{\partial(\tilde{r}\overline{\rho}v')}{\partial\tilde{r}}+\frac{\overline{\rho}}{\tilde{r}}\frac{\partial w'}{\partial\phi}=0 \qquad (5)$$

$$\overline{\rho}\left[\frac{\partial u'}{\partial t}+\overline{u}\frac{\partial u'}{\partial\tilde{x}}+v'\frac{d\overline{u}}{d\tilde{r}}\right]=-\frac{\partial p'}{\partial\tilde{x}}-g\rho' \qquad (6)$$

$$\overline{\rho}\left[\frac{\partial v'}{\partial t}+\overline{u}\frac{\partial v'}{\partial\tilde{x}}\right]=-\frac{\partial p'}{\partial\tilde{r}} \qquad (7)$$

$$\overline{\rho}\left[\frac{\partial w'}{\partial t}+\overline{u}\frac{\partial w'}{\partial\tilde{x}}\right]=-\frac{1}{\tilde{r}}\frac{\partial p'}{\partial\phi} \qquad (8)$$

The density of the mixture is related to the mass fraction by

$$\tilde{\rho} = \frac{\rho_j}{Y_j + (1 - Y_j) S} \tag{9}$$

where ρ_j is the density of the injected gas and S is the density ratio ρ_j/ρ_∞ (ρ_∞ is the density of the ambient gas medium). Rewriting Y_j in terms of ρ, we have

$$Y_j = \frac{1}{1-S}\left(\frac{\rho_j}{\tilde{\rho}} - S\right)$$

where, S is the ratio of the density of the injected fluid to that of the ambient fluid. Substituting the above expression in equation (3), linearizing, and neglecting the diffusive term, we obtain

$$\frac{\partial \rho'}{\partial t} + \bar{u}\frac{\partial \rho'}{\partial \tilde{x}} + v'\frac{d\bar{\rho}}{d\tilde{r}} = 0 \tag{10}$$

Using equation (10), equation (5) reduces to

$$\bar{\rho}\left[\frac{\partial u'}{\partial \tilde{x}} + \frac{1}{\tilde{r}}\frac{\partial(\tilde{r}v')}{\partial \tilde{x}} + \frac{1}{\tilde{r}}\frac{dw'}{d\phi}\right] = 0 \tag{11}$$

Normal mode disturbances are assumed given by

$$(u', v', w', p', \rho') = \left[\hat{u}(\tilde{r}), \hat{v}(\tilde{r}), \hat{w}(\tilde{r}), \hat{p}(\tilde{r}), \hat{\rho}(\tilde{r})\right] e^{i\left(\tilde{k}\tilde{x} - \tilde{\Omega}t + m\phi\right)} \tag{12}$$

where $i = \sqrt{-1}$; $\hat{u}, \hat{v}, \hat{w}, \hat{p}, \hat{\rho}$ are the amplitudes of the disturbances; $\tilde{k}$ is the wavenumber; $\tilde{\Omega}$ is the frequency, and m is the azimuthal wavenumber. For temporal linear stability analysis, the wavenumber, $\tilde{k}$, is real while the frequency $\tilde{\Omega} = \tilde{\Omega}_r + i\tilde{\Omega}_i$ is complex. The real part $\tilde{\Omega}_r$ is proportional to the disturbance frequency and the imaginary part $\tilde{\Omega}_i$ is the temporal growth rate of the disturbance. The disturbance gets amplified if $\tilde{\Omega}_i$ is positive. The ratio of $\tilde{\Omega}_r$ to k represents the wave speed, c_{ph} of the disturbance.

Substituting the expressions (12) in equations (6), (7), (8), (10) and (11), and manipulating the expressions, we obtain the following equation for the pressure disturbance:

$$\frac{d^2\hat{p}}{d\tilde{r}^2} + \left[\frac{1}{\tilde{r}} - \frac{2\frac{d\bar{u}}{d\tilde{r}}}{\bar{u} - \frac{\tilde{\Omega}}{\tilde{k}}} - \frac{1}{\bar{\rho}}\frac{d\bar{\rho}}{d\tilde{r}}\left(1 + \frac{ig}{\tilde{k}\left(\bar{u} - \frac{\tilde{\Omega}}{\tilde{k}}\right)^2}\right)\right]\frac{d\hat{p}}{d\tilde{r}} - \left(\tilde{k}^2 + \frac{m^2}{\tilde{r}^2}\right)\hat{p} = 0 \tag{13}$$

The variables are normalized using ρ_∞, U_j, and θ (the boundary layer momentum thickness). The nondimensionalized pressure disturbance equation for the varicose mode (m = 0) is

$$\frac{d^2P}{dr^2} + \left[\frac{1}{r} - \frac{2\frac{dU}{dr}}{U - \frac{\Omega}{k}} - \frac{1}{\rho}\frac{d\rho}{dr}\left(1 + i\frac{1}{Fr^2\frac{R}{\theta}\left(\frac{\rho_\infty}{\rho_j} - 1\right)k\left(U - \frac{\Omega}{k}\right)^2}\right)\right]\frac{dP}{dr} - k^2P = 0 \tag{14}$$

It should be noted that with no density gradient equation (14) reduces to the equation governing the instability of constant-density jets (Michalke, 1984). Also, as $r \to \infty$, and if gravitational effects are neglected, equation (25) is identical to the equation used by Yu and Monkewitz (1990) and Raynal et al. (1996) in the analysis of plane jets. Inclusion of buoyancy effects indicates that the stability characteristics are altered by the additional term present in equation (14).

The pressure disturbance must vanish at large radial distances from the jet and the pressure disturbance is finite at the jet axis (r = 0) therefore

$$\begin{aligned} &P(\infty) \to 0 \\ &P(0) \text{ is finite} \\ &\frac{dP(0)}{dr} = 0 \quad \text{due to symmetry} \end{aligned} \tag{15}$$

An eigenvalue problem is posed, for specified mean velocity and density profiles, by equation (12) along with the boundary conditions (15). Following Monkewitz and Sohn (1988), the base axial velocity and the density profiles are specified as a function of the local jet radius. The basic jet velocity profile, $U(r)$, is given by Michalke and Hermann (1982),

$$\frac{\bar{u}(\tilde{r}) - U_\infty}{U_j - U_\infty} = 0.5\left\{1 - \tanh\left[0.25\frac{R}{\theta}\left(\frac{\tilde{r}}{R} - \frac{R}{\tilde{r}}\right)\right]\right\} \tag{16}$$

where U_j is the injected jet uniform velocity and U_∞ is the uniform co-flow velocity. For this study the co-flow velocity was set to zero for a quiescent ambient gas and R is the radial distance of the center of the shear layer. R/θ is the jet parameter that characterizes the jet velocity profile at various axial positions. The values of the jet parameter used in this study are 10 and 5 corresponding to $\tilde{x}/(2R)$ = 1 and 2.67, respectively. This is within the near-injector region of the jet and allows for the effects of buoyancy to manifest as the jet proceeds downstream (Subbarao and Cantwell, 1992). Figure 2 illustrates the basic jet velocity profiles at these two locations. The shear layer widens as the jet proceeds downstream from $R/\theta = 10$ to $R/\theta = 5$ indicating the downstream development of the jet. A hyperbolic tangent profile is also assumed for the basic density profile in the shear layer,

$$\frac{\bar{\rho}(r)}{\rho_\infty} = 1 + \left(\frac{\rho_j}{\rho_\infty} - 1\right)\left\{0.5\left(1 - \tanh\left[0.25\frac{R}{\theta}\left(\frac{\tilde{r}}{R} - \frac{R}{\tilde{r}}\right)\right]\right)\right\} \tag{17}$$

Figure 3 illustrates the density profiles at R/θ = 10 for ρ_j/ρ_∞ = 1, 0.6, and 0.14.

A fourth-order Runge-Kutta scheme with automatic step-size control is used to integrate the equation (14). The infinite integration domain, $0 < r < \infty$ is divided into two finite domains: an inner domain $R \geq r \geq 0$ and an outer domain $r_\infty \geq r \geq R$, where R is the jet radius and r_∞ is a specified large radius where the gradients of the velocity and density are small. A shooting method is used to determine $\Omega(k)$ such that both P and $\frac{dP}{dr}$ are continuous at $r = R$. A parabolic complex zero-search

procedure was used to vary Ω for a specified k until the matching conditions were satisfied to a minimum accuracy within 10^{-10}.

RESULTS AND DISCUSSION

The near-injector region was investigated at axial locations along the jet represented by the jet parameter (R/θ) values of 10 $\left(\text{corresponding to } \frac{x}{2R}=1\right)$ and 5 $\left(\frac{x}{2R}=2.67\right)$, the value of 10 being closer to the injector exit. The density ratio, S, was varied from 1 (homogeneous shear-layer) to 0.14 (helium jet discharged into air), while varying the Froude number from infinity (no buoyancy) to 1.

The imaginary part of the complex frequency, Ω_i, is the temporal growth rate of the amplitude of the disturbance wave. The wavenumber k is the reciprocal of the wavelength. The temporal growth rate, Ω_i, the phase velocity, c_{ph}, and the wavenumber k were normalized using the shear-layer momentum thickness θ and the jet exit velocity U_j.

Effect of density ratio

In order to investigate the effect of an inhomogeneous shear layer only on the evolution of the jet instabilities with time, the Froude number was fixed at infinity (negligible gravity effect) and the density ratio (S) was varied from 1 to 0.14. The variation of the normalized temporal growth rate of the instabilities with the normalized wavenumber at $R/\theta = 10$ is presented in Figure 4. As the density ratio is reduced from 1 to 0.14, the range of unstable wavenumbers is increased by about 20%. This implies that the range of unstable wavelengths decreases when the gas jet density is reduced relative to the ambient gas density. The values of the temporal growth rates are also increased. The maximum growth rate is increased by about 21%, as the density ratio is decreased from 1 to 0.14. A decrease in the jet density results in the steepening of the density gradient in the shear layer, which leads to additional generation of vorticity, thus causing an increase in the disturbance growth rate. Also, the maximum growth rate occurs at a higher wavenumber with a decrease in the density ratio. The disturbance wave with the maximum growth rate is usually assumed to dominate the flow and so will be the disturbance that is observed in experiments. Thus, the above results imply that the disturbance wavelength that is observed in experiments is reduced (by about 8%) in the presence of a higher density ambient gas. Trends similar to those observed at $R/\theta = 10$ were observed at other axial locations.

Figure 5 depicts the variation of the phase velocity of the disturbances with wavenumber at $R/\theta = 10$. The phase velocity of the disturbance decreases with increasing wavenumber, indicating that the disturbances move with a velocity less than the jet velocity. Also, as the density ratio is reduced, the phase velocity decreases at all unstable wavenumbers. This also implies that the range of unstable frequencies increases as the density ratio is reduced; i.e., the frequency spectrum of the fluctuations now contains additional frequencies.

Effect of buoyancy

To study the effect of buoyancy on the jet temporal instability, the density ratio was fixed at 0.14 (corresponding to a helium jet injected into air), while the Froude number was varied from infinity (negligible buoyancy) to 1. Figures 6 and 7 display the variation of the temporal growth rates with wavenumber at R/θ = 10 and 5 respectively, as the Froude number (Fr) is reduced from infinity to 1. The temporal growth rates for the constant-density jet are included as a baseline for comparison. At all Froude numbers, the temporal growth rates exceed those of the constant-density jet at both $R/\theta = 10$ and 5. Also, the wavenumber corresponding to the maximum growth rates exceed those of the constant-density jet, even though this appears to be due to the change in density ratio. When the effect of changing the Froude number alone is considered, no significant change in the wavenumber corresponding to the maximum growth rate is observed, except for Fr = 1 at $R/\theta = 5$. Thus, it seems that gravity does not have a "significant" effect on the wavenumber corresponding to the maximum growth rate at Fr ≥ 1.

In Figure 6, at R/θ = 10, as the Froude number is reduced from infinity to 5, no significant change is observed in the values of the temporal growth rates. The growth rates are increased, though, as the Froude number is reduced further. The maximum growth rate increases by about 4.4%, when the Froude number is reduced from infinity to 2, but the range of unstable wavenumbers is not altered. At a Froude number of unity, the maximum growth rate is increased by about 18%, while the range of unstable wavenumbers is increased by a mere 3.4%. Results for various Froude numbers at a downstream location, are given in Figures 7 and 9. A comparison indicates that the temporal growth rates decrease for Froude numbers equal to infinity, 10, 5, and 2 as the jet proceeds downstream. The maximum growth rates decrease by about 7% for Fr = ∞ and 10, by about 6.4% for Fr = 5, and by about 2.3% for Fr =2. At Fr = 1, however, the maximum growth rate increases by about 14% while the wavenumber corresponding to the maximum growth rate is decreased by about 8%. As the Froude number is further reduced at this axial location, trends similar to those for R/θ = 10 are observed, except at Fr = 1 where there is a change in the wavenumber corresponding to the maximum growth rate.

Figures 8 and 9 display the variation of the phase velocities of the disturbances at various Froude numbers for R/θ = 10 and 5 respectively. At R/θ = 10, the influence of Froude number on the phase velocity, is to lower the phase velocities when compared to those of the constant density jet at most wavenumbers. But, at Fr = 1, for wavenumbers less than 0.02 the phase velocities are increased, and are even greater than 1. This suggests that disturbances at these low wavenumbers move with a velocity faster than the jet.

Subbarao and Cantwell (1992) observed the formation of "secondary vortex-ring-like structures" at a Richardson number of 1.6 (equivalent to Fr = 1.12) that accelerated rapidly upward within the core fluid and increased the entrainment and breakdown of the jet. The increased phase velocities at low wavenumbers may be associated with these secondary vortex-ring-like structures. As the jet moves downstream from R/θ = 10 to R/θ = 5, the increased phase velocities are evident at Fr = 2, with phase-velocities at Fr = 1 increasing further by about 18% for these low wavenumbers.

In order to understand the effect of buoyancy on the jet instability, the Froude number was reduced further to 0.2 for R/θ = 10 in Figures 10 and 11. It is seen that the growth rates and range of unstable wavenumbers are further increased with a reduction in Froude number. When Fr is reduced from infinity to 0.5, the maximum growth rate is increased by about 74% and the range of unstable wavenumbers is increased by about 14%, while the wavenumber corresponding to the maximum growth rate is decreased by about 8%. The maximum growth rate and range of unstable wavenumbers are increased by 187% and 31% respectively when Fr is reduced to 0.3 from infinity, while the wavenumber corresponding to the maximum growth rate is increased by about 8%. Reducing Fr from infinity to 0.2 results in a 350% increase in the maximum growth rate, 55% increase in the range of unstable wavenumbers and a 46% increase in the wavenumber corresponding to the maximum growth rate. Thus for Fr < 1, the growth rates are dramatically increased, signifying that the jet becomes highly unstable for buoyancy-driven jet flows. This observation is in agreement with the experiments conducted by Cetegen and Kasper (1996).

In Figure 11, the phase velocities are plotted as a function of wavenumber. As Fr is reduced below 1 to 0.2, the range of low wavenumbers corresponding to phase velocities greater than 1 is increased from 0.02 to 0.04. Also, the maximum phase velocity is almost doubled at Fr = 0.2. These results can be understood in light of the extra term in equation (14) due to the presence of gravity. The non-dimensional coefficient of the buoyancy term in this equation is

$$G = \frac{1}{Fr^2 \dfrac{R}{\theta}\left(\dfrac{\rho_\infty}{\rho_j} - 1\right)} = \frac{g}{\left(U_j^2 \;/\; \theta\right)} \qquad (18)$$

G is a non-dimensional number that compares the acceleration of the large-scale structures of the jet due to buoyancy to that due to inertial forces. The variation of G with Froude number for R/θ = 10 and 5 is indicated in Figure 12 at a density ratio of 0.14. At both R/θ = 10 and 5, for Froude numbers less than 1, G increases almost exponentially. Also, the values of G at R/θ = 5 are about double those at R/θ = 10. The increase in growth rates at Fr = 1 as the jet proceeds downstream from R/θ = 10 to R/θ = 5 is captured well by this variation in G. Thus, the effect of buoyancy at low Fr values is to cause the jet instability to increase dramatically. This could explain the reason for the abrupt breakdown of the jet large-scale structures noticed in helium-in-air experiments by Subbarao and Cantwell (1992) and Cetegen and Kasper (1996).

CONCLUSIONS

In this study, the instability characteristics of a low-density round gas jet injected into a high-density ambient gas were investigated. A linear temporal stability analysis was performed to solve for eigenvalues of the pressure disturbance equation obtained from the simultaneous solution of the equations of motion. The effects of buoyancy and density ratio on the evolution of the disturbances with time were determined.

A reduction in the density ratio steepens the density gradient in the shear layer, causing additional disturbance. Thus the temporal growth rates of the disturbances increase as the density ratio is decreased and the range of unstable wavenumbers also increases. The wavenumbers corresponding to the maximum growth rates also increase with decreasing density ratio. As the Froude number is reduced, the disturbance growth rates increase and the range of unstable wavenumbers also increase. A new non-dimensional number that compares the acceleration of the large-scale structures of the jet due to buoyancy to that due to inertial forces was found to play a significant role in the instability characteristics. At low Froude numbers, buoyancy causes the jet instabilities to increase exponentially which accounts for the abrupt breakdown of the jet large-scale structures observed in experiments.

ACKNOWLEDGMENTS

This work was supported by a grant from the NASA Microgravity Fluid Physics program.

REFERENCES

Buckmaster, J. and Peters, N., (1986) "The Infinite Candle and its Stability – A Paradigm for Flickering Diffusion Flames," *Twenty-First Symposium (International) on Combustion*, pp. 1829-1836.

Cetegen, B. M. and Kasper, K. D., (1996) "Experiments on the Oscillatory Behavior of Buoyant Plumes of Helium and Helium-Air Mixtures," *Physics of Fluids*, Vol. 8, No 11, pp. 2974-2984.

Cetegen, B. M., (1997-1) "Behavior of Naturally Unstable and Periodically Forced Axisymmetric Buoyant Plumes of Helium and Helium-Air Mixtures," *Physics of Fluids*, Vol. 9, No 12, pp. 3742-3752.

Cetegen, B. M., (1997-2) "Measurements of Instantaneous Velocity Field of a Non-Reacting Pulsating Buoyant Plume by Particle Image Velocimetry," *Combustion Science and Technology*, Vol. 123, pp. 377-387.

Cetegen, B. M. and Dong, Y. (2000) "Experiments on the Instability modes of Buoyant Diffusion Flames and Effects of Ambient Atmosphere on the Instabilities," *Experiments in Fluids*, Vol. 28, pp. 546-558.

Chen, L. D., Seaba, J. P., Roquemore, W. M., and Goss, L. P. (1988) "Buoyant Diffusion Flames," *Twenty-Second Symposium (International) on Combustion,* The Combustion Institute, pp. 677-684.

Cohen, J. and Wygnanski, I. (1987) "The Evolution of the Instabilities in the Axisymmetric Jet. Part 2. The Flow Resulting from the Interaction between Two Waves," *Journal of Fluid Mechanics*, Vol. 176, pp. 221.

Gebhart, B. (1993) *Heat Conduction and Mass Diffusion*, McGraw-Hill, New York.

Hamins, A., Yang, J. C. and Kashiwagi, T., (1992) "An Experimental Investigation of the Pulsation Frequency of Flames," *Twenty-Fourth Symposium (International) on Combustion/The Combustion Institute*, pp. 1695-1702.

Jendoubi, S. and Strykowski, (1994) "Absolute and Convective Instability of Axisymmetric Jets with External Flow," *Physics of Fluids*, Vol. 6, No. 9, pp. 3000-3009.

Kyle, D. M. and Sreenivasan, K. R., (1993) "The Instability and Breakdown of a Round Variable-Density Jet," *Journal of Fluid Mechanics*, Vol. 249, pp. 619-664.

Michalke, A. (1984) "Survey on Jet Instability Theory," *Progress in Aerospace Sciences*, Vol. 21, pp. 159-199.

Monkewitz, P. A. and Sohn, K. D. (1988) "Absolute Instability in Hot Jets," *AIAA Journal*, Vol. 26, pp. 911-916.

Pasumarthi, K. S., (2000) "Full Field Scalar Measurements in a Pulsating Helium Jet Using Rainbow Schlieren Deflectometry," *MS Thesis,* University of Oklahoma, Norman, Oklahoma.

Raynal, L., Harion, J.-L., Favre-Marinet, M. and Binder, G. (1996) "The Oscillatory Instability of Plane Variable-Density Jets," *Physics of Fluids*, Vol. 8, No. 4, pp. 993-1006.

Richards, C. D., Breuel, B. D., Clark, R. P. and Troutt, T. R., (1996) "Concentration Measurements in a Self-Excited Jet," *Experiments in Fluids*, Vol. 21, pp. 103-109.

Schlichting, H. (1979) *Boundary Layer Theory*, 7th edition, McGraw-Hill, New York.

Subbarao, E. R. and Cantwell, B. J., (1992) "Investigation of a Co-Flowing Buoyant Jet: Experiments on the Effects of Reynolds Number and Richardson Number," *Journal of Fluid Mechanics*, Vol. 245, pp. 69-90.

Yu, M.-H. (1990) "Local and Global Instability of Heated 2-D Jets and Wakes," *PhD Dissertation,* University of California.

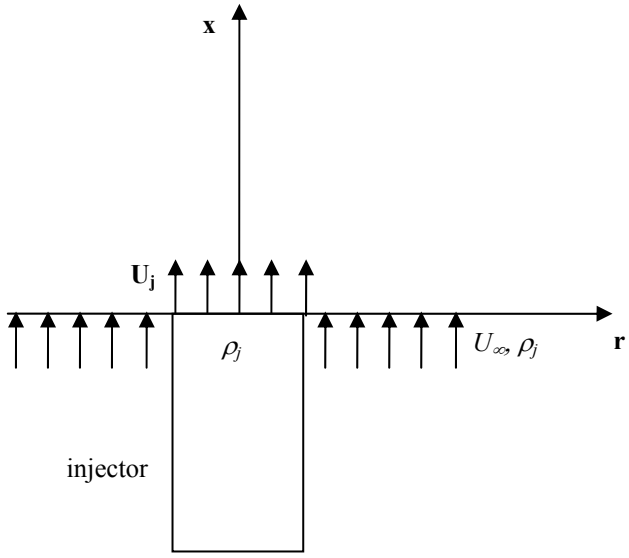

Figure 1: Schematic of a low-density round gas jet injected vertically upwards into a high-density ambient gas

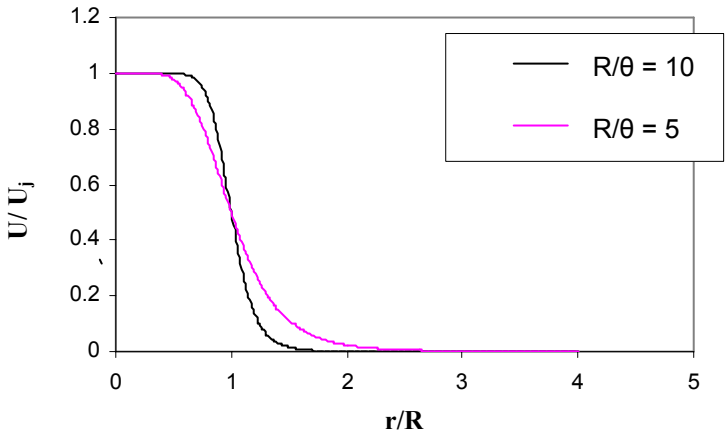

Figure 2: Nondimensionalized basic jet velocity profile for S = 1 at R/θ = 10 and 5

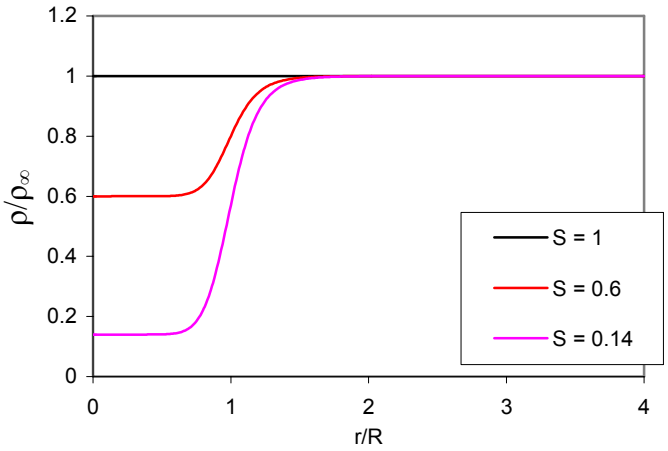

Figure 3: Density profile vs r/R for R/θ = 10 at S = 1, 0.6 and 0.14

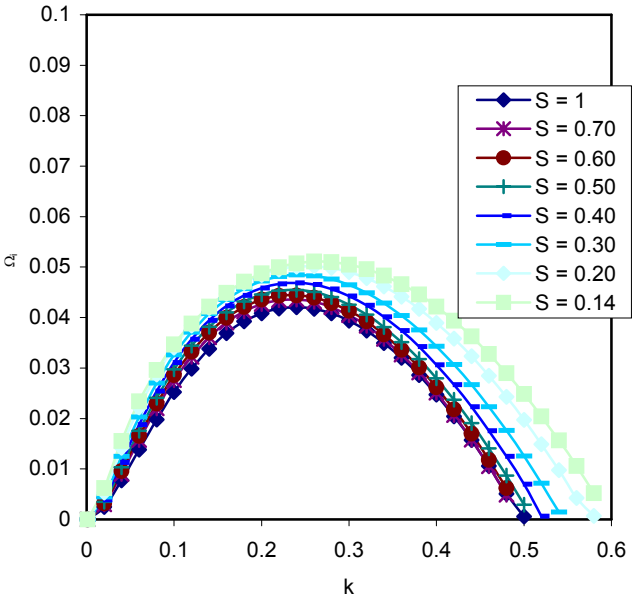

Figure 4: Temporal growth rate Ω_i as a function of wavenumber k for m = 0, R/θ = 10, Fr = infinity, S = 1, 0.7, 0.6, 0.5, 0.4, 0.3, 0.2, 0.14

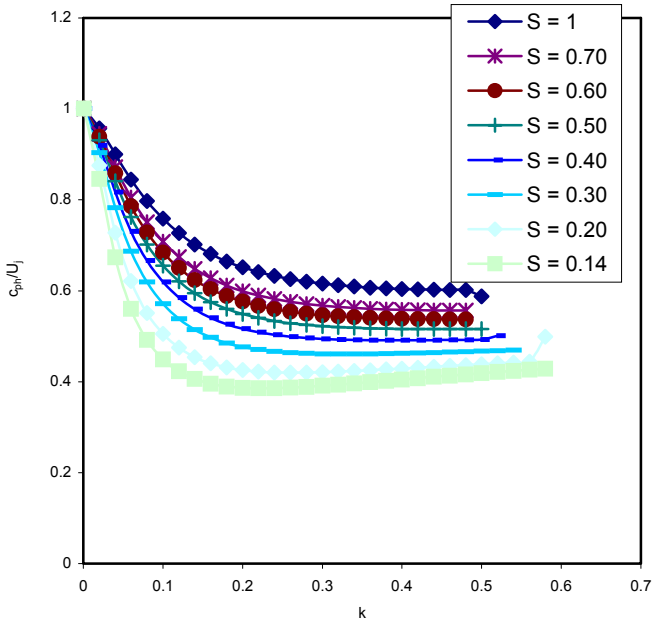

Figure 5: Phase velocity c_{ph} as a function of wavenumber k for m = 0, R/θ = 10, Fr = infinity, S = 1, 0.7, 0.6, 0.5, 0.4, 0.3, 0.2, 0.14

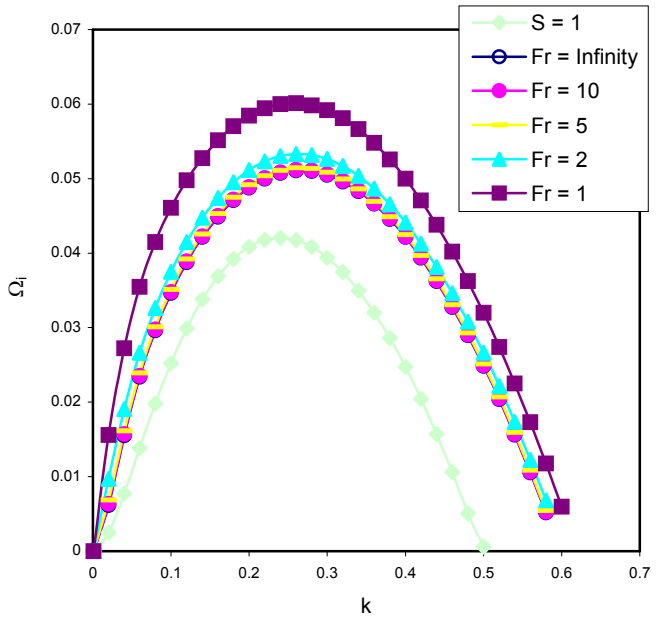

Figure 6: Temporal growth rate Ω_i as a function of wavenumber k for m = 0, R/θ = 10, S = 1 and 0.14, Fr = Infinity, 10, 5, 2, 1

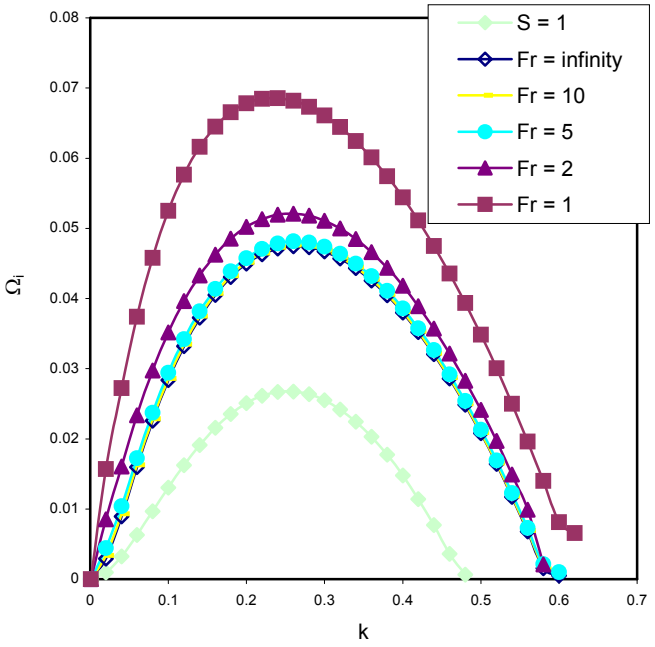

Figure 7: Temporal growth rate Ω_i as a function of wavenumber k for m = 0, R/θ = 5, S = 1 and 0.14, Fr = Infinity, 10, 5, 2, 1

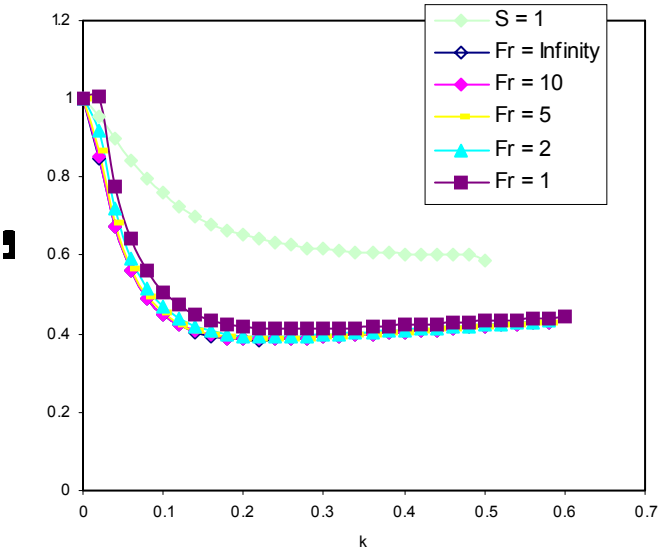

Figure 8: Phase velocity c_{ph} as a function of wavenumber k for m = 0, R/θ = 10, S = 1 and 0.14, Fr = Infinity, 10, 5, 2, 1

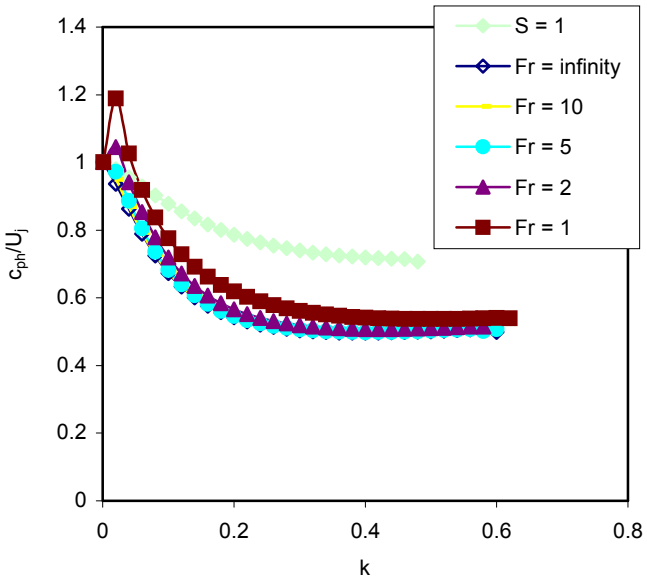

Figure 9: Phase velocity c_{ph} as a function of wavenumber k for m = 0, R/θ = 5, S = 1 and 0.14, Fr = Infinity, 10, 5, 2, 1

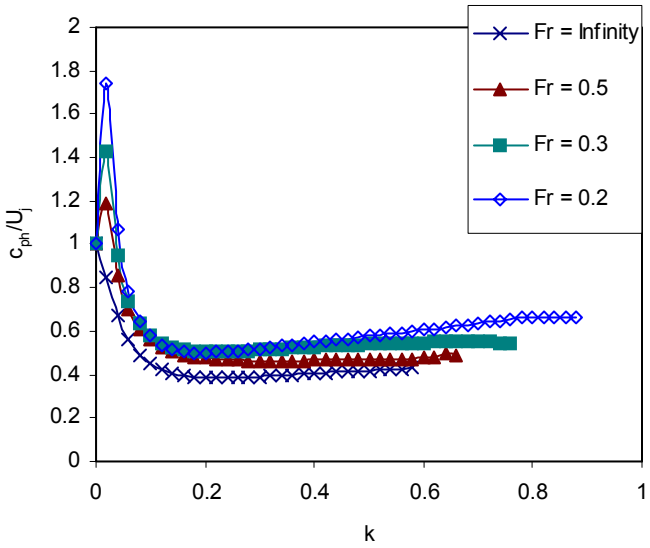

Figure 11: Phase velocity c_{ph} as a function of wavenumber k for m = 0, R/θ = 10, S = 0.14, Fr = Infinity, 0.5, 0.3, 0.2

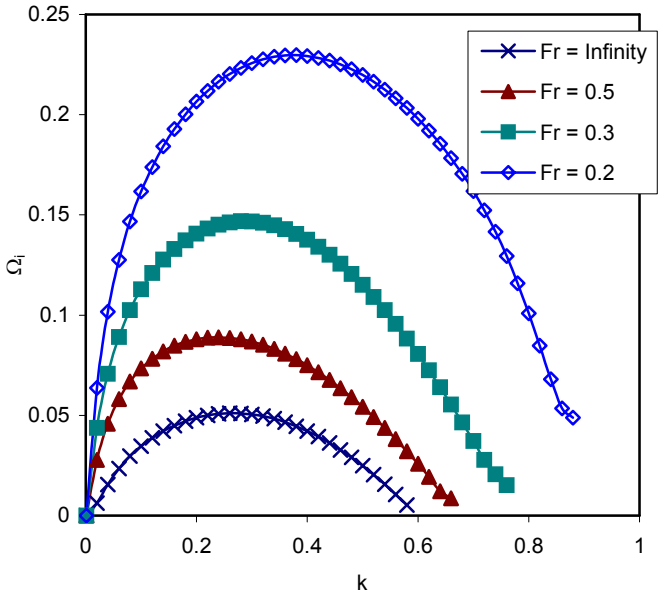

Figure 10: Temporal growth rate Ωi as a function of wavenumber k for m = 0, R/θ = 10, S = 0.14, Fr = Infinity, 0.5, 0.3, 0.2

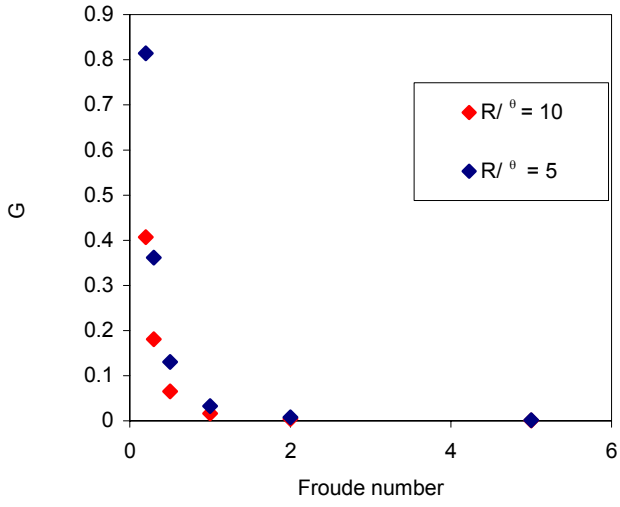

Figure 12: G vs Froude number for S = 0.14 at R/θ = 10 and 5